THREE-DIMENSIONAL COMPUTATIONAL SIMULATION OF MULTISCALE MULTIPHYSICS CELLULAR/PARTICULATE PROCESSES IN MICROCIRCULATORY BLOOD FLOW

by

KOOHYAR VAHIDKHAH

A dissertation submitted to the

Graduate School—New Brunswick

Rutgers, The State University of New Jersey

In partial fulfillment of the requirements

For the degree of

Doctor of Philosophy

Graduate Program in Mechanical and Aerospace Engineering

Written under the direction of

Professor Prosenjit Bagchi

And approved by

_____

_____

_____

_____

New Brunswick, New Jersey

OCTOBER, 2015

ABSTRACT OF THE DISSERTATION

Three-dimensional computational simulation of multiscale multiphysics cellular/particulate processes in microcirculatory blood flow

By

KOOHYAR VAHIDKHAH

Dissertation Director:

Professor Prosenjit Bagchi

Computational modeling and simulation is considered to study the concurrent multiscale/multiphysics phenomena associated with cellular/particulate transport in microcirculatory blood flow. The model integrates microhydrodynamics of different blood cells, complexity of vascular geometry, and nanoscale adhesive interactions. A finite element method (FEM) is used to model the cell membrane deformation with high accuracy, and is coupled to the bulk flow motion via a front-tracking method. The geometric complexities are simulated using a sharp-interface immersed boundary method, and the molecular adhesion is coarse-grained via a Monte Carlo method.

The following sequence of problems is addressed: (a) Hydrodynamic interaction between a platelet and a red blood cell (RBC) in a dilute suspension: 3D simulations of pairwise interaction between a platelet and an RBC in a wall-bounded shear flow are conducted. Based on the results, a mechanism of continual platelet drift towards the vessel wall is proposed. (b) Platelet transport and dynamics in blood flow: 3D simulations are considered to study the transport of platelets in semi-dense suspension of flowing RBCs. It is shown that the anisotropic diffusion of platelets contributes to the formation of platelet clusters, and may act as a hydrodynamic precursor to blood clot formation. (c) Microparticle shape effects on their transport and dynamics in blood flow: The shape effect of microscale targeting drug carrier particles on their margination, near-wall dynamics, and adhesion is quantified and explained by individual particle dynamics and interaction with RBCs. It is suggested that the local hemorheological conditions of the targeted site should be taken into account while selecting the optimum. (d) Blood flow in stenosed microvessels: 3D simulations of cellular motion through stenosed microvessels are considered. The Fahraeus-Lindqvist effect is shown to be significantly enhanced, due to the asymmetric distribution of the RBCs caused by the stenosis geometry. (e) Adhesion of microparticles in microvessels - role of RBCs and microparticle deformability: 3D simulations of the adhesion of deformable drug carrier particles in the flow of semi-dense RBC suspension through microvessels are conducted. It is shown that both the presence of RBCs and the particle deformability have a dual role in microparticle adhesion.

Acknowledgements

I would like to thank my adviser, Prof. Prosenjit Bagchi for his invaluable guidance, support and encouragement throughout my doctoral study. He has been an excellent mentor, and I significantly benefited from his academic experience and knowledge in this field. I also would like to thank my committee members, Dr. Drazer, Dr. Shojaei-Zadeh, and Dr. Zahn for providing me with valuable suggestions to improve my dissertation.

My sincere thanks and gratitude go to my family, especially to my parents, for their support at every stage of my life. Without them, my accomplishments would not be possible. I would like to specifically thank my wife, Homeyra, for the sacrifices she made for me throughout my studies at Rutgers University.

Lastly, I would like to thank all my colleagues at Rutgers University, in particular, Ali, Murthy, Dan, and Pete. Further, I would like to thank my dear friends Dana, and Pooya for always being there for me.

This research is partly funded by Grant No. NIH R01 HL103419 and NSF CBET-0846293. Computational support from the NSF-funded Teragrid resources at TACC is acknowledged.

Dedication

To Homeyra

Table of Contents

List of Tables

List of Figures

Chapter 1

Introduction

1.1 Circulatory System, Blood, and Blood Cells

The human circulatory system, which is made up of the heart, blood vessels, and the blood, is responsible for the transport of oxygen and nutrients. The entire circulation system can be divided into micro- and macrocirculation. Macrocirculation refers to the flow of blood in larger blood vessels, such as the aorta, and large arteries and veins, while microcirculation refers to blood flow in smaller vessels such as arterioles, venules, and capillaries. A vessel diameter of $\sim$500 μm is generally considered as the criterion to differentiate between micro- and macrocirculation.

Blood is a particulate suspension that is made up of different cellular components, namely erythrocytes (red blood cells or RBCs), leukocytes (white blood cells or WBCs), and thrombocytes (platelets) suspended in a liquid called plasma. Figure 1.1 shows a scanning electron microscope image of different blood cells. In addition to these cells, many sub-micron and nanoscale particulate components such as proteins, lipids, minerals, and enzymes are contained in plasma. Plasma, which constitutes about 55% of total blood volume, is almost 90% water (by volume).

The RBCs constitute the major particulate component of blood accounting for about 40 - 45% of the total blood volume. The volume fraction of RBCs is termed 'hematocrit'. The resting shape of an RBC is a biconcave disk, with an end-to-end

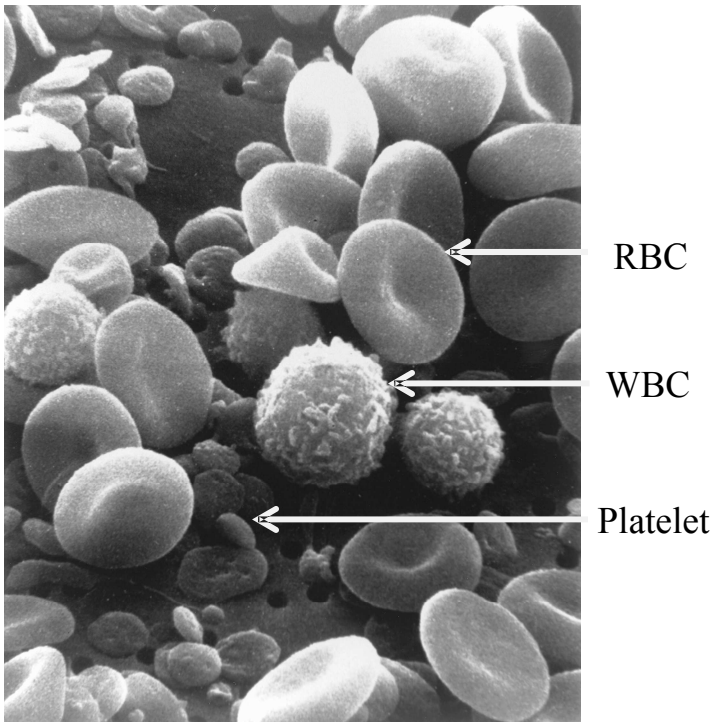

Figure 1.1: A scanning electron microscope image of red blood cells (RBCs), white blood cells (WBCs), and platelets. Image source: National Cancer Institute.

length of about 8 μm, and a thickness of nearly 2 μm. An RBC does not have a nucleus and is a fluid drop of hemoglobin enclosed by an elastic membrane. Hemoglobin is more viscous than plasma and facilitates the delivery of oxygen to the tissues. The RBC membrane is made of a lipid bilayer and a cytoskeleton, and is highly deformable. This property is essential for the transport of oxygen and nutrients to tissues, as it enables the RBCs to easily deform and squeeze through capillaries of diameters as small as 4 μm.

WBCs are the cells of the immune system that take part in protection against infectious disease. In healthy conditions, they constitute about 1% of blood volume; and in response to disease, the number of them is increased. During immune response, WBCs adhere to the site of injury inside the blood vessel. Then, they deform and

spread on the cell lining on the blood vessel wall (endothelial cells or ECs), and thereafter transmigrate through the endothelium. Following transmigration, the processes that are involved in repairing the damaged tissue take place. In the undeformed state, a WBC is nearly rigid and exhibits a spherical shape with a diameter of about 8-20 μm, and flows with minimal deformation. However, the significant excess area of the WBC membrane in the form of ruffles and folds enables it to undergo considerable deformation under external adhesive forces during inflammatory conditions [107].

Platelets (or thrombocytes) constitute an essential component of human blood; they play a major physiological role in the formation of a blood clot. Clotting is an important phenomenon that precedes the process of wound healing. Similar to WBCs, platelets detect the site of injury in blood vessels and adhere to it. Following adhesion, they form an aggregate which results in coagulation. A platelet has a disk-like shape, with an end-to-end length of about 3.6 μm and a thickness of nearly 1.1 μm. Prior to adhesion, platelets behave like nearly rigid particles in the blood flow. The number ratio of platelets to RBCs in normal conditions is about 1:10 to 1:20, and thus their volume fraction is negligible with respect to that of the RBCs [8].

1.2 Some Classical Hydrodynamic Processes in Microcirculatory Cellular Blood Flow

Several physiological phenomena in microcirculatory blood flow that have been addressed by principles of fluid mechanics are briefly discussed in the following sections.

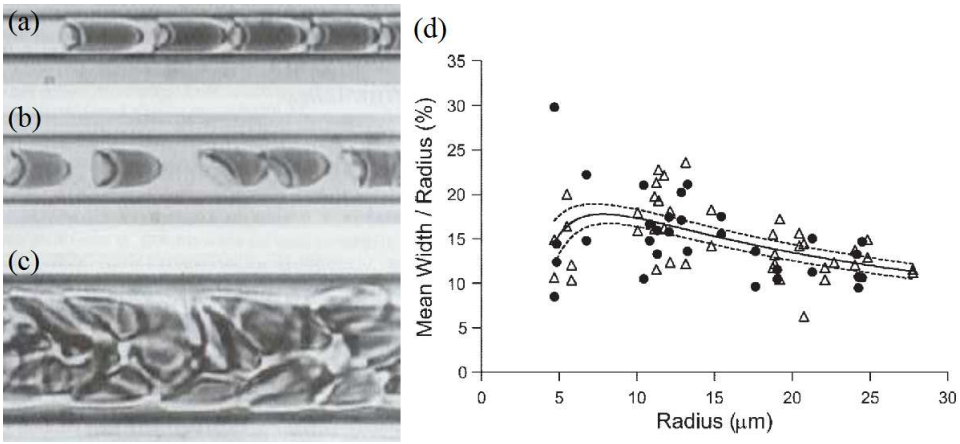

Figure 1.2: Flow of human red blood cells moving through glass tubes with approximate diameters of 4.5 μm (a), 7 μm (b), and 15 μm (c), in the experiments by Alex R. Pries [4]; the flow direction is from left to right. (d) Cell-free layer width as a fraction of arteriolar radius [83].

1.2.1 Lateral Migration of RBCs and Formation of the Cell-Free-Layer (CFL)

Deformability of RBCs is a key factor in the flow of blood in microcirculation. In a wall-bounded shear flow, the RBCs deform asymmetrically due to increased retardation of the cell motion in the vicinity of the wall. Such an asymmetric deformation results in a lift that drives the RBC away from the wall. A hydrodynamic lift also exists in a parabolic flow in absence of a wall as a result of shape asymmetry, and drives the cell laterally towards the lower flow gradient. In a confined geometry such as a cylindrical tube both wall effects and flow gradient effects are present. Therefore, an individual cell, while moving longitudinally with the flow, also continuously migrates in the lateral direction away from the wall and towards the center of the vessel [5].

Figure 1.2(a-c) shows the flow of RBCs in glass micro-tubes [4]. Figure 1.2(a) shows that in narrow capillaries with diameters significantly less than 10 μm, RBCs considerably deform into a 'parachute-like' shape in order to move through the vessel.

It is seen that an RBC fills the entire cross-section of the vessel, and thus one cell moves after another in a 'single-file' motion. Figure 1.2(b) shows that an increase in the vessel diameter results in the formation of a layer of plasma between the RBC and the wall, which is called the 'cell-free layer' or 'CFL'. An increased asymmetry in the shape of RBCs is is also observed in this figure. With a further increase in the vessel diameter, as shown in Figure 1.2(c), the regime of motion is converted to 'multi-file' motion, where the RBCs exhibit a 'slipper-like' shape. In this case, due to the significant asymmetry in cell shape, an RBC tends to significantly migrate towards the vessel centerline. However, the interaction with other cells prevents a continuous migration away from the wall. In fact, constant hydrodynamic interactions between particulate components of a suspension under shear result in a particulate dispersion, which on a collective basis lead to a shear-induced diffusion [84, 85]. In the case of RBCs, a balance between the shear-induced diffusion and the migration away from the wall in the semi-steady state results in the formation of a cell-free layer near the wall and an 'RBC-rich zone' near the vessel center.

Experimental measurements of the CFL thickness in microvessels of different diameters have shown an interesting nonlinear behavior. Figure 1.2(d) shows the ratio of the CFL thickness to the blood vessel radius as a function of the vessel size [83]. It is seen that with an increase in the vessel size, the ratio initially increases, and then shows a decreasing trend. Such behavior, which is attributed to the change in the regime of RBC motion [83], plays an important role in the nonlinear characteristics of blood flow in microvessels, as discussed in the following section.

1.2.2 Fahraeus-Lindqvist and Fahraeus Effects

At the macroscopic level, the size of an RBC is negligible with respect to the vessel diameter. Thus, from this perspective, the flow behaves as a single-phase Newtonian fluid. At the microscopic level, however, the motion and deformation of each cell become important. The resulting behavior of blood is then non-Newtonian. An example of the non-Newtonian behavior of blood is the Fahraeus-Lindqvist effect. To present this effect, we define the apparent or relative viscosity of blood as $\mu_{\text{rel}} = Q_P/\overline{Q}$ where Q_P is the mean flow rate of plasma (i.e., no RBC) in the blood vessel, and $\overline{Q}$ is the mean flow rate in presence of the cells. The Fahraeus-Lindqvist effect, as shown in Figure 1.3(a) refers to a decrease in the apparent viscosity of blood with decreasing the vessel diameter. As the tube diameter is decreased below ~ 500 μm, the relative viscosity is reduced and reaches a minimum at ~ 10 μm. Further decrease results in a significant increase in the viscosity. A related phenomenon called Fahraeus effect, which is shown in Figure 1.3(b), refers to a decrease in hematocrit as the vessel diameter is decreased from ~ 500 to ~ 10 μm, and an increase in hematocrit upon further decrease in diameter.

The above two phenomena are attributed to the variations in the CFL thickness with the vessel diameter. As the microvessel diameter is decreased below ~ 500 μm, the CFL fraction of the blood vessel increases (see Figure 1.2(d)). This implies a reduction in the RBC-rich core, which is more viscous than plasma, and consequently a decrease in the apparent viscosity of blood. Additionally, as the number of cells inside the microvessel is reduced due to a decrease in the vessel size, the friction between the adjacent cells is also decreased. Such reduction contributes to the decrease in the apparent viscosity of blood. Further decrease in the blood vessel diameter below $\sim$

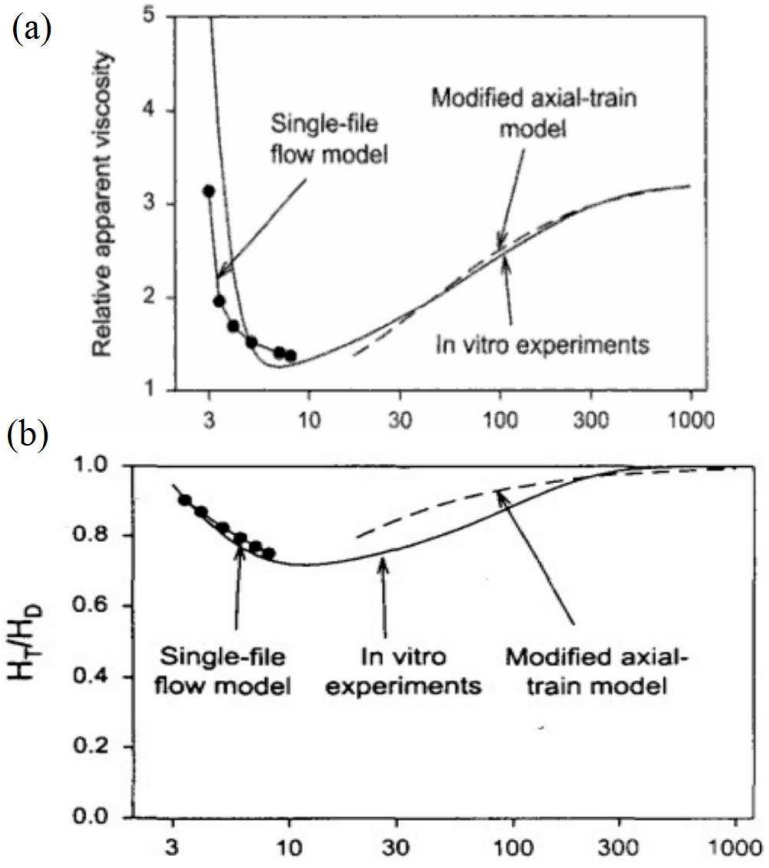

Figure 1.3: (a) Effect of tube diameter on the relative apparent viscosity for 45% volume fraction of RBC. Solid curve is the empirical fit to data. (b) Effect of tube diameter on the ratio between tube hematocrit, H_T and discharge hematocrit H_D [7].

10 μm converts the regime of motion of RBCs to a single-file one. In this range, the CFL fraction decreases with a decrease in the vessel diameter, which results in an increase in the apparent viscosity of blood. Note that the significant rate of increase that is observed in Figure 1.3(a) is due to the elimination of CFL and the high friction between the RBC membrane and the vessel wall.

Similar to the Fahraeus-Lindqvist effect, the Fahraeus effect is also explained by the dependence of the CFL fraction to the vessel size. A larger cell free layer indicates a lower hematocrit and vice versa. Therefore, the initial increasing and the subsequent decreasing behavior that is observed in Figure 1.2(d) for CFL results in an initial decrease followed by an increase in hematocrit as the vessel diameter increases [4, 7].

1.2.3 Platelets Margination

Several experiments on particulate transport in blood flow have shown that platelets tend to concentrate near the vessel walls [12, 13, 15]. These studies have also shown that the near-wall excess of the platelets does not occur in absence of the RBCs [14,16]. Figure 1.4 shows the experimental results on concentration profiles of RBCs and platelets across a tube, demonstrating the near-wall accumulation of the platelets. The formation of an RBC-rich zone that was mentioned in Section 1.2.1 is also observed in this figure. The phenomenon of platelets drift from the RBC-rich zone towards the CFL near the vessel walls is known as 'margination'.

Several hypotheses have been proposed to explain the margination of platelets. For instance, one is the volume exclusion phenomenon where it is suggested that the platelets are pushed towards the wall by the lateral motion of the RBCs toward

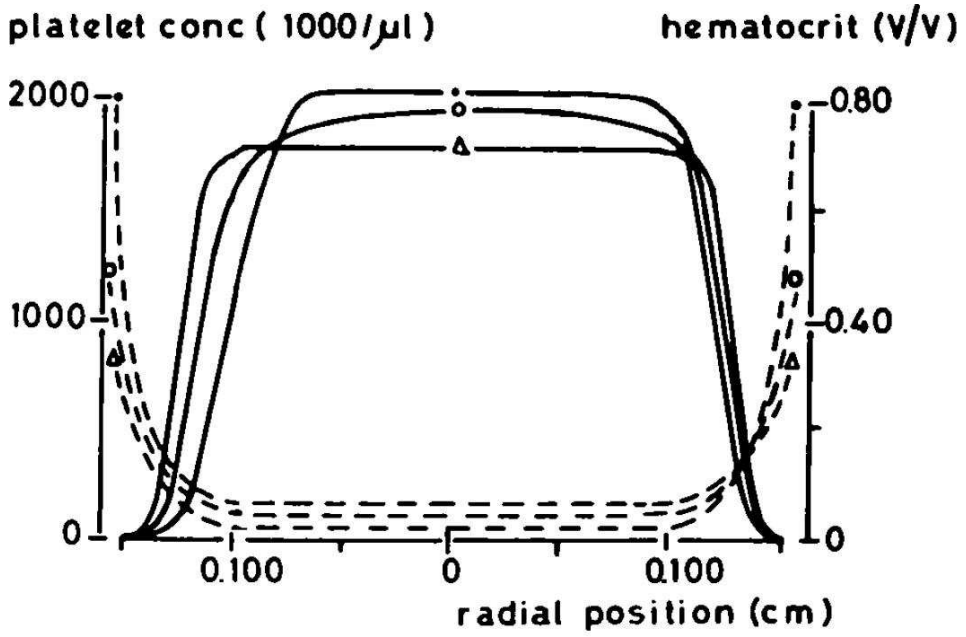

Figure 1.4: RBCs (solid lines) and platelets (dashed lines) lateral concentration profiles in a glass tube at different shear rates [16].

the center of the vessel [16–24]. Another mechanism that is proposed is the spatial dependency of the rate of collision with RBCs. In a shearing flow, the continuous collisions between the RBCs and platelets result in a lateral dispersal of the platelets. As mentioned in Section 1.2.1, on a collective basis, such lateral spreading results in a shear-induced diffusion. Since the RBC concentration is decreasing from the vessel center towards the wall, the platelets laterally drift from the RBC-rich core, where the collision rate is high, towards the CFL, where the collision rate is low [22–24, 28, 29, 159].

1.3 Multiscale/Multiphysics Processes in Microcirculatory Cellular Blood Flow

Indeed, there are many processes of physiological importance in microcirculatory blood flow that, as noted above, can be addressed by classical fluid mechanics. However, there are also phenomena that are multiscale/multiphysics in nature, and, thus, cannot be addressed purely from a fluid mechanics standpoint. Two examples are presented in the following sections:

1.3.1 Thrombogenesis and Microvascular Stenosis

Thrombogenesis refers to the formation of a blood clot (thrombus) which is the first stage of the process of wound healing. Platelets are the main cellular components of blood that participate in thrombogenesis. The surface of a platelet is populated with adhesion molecules that can specifically bind to molecules that are exposed to the flow in case of a disruption in the endothelial cell lining on the vessel wall. This enables the platelets to detect the site of vascular injury, and following adhesion, form a thrombus on the vessel wall.

Blood clotting can also have a detrimental effect as in the case of the abnormal formation and growth of a thrombus (thrombosis), which results in a vascular stenosis and eventual blockage of blood flow.

Figure 1.5 demonstrates the thrombogenic cascade. As shown in the figure, thrombogenesis, involves many processes that are highly multiscale/multiphysics. These processes are briefly explained below.

At the macroscale, a vascular stenosis disrupts the tranport of oxygen/nutrient to

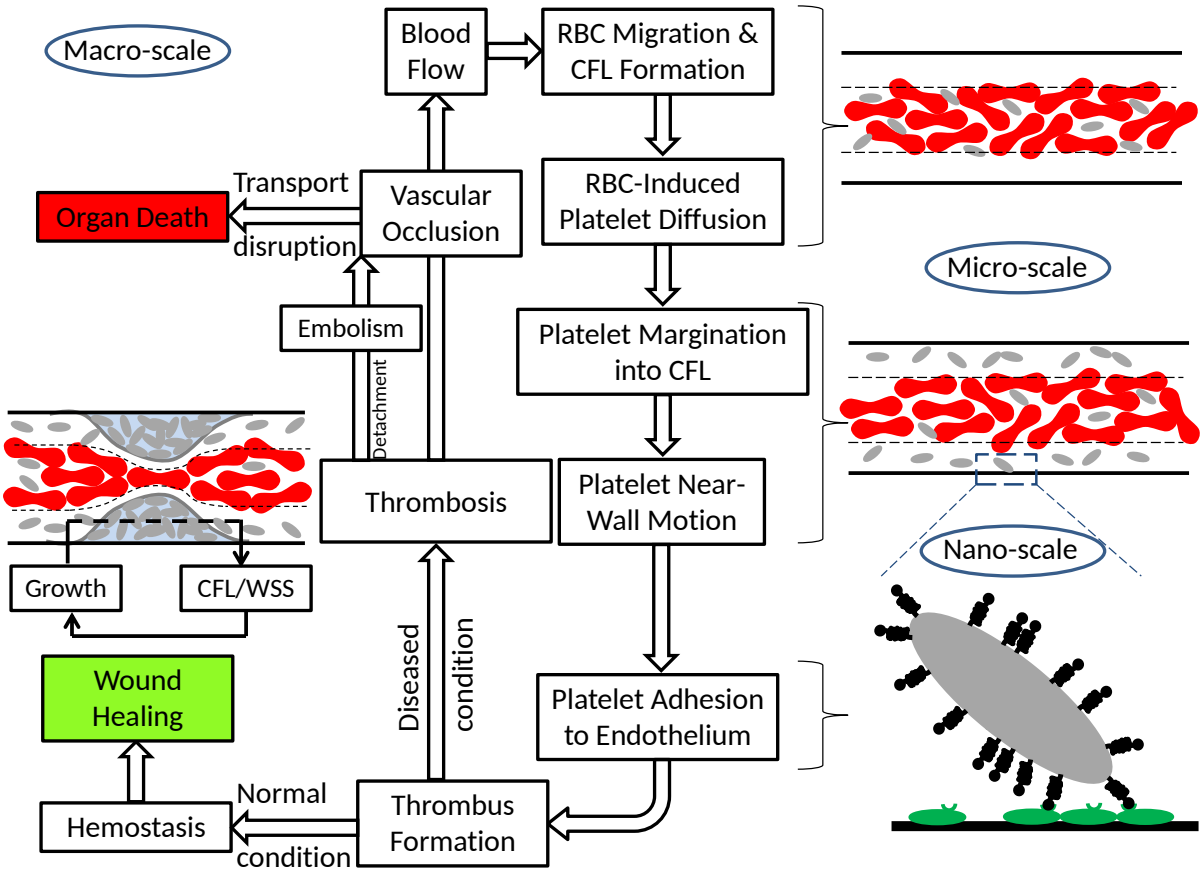

Figure 1.5: Thrombogenic cascade as an example of multiscale/multiphysics processes in circulatory blood flow.

tissues by blocking the passage of blood flow. Vascular occlusion can also occur when a blood clot breaks free and forms a mobile embolus that blocks the flow downstream (embolism) [9–11]. Obstruction of the blood flow can have severe consequences such as organ malfunction or even death. In case of the vessels supplying blood to the heart and brain, such pathological conditions may result in a heart attack or stroke.

At the microscale, fluid flow characteristics are of great importance in thrombogenesis. As mentioned earlier, the formation of a thrombus is associated with a rupture in the endothelial cells on the blood vessel walls. It is known that ECs respond to fluid flow characteristics, especially the wall shear stress (WSS) [11,64–67,89,90], and thus, complex flow conditions (e.g. flow reversal) can affect the growth of a thrombus [92–94]. Not only the mean shear stress, the time-dependent flow oscillations have also been observed to affect the EC response and consequently the thrombogenesis [91, 93]. The fluid flow itself is significantly affected by the geometry of a thrombus. For instance, the CFL thickness is altered about the constriction [78]. Variations in CFL result in changes in wall shear stress. It could also affect the near-wall accumulation of platelets.

In addition to the mean flow features such as CFL and WSS, time-dependant oscillations of the flow are also affected by the interactions between RBCs and the stenosis geometry. These phenomena directly determine the growth, and consequently the geometry of the thrombus itself. Additionally, a number of processes discussed in the previous section are also associated with thrombogenic cascade at microscale: migration of RBCs toward the center of the vessel, formation of a near-wall CFL, and margination of platelets into the CFL. Such phenomena are of great importance as they result in the platelet–wall proximity which is essential for platelet adhesion.

At the nanoscale, the adhesion of platelets to the vessel wall is facilitated through the interaction between adhesion molecules. Cell adhesion molecules or CAMs, are proteins located on the surface of a cell, that play the key role in adhesion of the cell to other cells or to the vessel wall. These proteins are transmembrane 'receptors' that are composed of three domains: (i) intracellular domain that interacts with the cell cytoskeleton, (ii) transmembrane domain, and (iii) extracellular domain that interacts with other CAMS, such as the ones that are located on the substrate (see the schematic at the bottom right of the Figure 1.5). Two important families of the CAMS are selectins and integrins that are involved in blood cells adhesion. For instance, selectins are expressed on WBC membrane (L- and P-selectins such as P-selectin-glycoprotein ligand-1 or PSGL-1) and endothelial cells (P- and E-selectins) and mediate WBC adhesion and rolling [26,27]; and integrins are involved in platelet adhesion.

In case of an injury to a blood vessel, the endothelium that is attached to the subendothelial collagen by a glycoprotein called 'von Willebrand factor' or 'vWF', is disrupted and vWF is exposed to the flow. Adhesion of a flowing platelet is then mediated via binding interaction between the α subunit of Glycoprotein Ib (GPIb) receptors on the platelet surface and the A1 domain of subendothelial collagen-bound vWF. The GPIbα-vWF-A1 binding extends the duration of the platelet-vessel wall contact and leads to the formation bonds between other CAMs such as integrin $\alpha_2\beta_1$ with subendothelial collagen, which in turn results in platelet firm adhesion [25].

The adhesive bonds are constantly being formed and broken by a reversible chemical reaction. Under a flowing environment, the hydrodynamics also affect the bond breakage as the bound state of the adhesion molecules is stretched and may be broken,

under the application of an external force. Therefore, the chemical reaction is intricately coupled to the platelet dynamics, and in turn RBC hydrodynamics. Platelet adhesion is then followed by the secretion of chemicals (e.g. thrombin) that mediates significant morphological changes in the shape of adhered platelets. Following this process, which is called platelet activation, a platelet aggregate is formed on the site injury.

Clearly, the above discussion shows that the role of platelets in thrombogenesis cannot be addressed solely based on fluid mechanics, as many of the involved processes are not only multiphysics in nature, but also highly inter-coupled at different scales.

1.3.2 Drug Delivery and Biomedical Targeting

The human circulatory system is subjected to various pathological conditions such as metastasis of tumor cells, development of athero/arteriosclerotic plaque, and –as discussed in the previous section– formation of micro-thrombus and micro-emboli. In treatment of these severe pathological conditions, targeted delivery of therapeutics to the site of injury with the highest possible efficiency is desired so that the potential adverse effect on the surrounding healthy tissues is minimized. Similarly, in biomedical imaging, efficient delivery of contrast agents to targeted cells is required. To successfully achieve the goal of efficient delivery of such agents, they are combined with specific receptor molecules that can bind to overexpressed ligands at the site of damage. Since micro- and nanoparticles can be engineered to carry different molecules, they are widely used as vascular targeting carriers (VTCs) of therapeutics and imaging agents [32, 33].

Figure 1.6 shows the drug delivery cascade, in which the following processes are

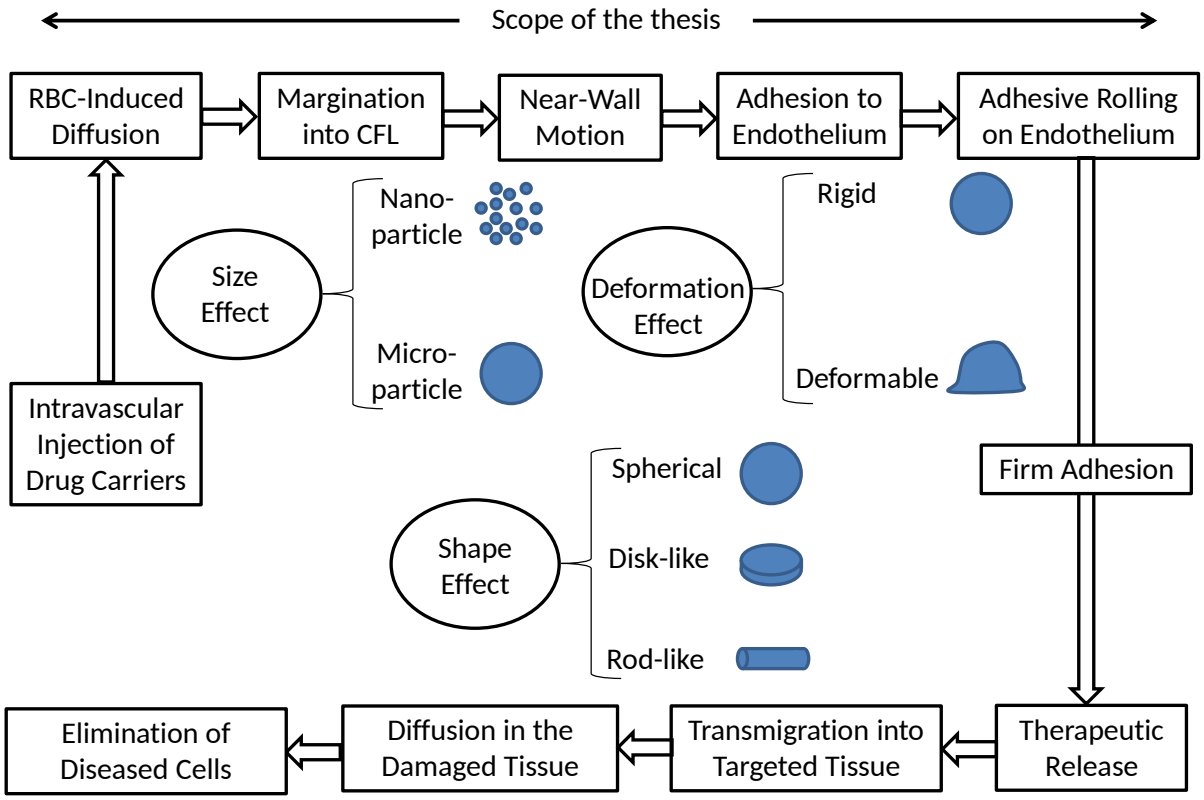

Figure 1.6: Drug delivery cascade.

involved: To inhibit the disease progression, VTCs are injected into blood vessels. At the microscale, similar to the platelet transport in the thrombogenic cascade, the processes through which VTCs are brought into close proximity of the damaged tissue are the RBC-induced diffusion and margination into the CFL. Inside the CFL, frequent physical contacts between the surface of the marginated VTC and the vessel wall at the targeted site facilitates the binding reaction between adhesion molecules at the nanoscale. The molecular bond dynamics result in the adhesive rolling of VTCs on the endothelium which is followed by firm adhesion. Thereafter, the VTC releases therapeutic agents. The drug molecules, then, transmigrate through the endothelial walls and diffuse into the damaged tissue and begin the elimination of the targeted diseased cells to repair the tissue.

To efficiently deliver the required amount of drug dosage to the injured tissue, one should design a VTC that satisfies several criteria at different scales: (i) At the microscale, the designed VTC should quickly marginate from the RBC-rich zone towards the CFL. The longer the VTCs stay in circulation, the longer they are exposed to the immune system which can eliminate them before successful delivery of therapeutics (as they are considered as 'foreign' substance). (ii) At the sub-micron scale, following margination and entry into the CFL, a 'well-designed' VTC should make frequent physical contacts with the vessel wall to increase the likelihood of adhesion to the targeted site. (iii) Subsequently, at the nanoscale the adhesive motion of the VTC on the vessel wall takes place. It is important for the VTC to stably adhere to the targeted site against the hydrodynamic forces.

From the above discussion, it is clear that designing an efficient VTC is an extremely challenging problem as it needs to take into consideration a plethora of multiscale/multiphysics issues. One aspect of the design is the determination of optimal physical characteristics of a VTC. These physical characteristics involve the *shape* (e.g., spherical, ellipsoidal, disk- and rod- like), *size* (from nano- to micron-sized carriers) and *deformability*. As such, a great deal of research is being pursued in this area [43–47, 95, 96].

For instance, as far as *size* is concerned, several studies have suggested the superiority of micron-sized VTCs compared to nano-VTCs in margination from the RBC-rich zone into the CFL [55–57]. Note that nanoparticles are considerably more desirable as drug carriers due to their significantly high diffusivity in tumor vasculature [43]. As far as VTC *shape* is concerned, nonspherical particles, such as disk-like or rod-like particles have been proposed to enhance margination and adhesion propensities compared to the commonly used spherical ones [48–55, 57–60]. However, the near-wall hydrodynamic behavior of these particles during interactions with RBCs is unknown. Similary, their adhesive rolling behavior on the vessel wall in the presence of RBCs has not been fully addressed. In terms of VTC *deformability*, it has been suggested that targeting is improved by using deformable carrier particles such as capsules and vesicles (liposomes) due to advantages in adhesive rolling [95, 96]. Note that as mentioned in previous sections, deformable particles tend to migrate away from the wall and concentrate near the center. This can significantly limit their margination and the possibility of contact with the vessel wall, thereby raises questions about their applicability.

Evidently, designing an efficient drug carrier is a significant challenge due to a

number of multiscale/multiphysics issues involved during the transport of the VTCs in blood flow and their corresponding design criteria that may be even be contradictory.

1.4 Scope of the Thesis

Addressing the above examples in their entirety is a task beyond the scope of one PhD thesis, as many of the involved phenomena are highly complex and interdisciplinary. Within the scope of the current thesis, we focus on the processes involving the microscale cellular hydrodynamics and the nanoscale adhesion. We embark on a 3D computational fluid dynamics (CFD) study that integrates (i) the deformation and dynamics of each individual blood cell with high accuracy, (ii) hydrodynamic interactions of multiple heterogeneous cells in semi-dense suspension, (iii) coarse-grain modeling of molecular adhesion between the molecules on the wall and cell membrane/particle surface, and (iv) geometric complexities of the microvasculature. The unique feature of the current work is that the above modules have been incorporated in a unified methodology. While the method can be applied to a large number of problems associated with the microcirculatory blood flow under normal and pathological conditions, here, we identify a sub-class of five related problems as the undertakings of the thesis, as noted below:

1. **Numerical methodology (Chapter 2):** We employ an accurate well-developed well-validated three-dimensional model for cell dynamics in viscous flow within the framework of the immersed boundary/front-tracking method. The model includes (i) a finite element method (FEM) for large deformations of the RBC with the most comprehensive model for the cell membrane that includes the resistance

against shear, area dilatation, and bending, as well as the viscosity difference between the hemoglobin and the surrounding fluid, (ii) a stochastic Monte Carlo-based lottery method to coarse-grain the nanoscale binding reaction between the adhesion molecules, (iii) a front-tracking method to consider the coupling between the flow dynamics and the membrane deformation, (iv) a finite-difference/spectral method for simulation of the flow inside and outside of the cells, and (v) a sharp-interface immersed boundary method to model the complex geometry of blood vessels.

2. **Hydrodynamic interaction between a platelet and an RBC in a dilute suspension (Chapter 3):** As discussed in Section 1.2.3, continuous interactions between platelets and RBCs in the flow of blood results in the margination of platelets from the RBC-rich zone into the CFL. At the microscale, such interactions arise from individual hydrodynamic collisions between RBC-platelet pairs. Therefore, a pairwise collision can be viewed as the fundamental process that collectively leads to margination. More specifically, the effect of RBC motion and deformation on platelet dynamics is of interest in this chapter.

Two types of dynamics have been observed for an isolated RBC in shear flow: at relatively high shear rates it exhibits a 'tank-treading' motion in which the membrane and the interior fluid make a rotary motion (see Figure 1.7(a)), while at low shear rates it exhibits a tumbling or a rigid body-like flipping motion (see Figure 1.7(b) [161, 163]. The effect of these dynamics on platelet motion has not been addressed in the literature. Moreover, near the edge of the CFL, the RBC concentration is relatively low and the flow can be considered as a dilute binary suspension. Hence, pairwise RBC-platelet hydrodynamic interactions in close proximity to a bounding wall could model the cellular interactions at the CFL edge. Of particular interest is

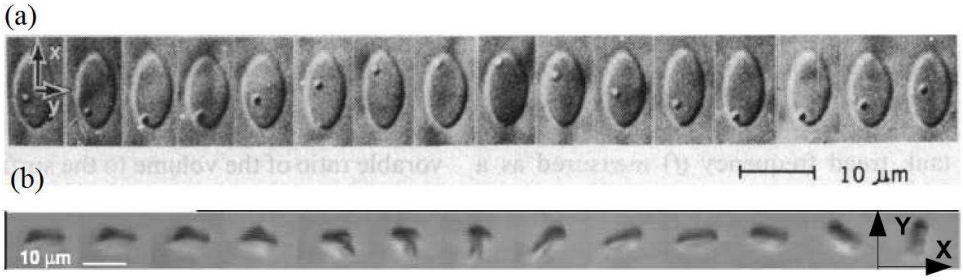

Figure 1.7: Experimental observations of tank-treading and tumbling motions in red blood cells. Shear flow is in the x-direction in both cases. (a) Observation of tank-treading motion with a time interval of 40 ms by Fischer et al. [161]. (b) Observations of tumbling motion with a time sequence of 1 s by Abkarian et al. [163].

the wall effect on the nature of RBC–platelet interaction, and implications on platelet margination.

To quantify the effects of the wall and the RBC dynamics on the motion of platelets, we present three-dimensional simulations of the hydrodynamic interaction between an RBC and a platelet in a wall-bounded shear flow. We observe two types of interaction: a crossing event in which the platelet approaches the RBC, rolls over it, and continues in the same direction; and a turning event in which the platelet turns away before coming close to the RBC. The effects of the initial platelet–RBC relative configuration, RBC dynamics, and the wall on the crossing and turning trajectories are discussed in detail. Then, a mechanism of continual platelet drift towards the wall by a succession of turning and crossing events is proposed.

3. **Platelet transport and dynamics in blood flow (Chapter 4):** The essential role of RBCs in platelet margination has been mostly considered on an average basis. For instance, as mentioned in Section 1.2.3, the lateral variations in the average concentration profile of RBCs have been hypothesized to affect the RBC-platelet collision rate and consequently platelet margination [159]. In addition to the non-uniformity in the average RBC concentration, the transient microscopic

structure of the RBC suspension is also anisotropic in shear flow due to the formation and dissociation of RBC clusters [130]. The effect of such an anisotropic configuration on platelet transport inside the RBC-rich zone is unknown.

The margination phenomenon, or platelets 'lateral' drift, has motivated a considerable amount of research on the transport of platelets in shear flow in the lateral direction (perpendicular to the flow direction) [16–24,36,37,41,42]. However, platelet dynamics in the transverse direction have not been fully addressed in the literature, in spite of the fact that significant displacement in the transverse direction has been observed in pairwise collisions in shear flow [40]. In the case of platelets motion in the RBC-rich zone, such a displacement can collectively result in diffusive motion along the transverse direction. Similarly, inside the CFL, the marginated platelets are continuously interacting with the flowing RBCs. The effect of such interactions on platelet near-wall motion, specifically in the transverse direction, is unknown.

In this chapter, we perform simulations of many-cell binary suspension of RBCs and platelets to focus on the 3D effects of the platelet-RBC interaction as well as the RBC suspension microstructure on platelet margination and near-wall dynamics in a shear flow. We find that the RBC distribution in whole blood becomes naturally anisotropic and creates local 'clusters' and 'cavities'. A platelet can enter a 'cavity' and use it as an 'express lane' for fast margination towards the wall. Once near the wall, the 3D nature of the platelet-RBC interaction results in a significant platelet movement in the transverse direction, which leads to the formation of platelet clusters, and may act as a hydrodynamic precursor to blood clot formation.

4. **Microparticle shape effect on their transport and dynamics in blood flow (Chapter 5):** We study the transport of vascular targeting carriers in whole

blood by modeling them as microparticles of different shapes (spherical, oblate, and prolate). We aim to quantify the microparticles' shape effect on their margination, near-wall dynamics, and adhesion. Our results show that microparticles of different shapes interact differently with the RBCs leading to their different behaviors during each stage of microparticle transport from the RBC-rich zone towards the vessel wall. Specifically, we show that microparticles' rotational orientation in three-dimensional space and the frequency of their collisions with the flowing RBCs in the presence of a bounding wall are the key factors dictating their differential behavior. Quantification of such micro-scale dynamics of individual particles and their influence on particle margination and adhesion in whole blood does not exist in the literature, and is the focus of this chapter.

5. **Blood flow in stenosed microvessels (Chapter 6):** As mentioned in Section 1.2.2, due to the significance of discrete RBC motion and deformation at the microscale, blood behaves as a non-Newtonian fluid in microvessels [80]. The illustrations of such non-Newtonian behavior are the Fahraeus and Fahraeus-Lindqvist effects, which are explained by the variations in the CFL thickness with respect to the tube diameter. In a stenosed microvessel, the CFL is expected to be affected by geometric focusing of RBCs. Specifically, the CFL thickness is spatially changed about the constriction [78]. These variations are in turn expected to affect the Fahraus and Fahraeus-Lindvist effects. The possible alteration of these effects in microstenosis geometry has not been addressed in the literature. Similar to the mean flow characteristics such as CFL thickness and relative viscosity, the temporal and spatial flow oscillations are also subjected to changes due to stenosis geometry.

In this chapter, we study the flow of RBCs in stenosed microvessels, typical of

small arterioles. We observe that the Fahraeus-Lindqvist effect is considerably enhanced due to the presence of a stenosis. The spatial variations of CFL thickness about the stenosis geometry is obtained and used to explain such an enhancement. We also observe that the discrete motion of the RBCs through the stenosis causes large time-dependent fluctuations in flow properties which are nonexistent in absence of the RBCs. Our results show a significant asymmetry in the average as well as transient flow characteristics about the stenosis geometry. The physiological implications of the asymmetry are also discussed.

6. **Adhesion of microparticles in microvessels: role of RBCs and microparticle deformability: (Chapter 7):** As mentioned in Section 1.3.2, the use of deformable particles as vascular targeting carriers is of interest due to their superior performance in adhesive rolling [95, 96]. It was also mentioned in Section 1.2.1 that a deformable particle tends to migrate away from the vessel wall [5]. This is considered an adverse characteristic in terms of targeting applications, as it limits the margination and wall–contact possibility of the particle. Both the migration rate of a deformable particle and its adhesive rolling motion are dependent on the particle size and deformability as well as the microvessel pseudo-shear rate. The dual role of the particle deformability in its transport to the vessel wall, and its dependence on the aforementioned parameters, motivates a quantitative study on the effects of size/deformability of microparticles on their adhesion propensity.

In this chapter, we perform simulations on adhesion of microparticles of different size and deformability in microvessels of different diameters to quantify pre- and post-wall-contact phenomena, namely the RBC-induced initial adhesive bond formation, and the following adhesive rolling of microparticles in presence of the RBCs. We

observe that there exists a critical size for deformable microparticles above which the RBC-induced microparticle adhesion does not take place. This critical size is observed to be dependent on the microvessel diameter, particle deformability, and the pseudo-shear rate. We also observe that the presence of RBCs increases the rolling velocity of adhered particles.

Note that each of the above chapters has been published or is being considered for publication as a separate journal article. Therefore, minor repetitions in the introduction sections of the chapters are acknowledged, as each work is intended to stand alone.

Chapter 2

Numerical Methodology

The computational model considered here is within the framework of the front-tracking/immersed boundary method. This method has been developed to study the deformation of suspended cells enclosing a liquid, which may have different properties from the suspending liquid [131–133]. The main idea of the immersed boundary method is to use a single set of equations for both fluids, inside and outside a cell/particle. The fluid equations are solved on a fixed Eulerian grid, and the interface (i.e. cell membrane/particle surface) is tracked in a Lagrangian manner by a set of marker points. This is shown in Figure 2.1. Note that the fluids are considered to be incompressible.

The method is implemented via a computer code consisting of four major modules: (i) The model for deformation of a suspended cell membrane/particle surface, which is implemented using a finite element method. Within this module, the forces that are created due to the elastic deformation of the membrane are computed on a 3D triangular Lagrangian mesh that is used to discretize the membrane surface. (ii) The adhesion model which simulates the interactions between adhesion molecules on the membrane and the wall, and is implemented via a stochastic Monte Carlo-based method. This module computes the adhesive forces applied to the discretized particle surface. (iii) The coupling between the fluid flow dynamics and the membrane deformation and motion which is implemented using the front-tracking/immersed

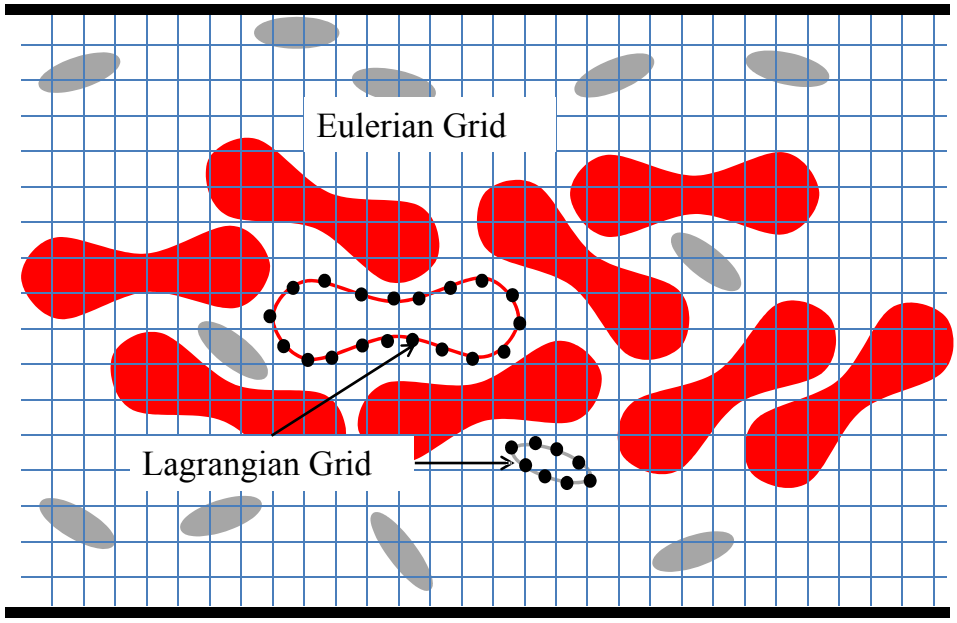

Figure 2.1: Schematic of the computational Eulerian and Lagrangian grid.

boundary method. This module interpolates the forces from the Lagrangian membrane mesh to the Eulerian fluid grid and the velocities from the fluid grid to the membrane mesh. (iv) The viscous fluid model which is implemented via a finite-difference projection-based CFD flow solver. This module computes the flow velocity on the Eulerian grid while taking into account the interpolated membrane forces. The interpolated velocities on the Lagrangian nodes are then used to compute the deformation/motion of the cell/particle. (v) The model for geometric complexity that is used to simulate the tubular and stenosis boundaries. This module, which is implemented using a sharp-interface immersed boundary method, applies the flow boundary conditions on the complex geometries.

Note that the cell/particle deformation and/or motion in our simulations are purely due to hydrodynamic interactions (as well as adhesive bond dynamics in case of adhesive motion on a substrate), and the Brownian diffusive behavior is not taken

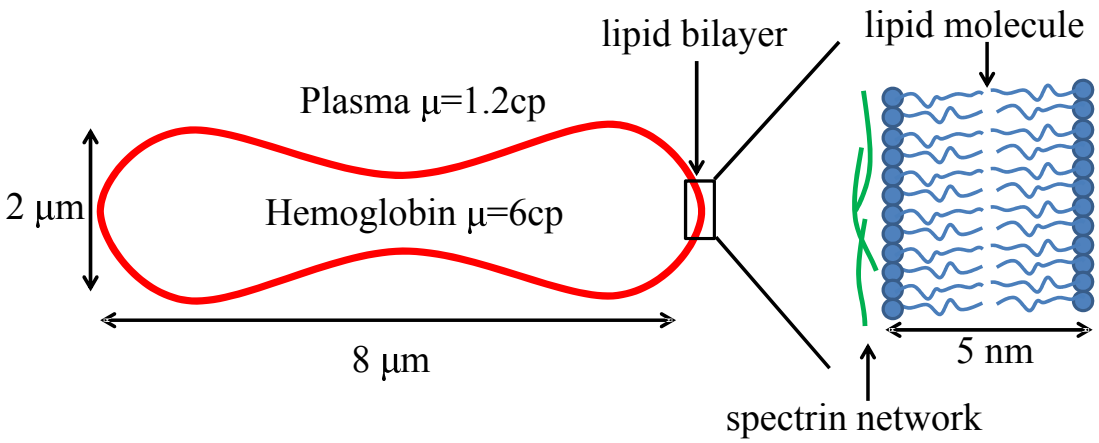

Figure 2.2: Schematic of biconcave resting shape of an RBC and basic molecular structure of its membrane.

into account.

For the simulations of this thesis, module (ii) is implemented and embedded into a well-developed well-validated computer code that includes modules (i), (iii), (iv), and (v). In the following sections, the existing numerical methodology is briefly explained. A more detailed description of the implemented model for adhesion is then followed.

2.1 Model of Cells and Particles

2.1.1 Red Blood Cell Model

As mentioned in the previous chapter, the resting shape of an RBC is an 8×2 μm biconcave disk. The RBC membrane is made of a lipid bilayer and a two-dimensional cytoskeleton in the form of a network of spectrin filaments [1,2]. Figure 2.2 schematically demonstrates the shape and the structure of an RBC membrane. The RBC membrane structure results in resistance against shear deformation, area dilatation, as well as bending [3, 4].

The biconcave shape of a red blood cell is prescribed as

$$x = R\eta\,; \qquad y = \frac{R}{2}\sqrt{1-r^2}(C_0 + C_2 r^2 + C_4 r^4)\,; \qquad z = R\zeta\,, \tag{2.1}$$

where $\eta^2 + \zeta^2 = r^2$, and R is adjusted to control the cell volume [8]. The surface area and the volume of the red blood cell are taken to be 134.1 μm^2 and 94.1 μm^3, respectively [8]. The initial shape is stress-free. The coefficients C_0, C_2, and C_4 are taken to be 0.207, 2.003, and -1.123, respectively [8].

As discussed before, a complete elastic model for RBCs must include all essential properties of the cell membrane, namely, the resistance against shear deformation, area dilatation, and bending. The first two types of deformation are modeled using the strain energy function developed by Skalak et al. [140] for an RBC membrane as

$$W_e = \frac{E_s}{4}\left[\left(\frac{1}{2}I_1^2 + I_1 - I_2\right) + \frac{C}{2}I_2^2\right]\,, \tag{2.2}$$

with I_1 and I_2 defined as

$$I_1 = \epsilon_1^2 + \epsilon_2^2 - 2\,; \quad I_2 = \epsilon_1^2\epsilon_2^2 - 1\,, \tag{2.3}$$

where ϵ_1 and ϵ_2 are the principal stretch ratios, E_s is the surface Young's modulus, and CE_s is the modulus associated with the surface area dilatation. The Skalak law behaves linearly in the small-deformation domain, with $E_s = 2G_s(2 + C)/(1 + C)$, where G_s is the surface shear modulus [141]. The area dilatation may be restricted by a large value of C as in case of an RBC for which the surface is nearly area-incompressible. The corresponding in-plane elastic force on the membrane is, $\mathbf{f}_e$,

obtained by applying the principle of virtual work (see Section 2.2 for details).

The bending resistance is modeled following Helfrich's [142] formulation for bending energy

$$W_b = \frac{E_b}{2} \int_S (2\kappa - c_o)^2 \, \mathrm{d}S + E_g \int_S \kappa_g \mathrm{d}S \,, \tag{2.4}$$

where E_b is the bending modulus associated with the mean curvature κ, E_g is the bending modulus associated with the Gaussian curvature κ_g, and c_o is the spontaneous curvature which reflects the initial or intrinsic curvature of the membrane (taken to be -2.09 in our simulations [178]). Then, the expression for the bending force at each Lagrangian point becomes [142]

$$\mathbf{f}_b = E_b \left[(2\kappa + c_o) \left(2\kappa^2 - 2\kappa_g - c_o \kappa \right) + 2 \, \Delta_{LB} \, \kappa \right] \mathbf{n} \tag{2.5}$$

where Δ_{LB} is the Laplace–Beltrami operator [143].

As mentioned before, the cell membrane/particle surface is discretized using flat triangular elements. It is assumed that the elements remain flat during simulations. The triangulated surface mesh needed for the simulations is obtained from the GNU Triangulated Surface (GTS) Library. Such a mesh is shown for an RBC (bottom-left) and other sample particles in Figure 2.3. Note that the forces $\mathbf{f}_e$ and $\mathbf{f}_b$ are computed at each node in the Lagrangian mesh.

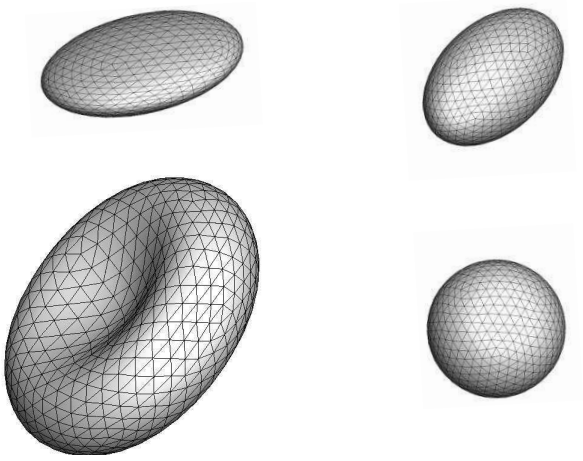

Figure 2.3: Discretization of the cell membrane/particle surface. The actual number of triangles is much higher than what is shown.

2.1.2 Platelet/Microparticle Model

To model the nearly-rigid characteristics of platelets and microparticles, similar model that is used for the RBC membrane is incorporated with significantly large shear modulus, the maximum value of which is dictated by stability limitation of the numerical simulation. Additionally, since the deformation is negligible in these particulate components, the bending model is replaced by a simpler one following Dupin et al. [144]. In this approach a geometrical constraint is applied to the cell membrane/particle surface through bending moments that tend to preserve the initial curvature of the surface at each Lagrangian node. These bending moments, the magnitudes of which are proportional to the departure from the initial local curvature, are exerted through applying the following force on each node

$$\mathbf{f}_b = \left(E_b \frac{\Delta\theta_{lm}}{\theta^0_{lm}} \right) \tilde{n} \left(\Psi \right) \tag{2.6}$$

where $\tilde{n}(\Psi)$ is the unit vector normal to the triangular element surface Ψ, θ^0_{lm} is the initial angle between element Ψ and the adjacent element that has nodes l and m in common, $\Delta\theta_{lm}$ is the instantaneous deviation from that value, and E_b is a bending rigidity constant. Also, to ensure that the local and total stress on the membrane are not changed by the bending constraint, an equal and opposite force is distributed equally to nodes l and m. Figure 2.3 shows a platelet (top-left) and two sample microparticles (right) in our simulations.

For deformable microparticles, similar model that is explained in the previous section is used only without incorporation of any bending rigidity, and for perfectly rigid microparticles, a variation of the sharp-interface immersed boundary method (see Section 2.5) for moving solid objects is employed.

2.2 Finite-Element Treatment of a Cell/Particle Elastic Surface

The deformation of the membrane is treated using a finite element model developed by Charrier et al. [137], Shrivastava and Tang [138], and later implemented by Eggleton and Popel [139] within the framework of immersed boundary method to consider large deformation of cells. First, as shown in the previous section, the membrane is discretized using flat triangular elements (see Figure 2.3). A Lagrangian node on the surface is surrounded by five or six triangular elements. It is assumed that the elements remain flat even after large deformation of the capsule. In the model, the forces acting on the three vertices of a triangular element are obtained by computing the displacements of the vertices of the deformed element with respect to the undeformed element. For this purpose, the undeformed and the deformed surface elements

are transformed to a common plane, P, using rigid-body rotations. This reduces the problem to a 2D (planar) deformation on $\{x^P\ ,\ y^P\}$, where x^P and y^P denote a local coordinate system attached to the plane P. The three vertices of a triangular element are denoted as l,m, and n. To compute the membrane force $\mathbf{f}_e$ the principle of virtual work is used as

$$\mathbf{f}_e = -\partial W_e/\partial \mathbf{v}, \tag{2.7}$$

where $\mathbf{v}$ is the displacement of a vertex and W_e is the strain energy function. Inside the common plane P, the above formula can be written as

$$\mathbf{f}_l^P = \frac{\partial W_e}{\partial \epsilon_1}\frac{\partial \epsilon_1}{\partial \mathbf{v}_l} + \frac{\partial W_e}{\partial \epsilon_2}\frac{\partial \epsilon_2}{\partial \mathbf{v}_l} \tag{2.8}$$

for the vertex l, and similarly for vertices m and n. Here, the force $\mathbf{f}^P$ lies in plane P, and as mentioned in the previous section, ϵ_1 and ϵ_2 are the principal values of the in-plane stretch ratios. It is assumed that the displacement $\mathbf{v}$ varies linearly inside the element so that

$$\mathbf{v} = N_l\mathbf{v}_l + N_m\mathbf{v}_m + N_n\mathbf{v}_n \tag{2.9}$$

and the shape functions N_l, N_m, and N_n are expressed as

$$N_l = a_l x^P + b_l y^P + c_l \tag{2.10}$$

for the vertex l, and similarly for vertices m and n. The coefficients a_l, b_l, and c_l are found by letting $N_l = 1$ at vertex l, and $N_l = 0$ at vertices m and n, and so on. Once

the shape functions are known, the displacement gradients within the element, such as $\partial \mathbf{v}/\partial x^P$, and $\partial \mathbf{v}/\partial y^P$, can be found by differentiating 2.9 (see [136,138] for details). The in-plane forces for an individual element are then needed to be transformed to the global coordinates. The resultant force at any node is obtained by vector resultant of the forces contributed by all the elements which share that node.

2.3 Flow Solver

The fluid motion is governed by the continuity and Navier-Stokes equations as

$$\nabla \cdot \mathbf{u} = 0\,, \tag{2.11}$$

$$\rho \left[\frac{\partial \mathbf{u}}{\partial t} + \mathbf{u} \cdot \nabla \mathbf{u} \right] = -\nabla p + \nabla \cdot \mu (\nabla \mathbf{u} + (\nabla \mathbf{u})^T)\,, \tag{2.12}$$

where $\mathbf{u}\,(\mathbf{x}, t)$ is the fluid velocity, ρ is the density, p is the pressure, and μ is the fluid viscosity. Here, $\mu\,(\mathbf{x}, t)$ is a single variable used to denote the viscosity of the entire fluid. Therefore, $\mu = \mu_i$ inside the cell and $\mu = \mu_o$ outside. Mathematically, we define μ using an indicator function $I(\mathbf{x})$, which is unity inside the cell and zero outside. Thus, μ is given by a single expression for every Eulerian point in the fluid as

$$\mu(\mathbf{x}) = \mu_o + (\mu_i - \mu_o) I(\mathbf{x})\,. \tag{2.13}$$

As the cell/particle moves and/or deforms, μ needs to be updated. This is done by solving a Poisson equation for the indicator function $I(\mathbf{x}, t)$ as

$$\nabla^2 I = \nabla \cdot \mathbf{G}\,, \tag{2.14}$$

$$\mathbf{G} = \int_S \delta(\mathbf{x} - \mathbf{x}')\mathbf{n} d\mathbf{x}\,, \tag{2.15}$$

where δ is the three-dimensional Dirac-Delta function, $\mathbf{x}'$ is a location on the cell /particle surface, $\mathbf{x}$ is a location in the flow, and $\mathbf{n}$ is the unit vector that is normal to the cell membrane/particle surface and directing outward.

The membrane force density $\mathbf{f}$ arises due to the deformation of cell/particle, and is computed using the finite-element method described in the previous section. The force density includes the previously mentioned $\mathbf{f_e^m}$ and $\mathbf{f_b}$ as well as adhesion forces (see Section 2.5 for adhesion model). Having $\mathbf{f}$ evaluated, the membrane and the fluid are coupled in a two-way manner by adding a source term $\mathbf{B}$ to the right hand side of (2.12). The source term $\mathbf{B}$ is related to $\mathbf{f}$ as

$$\mathbf{B}(\mathbf{x}, t) = \int_S \mathbf{f}(\mathbf{x}', t)\delta(\mathbf{x} - \mathbf{x}')d\mathbf{x}'\,. \tag{2.16}$$

Further, the δ-function is constructed by multiplying three 1D δ-functions as

$$\delta(\mathbf{x} - \mathbf{x}') = \delta(x - x')\delta(y - y')\delta(z - z')\,. \tag{2.17}$$

For numerical implementation, however, a smooth representation of δ-function is used as

$$\begin{aligned} D(\mathbf{x} - \mathbf{x}') &= \frac{1}{64\,h^3}\prod_{i=1}^{3}\left(1 + \cos\frac{\pi}{2h}(x_i - x_i')\right) \quad \text{for} \quad |x_i - x_i'| \le 2h\,, \quad i = 1, 2, 3\,, \\ D(\mathbf{x} - \mathbf{x}') &= 0 \qquad \text{otherwise}\,, \end{aligned} \tag{2.18}$$

where h is the Eulerian grid size (Unverdi and Tryggvason [132]). As a result, the interface force varies smoothly over four Eulerian grid points surrounding the interface.

In discrete form, the integral in (2.16) can be written as

$$\mathbf{B}(\mathbf{x}_j) = \sum_i D(\mathbf{x}_j - \mathbf{x}_i')\mathbf{f}(\mathbf{x}_i')\,, \tag{2.19}$$

where i and j represent Lagrangian and Eulerian points, respectively.

The computational domain is discretized using a fixed (Eulerian) rectangular and uniform grid. A combined second-order finite-difference scheme and Fourier transform is used for the spatial discretization, and a second-order time-split scheme is used for the temporal discretization of Navier-Stokes equations. In this method, the momentum equation is split into an advection–diffusion equation and a Poisson equation for the pressure. The body-force term is retained in the advection–diffusion equation. In case of a pressure driven flow, a body force is added to the Navier–Stokes equation at each Eulerian node. The nonlinear terms are treated explicitly using a second-order Adams-Bashforth scheme, and the viscous terms are treated semi-implicitly using the second-order Crank-Nicholson scheme. The resulting linear equations are inverted using an ADI (alternating direction implicit) scheme to yield a predicted velocity field. The Poisson equation is then solved to obtain pressure at the next time level. Using the new pressure, the velocity field is corrected so that it satisfies the divergence-free condition. Details of the method can be found in [134–136].

2.4 Interface Tracking

The cell membrane/particle surface is tracked in a Lagrangian manner. After solving Navier-Stokes equations for the pressure and velocity fields, the no-slip condition on the cell membrane/particle surface is imposed by extracting the surface velocity from

the surrounding fluid at each time step as

$$\mathbf{u}_S(\mathbf{x}', t) = \int_S \mathbf{u}(\mathbf{x}, t)\delta(\mathbf{x} - \mathbf{x}')d\mathbf{x}\,. \tag{2.20}$$

Though the summation is over all the Eulerian grid points, only the local points contribute to the interface velocity. The discrete form of the delta function used here is the same as Equation (2.18). The Lagrangian points on the interface are then advected as

$$\frac{d\mathbf{x}'}{dt} = \mathbf{u}_S(\mathbf{x}', t)\,. \tag{2.21}$$

Numerically, the above equation is treated explicitly using the second-order Adams-Bashforth scheme.

2.5 Adhesion Model

Biological adhesion is mediated by membrane proteins or adhesion molecules at the nanoscale. Adhesion is facilitated by means of a binding reaction between the molecules on the cell surface called 'receptors' and the ones on the substrate called 'ligands' [145]. Figure 2.4 schematically shows the adhesion of a cell to the substrate via receptor-ligand binding.

The adhesion model that is implemented to coarse-grain the binding reaction in our multiscale simulations is based on the model proposed by Bell [146, 147]. In this model, the chemical reaction between the adhesion molecules is coupled with the tensile force applied to the bonds. Through this coupling, the multiscale/multiphysics nature of the particulate dynamics in microcirculation is considered in our simulations, as the forces applied on the nanoscale bound adhesion molecules are determined

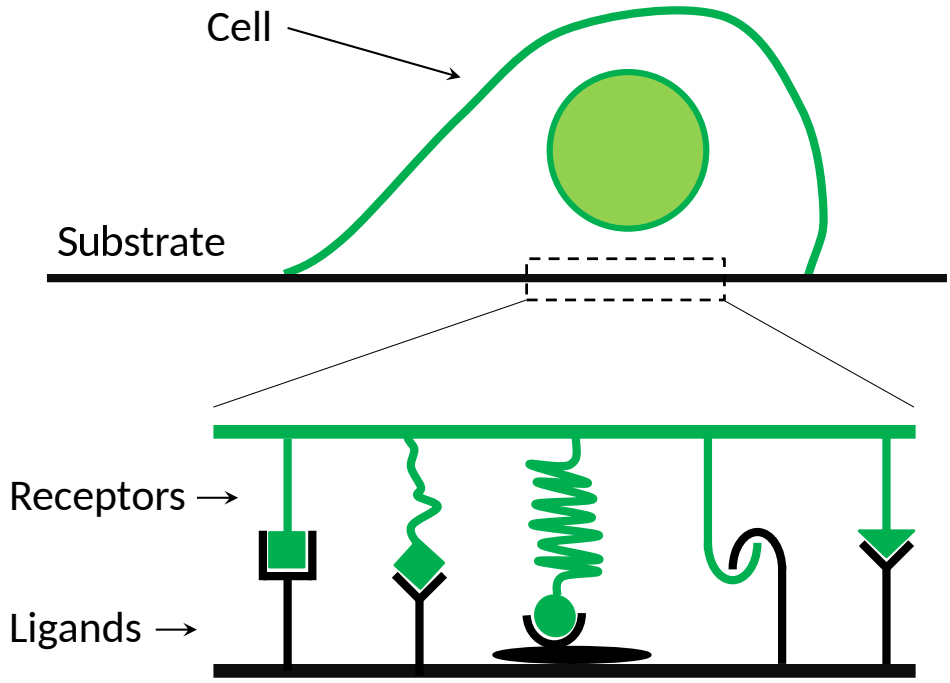

Figure 2.4: Schematic of the adhesion of cell to substrate via receptor-ligand binding.

by the microscale deformation and motion of individual cells. The details of the adhesion model and the numerical implementation of that in the immersed boundary method is described in what follows.

Consider the following reversible chemical reaction between the receptor (R) and ligand (L) molecules that results in a bound state (B)

$$L + R \underset{k_0^r}{\overset{k_0^f}{\rightleftharpoons}} B, \tag{2.22}$$

where k_0^f and k_0^r are the forward and reverse reaction rate constants.

The bound state, B, could be stable due to electrostatic, van der Waals, or hydrogen bond interactions. Now, consider a case such as cell adhesion to endothelium, in which a large number of receptors are bound to their corresponding ligands. Since the reaction is reversible, an external force is not necessarily required to separate the

adhesion molecules and detach the cell from the substrate. However, the probability of cell detachment in absence of an external force is relatively low as the simultaneous breakage of all receptor-ligand bonds is unlikely. Therefore, a rapidly applied rupture force, such as hydrodynamic drag or a force due to interactions with other flowing cells is required for cell detachment.

To connect such an external force with the aforementioned reaction, Bell [146] considered the kinetic theory of solid materials where the bond lifetime is written as

$$\tau = \tau_0 exp\left(\frac{(E_0 - \gamma f)}{k_B T}\right), \tag{2.23}$$

where τ_0 is the inverse of a natural frequency of atoms oscillations in the solid ($\sim 10^{-13}$ s), E_0 is the bond energy, f is the force applied to the bond, γ is an empirical parameter accounting for the structure of the solid , k_B is the Boltzmann constant, and T is the solid temperature. Bell [146] proposed that the above equation can also be applied to receptor-ligand bonds in biological adhesion.

In such a case, τ(f = 0) is identified with the inverse of reverse reaction rate constant $(1/k_0^r)$, and γ is approximately r_0, or reactive compliance so that when $f = E_0/r_0$, $\tau = \tau_0$. The reactive compliance basically characterizes the response of a receptor to an external force. Lower values of r_0 correspond to smaller changes in dissociation tendency of bonds, and consequently higher probability of maintaining adhesion in presence of an applied force. Now, the coupling between the bond force and the chemical reaction can be written as

$$k_r = k_r^0 exp\left(\frac{r_0 f}{k_B T}\right), \tag{2.24}$$

where k_r denotes the rate of bond dissociation, and T is considered to be human body temperature.

The values of k_0^r and r_0 have been determined for different receptor-ligand pairs via experimental data on stop-time distributions of cells that are perfused over sparsely populated substrates. The measurement of force-driven dissociation of single bonds by dynamic force microscopy have shown that Bell model is valid over typically 'fast' loading conditions, as is the case in our simulations due to hydrodynamic forces [97]. Sample values for of k_0^r and r_0 for different receptor-ligand pairs can be found in [149, 150].

The stretched bound adhesion molecules are assumed to behave like Hookean linear springs [97, 148–151]. Although the Young modulus of proteins can vary by orders of magnitudes, and the exact value of spring constants are not known for many receptor-ligand bonds [150], classical modeling studies [148–150] on cell adhesion have demonstrated the ability of such linear-spring model in reproducing experimental data. Therefore, by replacing f with $k_0(l-\lambda)$, where k_0 is the spring constant, l is the bond length, and λ is the bond free length, in (2.24), the dissociation rate becomes

$$k_r = k_r^0 exp\left(\frac{r_0 k_0 \left(l-\lambda\right))}{k_B T}\right) \tag{2.25}$$

Once k_r is known, by analogy with the classical equilibrium constant, a rate of bond formation, k_f, can be defined from the Boltzmann distribution for affinity [97, 147]

$$\frac{k_f}{k_r} = \frac{k_f^0}{k_r^0} exp\left(\frac{-k_0 \left(l-\lambda\right)^2}{2k_B T}\right) \tag{2.26}$$

which takes the form

$$k_f = k_f^0 exp\left(k_0\left(l-\lambda\right)\frac{r_0 - 0.5\left(l-\lambda\right)}{k_B T}\right) \tag{2.27}$$

The value of k_f^0 has not been adequately determined by experiments for many receptor-ligand pairs. Therefore, it is adjusted by simulations [97].

To implement the formation and breakage of adhesive bonds, a stochastic Monte Carlo simulation is used [149]. Consider a free adhesion molecule on a cell surface at a distance x from the substrate in a single simulation time-step, Δt. Assuming the variation in x is negligible over Δt, the governing equation for the probability that such a molecule becomes bound during the time interval can be written as

$$\frac{dP_b}{dt} = k_f\left(1 - P_b\right), \tag{2.28}$$

where $1 - P_b$ is the probability that the molecule remains free during the time step. Integrating the above equation from 0 to Δt, gives the probability of binding at the end of the timestep as

$$P_b = 1 - exp\left(-k_f \Delta t\right) \tag{2.29}$$

During each Δt in the simulations the value of P_b is computed based on the above formula for each adhesion molecule. To determine if a new bond is formed, a random number N_1 between 0 and 1 is generated and compared to P_b. The adhesion molecule becomes bound if $P_b > N_1$. Similarly, the probability of the breakage of an existing

bond is computed from

$$P_r = 1 - exp\left(-k_r \Delta t\right) \tag{2.30}$$

The computed value is compared to another random number generated between 0 and 1, N_2, and the bond is broken if $P_r > N_2$.

The random numbers are generated using a built-in random number generator in FORTRAN called DURAND. This subroutine uses the multiplicative congruential method to generate the random numbers with a user-specified initial input argument, S. The value of S is specified between 1.0 and 2147483647.0. Different sets of random numbers are generated for comparison with the forward and the reverse rate probabilities. The values of S for comparison with the forward rate probability are specified as functions of the number of adhesion molecules available on the cell surface. For comparison with the reverse rate probability, the random number is generated using the value of S specified as a function of the number of bonds existing at that time step. The unbiasedness of the generated random numbers was confirmed by obtaining a uniform distribution between 0 and 1. Once the formation/breakage of new/existing bonds are determined at the end of the time interval, the adhesive forces are computed from $f = k_0 \left(l - \lambda\right)$ and applied to the Lagrangian nodes at which the adhesion molecules are located. Thus, by adding the adhesive forces to $\mathbf{f}(\mathbf{x}', t)$ in Equation (2.16) the nanoscale adhesive molecular bond dynamics is coarse-grained in the exisiting model.

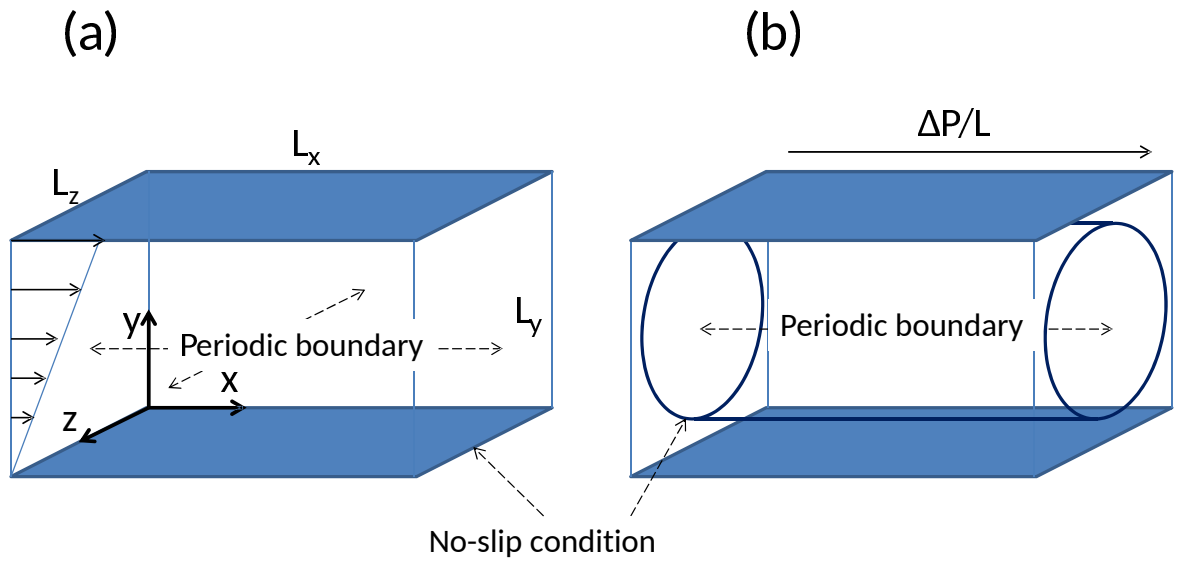

Figure 2.5: Schematic of the computational domain for whole blood (a) and microvessel (b) simulations.

2.6 Problem Setup

Two different flow setups are considered in this thesis for the problems under consideration. For the simulations associated with particulate transport in whole blood which is the subject of Chapters 3 to 5, a wall-bounded shear-flow with no mean pressure gradient is employed (see Figure 2.5(a)); and for the simulations of blood flow inside microvessels, as considered in Chapters 6 and 7, a pressure-driven tube flow is used (see Figure 2.5(b)).

As shown in Figure 2.5(a), for the shear-flow setup we consider a three-dimensional computational domain bounded by two infinite flat plates placed parallel to the x-axis in a Cartesian coordinate system. Here, x is the direction of the flow, y is the direction of velocity gradient, and z is the direction of vorticity of the undisturbed flow.

The channel is assumed to be infinitely long in the x and z directions. We use

periodic boundary conditions in these directions to reduce the size of the computational domain. Further, the no-slip boundary condition is imposed on the walls. In the absence of any cells, we have linear shear flow at zero pressure-gradient driven by the two walls of the channel as

$$\mathbf{u}^{\infty} = \{\dot{\gamma} y,\, 0,\, 0\}\ , \tag{2.31}$$

where $\dot{\gamma}$ is the shear rate.

As demonstrated by Figure 2.5(b), in order to simulate the flow inside microvessels, we incorporate a sharp-interface immersed boundary method to include the tubular geometry into the above computational domain (a brief description of this method is presented in the next section). In such a configuration, the flow is initially stagnant and is driven by a mean pressure gradient which is defined in the dimensionless form as

$$\beta = -\frac{\left(\frac{d\overline{P}}{dx}\right)}{\left(\frac{16\mu_o U_c}{D^2}\right)} \tag{2.32}$$

No-slip boundary conditions is applied on the microvessel tubular wall that is simulated by the sharp-interface method. The details of the problem setup for each problem considered is also presented in each corresponding chapter.

2.7 Sharp-Interface Immersed Boundary Method for Complex Geometries

As mentioned in previous sections, to simulate rigid boundaries of arbitrary complexity, a sharp-interface immersed boundary method is used in our model. This method is specifically used in simulations associated with microstenosis (Chapter 6), and adhesion in microvessels (Chapter 7), where the rigid boundaries contain significant curvatures that may even be spatially varied. The basic premise of this method is to enforce the velocity at grid points immediately interior to the solid object to be values such that the desired velocity on the boundary of the solid will be achieved. These grid points immediately interior to the solid object, termed as 'Ghost Nodes', have at least one adjacent grid point outside the object in the fluid domain. Grid points that do not have any adjacent fluid nodes are termed 'Solid Nodes'.

The value to be imposed on each Ghost Node is determined using a 'Boundary Intercept' (BI) and an 'Image Point' (IP). The BI is the point on the immersed boundary that is closest to the ghost node, while the IP is the mirror image of the ghost node in the fluid domain, across the boundary intercept. For the velocity, the boundary condition to be imposed at the BI is of a Dirichlet type, and the value at the BI is taken to be the average of values at the ghost node and the IP. Therefore, to impose a desired velocity at the BI, the value enforced at the ghost node is

$$\mathbf{u}_{GN} = 2.0\mathbf{u}_{BI} - \mathbf{u}_{IP} \tag{2.33}$$

2.8 Grid Resolution Test

The model we use in this study was initially developed to simulate the dynamics and deformation of capsules with elastic membrane. Such model has been previously validated against the theories, experiments and several other boundary integral and front-tracking numerical results. A detailed validation of the methodology and test of numerical convergence was given in [134, 152] for initially spherical capsules with no bending rigidity. Further validation for the bending model that is used for the RBCs was presented in [153].

Chapter 3

Hydrodynamic Interaction Between a Platelet and an RBC in a Dilute Suspension

3.1 Introduction

As mentioned in Chapter 1, platelets play a critical physiological role in the formation of hemostatic plug at vascular walls, and in the growth of thrombosis under pathological conditions [9–11]. Experiments with whole blood as well as ghost cell suspension showed an elevated platelet concentration near the wall [12, 13, 15, 16, 19, 20, 22, 157]. This phenomenon of platelet margination (also known as lateral drift) serves to enhance hemostatic or thrombotic events as it increases the number of platelets available for capture near the wall. Margination of the platelets toward the vascular wall is critically dependent on their interaction with the RBCs which has been illustrated in several experiments [17, 18, 154–156]. These studies have demonstrated that the near-wall excess was absent in platelet-rich plasma and in suspension of hardened RBCs [14, 21], and only occurred when the hematocrit was above a threshold level beyond which the accumulation was observed to increase with increasing hematocrit [20].

Several possible mechanisms are thought to underlie the margination process. The first is the volume exclusion process whereby the platelets are pushed towards the wall by the lateral motion of the RBC towards the center of the vessel [15, 154].

The second mechanism is the spatially dependent collision rate [20,159]. In a shearing flow, the continuous collision between the RBC and platelets results in significantly higher shear-induced diffusion of the platelets than the Brownian diffusion [23,24,158]. Since the RBC migration causes a concentration gradient, a net flux of platelets occurs from a region of higher collision rate to a region of lower collision rate [159]. Also, the RBC is sterically excluded from the plasma layer nearest the wall. If platelets entering the plasma layer have difficulty crossing back into the bulk flow, an accumulation of platelets can occur.

The above mechanisms are, however, not complete as they do not consider certain details of the suspension. For example, the volume exclusion model is incompatible with the fact that the RBC migration occurs faster than the platelet margination [159]. The collision model is also incomplete since the RBC concentration gradient occurs over a small length [160]. Also neglected in the models are the effect of the finite size of RBC and platelet as noted in [28, 29], the differences in their shapes, and the different dynamical behavior of the RBC, namely, the tank-treading and tumbling, observed under different shear rates [161–165]. It is also ambiguous which of these mechanisms prevail under specific conditions of hematocrit, shear rate, or shear rate gradients. Identification of these mechanisms through experimental observation in a dense multicomponent suspension is a very difficult task. High-fidelity computer simulations which model blood as a suspension of finite-size particles provide an alternative approach for verification of these mechanisms as well as obtaining further insights of the margination process. In the following, we discuss a few of the computer simulation studies. Al-Momani et al. [34] simulated RBC–platelet interaction in two-dimensions by modeling the RBCs as elastic particles. In addition to

reproducing several experimental observations, such as the increasing effect of hematocrit on platelet margination, Al-Momani et al. mentioned that the margination process seemed to occur due to the fluctuating hydrodynamic stresses that the RBCs imparted on the platelets, rather than the direct collision or volume exclusion. Crowl and Fogelson [36, 37] employed a two-dimensional immersed boundary-lattice Boltzmann method, and found that the platelet diffusivity was radially-dependent, and that the enhanced diffusivity in the core of the vessel along with the volume exclusion could partly explain platelet margination. Moreover, they proposed an additional drift mechanism that was localized at the edge of the RBC-depleted layer. Zhao and Shaqfeh [41], and Zhao et al. [42] performed the first fully-resolved three-dimensional simulations of RBC–platelet suspension using a spectral boundary integral method and demonstrated that the platelet margination was a shear-induced diffusional process in which the wall normal velocity fluctuations propelled the platelets toward the wall.

The aforementioned computer simulations have provided a wealth of understanding on the collective or averaged motion of the platelets. Such collective motion arises from the interaction between an RBC and a nearby platelet. Hence, important knowledge can be obtained also by looking at such pairwise collisions [166]. In particular, the role of the RBC dynamics on the deflection of individual platelet trajectory can be quantified without the 'noise' generated by other cells. It is well known that an isolated RBC in shear flow exhibits two types of dynamics: a tank-treading motion in which the cell behaves like a fluid droplet and orients at a fixed angle with the flow direction while the interior liquid (hemoglobin) and the cell membrane make a rotary motion, and a tumbling motion in which the cell makes a rigid body-like

flipping motion [161–165]. The question of how these two different dynamics affect the platelet trajectory has not been addressed in the literature, although prior experiments and simulations suggested an increasingly higher value of the platelet diffusivity with decreasing RBC deformability [21, 42]. The importance of understanding individual pairwise collision is aptly emphasized in a recent theoretical work in which the platelet adhesion was shown to be controlled by rebounding collisions with the near-wall RBCs and the finite size of the platelets [28,29]. It is also unknown whether the presence of a bounding wall changes the nature of the pairwise interaction. By simulating platelet-platelet interaction in three-dimensions, Mody and King [128,129] demonstrated that the near-wall collision frequency was significantly greater than the one far from the wall. Similar work on the near-wall RBC–platelet interaction is lacking.

In this chapter we present three-dimensional numerical simulations of the hydrodynamic interaction between a platelet and a red blood cell in a wall-bounded linear shear flow mimicking a parallel-plate flow chamber. We find that the pairwise interaction results in two different types of platelet trajectory: turning and crossing. The dynamics of the RBC (tank-treading versus tumbling) and the wall proximity are shown to have a significant influence on the turning and crossing events. Our results tend to suggest that the turning and crossing events, when they occur in succession, serve as an effective mechanism for continual anisotropic dispersal of the platelets from the RBC-rich region of the vessel towards the wall.

3.2 Problem Setup

Hydrodynamic interaction between an RBC and a platelet is simulated in a simulation setup in which the RBC–platelet pair is suspended in a linear shear flow between two parallel plates that are 35 μm apart (Figure 3.1). The flow domain is a rectangular box the lengths of which in the x and z directions are 35 and 18 μm, respectively. Details of computational domain and the boundary conditions are presented in Chapter 2. The initial location of the RBC and platelet centers-of-mass with respect to the bottom wall are denoted by Y_C and Y_{PLT}, respectively, and the difference $Y_{PLT} - Y_C$ is denoted by ΔY_0.

In the simulations, the governing equations are solved in dimensionless form. We use the radius of the equivalent sphere $a_o = (3V/4\pi)^{1/3}$ as the length scale, where V is the cell volume, and the inverse shear rate $\dot{\gamma}^{-1}$ as the time scale to make the equations dimensionless. The dimensionless time is denoted by $t^* = t\dot{\gamma}$. The major control parameter in dimensionless form is the capillary number of the RBC defined as $\mathrm{Ca} = \dot{\gamma}\,\mu_o\,a_o/2G_s$, where μ_o is the dynamic viscosity of the suspending medium. The capillary number represents the ratio of the viscous (fluid) force to the elastic force. We consider two values of Ca, 0.03 and 0.7. Considering the mechanical properties of the RBC membrane reported in the literature, $G_s \approx 10^{-3}$ dyn/cm, and $a_o \sim 3$ μm, the two values of Ca considered here correspond to shear rates of about 50 and 1000 1/s. For the lower value, the fluid force is weaker than the elastic force. Then the RBC is nearly rigidified and performs the tumbling motion. For the higher value of Ca, the elastic force is weaker, and a large deformation of the RBC occurs whereby it loses the initial biconcave shape. In this case, the RBC performs the tank-treading motion. It should be noted that for normal RBC suspended in plasma, the internal to external

viscosity ratio is about 5. At this high viscosity ratio, a steady tank-treading motion was not experimentally observed even at high capillary numbers. However, tank-treading at higher viscosity ratio can occur in a dense RBC suspension [167, 171]. Therefore, as we focus on the effect of RBC dynamics, namely tank-treading and tumbling, on the platelet motion in a dilute suspension, the RBC internal viscosity is assumed to be the same as the suspending medium viscosity μ_o, so that the tank-treading motion is reproduced at moderate capillary numbers such as Ca=0.7. The other relevant parameters are the initial lateral separation (along y direction) of the centers-of-mass of the RBC and platelet, $\Delta Y_o = Y_{PLT} - Y_C$. Additional geometric parameters are introduced later as needed. The capillary number for the platelet, defined in the similar way as above, is kept fixed at 0.002 so that it behaves as a nearly rigid particle. The dimensionless bending rigidity, $E_b^* = E_b/2a_o^2 G_s$ is set to 0.01. The global and local surface area dilatation is ensured to be less than 0.5%, as the cell membranes are nearly area-incompressible. The effect of inertia is small as the Reynolds number $\mathrm{Re} = \rho a_o^2 \dot{\gamma}/\mu_o \approx 10^{-2}$. All results are presented relative to the RBC center-of-mass. It may be noted that we neglected the presence of glycocalyx on the vessel wall which may influence the radial migration of the cells near the wall, see e.g., [168].

3.3 Results

In the following, the first two sections present the results when the RBC–platelet pair is located away from a wall. For such a configuration, the RBC is initially placed at the center-line of the channel, which is about 18 microns from the wall. We have separately verified that the dynamics of RBC does not show any appreciable

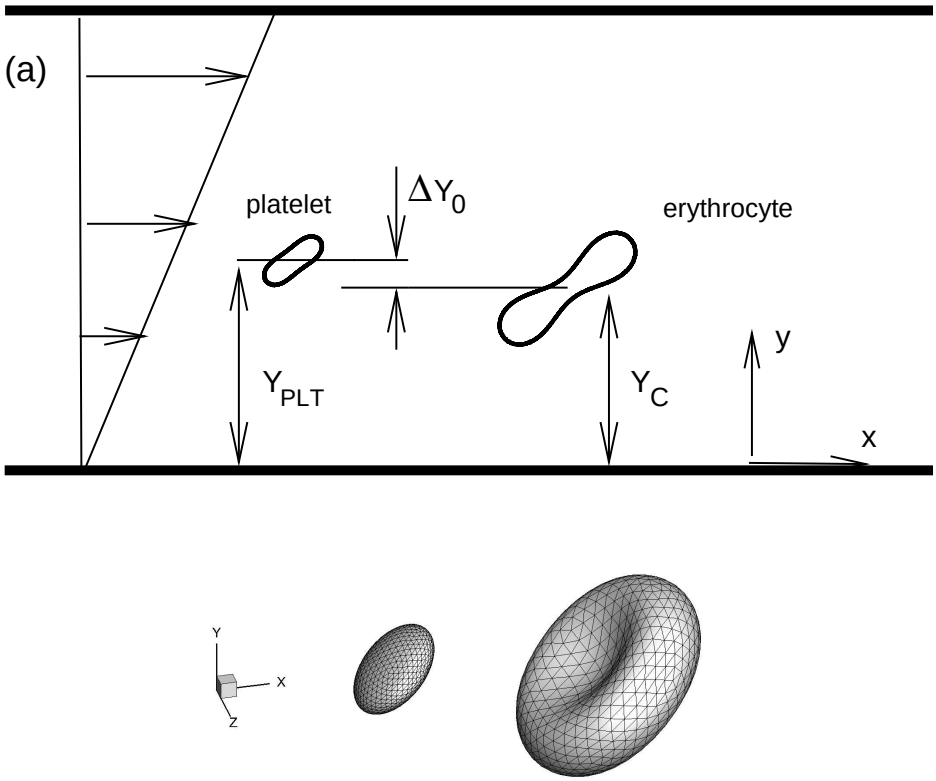

Figure 3.1: (a) Schematic of the computation geometry. (b) Discretization of the cell surface. The actual number of triangles (20480) is much higher than what is shown. The results will be plotted relative to the RBC center-of-mass.

difference by taking a bigger channel height ($\gtrsim$ 35 μm) and placing the RBC even further away from the wall. RBC deformation, inclination angle, and dynamics remain nearly unchanged. Furthermore, the wall effect (e.g., wall-induced lateral velocity of a deformable drop) is known to decrease as inverse square of the distance from the wall. Thus, the wall effect is negligible for such a configuration. The effect of wall proximity is considered in the third section.

3.3.1 Turning and Crossing Trajectories

First we consider the RBC–platelet interaction in presence of a tank-treading RBC (Ca = 0.7). Figure 3.2 shows the sequence of the RBC–platelet interaction obtained from our simulations for such a run. As evident from the figure, during the tank-treading motion the biconcave resting shape of the RBC is lost, and it assumes an elongated oblate shape aligning at an angle with the flow direction, while the cell membrane and the interior hemoglobin make a rotary motion. A marker point is tracked along the RBC membrane to illustrate the tank-treading in the figure. Such a motion is also accompanied by a small amount of time-dependent deformation characterized by periodic stretching and compression of the RBC, and a small angular oscillation, as shown in the figure and also observed elsewhere [163–165]. In comparison, being nearly rigid, the platelet undergoes a flipping motion in agreement with Jeffery's theory for rigid ellipsoids [169]. Two different types of interactions, a crossing and a turning, are observed depending on the initial lateral separation ΔY_o of the platelet center-of-mass relative to the RBC. In a crossing-type interaction (Figure 3.2(a)), the platelet comes close to the RBC, rolls over it, and continues to move in the same direction. During the process, the rigid platelet causes some amount of deformation

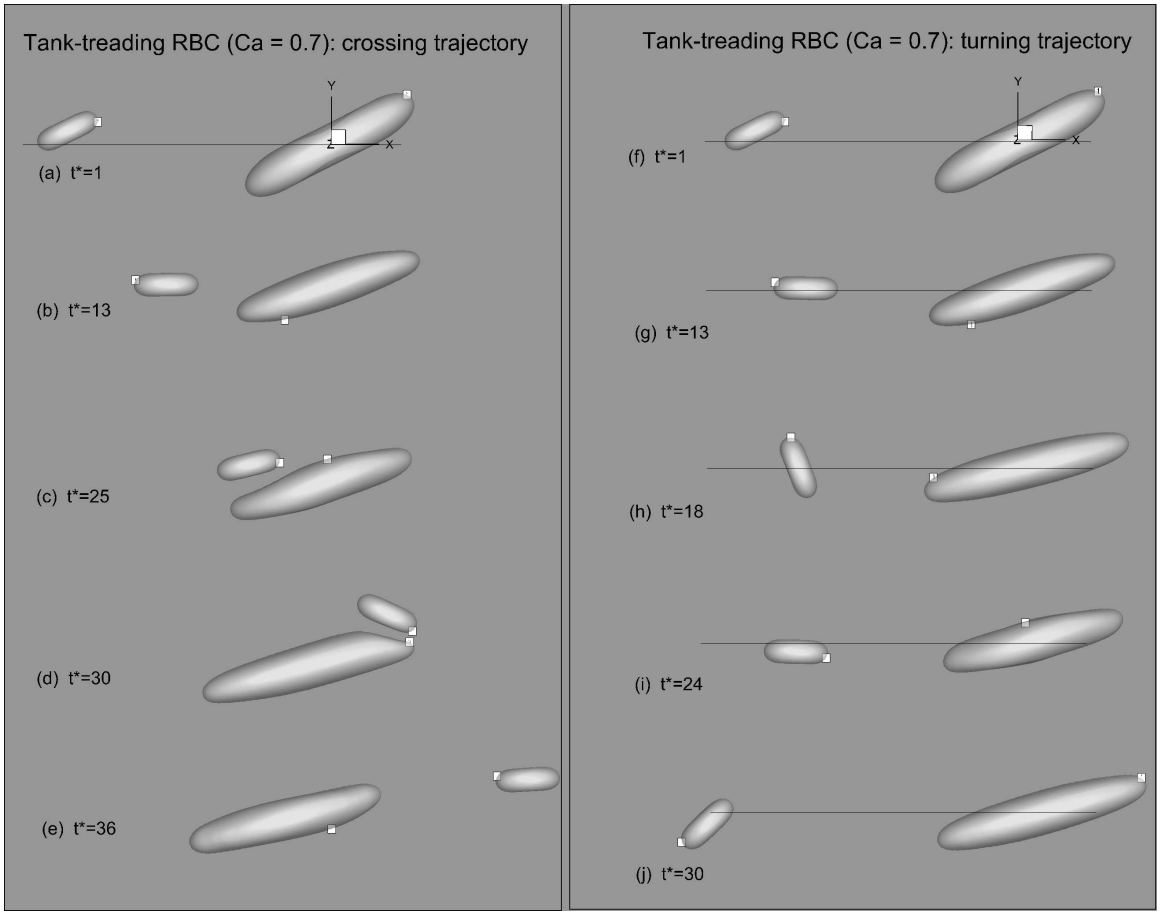

Figure 3.2: Simulation results showing the sequence of two different types of interactions in presence of a tank-treading RBC. Here Ca = 0.7 is corresponding to $\dot{\gamma} \approx 1000$ 1/s. (a)–(e) Crossing-type interaction. (f)–(j) Turning interaction. Marker points are shown in the cell surface which rotates along the surface indicating a tank-treading motion of the RBC. $t^* = 30$ corresponds to a 30 msec interaction.

of the relatively flexible RBC as visible in the figure. After the interaction, the lateral separation ΔY is higher than the initial offset ΔY_o. In a suspension of many particles, such increased separation due to binary interaction leads to the shear-induced diffusion. In a turning-type interaction (Figure 3.2(b)), the platelet first approaches the RBC, but then reverses its motion and turns away without coming close to the RBC. The turning event illustrates a long-range interaction as it occurs when the platelet is several diameters away from the RBC.

The trajectory of the platelet relative to the tank-treading RBC is shown in Figure 3.3 for several runs in which the initial lateral separation ΔY_o is varied. It is observed

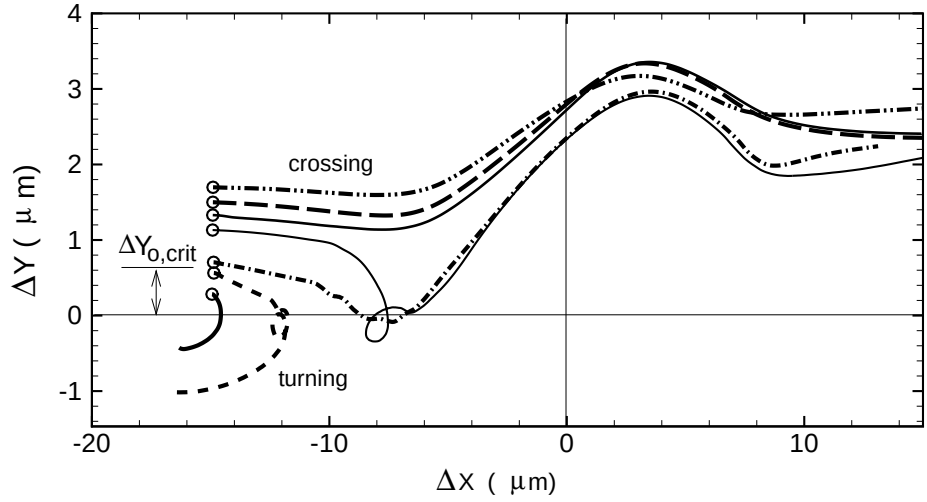

Figure 3.3: The trajectory of the platelet center-of-mass relative to a tank-treading RBC. The initial location of the platelet is marked by ∘ here and hereafter. Results from seven simulations are presented with different initial lateral separation ΔY_o. The turning trajectory is observed for $\Delta Y_o \leq 0.56$ μm, and the crossing trajectory is observed for $\Delta Y_o \geq 0.7$ μm.

that the crossing events occur for $\Delta Y_o \geq 0.7$ μm, and the turning events occur for $\Delta Y_o \leq 0.56$ μm. The results suggest that there is a critical separation $\Delta Y_{o,crit}$; the turning events occur when $\Delta Y_o \leq \Delta Y_{o,crit}$, and the crossing events occur when $\Delta Y_o \geq \Delta Y_{o,crit}$.

In Figures 3.2 and 3.3, the initial orientation of the RBC and platelet major axis with respect to the flow direction was set to $\pi/4$. For nonspherical particles, as is the case, the relative orientation at the time of collision is expected to affect their trajectory. Hence, we explore the effect of the initial relative orientation $\Delta\theta_o = \theta_{\mathrm{o,rbc}} - \theta_{\mathrm{o,plt}}$ between the platelet and RBC major axes, where $\theta_{\mathrm{o,rbc}}$ and $\theta_{\mathrm{o,plt}}$ are the initial orientation of the RBC and platelet, respectively.

It should be mentioned that the tank-treading RBC considered here aligns at a mean angle of approximately 17^o with the flow direction which is independent of the initial orientation of the RBC at the start of the simulations. In other words, the

RBC has a preferred orientation in the tank-treading motion [163–165]. In contrast, the platelet has no preferred orientation due to its flipping motion, although it tends to spend longer in the horizontal orientation [169]. Hence, different values of $\Delta\theta_o$ were considered. For each $\Delta\theta_o$, a range of initial separation ΔY_o is considered. For each run, the crossing or turning events are noted. These results are shown in a phase plot in the $\Delta\theta_o$–ΔY_o plane in Figure 3.4(a). As the figure demonstrates, a crossing event is observed for all values of $\Delta\theta_o$ if $\Delta Y_o > 0.7$ μm. For $\Delta Y_o < 0.6$ μm, a turning trajectory is observed regardless of the value of $\Delta\theta_o$. The value of the critical separation $\Delta Y_{o,crit}$ is found to lie between 0.6 and 0.7 μm for the tank-treading RBC. The occurrence of the turning or crossing event is independent of the relative orientation of the RBC/platelet pair, but depends on the initial separation ΔY_o. However, the actual trajectory is dependent on $\Delta\theta_o$. Figsure 3.4(b) and (c) show representative platelet trajectories for crossing and turning events, respectively, for different values of $\Delta\theta_o$. As these figures demonstrate, the exact trajectory is indeed dependent on $\Delta\theta_o$, but the occurrence of the turning or crossing event is not.

Another important observation in Figures 3.4(b) and (c) is the wide variability of the platelet trajectory over the range of $\Delta\theta_o$ for a fixed ΔY_o. For the turning trajectories shown in Figure 3.4(b) for four different values of $\Delta\theta_o$, the platelets are deflected in to different regions of the flow. This happens because the tank-treading RBC undergoes a small-amplitude shape and angular oscillation that introduces a weak time-dependency of the streamlines. This result is remarkable as it shows how the platelets can be dispersed by the RBC via a long-range interaction. A wide variability of the platelet trajectory can also happen during the crossing events as shown in Figure 3.4(c). Here a small change in the initial separation ΔY_o can lead to

a wide variation in the post-interaction separation. It is also evident in Figure 3.4(c) that a monotonic change in ΔY_o does not cause a monotonic change in the post-interaction separation. In other words, a platelet released at a smaller ΔY_o can end up at a larger post-interaction separation, whereas a platelet released at a larger ΔY_o can end up at a smaller separation. In some simulations, we observe that the post-interaction separation does not reach a steady value even when the platelet has moved away from the RBC. It is interesting to compare these results with that of deformable sphere-sphere interaction for which a sample trajectory obtained from our simulations is shown in Figure 3.4(c). For the sphere-sphere interaction, a crossing event always leads to an increased lateral separation, and a monotonic change in ΔY_o leads to a monotonic change in the post-interaction separation [40, 170], unlike what is seen here for the RBC–platelet interaction. Thus the wide variability of the trajectories observed in the RBC–platelet interaction is absent in the sphere-sphere interaction, and is essentially due to the nonspherical shapes of these cells. This observation also suggests that the shear-induced diffusion process in the RBC–platelet suspension is more complex with a significantly greater amount of anisotropic mixing than that in a spherical particle suspension.

For the crossing-type interactions for which the post-interaction lateral separation ΔY_f reaches a steady value, the deflection of the platelet trajectory can be quantified as $\delta = \Delta Y_f - \Delta Y_o$ which can be considered as an indirect measure of the platelet drift arising from the crossing-type collisions (see inset of Figure 3.5(a) for definition). Figure 3.5(a) shows δ as a function of ΔY_o for different $\Delta\theta_o$ for the tank-treading RBC. For a deformable sphere-sphere collision, δ continually decreases with increasing ΔY_o as noted earlier. While this trend is generally observed for the RBC–platelet

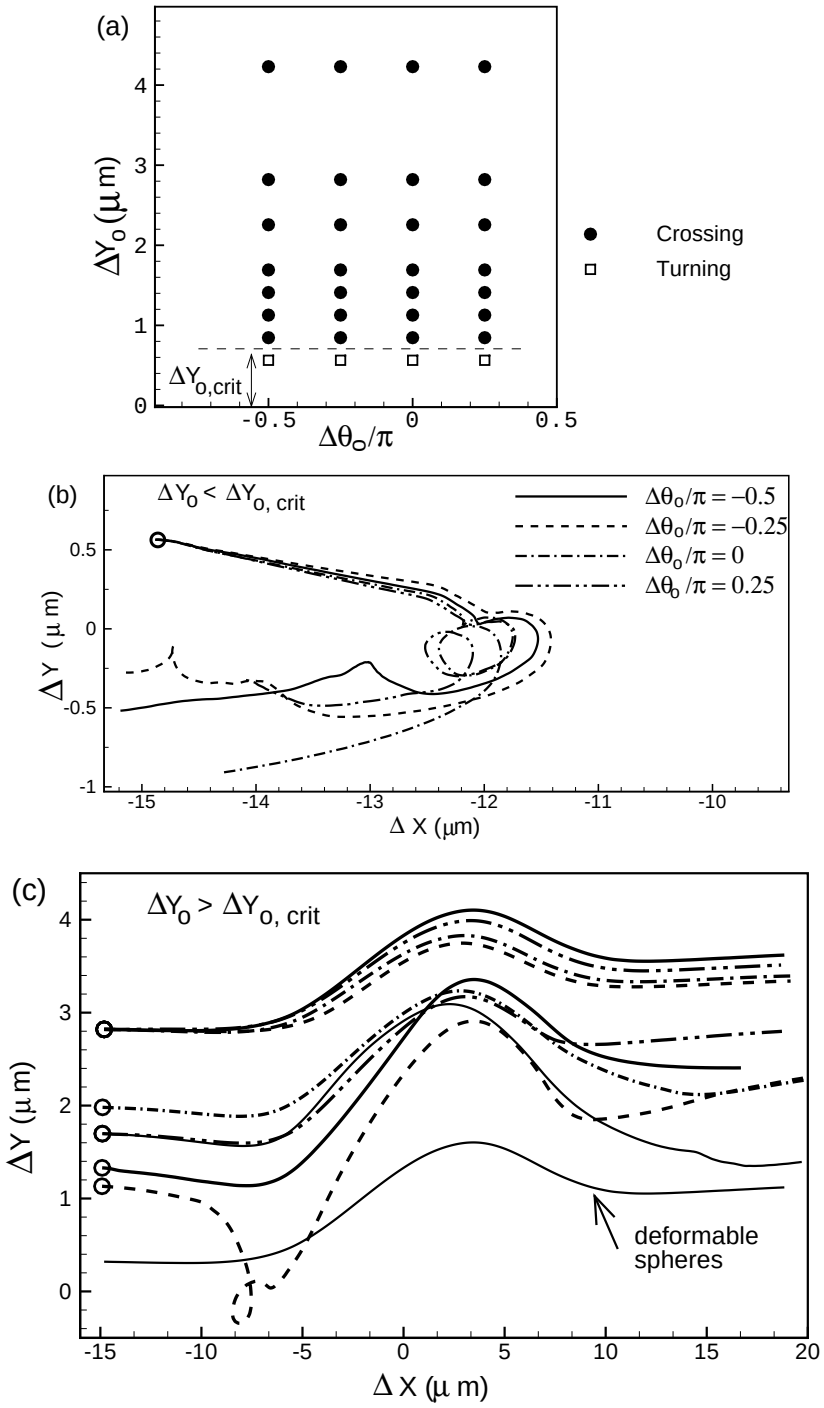

Figure 3.4: Effect of initial relative orientation $\Delta\theta_o$ on turning and crossing events in presence of a tank-treading RBC. (a) Phase plot in $\Delta\theta_o$–ΔY_o plane. (b) and (c) sample trajectories obtained with different $\Delta\theta_o$ for turning and crossing events, respectively. The wide variability of the platelet trajectory is illustrated in (c) that is absent in deformable sphere-sphere interaction.

interaction, the data in Figure 3.5(a) shows a more complex trend that δ has a non-monotonic dependency on ΔY_o with a local minimum at $\Delta Y_o \sim 1.3 - 1.8$ μm. While the actual value of δ is dependent on $\Delta\theta_o$ resulting in the scatter of the data, all curves for different $\Delta\theta_o$ show the similar qualitative trend.

It should be mentioned that the above results for δ are obtained for the RBC–platelet pair located away from a wall. The positive (or, negative) values of δ in the figure do not imply whether the platelet move away from (or, toward) the wall. It simply means the amount of additional lateral (or, cross-stream) displacement of the platelet upon interaction.

The non-monotonic variation of δ can be understood by recalling that during the crossing-type interactions, the platelet can cause a deformation of the RBC as observed in Figure 3.2(a). Analysis of the RBC shape suggests that the platelet causes a dimple upon collision near the RBC center, and thereby it is drawn closer to the cell resulting a reduced value of ΔY_f. The time-dependent RBC deformation during the collision process can be quantified by the Taylor deformation index $D = (L - B)/(L + B)$ where L and B are respectively the longest and shortest end-to-end lengths of the RBC in the shear plane passing through the center-of-mass. The deformation index which is plotted in the inset of Figure 3.5(b) as a function of time shows an increase at the time of collision. The change in the deformation index ΔD, defined as the difference in the maximum value of D reached during the collision and the value of D before the collision is shown in Figure 3.5(b) as a function of ΔY_o. A comparison of Figures 3.5(a) and (b) readily suggests that the minimum δ occurs at the same ΔY_o at which ΔD is maximum implying that the non-monotonic nature of the platelet deflection δ is due to the collision-induced deformation of the RBC. For

larger separation, the platelet does not come close enough to impart any deformation, and its deflection follows that of the streamlines. Hence, in this range, δ continually decreases with increasing ΔY_o since the streamlines away from the RBC deflect less than those near the RBC.

We have also simulated transport of passive tracers as massless point-particles in presence of the tank-treading RBC. The deflection of the tracer particles is plotted in Figure 3.5(a) which shows a continuous decrease with increasing ΔY_o, unlike the non-monotonic trend observed for the platelet. Except the local minimum near $\Delta Y_o \sim 1.3 - 1.8$ μm, the platelet deflection is generally higher than the tracer particle deflection. The peak deflections of the platelet at $\Delta Y_o \sim 0.8$ μm and 2.2 μm are nearly two-fold higher than that of the tracer particle.

3.3.2 Tank-Treading versus Tumbling RBC

Next we consider the RBC–platelet interaction when the RBC is in tumbling motion. As in case of a tank-treading RBC, here we also observe two types of interaction, crossing and turning. However, it is observed that the critical separation $\Delta Y_{o,crit}$ is higher for the tumbling RBC. Thus, the turning event occurs more often when the RBC is tumbling than when it is tank-treading. For the same values of $\Delta Y_{o,crit}$ near the critical value, a crossing trajectory is observed when the RBC is tank-treading, but a turning trajectory is observed when it is tumbling. In addition to the turning and crossing, a third type of interaction is observed in presence of the tumbling RBC. Here the platelet first approaches the RBC in a way that resembles a crossing interaction. But as it gets closer, it appears to 'ride' on the RBC with its major axis staying parallel to that of the RBC. After about a half tumble of the RBC, the

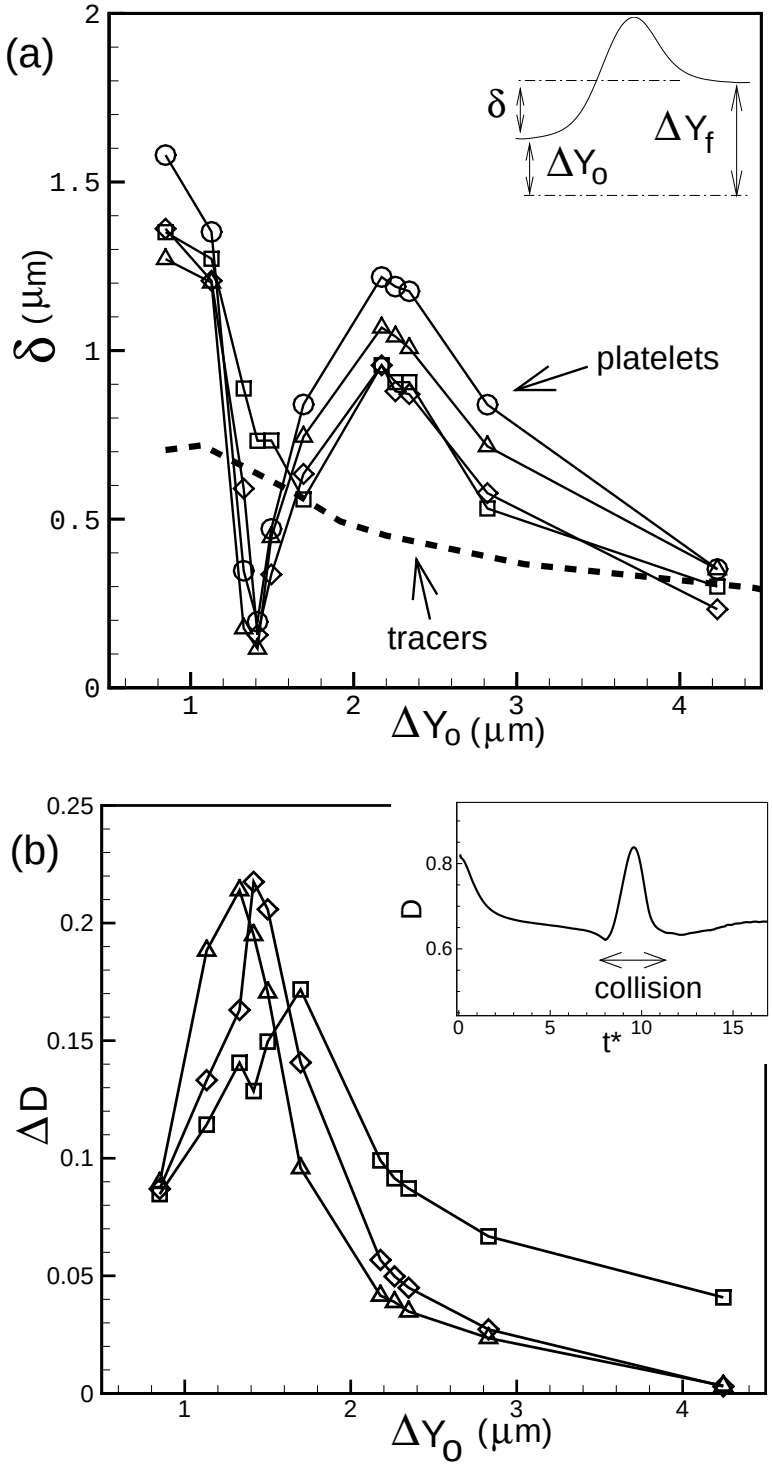

Figure 3.5: (a) Deflection δ of platelet trajectory for the tank-treading RBC as a function of ΔY_o and for different values of $\Delta\theta_o = \pi/4$ (Δ), 0 ($\diamond$), $-\pi/4$ ($\square$), $-\pi/2$ ($\circ$). The dashed line represents the deflection of passive tracers. (b) The change in RBC deformation index ΔD upon collision with the platelet is plotted. Inset shows the time-dependent deformation index D increases during the collision.

platelet starts to move away in the manner of a turning event. Note that the riding event is a close-range interaction unlike a turning event.

In presence of the tumbling RBC, the initial relative orientation $\Delta\theta_o$ makes a greater effect on the platelet motion in two different ways. First, for a given initial separation ΔY_o, it is possible to have three different types of interaction, namely, crossing, turning and riding, depending on the values of $\Delta\theta_o$. This is in stark contrast to the tank-treading RBC for which turning and crossing events were determined by ΔY_o only. As a result, critical separation $\Delta Y_{o,crit}$ has a greater margin of uncertainty in tumbling RBC. The phase plot in the $\Delta\theta_o$–ΔY_o plane for the tumbling RBC is shown in Figure 3.6(a). A crossing event is observed for all values of $\Delta\theta_o$ if $\Delta Y_o \gtrsim 2.0$ μm, and a turning event is observed if $\Delta Y_o \lesssim 0.7$ μm. But in the range $\Delta Y_o \sim 0.7-2.0$ μm, all three types of interaction is possible depending on $\Delta\theta_o$. Two examples are shown in Figure 3.6(b) where the platelet trajectory is plotted relative to the RBC for different values of $\Delta\theta_o$ but two fixed values of ΔY_o, 0.85 and 1.3 μm. For $\Delta Y_o = 0.85$ μm, a crossing trajectory is observed when $\Delta\theta_o/\pi = -0.25$, a turning trajectory is observed when $\Delta\theta_o/\pi = -0.5$ and 0.25, and a riding trajectory is observed when $\Delta\theta_o/\pi = 0$. Secondly, in the crossing-type interaction, a wider variation in the post-interaction separation is observed in the tumbling RBC runs than that observed before in the tank-treading runs.

The deflection δ of the platelet trajectory for the crossing-type interactions in presence of the tumbling RBC is plotted in Figure 3.6(c) as a function of ΔY_o for different $\Delta\theta_o$. While the general trend that δ decreases with increasing ΔY_o is observed, a significantly larger scatter in the data is evident here than that observed earlier for the tank-treading RBC due to the wider variation of the platelet trajectory.

In some cases, δ is found to be negative when the post-interaction lateral separation is smaller than the initial separation. Also plotted are the deflection of the tracer particles which show even more scatter and larger negative values. Evidently, the tumbling RBC creates a greater mixing than the tank-treading RBC.

3.3.3 Near-Wall Interaction

Next we consider the effect of wall proximity on the RBC–platelet interaction. The pairwise interaction is simulated in the linear shear flow by releasing the RBC–platelet pair at different distances Y_C from one wall. The turning and crossing events are obtained from the simulations by varying the initial lateral separation ΔY_o. The results are shown in Figure 3.7 as a function of Y_C and ΔY_o. This figure shows that the critical separation $\Delta Y_{o,crit}$ separating the crossing and turning events increases significantly near the wall with nearly a 3-fold increase from about 0.6 μm to 1.8 μm as Y_C is reduced from 18 to 4 μm in presence of the tank-treading RBC (Figure 3.7(a)). This increase in $\Delta Y_{o,crit}$ is due to an increase in the lateral extent over which closed streamlines occur as the wall is approached. The increased $\Delta Y_{o,crit}$ near the wall suggests that the turning events have a higher probability to occur than the crossing events. We also observe that the deflection in the platelet trajectory due to the turning events is greater when it happens near the wall than away from the wall. It will be argued later that this increased $\Delta Y_{o,crit}$ provides a mechanism of continual platelet dispersal from the RBC-rich region of the vessel to the RBC-depleted plasma layer near the wall. The near-wall effect during a tumbling motion is presented in Figure 3.7(b) which shows that $\Delta Y_{o,crit}$ is higher than that obtained for the tank-treading RBC.

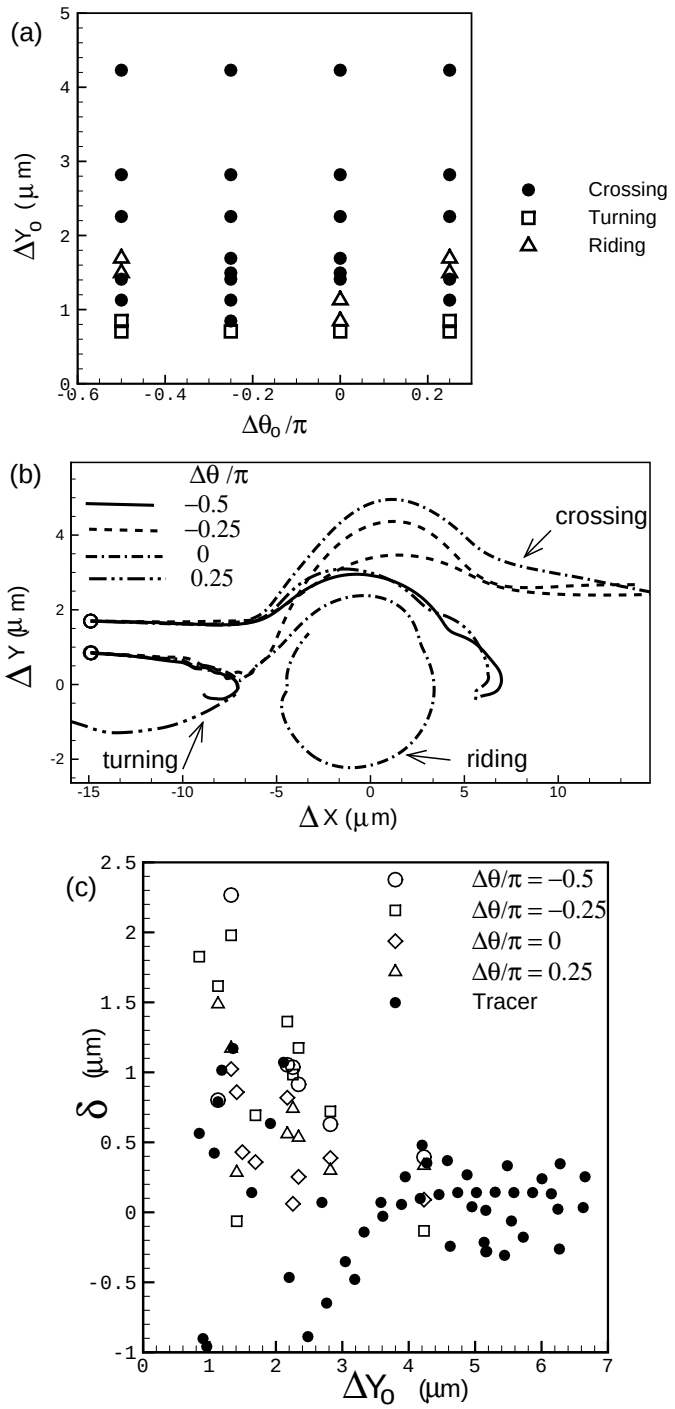

Figure 3.6: Effect of initial relative orientation $\Delta\theta_o$ on turning, crossing and riding events in presence of a tumbling RBC. (a) Phase plot in $\Delta\theta_o$–ΔY_o plane. (b) sample trajectories obtained with different $\Delta\theta_o$ and ΔY_o. Turning, crossing and riding trajectories are observed for the same ΔY_o at different $\Delta\theta_o$. (c) Platelet and tracer particle deflections δ in presence of a tumbling RBC.

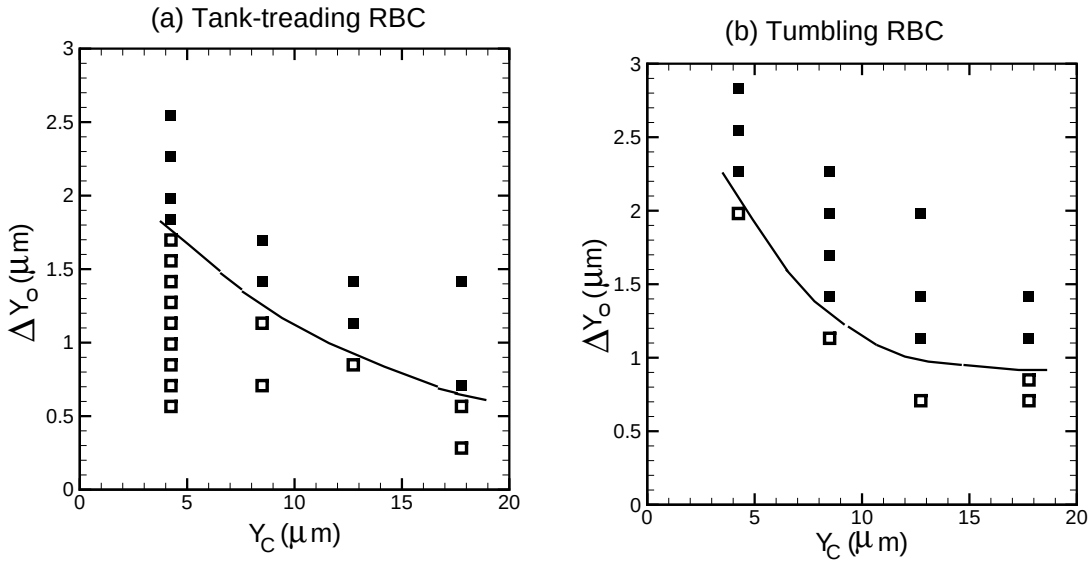

Figure 3.7: Effect of wall proximity on turning and crossing events in presence of (a) tank-treading and (b) tumbling RBC. The RBC/platelet interaction is simulated by releasing the RBC–platelet pair at various distances Y_C from the wall and for varying initial vertical separation ΔY_o. Open symbols indicate turning and filled symbols indicate crossing events.

When the RBC–platelet interaction occurs far away from a wall, the occurrence of the turning or crossing events depends only on the relative velocity between the RBC and the platelet, and hence, on the initial lateral separation ΔY_o, but not on the initial separation between the cells and the wall, Y_C or Y_{PLT}. One important consequence of the wall proximity is that the interaction depends not only on ΔY_o, but also on Y_C and Y_{PLT}. The results shown in Figure 3.7 correspond to the scenario when the platelet is released further away from the wall than the RBC, i.e., $Y_{PLT} > Y_C$. We have also performed simulations when the platelets are released closer to the wall than the RBC, i.e., $Y_C > Y_{PLT}$. Figure 3.8 compares the platelet trajectories for these two configurations at three values of the lateral separation $|\Delta Y_o|$. Our simulations show that for the same value of $|\Delta Y_o|$ a turning event occurs when $Y_{PLT} > Y_C$, but a crossing event occurs when $Y_C > Y_{PLT}$. This result suggests that the value of the

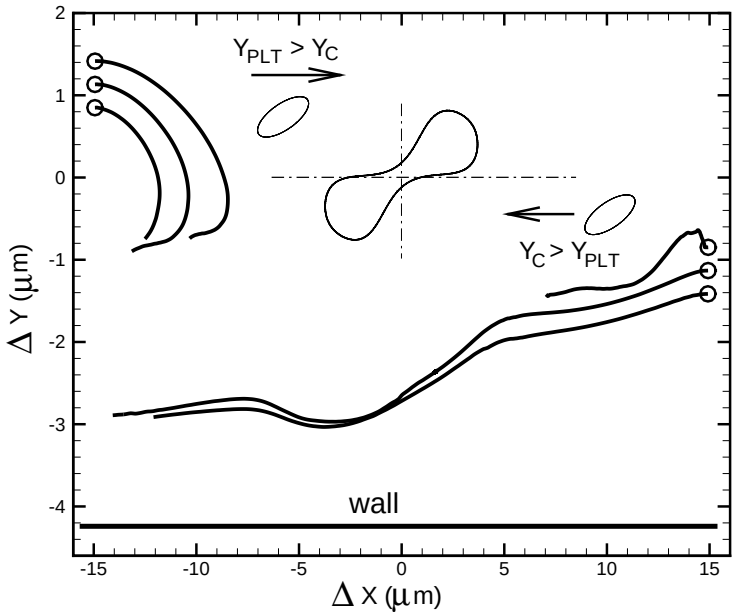

Figure 3.8: Differential effect of wall proximity: For the same $|\Delta Y_o|$, a turning trajectory is observed when the platelet is located further away from the wall than the RBC ($Y_{PLT} > Y_C$), and a crossing trajectory is observed when the platelet is located closer to the wall ($Y_C > Y_{PLT}$).

critical separation $\Delta Y_{o,crit}$ strongly depends on whether the RBC or the platelet is located closer to the wall. It also suggests that, near the wall, the turning events have a higher probability to occur when $Y_{PLT} > Y_C$, but the crossing events have a higher probability to occur when $Y_C > Y_{PLT}$.

3.3.4 Streamlines and Forces

The different types of interaction observed here can be partly explained by analyzing the streamlines around the RBC as shown in Figure 3.9(a-c). For the tank-treading case, the streamlines remain unchanged in time as the RBC motion is nearly steady. There is a critical lateral length y_o below which the streamlines turn around, and above which they extend from $-\infty$ to $+\infty$. The crossing event usually occurs when the platelet is released above this critical y_o, and a turning occurs when it is released

below the critical y_o. It should, however, be mentioned that unlike a passive tracer, a platelet because of its finite size is not going to follow a streamline exactly. Unlike in the tank-treading case, the streamlines around a tumbling RBC are highly time-dependent due to the changing orientation of the RBC. The closed streamlines are observed at some instants but not always. Hence the turning and crossing events in this case would depend on the instantaneous location and orientation of the platelet relative to those of the RBC. Further, closed streamlines can exist in a narrow region around the RBC. If the platelet is trapped in this region, a riding trajectory would occur. The dynamic nature of the streamlines around a tumbling RBC leads to a more complex platelet trajectory than that observed in presence of a tank-treading RBC.

The forces acting on the platelet during different types of interactions are shown in Figure 3.9(d). These forces are computed by spatially averaging the membrane forces over the cell surface. It may be noted that there are only two types of forces that are experienced by the platelet-RBC: the hydrodynamic force, and the collision force. No other types of force (e.g. electrostatic repulsion, adhesion) are considered here. In case of turning behavior, the RBC and the platelet do not come close to each other; so there is no collisional force. The platelet trajectory is entirely determined by the deflection of the streamlines due to the presence of the RBC as shown earlier. In this case, the force on the platelet is purely hydrodynamic. In case of crossing and riding behaviors, the collisional force arises in form of the lubrication force (which is again hydrodynamic in nature) generated in the narrow gap between the RBC and the platelet. Our data shows that the force magnitude increases significantly during the encounter which implies that the collisional force is much higher than

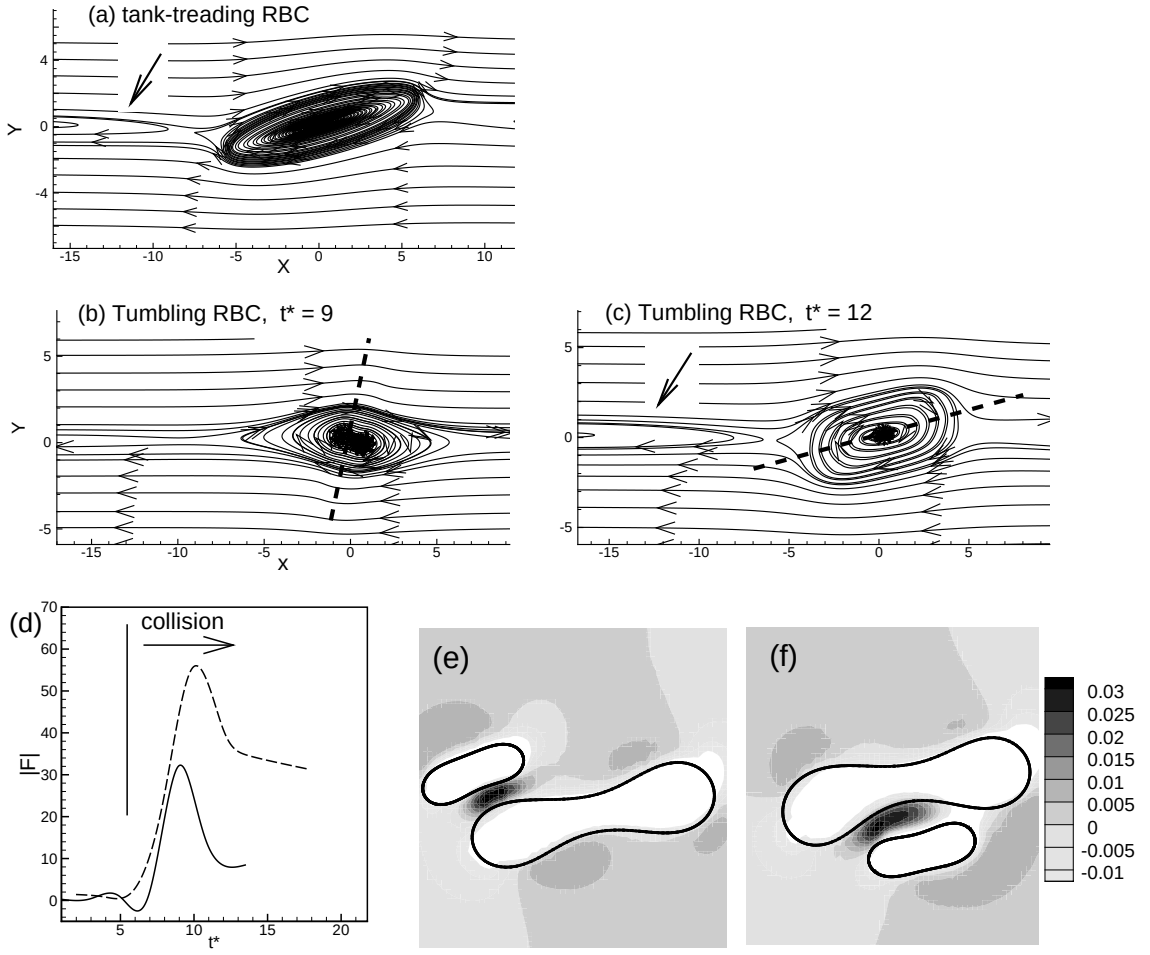

Figure 3.9: (a)-(c): Streamlines around a tank-treading RBC (a), and a tumbling RBC (b–c) showing closed (indicated by the arrow) and open streamlines. The thick dash lines in (b) and (c) indicate the instantaneous alignment of the RBC major axis. (d): Spatially averaged force on the platelet as a function of time for a representative crossing (——) and riding (- - - - -). (e)-(f): Contours of pressure for riding at two time instances.

the hydrodynamic force. Our data further shows that the force magnitude is much higher during the riding interaction than the crossing interaction. This is because the platelet nearly sticks to the RBC for a longer time during the riding interaction. In order to see the origin of these forces, we plot the contours of pressure in the shear plane for a riding interaction in Figure 3.9(e-f). This clearly shows that the pressure in the gap between the RBC and the platelet increases significantly during the close interaction leading to the lubrication force as the fluid is squeezed during the collision.

3.4 Conclusion

In this chapter we presented three-dimensional numerical simulations of hydrodynamic interaction between an RBC and a platelet in a wall-bounded shear flow. Instead of considering a suspension of multiple cells, we focused on an isolated RBC–platelet pair to quantify the influence of the tank-treading and tumbling dynamics and the wall proximity on the deflection of individual platelet trajectory without the 'noise' from other cells. Our results suggested the existence of two types of interaction. In a crossing-type interaction the platelet comes in close proximity to the RBC, rolls over it, and continues to move in the same direction. In a turning-type interaction, the platelet turns away before coming close to the RBC. The occurrence of any one of these events depends on the initial lateral separation ΔY_o between the platelet and RBC centers-of-mass. The crossing events occur when ΔY_o is above a critical separation $\Delta Y_{o,crit}$, and the turning events occur when ΔY_o is below $\Delta Y_{o,crit}$. Similar crossing and turning events have been observed during the interaction of two identical (homotypic) RBCs and liquid drops in shear flow [40, 166, 170]. The work presented in this chapter deals with heterotypic particles.

The presence of a bounding wall is observed to have a significant influence on the crossing and turning events. When the RBC–platelet interaction occurs far away from a wall, the occurrence of the turning or crossing events depends only on the relative velocity between the RBC and the platelet as determined by their initial separation ΔY_o in a linear shear flow. In presence of a wall, the interaction depends not only on ΔY_o, but also on the lateral separation between the cells and the wall, Y_C and Y_{PLT}. When the RBC is released closer to the wall than the platelet, i..e. $Y_{PLT} > Y_C$, the critical separation $\Delta Y_{o,crit}$ is observed to increase almost 3-fold. This result implies

that the turning events have several-fold higher probability to occur than the crossing events when the RBC is flowing closer to the wall than the platelet. On the contrary, if the platelet is initially located closer to the wall than the RBC, i.e., $Y_{PLT} < Y_C$, the critical separation $\Delta Y_{o,crit}$ was observed to be significantly lower, implying that the crossing events are more likely to occur in this scenario.

We now propose a mechanism of continuous platelet dispersal from the core of the vessel towards the wall based on the trajectory deflection. Consider the RBC flowing at the edge of the plasma layer as shown in Figure 3.10. If a platelet is initially located in the RBC-rich region (scenario '(A)' as marked in the figure), i.e., $Y_{PLT} > Y_C$, a turning event is likely to occur (since $\Delta Y_{o,crit}$ is large as found by the simulations and shown in Figure 3.7) which will bring it in to the plasma layer. At this time, the platelet is located closer to the wall than the RBC (i.e., $Y_{PLT} < Y_C$). Now if another pairwise interaction occurs, that would likely result in a crossing event (since $\Delta Y_{o,crit}$ is small) bringing the platelet even closer to the wall (scenario '(B)' as marked in the figure). Our numerical trajectory in Figure 3.8 showed that after the event '(B)' the platelet center-of-mass can be within one micron from the wall giving it the opportunity to bind to the wall. Thus, the turning and crossing events, when occur in succession as shown here, provide an effective mechanism to continually drive the platelets away from the RBC-rich region of the vessel in to the RBC-depleted plasma layer and further towards the wall.

The influence of RBC deformation and the finite cell size is most noticeable in the computed lateral deflection δ which can be considered as an indirect measure of the platelet drift due to the crossing events. While δ is generally observed to decrease with increasing initial RBC–platelet separation ΔY_o, it shows a pronounced local minimum

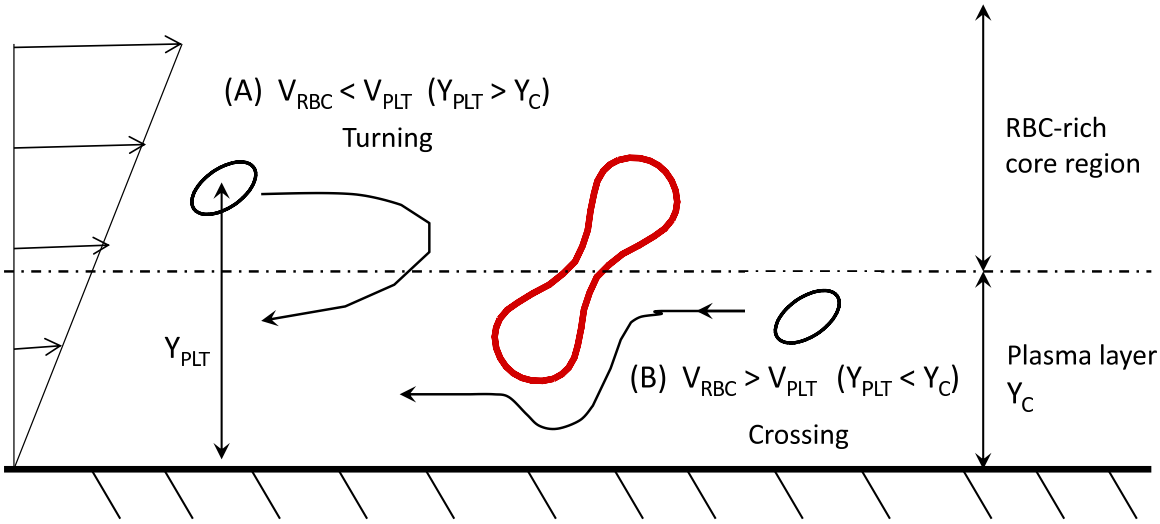

Figure 3.10: A proposed mechanism of continuous platelet dispersal from the RBC-rich region of the vessel towards the wall based on the trajectory deflection by a succession of turning and crossing events occurring due to the interaction with an RBC flowing near the edge of the plasma layer. When the platelet is initially located farther away from the wall than the RBC, a turning event has the higher probability to occur (since $\Delta Y_{o,crit}$ is large) that would bring the platelet from the RBC-rich region to the plasma layer (scenario '(A)' in the figure). If a subsequent interaction occurs, a crossing event is likely to occur (since the platelet is now located closer to the wall than the RBC and $\Delta Y_{o,crit}$ is small), bringing the platelet even closer to the wall (scenario '(B)').

at $\Delta Y_o \sim 1.3 - 1.8$ μm. This nonmonotonic trend of δ is due to the deformation of the RBC caused by the platelet upon collision. We showed that the local minimum in δ is accompanied with an increase in the RBC deformation index. The finding that a platelet can impart a considerable deformation to the RBC underscores the importance of considering the finite size of the platelet in any theoretical model of platelet drift [28,29]. It also has other biological implication as RBC deformation was shown to increase ATP release [171], and the presence of ATP is known to initiate platelet aggregation [20]. Additionally, the non-monotonic trend of δ is not observed for deformable sphere-sphere collision, and for tracer particle deflection. The platelet deflection is generally observed to be higher than the tracer deflection, except near the local minimum, and is likely caused by an increased volume exclusion due to the finite platelet size.

The different dynamics of the RBC, i.e., the tank-treading and the tumbling motion, are observed to cause considerable differences in the platelet motion. Most notably, the critical lateral separation $\Delta Y_{o,crit}$ is found to be higher for the tumbling RBC. This finding is important as the tank-treading motion occurs at relatively high shear rates while the tumbling motion occurs at low shear rates. The tumbling motion can also occur due to the loss of deformability caused by various pathological conditions of the RBC, which is believed to be associated with higher risk of thrombogenesis [167].

Another important result is the wide variability of the platelet trajectory observed over the range of initial inclination and lateral separation that is absent in the deformable sphere-sphere interaction. For the deformable sphere-sphere interaction, a crossing event always leads to an increased lateral separation, and a monotonic change in ΔY_o leads to a monotonic change in the post-interaction separation. In contrast, such a monotonic change is not observed for the RBC–platelet interaction. In some simulations, we observed that the post-interaction separation was less than the initial separation leading to a negative value of δ, in a stark contrast to the sphere-sphere collision. This result not only underscores the importance of incorporating the effect of the nonspherical shapes and finite size of the RBC and platelet in any drift model [28, 29], it also suggests that the shear-induced diffusion process in the RBC–platelet suspension is more complex than that in a spherical particle suspension. The variability of the platelet trajectory is observed to increase significantly when the tumbling RBC is considered resulting in a larger scatter in δ. This result is in qualitative agreement with the experimental observation that the platelet diffusivity increases with decreasing RBC deformability [21].

The numerical data can be used to make an approximate estimate of the enhanced platelet diffusion coefficient in presence of the RBCs. Taking the value of δ to be ~ 1 μm from Figure 3.5(a), a shear rate in the range of 100–1000 s^{-1} for which a normal red blood cell would be tank-treading, and the interaction time of $t \sim 0.01 - 0.1$ s obtained from the simulations (corresponding to a dimensionless time of $t^* \sim 10$), we find a diffusion coefficient $D_{eff} \sim \delta^2/t = 10^{-6} - 10^{-7}$ cm^2/s. Although this is a simple estimate, and is based on a single cells rather than an actual suspension, this value is surprisingly similar to the ones reported in experiments [23, 24, 158], and computer simulations with multicellular suspension [37], and nearly 2 to 3 orders of magnitude higher than the Brownian diffusion coefficient of $\sim 10^{-9}$ cm^2/s [172].

In conclusion, we have presented three-dimensional numerical simulation of hydrodynamic interaction between a platelet and an RBC. We observed a wide variability in the platelet trajectory under the influence of the tank-treading and tumbling motion of the RBC, and proposed a mechanism of continual platelet removal from the core of a vessel towards the plasma layer. While the realistic blood flow is a dense suspension, and the platelet drift is the result of the multicellular interaction, understanding the two-body interaction as presented here is a first step before addressing the more complex problem of platelet drift in whole blood (which is the subject of Chapter 4). The work presented in this chapter shows that even the two-body interaction could be quite complex due to the nonspherical cellular shape, RBC deformation, and tank-treading and tumbling motion. Nevertheless, the numerical methodology is extended to consider multiple cells in order to study the mechanism of platelet/microparticle drift in a suspension, as presented in the following two chapters (Chapters 4 and 5).

Chapter 4

Platelet Transport and Dynamics in Blood Flow

4.1 Introduction

As mentioned in Chapters 1 and 3, platelets or thrombocytes constitute an essential component of human blood due to their role in the formation of hemostatic plug and thrombus [9–11]. These phenomena require the platelets to come within a close proximity to the vessel wall, initiating platelet–wall contact followed by adhesion. Experiments with flowing blood showed an elevated platelet concentration near the wall [12–15]. It has long been known that the RBCs play a critical role in platelet margination and near-wall excess [17–20]. As mentioned in Chapter 1, normal healthy RBCs are extremely deformable [5, 21]. In a shear flow, the RBCs experience a wall-normal force which arises due to their deformation, and propels them away from the wall. By volume exclusion, the platelets marginate towards the wall [17–21, 23, 24, 159]. The migration also causes a nonuniform RBC concentration in the wall-normal direction, and, hence a spatially varying RBC–platelet collision rate resulting a collision-induced platelet margination [23, 24, 28, 29, 159]. Once marginated, the dynamics of the platelets within the near-wall CFL can also be affected by the flowing RBCs at the edge of the CFL. The dynamics of the marginated platelets inside the CFL, in turn, determines the probability of platelet–wall contact. The importance of RBC–platelet interaction is aptly emphasized in a recent theoretical work in which the

platelet adhesion was shown to be controlled by the RBC–platelet pairwise collision and the finite size of the platelets [28, 29].

Quantification of the RBC–platelet interaction at the cellular scale and its connection to the macroscale platelet transport through experimental observation in whole blood is a difficult task. High-fidelity computer simulations which model blood as a suspension of finite-size cellular components provide an alternative approach. Several 2D models, e.g. Refs. [34–39], have emerged over the past years using this approach. In addition to reproducing many experimental observations, these studies have provided new insights on the RBC–platelet interaction. For example, AlMomani et al. [34] showed that the fluctuations in the hydrodynamic stresses imparted by the RBCs also resulted in platelet margination. Crowl and Fogelson [36,37] found that the platelet diffusivity was spatially varying, which along with the volume exclusion could partly explain platelet margination. Moreover, they proposed an additional spatially-varying drift which enhanced the RBC-induced margination and also prevented the platelets from re-entering into the RBC-rich zone thereby acting as a barrier. More recently, Skorczewski et al. [38] considered platelet dynamics near a thrombus, and observed that platelet tumbling near the vessel wall was strongly influenced by nearby RBCs, and that the thickness of the CFL was greatly reduced near the thrombus.

While the aforementioned 2D models have provided a wealth of understanding on platelet–RBC interaction, one major limitation was the absence of platelet movement in the transverse direction, i.e., along the direction of the vorticity of the shear flow. The RBC–platelet collision is fundamentally three-dimensional in nature. Prior 3D model studies of pairwise collision of deformable particles in shear flow showed that a significant displacement of the particles could occur in the transverse direction

[40]. In case of platelets, such movements can collectively lead to a diffusion in the transverse direction. Therefore, consideration of platelet motion in the vorticity direction can greatly influence their near-wall dynamics and adhesion. The first 3D simulation of RBC–platelet suspension was reported by Zhao and Shaqfeh [41] and Zhao et al. [42] who observed that the margination was irreversible and that the platelet diffusivity was inhomogeneous in the wall-normal direction. Additionally, their 3D model supported the notion of the additional drift proposed by the 2D model of Fogelson and coworkers [36,37]. However, as noted in [41,42], the 2D model overpredicted the platelet diffusivity.

Evidently, there is a need for further understanding of platelet dynamics in whole blood based on 3D simulations. In addition to the translational diffusion in the third dimension, the 3D nature of the RBC–platelet collision can result in a rotational diffusion about the flow direction leading to a variation in the off-shear plane orientation of the platelets. Quantification of such off-shear plane rotation and its influence on platelet dynamics does not exist in the literature. Furthermore, in a shear flow, deformable particles, such as the RBCs, often form clusters leading to a local anisotropy in the RBC concentration [130]. How such anisotropic RBC concentration affects platelet margination, and how the anisotropic platelet diffusion affects the near-wall platelet dynamics are not known. To that end, in this chapter we present a high-fidelity cellular-scale 3D computational model of platelet dynamics in whole blood. The dynamics and the large deformation of the RBCs are resolved with high accuracy in our model. From the simulation results, we show that the RBC distribution in whole blood becomes naturally anisotropic and results in a fast and discontinuous platelet margination. The platelet translational diffusion inside the

CFL is observed to be anisotropic, and as a result, leads to platelet cluster formation, and increases the likelihood of clot formation. This study demonstrates the ability of the cellular-scale 3D models of whole blood in understanding platelet margination and near-wall platelet dynamics.

4.2 Problem Setup

Margination of platelets and their near-wall dynamics are simulated in whole blood in 3D. The whole blood is represented as a suspension of many RBCs and platelets. We consider a linear shear flow $\mathbf{u} = \{\dot{\gamma}y, 0, 0\}$ bounded between two walls mimicking a parallel-plate Couette flow chamber. Here $\dot{\gamma}$ is the shear rate, x is the flow direction, y represents the velocity gradient direction, and z is the vorticity direction (Figure 4.1). More details on the computational domain and boundary conditions are given in Chapter 2. The surface of each RBC is discretized using 20480 triangular elements (or, 10242 Lagrangian nodes), and platelet using 1280 triangular elements (or, 642 nodes). Similar to Chapter 3, we use the radius of the equivalent sphere $a_o = (3V/4\pi)^{1/3}$ as the length scale, where V is the RBC volume, and the inverse shear rate $\dot{\gamma}^{-1}$ as the time scale. The RBC and platelet membrane shear moduli are 2.5×10^{-6} N/m, and 1.7×10^{-4} N/m, respectively. The dimensionless time is denoted by $t^* = t\dot{\gamma}$. The effect of inertia is small as the Reynolds number $\mathrm{Re} = \rho a_o^2 \dot{\gamma}/\mu_o \lesssim 10^{-2}$, where μ_o is the plasma viscosity.

We performed a total of 18 simulations of whole blood suspension at a constant shear rate $\sim 1000\ \mathrm{s}^{-1}$, and hematocrit H_t ranging from 9 to 36%. The channel lengths considered are 36, 54, and 71 μm, with heights 27, and 54 μm. One limitation of the simulations is the relatively smaller computational domain compared to an actual

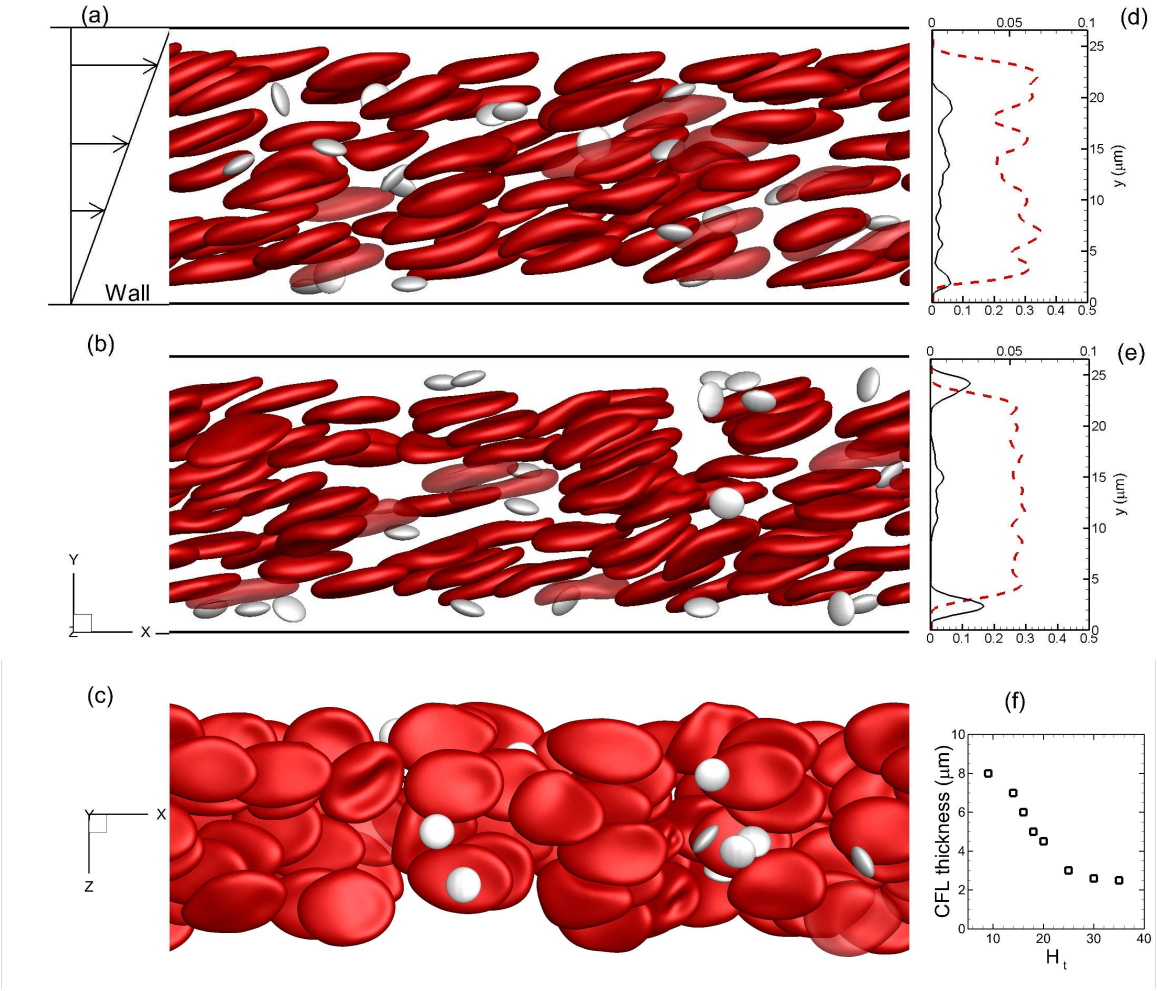

Figure 4.1: Representative snapshots showing instantaneous cell distribution from our whole blood simulation in shear flow at hematocrit $H_t = 23\%$ in a channel of 71 μm length and 27 μm height. (a) and (b) are views along the vorticity (z) direction at dimensionless time $t^* = 20$ and 450, and (c) is the view from the bottom of the channel at $t^* = 450$. RBCs are shown in red and platelets in gray. (d) and (e) show the average RBC (red, dash line, and bottom axis) and platelet (black, continuous line, and top axis) concentration distribution across the channel height at times $t^* = 20$ and 450. (f) shows the average thickness of the RBC-depleted region (CFL) near the wall as a function of H_t.

blood vessel and the use of a periodic boundary condition, which are needed to make the 3D calculations tractable for very long simulations. The Eulerian resolution is $\sim$ 9 mesh points/μm in y direction, and 6.8 mesh points/μm in x and z directions. There are at least 53 Eulerian points across one RBC diameter, which is sufficient to resolve the cell dynamics. The number of RBCs in the computational box ranges from 32 to 90, and platelets from 4 to 20. For normal blood, the RBC to platelet count is $\sim$16-20:1 [8]. We considered a higher platelet count that could occur locally in a blood vessel under pathological and non-physiological conditions.

4.3 Results

4.3.1 Platelet Margination and the Role of RBC Suspension Microstructure

Figure 4.1 shows three snapshots of platelet margination through flowing RBCs in whole blood suspension. The RBCs and platelets are distributed randomly in the beginning of the simulation. Figures 4.1(a) and (b) show the cell distribution at $t^* \approx 20$ and 450. Accumulation of platelets near the walls is observed in Figure 4.1(b). The RBCs are deformed significantly; the resting biconcave shape is no longer visible and the cells assume a more elongated disk-like shape. The motion of each cell is quite irregular due to interaction with the neighboring cells which results in further deformation. Figure 4.1(b) reveals that the RBCs often flow in 'clusters' in which they are stacked vertically. Note that there is no adhesion potential used in the current model. Indeed, they are important if RBC aggregation and platelet coagulation are considered. But our interest in this chapter is not aggregation or coagulation.

Since cell aggregation is not considered in our model, these clusters are formed naturally due to cellular motion driven by hydrodynamics forces. Furthermore, since the RBCs are deformable, the lubrication force between adjacent cells prevents them from physical contact. Thus, as long as there is sufficient Eulerian resolution ($\gtrsim 4$ points) between adjacent membranes, simulations are stable. Also visible in Figure 4.1(b) are 'cavities' that are plasma-rich regions formed between adjacent clusters. These clusters and cavities form the microstructures in the suspension, making the instantaneous and local RBC distribution highly anisotropic. Prior studies of sheared suspension flows have shown microstructure formation and resulting anisotropy [130]. As will be shown later, the RBC microstructure in whole blood has a significant role in platelet margination. Figures 4.1(d) and (e) show the RBC and platelet concentration distributions. Formation of an RBC-depleted region or CFL, and elevated platelet concentration near the walls are evident. The average CFL thickness obtained from the simulations is shown in Figure 4.1(f) and ranges from 2.5 to 8 μm for hematocrit 36 to 9%, respectively.

Sample trajectories of marginating platelets are shown in Figure 4.2(a). Two different types of trajectories can be identified. In one type (marked by 'A' in the figure), a continuous but slow diffusive motion of a platelet towards the wall occurs throughout the entire margination process. This is the well-known shear-induced diffusion that is a result of the interaction between a platelet and individual RBC [17–19, 21, 159]. It is a rather slow process as the platelets undergoing such a motion are rarely observed to reach the wall even after 500 dimensionless time in the simulation. In the second type, marked by 'B' in the figure, the margination appears to be a discontinuous process, and consists of three phases: A slow lateral diffusive motion

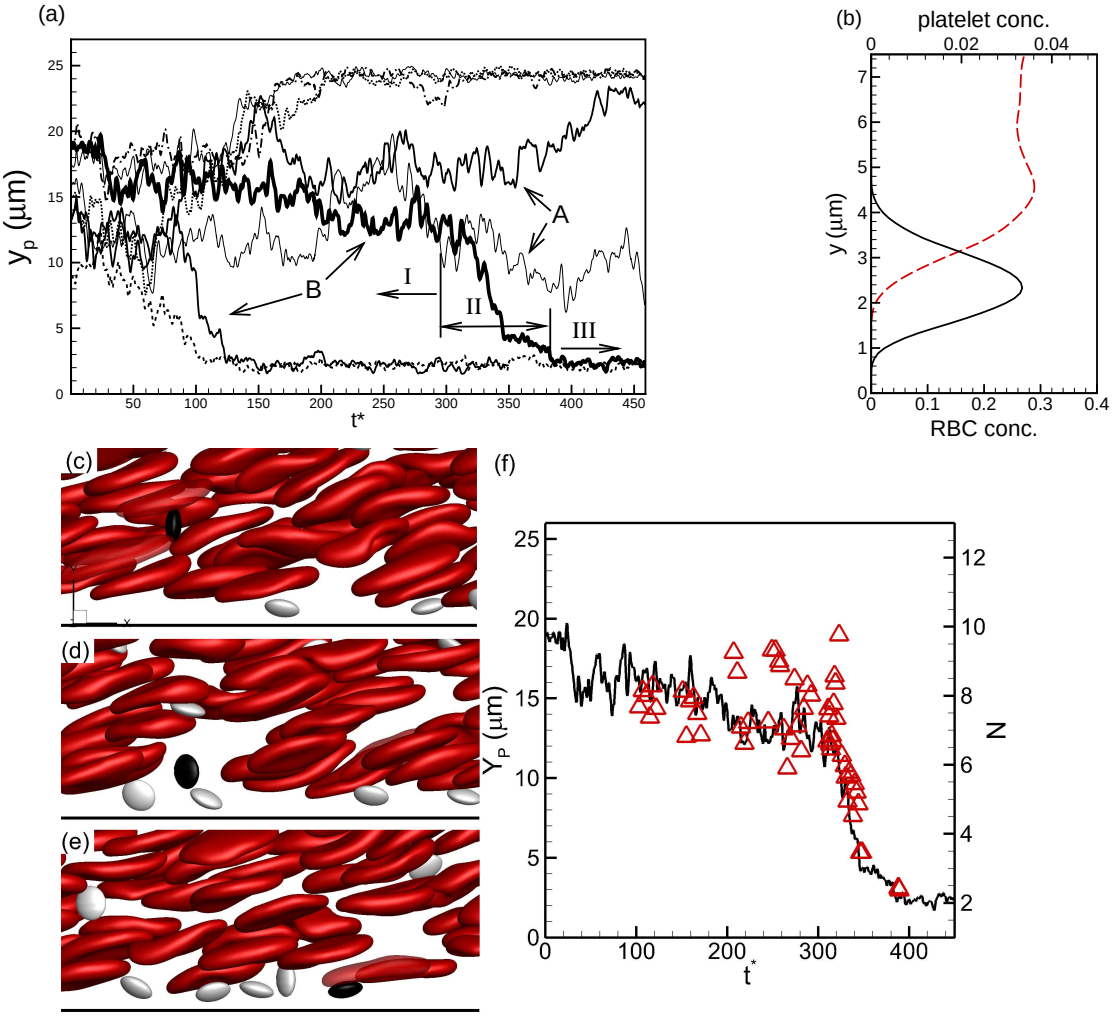

Figure 4.2: (a) Sample platelet trajectories from simulations in channels of 27 μm height. 'A' identifies platelets with a 'continuous and slow' diffusive motion, and 'B' identifies platelets with a 'discontinuous and fast' motion. For type 'B', the margination consists of a slow diffusive motion (phase I), an abrupt and large change in platelet lateral position (phase II), and a nearly wall-parallel motion inside the CFL (phase III). (b) RBC (red, dash line, and bottom axis) and platelet (black, continuous line, and top axis) concentrations distribution near the CFL. Marginated platelets mostly concentrate just outside the RBC-rich zone. (c)-(e) Time resolved snapshots to show that the phase II in type 'B' trajectory is a result of a platelet (shown in black) first getting pushed by a RBC cluster and then entering into a cavity, and finally marginated to the CFL. (f) The trajectory of the platelet (black line, left axis) identified in the snapshots is shown along with the number of RBCs N (red triangles, right axis) found instantaneously in a spherical volume of radius $3a_0$ surrounding the platelet.

while the platelets remain within the RBC-rich region (marked as 'I' in figure). During this motion, the platelets mostly drift longitudinally along the flow direction while their lateral drift is small. This is followed by a fast lateral movement which brings the platelets abruptly out of the RBC-rich layer and into the CFL (marked as phase 'II' in figure). Once within the CFL (phase III), the platelet trajectories are nearly parallel to the vessel wall with fluctuations caused by their collision with the RBCs. Figure 4.2(b) shows the RBC and platelet concentration near the CFL. Marginated platelet mostly accumulate just outside the RBC-rich zone, and their concentration decreases as the wall is approached. As a result, marginated platelets are subjected to continuous collisions with the RBCs flowing at the CFL edge. As will be shown later, such collisions dictate the platelet dynamics inside the CFL.

The discontinuous margination was noted recently by Lee et al. [55] in their experimental study of submicron particle dispersion in mouse microvasculature. Platelet trajectories presented in [42] also suggest the occurence of such fast margination. Our simulations suggest that the discontinuous margination is due to the microstructures formed by the RBCs. If a platelet is first hit by a cluster and then enters into a cavity, a large and sudden change in its lateral position can occur. If the cavity extends from near the wall into the RBC-rich region, such an interaction can abruptly bring the platelet out of the RBC-rich layer and into the CFL. Thus the platelet can use the cavity as an 'express lane' for a fast margination towards the wall. Due to the resemblance of the platelet trajectories we term this behavior as *waterfall phenomenon*. Figures 4.2(c)-(e) show time-lapse snapshots illustrating the discontinuous margination process. In Figure 4.2(c), a platelet interacts with RBC clusters (phase I), following which it enters into a cavity in Figure 4.2(b) (phase II). A significant

drop in its lateral position occurs during this phase. Thereafter, the platelet enters into the CFL (phase III). To further elaborate the roles of microstructure, we compute the local RBC count by considering a spherical volume of radius $3a_0$ surrounding the platelet (Figure 4.2(f)). The RBC count becomes higher before the onset of the abrupt drop in platelet lateral position, implying an encounter with one or more RBC clusters. Thereafter, both the RBC count and the platelet position drop rapidly implying a fast lateral movement of the platelet through a cavity. We did not find any correlation between the rapid platelet margination and hydrodynamics pressure or stress field. The cavity-assisted margination is likely due to a volume exclusion effect.

4.3.2 Platelet Diffusion in the RBC-Rich Region and in the CFL

The platelet trajectories in Figure 4.2(b) show that the marginated platelets do not re-enter into the RBC-rich region. Thus the margination process is irreversible as noted earlier [36, 37, 41, 42]. The observation also supports the notion that the RBCs flowing near the edge of the CFL provides a barrier against the platelets [36, 37]. Furthermore, trajectory inside the CFL suggests that the lateral (y) movement of the platelets is significantly hindered due to the confinement effect from the wall and the RBCs flowing at the CFL edge. As a result, the platelet motion inside the CFL is not purely diffusive. To compare platelet diffusion inside the RBC-rich region and inside the CFL, the mean-squared displacement (MSD) in y-direction is shown in Figure 4.3(a). Inside the RBC-rich region, the MSD is linear after the initial transience suggesting a diffusive transport. The platelet diffusivity in the lateral direction inside the RBC-rich region is obtained as $\sim 3 \times 10^{-7}$ cm^2/s at shear rates ~ 1000 s^{-1}

which is in agreement with previously reported values [24, 41], and is 2 to 3 orders of magnitude higher than the Brownian diffusivity, suggesting the RBC-augmented diffusion. In contrast, the MSD inside the CFL does not grow with time after the initial transience suggesting that the lateral motion of the marginated platelets is not diffusive due to the confinement provided by the RBCs and the wall.

As a further quantification of the platelet diffusive motion, root-mean-squared (rms) velocity fluctuations for the wall-normal direction (v') and for the vorticity direction (w') are computed. Note that in our 3D model, platelets can move in z direction due to platelet-RBC interaction although there is no mean flow in z. Figure 4.3(b) shows the rms fluctuations inside the RBC-rich zone as functions of hematocrit. Both v' and w' increase with increasing hematocrit due to increasing platelet–RBC collisions. Interestingly, though w' values are smaller than v', they are comparable, suggesting a significant diffusion in the transverse direction. By considering separate simulations of an interacting RBC and a platelet in a shear flow, we have verified that such interaction can often result in a significant platelet displacement in the z-direction although there is no mean flow in z. Similar observation has been obtained in the past for pairwise interaction of deformable particles in 3D in shear flow [40]. Therefore, our 3D simulations show that in whole blood, platelet diffusion in the transverse direction is comparable to that in the wall-normal direction.

Figure 4.3(c) compares v' and w' inside the CFL. Here v' is significantly less than that in the RBC-rich zone, due to the hindered lateral motion of the platelets. w' is also less than that obtained inside the RBC-rich zone, but it is higher than v', and increases with decreasing CFL thickness. This is because reducing the CFL thickness results in more frequent RBC–platelet collision; while the platelets cannot

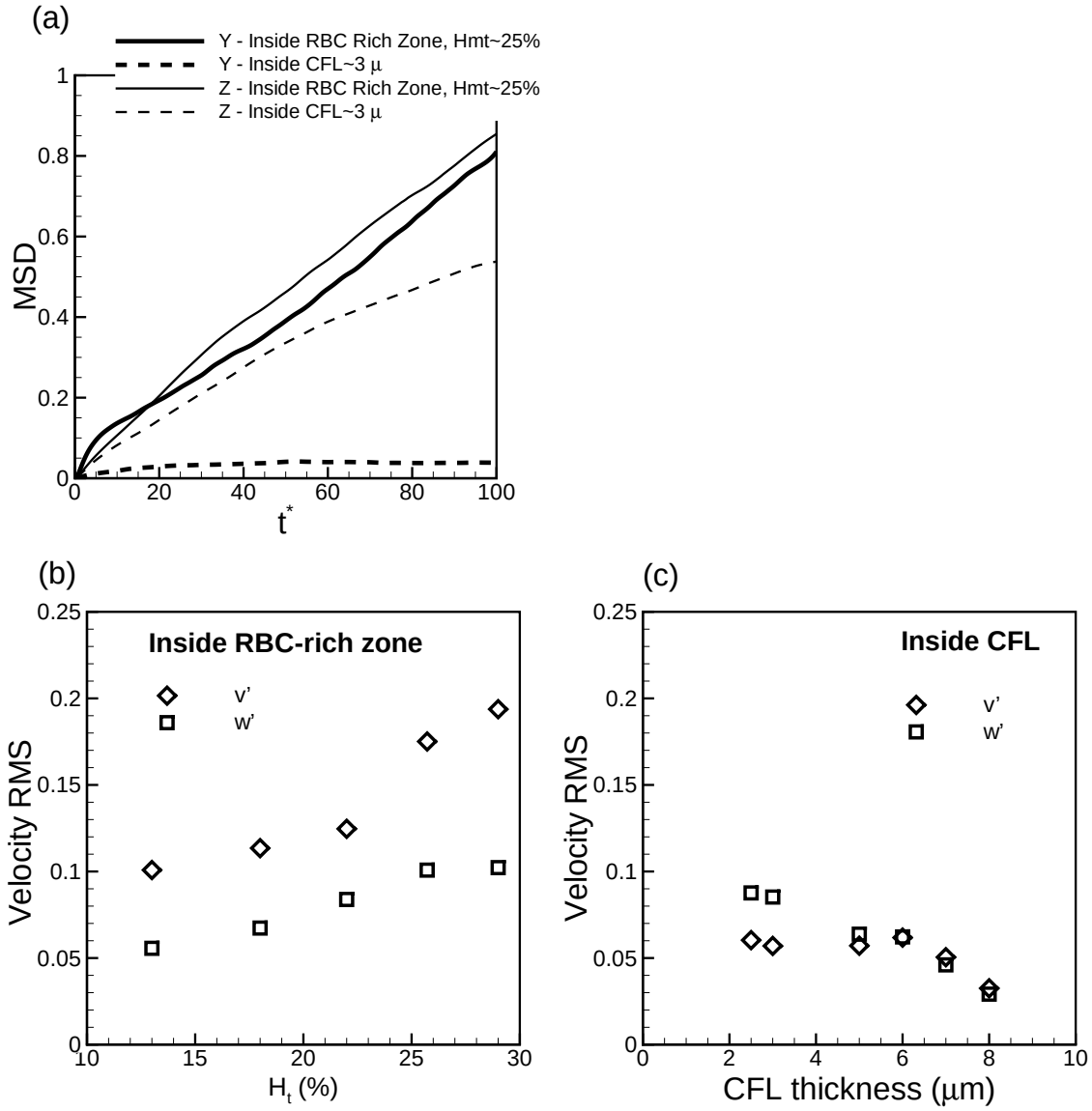

Figure 4.3: (a) Mean-squared-displacement $\langle y'^2 \rangle$ for lateral (wall-normal) motion for platelets inside the RBC-rich zone (thick solid line) and inside the CFL (thick dash line), and $\langle z'^2 \rangle$ inside the RBC-rich zone (thin solid line) and inside the CFL (thin dash line). (b) and (c) show RMS velocity fluctuation of platelets inside the RBC-rich zone and inside the CFL, respectively, in wall-normal direction (v', $\diamond$) and transverse direction (w', $\square$).

move in the wall-normal direction due to confinement, they can easily move in the transverse direction. This result implies that platelet diffusion inside the CFL is anisotropic; diffusion is hindered in the wall-normal direction, but could be higher in the transverse direction.

4.3.3 Formation of Platelet Clusters

As a result of the transverse motion, marginated platelets come close to each other and form clusters as shown in Figure 4.4(a). Such cluster formation could be a precursor to clot formation if the platelets are activated. We observe clusters of varying size, and of multiple numbers. Figure 4.4(b) shows the size and number of clusters over time in a simulation with 17% hematocrit and a CFL thickness of 6 μm. A cluster is identified when the surface-to-surface distance between adjacent platelets is less than $\sim$750 nm. Using this criterion we determine the cluster size, i.e., the number of platelets in a given cluster, and also track the number of clusters in the simulations. Figure 4.4(b) shows that the size and number of clusters are highly dynamic and varying from zero to five, and from zero to four, respectively, over time for the specific simulation considered. Note that the platelets are randomly drawn to each other and the cluster formation is entirely due to RBC–platelet interaction and platelet diffusion, as our model does not consider platelet activation. Furthermore, since our model does not consider platelet aggregation, these clusters exist for a short time.

We find that the size and probability of formation of the platelet clusters are highly dependent on the CFL thickness. Figure 4.4(c) shows the probability of finding a cluster of size three to five in two different groups based on the thickness of the

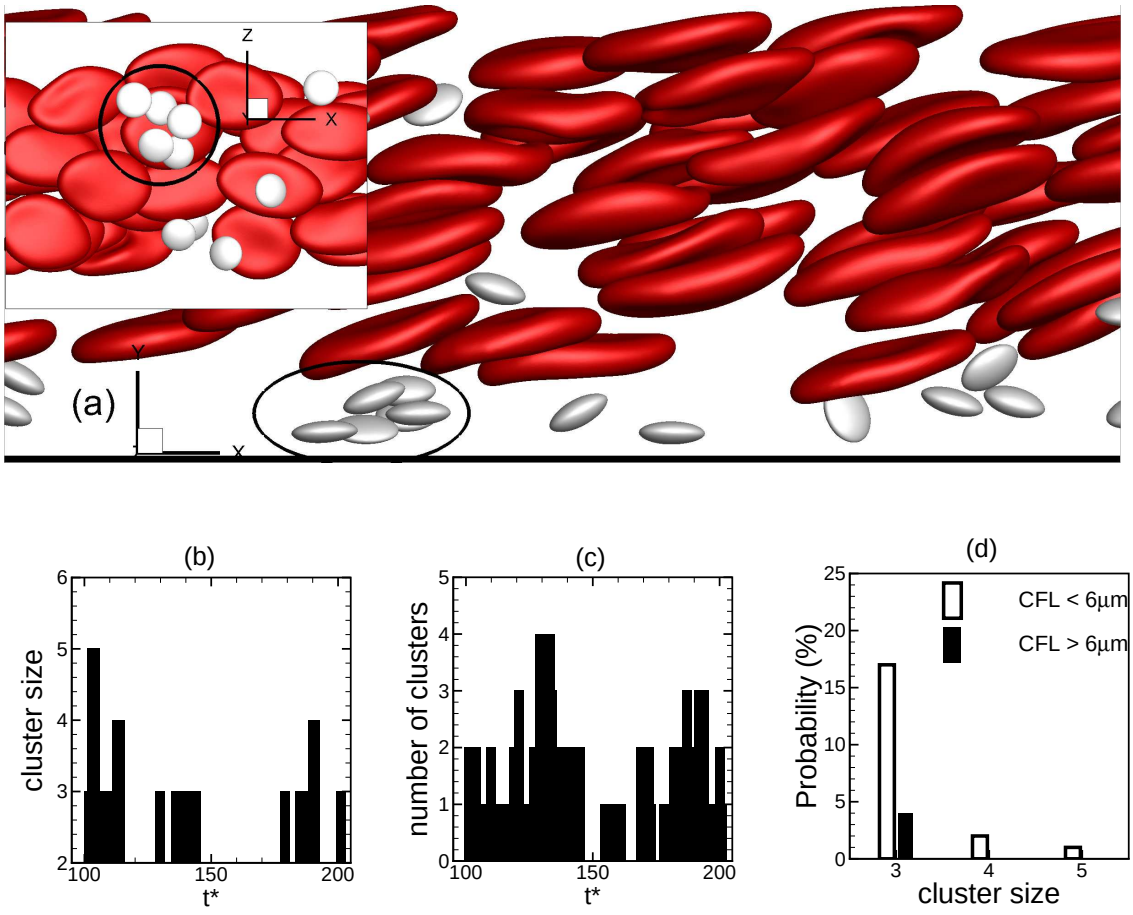

Figure 4.4: (a) Formation of platelet cluster inside the CFL. Inset shows the view from the bottom of the channel. (b) and (c) show the size and number of the clusters over time in a simulation at $H_t = 17\%$ (CFL thickness 6μm). (d) Probability of finding a cluster of size three to five for CFL thickness ≤ 6 μm (unfilled bars), and > 6 μm (filled bars).

CFL as ≤ 6 μm, and > 6 μm. A thinner CFL significantly increases the probability by increasing both the size and the number of clusters. For CFL thickness > 6 μm, the largest cluster observed consists of three platelets, whereas for CFL thickness ≤ 6 μm the largest cluster contains five platelets. The probability of finding a cluster of three platelets is $\sim$4% for CFL thickness > 6 μm and 17% for CFL thickness ≤ 6 μm. The probability decreases significantly with increasing cluster size. Thus, the large clusters form only occasionally and are short-lived.

4.3.4 Comparison of Platelet Dynamics in the RBC-Rich Zone and the CFL

In absence of the RBCs, an isolated platelet flowing near a wall executes either a tumbling or a sliding motion [173,174]. The tumbling is characterized by a rotational (flipping) motion like a rigid ellipsoid. Far from a bounding wall, the tumbling dynamics is described by the theoretical work of Jeffery [169]. Near a wall, the period of tumbling increases due to an additional drag induced by the wall. Very close to the wall, a full tumbling is no longer possible; instead, the sliding motion occurs. During sliding, the platelet long axis remains nearly parallel to the wall and oscillates slowly with a small amplitude. If an isolated platelet is released in the flow with its axis of revolution normal to the wall, our simulation predicts that the sliding motion occurs when the platelet center $y_p \lesssim 1.5$–1.7 μm, and the tumbling occurs above this distance.

Figure 4.6 shows how platelet dynamics is affected in presence of RBCs in 3D whole blood simulation. Apart from lateral location of the platelet center (y_p), two

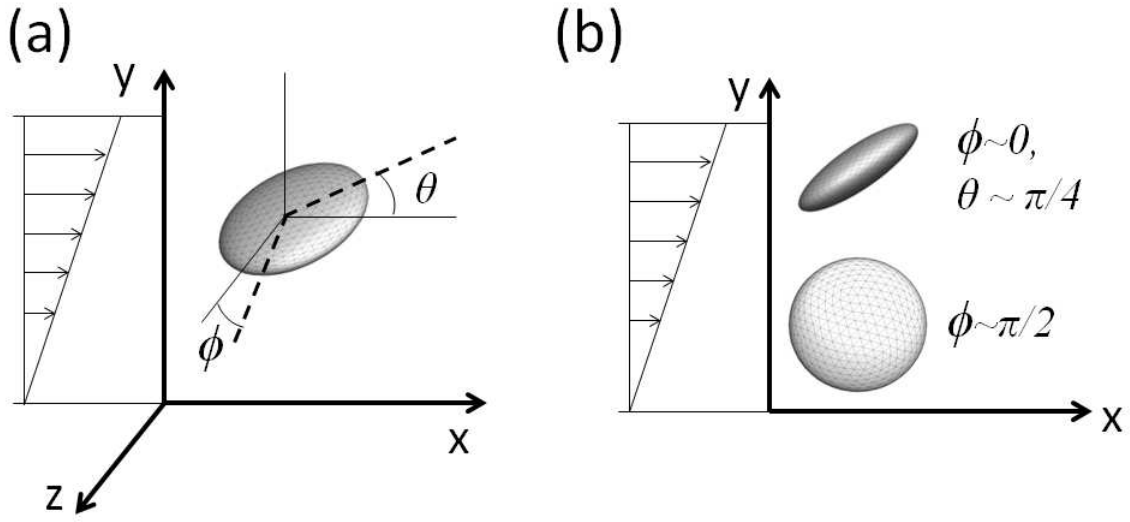

Figure 4.5: (a) Definition of the off-shear plane angle ϕ, and the tumbling angle θ; ϕ is the angle between the major axis of the platelet contour in y-z plane and the z axis, and θ is the angle between the major axis of the platelet contour in the shear plane (x-y plane) and the flow direction, x. (b) Examples showing the platelet inside the the shear plane (top) and along the vorticity axis (bottom).

angles are used to illustrate the platelet dynamics: an angle θ (tumbling angle) between the major axis of the platelet contour in the shear plane and the flow direction (x), and an angle ϕ (off-shear plane angle) between the major axis of the platelet contour in y-z plane and the z axis (see Figure 4.5). $\phi = 0$ means the axis of revolution is in the shear plane so that the platelet is oriented parallel to the wall. For $\phi \neq 0$ the axis of revolution tilts out of the shear plane. Thus, ϕ quantifies platelet rotation about the flow direction that is absent in a 2D model. For tumbling, θ varies between $\pm\pi/2$, and for sliding both θ and ϕ are ≈ 0.

Figure 4.6 shows that platelet dynamics in presence of RBCs is very irregular, unlike the periodic motion of an isolated platelet. Within the RBC-rich zone, the tumbling dynamics occurs but in an irregular manner (Figure 4.6(a)). Within the CFL, both tumbling and sliding are observed depending on the platelet center-to-wall distance. In addition, an intermittent dynamics is observed in which the tumbling

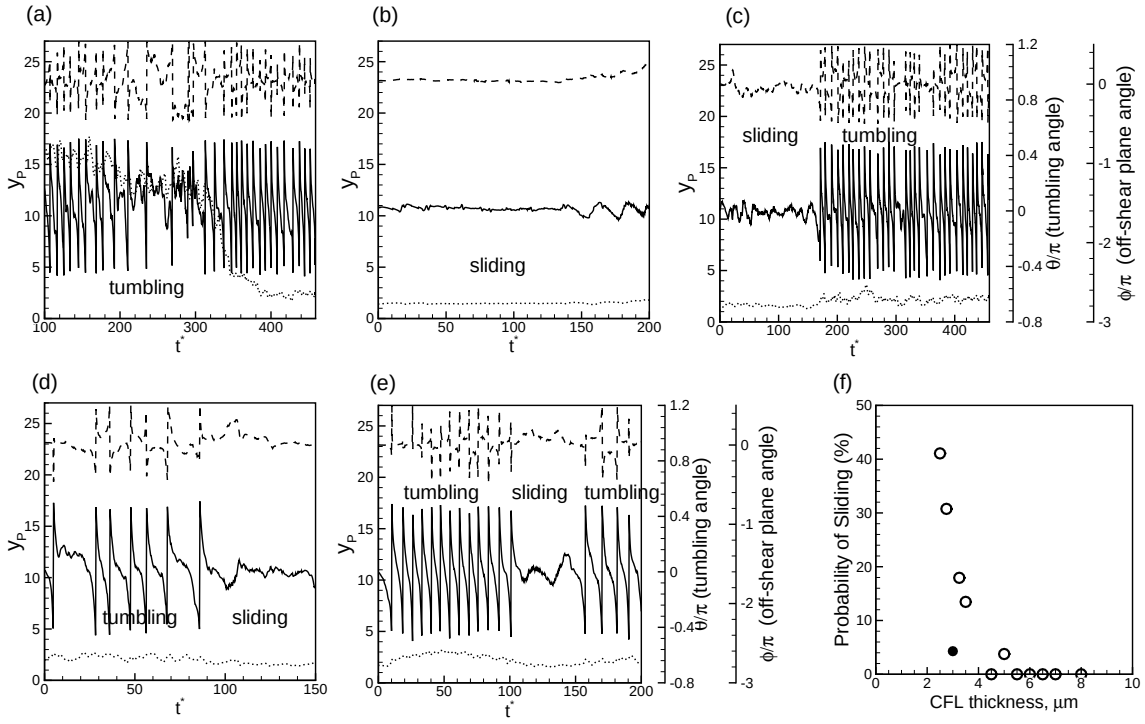

Figure 4.6: (a)-(e) Platelet dynamics in 3D whole blood simulation. Shown here are lateral location of the platelet center (y_p, dotted line, left axis), tumbling angle (θ, solid line, first right axis), and off-shear plane angle (ϕ, dashed line, second right axis). (f) Probability of platelet sliding motion as a function of CFL thickness for platelets distributed within the entire CFL (○), and for platelets that are located just outside the RBC-rich zone (●).

is converted to sliding and vice versa. Figure 4.6(c) shows a sliding-to-tumbling transition, and Figure 4.6(d) shows a tumbling-to-sliding transition. Figure 4.6(e) shows a tumbling to sliding conversion, and then back to tumbling. We find that such transitions are due to the collisions of the marginated platelets with the RBCs flowing at the edge of the CFL. In 3D, such collisions result in large off-shear plane angle ϕ. Our own modeling and prior 3D modeling showed that for an isolated platelet the sliding can change to tumbling if it is released with a large ϕ [173]. Therefore, in whole blood, the 3D nature of platelet–RBC interaction results in platelet rotation out of the shear plane, which in turn converts the sliding to tumbling. As noted earlier in Figure 4.2(b), the concentration of marginated platelets peaks just at the CFL edge, resulting in frequent collisions with the RBCs. Furthermore, often times the marginated platelets accumulate in the plasma-rich cavities near the CFL, and tumble due to reduced confinement.

To quantify the role of the CFL thickness on platelet dynamics, we compute the probability of sliding (Figure 4.6(f)). The results are grouped in two sets: in the first set, platelets distributed throughout the CFL are considered, and in the second set marginated platelets flowing near the edge of the CFL are considered. For the first set, Figure 4.6(f) shows that the sliding motion occurs when the CFL thickness becomes comparable to the platelet size (~ 3.5 μm). Note that this CFL thickness corresponds to a platelet center-to-wall distance of ~ 1.75 μm, which is close to the length scale below which an isolated platelet exhibits the sliding motion, as mentioned above. The probability of sliding increases with decreasing CFL thickness as platelet tumbling is increasingly impeded due to confinement. However, the collision effect seems to be dominant; even for a CFL thickness as small as 2.5 μm (36% hematocrit), only $\sim$40%

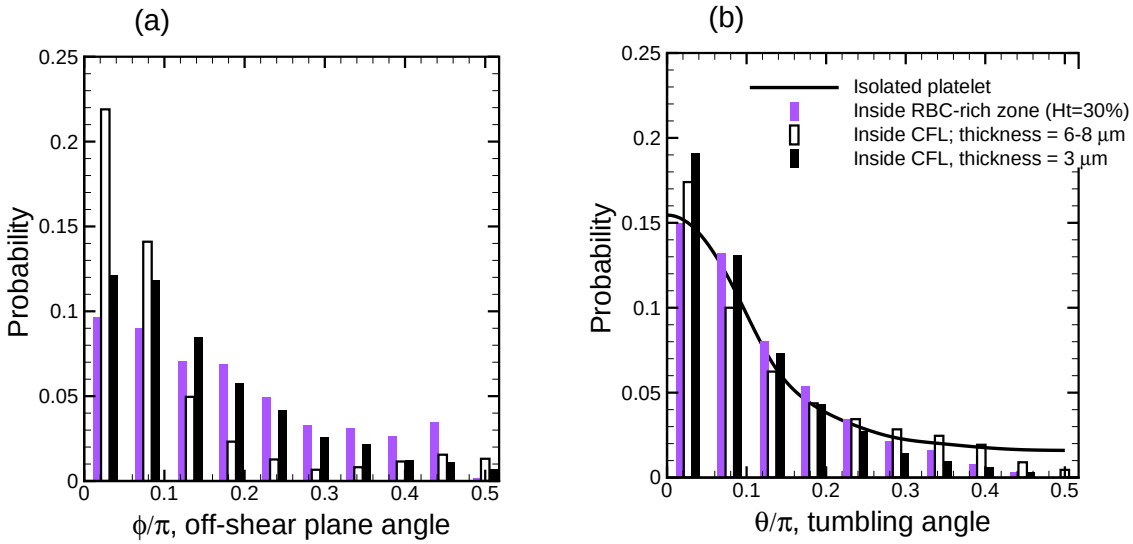

Figure 4.7: Platelet orientation in 3D: Probability distribution of the off-shear plane angle ϕ (a) and tumbling angle θ (b) for platelets inside RBC-rich zone (magenta bars), for platelets inside CFL of thickness 6–8 μm (unfilled bars), for platelets inside CFL of thickness 3 μm (black bars), and for isolated platelet far from a wall (line).

platelets are observed to slide. For the second set, for which the CFL thickness is ~ 3 μm, less than 5% platelets is observed to slide. Therefore, the RBC–platelet collision significantly reduces the probability of sliding even when the CFL thickness is small.

To quantify platelet orientation in 3D, we plot the probability distribution of the off-shear plane angle ϕ and the tumbling angle θ in Figure 4.7 for three sets of platelets: for platelets inside the RBC-rich zone, and for marginated platelets inside the CFL of thickness 3 μm and 6–8 μm. Inside the RBC-rich zone, the distribution of ϕ is relatively uniform although it is higher as $\phi \longrightarrow 0$. The distribution becomes more biased towards $\phi = 0$ when marginated platelets are considered. For the higher CFL thickness, the RBC–platelet collision is less frequent, and hence a significantly higher probability near $\phi = 0$ is observed. For the reduced CFL thickness, increased collision with the RBCs results in platelet axis tilting out of the shear plane, and reduces the the probability of $\phi \approx 0$. The probability distribution of the tumbling

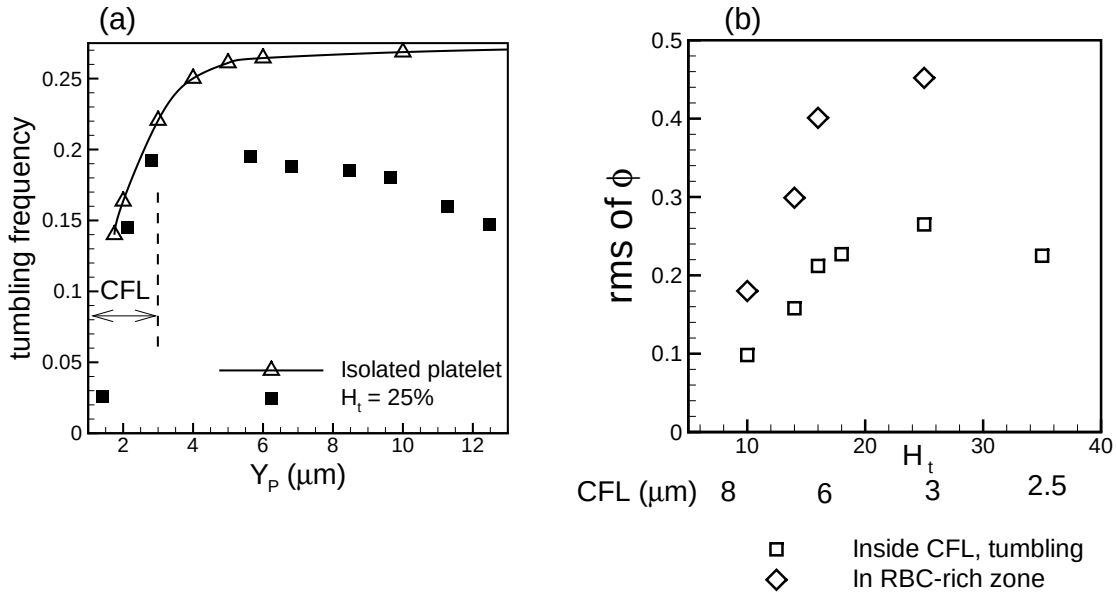

Figure 4.8: (a) Platelet tumbling frequency in dimensionless form as $2\pi/\dot{\gamma}T$ as a function of distance from the wall in whole blood (filled squares) at 25% hematocrit, and for an isolated platelet (Δ). The CFL thickness is 3 μm as shown. (b) RMS of off-shear plane angle ϕ as a function of hematocrit. Shown here are the data for platelets flowing inside the RBC-rich zone ($\diamond$), and for tumbling platelets flowing inside the CFL ($\square$). Also marked below the bottom axis is the thickness of the CFL.

angle θ is shown in Figure 4.7(b) for the above three sets, and also for an isolated platelet based on Jeffery's theory [169]. The probability at $\theta \approx 0$ is higher for the marginated platelets than those in the RBC-rich zone, and increases with decreasing CFL thickness due to the increasing number of sliding platelets.

The platelet tumbling frequency in whole blood is shown in Figure 4.8(a) as a function of the distance from the wall for $H_t = 25\%$. Also shown is the tumbling frequency of a platelet in absence of the RBCs which approaches Jeffery's theory [169] far from the wall, but decreases rapidly as the wall is approached due to a wall-induced drag. This qualitative picture is significantly affected in whole blood. Figure 4.8(a) shows that within the RBC-rich zone the average tumbling frequency is significantly below that of an isolated platelet. The reduced frequency is likely due to the geometrical confinement imparted by the surrounding RBCs. As the

CFL is approached, the frequency increases due to a reduction in the local RBC concentration. Inside the CFL, the wall effect becomes more important, and the frequency decreases as the wall is approached in a qualitatively similar manner of an isolated platelet. Thus, in whole blood, the highest tumbling frequency occurs for the platelets that are flowing near the edge of the CFL.

4.3.5 Angular Fluctuation and Rotational Diffusion

To further quantify the 3D nature of platelet–RBC interaction, we obtain the rms of the fluctuations of the off-shear plane angle ϕ (Figure 4.8(b)). Inside the RBC-rich zone, the rms increases with increasing hematocrit, due to increasing platelet–RBC collisions. Fluctuations are significant, and the rms is as high as 0.45 radian. For $H_t \gtrsim 25\%$, the rms appears to reach a plateau due to increased RBC confinement. Inside the CFL, the rms is reduced compared to that inside the RBC-rich zone, and shows a nonmonotonic trend with respect to the CFL thickness. The rms first increases with decreasing CFL thickness due to more platelet–RBC collisions, but then decreases as a result of increasing confinement as the CFL thickness becomes very small. We compute the mean-squared angular displacement $\langle \Delta\phi'^2 \rangle$, and obtain the platelet rotational diffusivity as $D_\phi = \langle \Delta\phi'^2 \rangle / 2t \approx 1$–$4\ \mathrm{s}^{-1}$ for shear rate $\sim 1000\ 1/\mathrm{s}$, which is nearly one to two orders of magnitude higher than the rotational Brownian diffusion [175].

4.3.6 Implication in Platelet-Wall Adhesion

As a measure of platelet-wall adhesion likelihood, the minimum distance Y_{min} between a platelet surface and the wall over time is shown in Figure 4.9(a) for a marginated

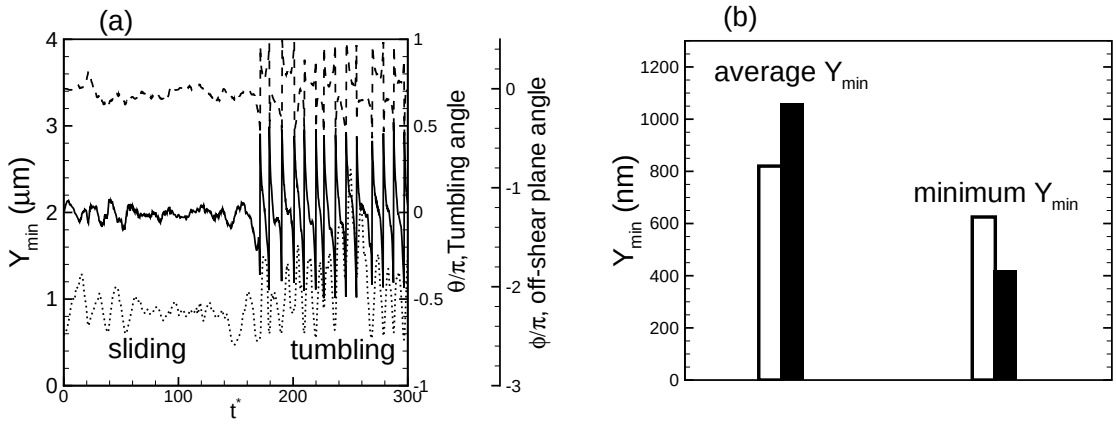

Figure 4.9: Minimum distance Y_{min} (black line, left axis) between a platelet surface and the wall over time for a marginated platelet. Also shown are tumbling angle θ (green line), and off-shear plane angle ϕ (blue line). (b) Average and lowest values of Y_{min} for tumbling (filled bars) and sliding (unfilled bars) platelets.

platelet. The time history shows that Y_{min} varies significantly over time. In general, our results show that in presence of the RBCs, Y_{min} is reduced more when a platelet is tumbling than when sliding. This result is consistent with earlier studies on isolated platelet which found that a tumbling-like dynamics termed as 'pole-vaulting' brings the platelets closest to the wall [173]. However, we find that in whole blood, large fluctuations in the off-shear plane angle ϕ can also bring a sliding platelet very close to the wall (Figure 4.9(a)). To quantify how tumbling and sliding dynamics affect the wall–platelet proximity, we obtain the average of Y_{min} by averaging over time and number of platelets (~ 50), and the lowest value of Y_{min}, from simulations with H_t ranging from 25–35%. We obtain the average $Y_{min} \approx 1060$ nm for the tumbling platelets, and 860 nm for the sliding platelets. In contrast, the lowest Y_{min} found is ≈ 420 nm for tumbling platelets, and 625 nm for the sliding platelets (Figure 4.9(b)). The platelet–wall adhesion is mediated via vWF molecules [9–11, 38]. Our results imply that the initial contact between a platelet and the wall may occur during the tumbling phase and by the ultralarge vWF molecules with a length scale of 250 to 750

nm. However, these bonds can easily break due to large wall-normal and transverse velocity fluctuations, and due to higher tumbling frequency as noted earlier in Figure 4.8(a). The sliding platelets are more likely to form stable adhesion with the wall.

4.4 Conclusion

We presented a 3D modeling study of platelet dynamics in whole blood. Our model successfully predicts the formation of the RBC-depleted zone (CFL) and the near-wall excess of platelets. We focus on the platelet dynamics close to and inside the CFL, and show that this region plays a critical role in clot formation by affecting the near-wall platelet motion, and platelet–wall contact. We found that the cellular microstructures formed by the RBCs in a shear flow play a critical role in platelet margination. These microstructures are formed by the RBCs stacked along the wall-normal direction making the instantaneous RBC distribution highly anisotropic. The anisotropy occurs naturally by hydrodynamic forces and creates local 'cavities' in RBC distribution. A platelet can enter a cavity and use it as an 'express lane' for a fast margination towards the wall. While it is known that platelets experience an augmented diffusion due to their interaction with the RBCs [17–20], the present finding suggests a further augmentation that is a result of the local anisotropy in the RBC distribution.

Inside the CFL, platelets motion in the wall-normal direction is severely hindered as they are confined between the wall and the RBCs flowing at the edge of the CFL. As a result, the wall-normal motion of the platelets is not purely diffusive inside the CFL. In contrast, inside the RBC-rich zone, the platelet diffusivity in the wall-normal direction is found to be 2 to 3 orders of magnitude higher than the Brownian diffusion.

An important outcome of our 3D simulation is the quantification of platelet motion in the transverse (vorticity) direction. The 3D nature of the platelet–RBC interaction results in a significant platelet movement in the transverse direction. This observation is consistent based on prior 3D model studies of pairwise collision of deformable particles in shear flow which showed a significant displacement of the particles in the vorticity direction [40]. In whole blood, such movements collectively lead to platelet diffusion in the transverse direction that cannot be predicted from a 2D simulation. We find that inside the RBC-rich zone, platelet velocity fluctuations in the transverse direction are comparable to that in the wall-normal direction. Relating the rms of the velocity fluctuations to the diffusivity ($D \approx v'^2\tau$), we infer that inside the RBC-rich zone the platelet diffusivity in the transverse direction is slightly smaller but comparable to the diffusivity in the wall-normal direction. Inside the CFL, the results are completely different: the platelet movement is severely hindered in the wall-normal direction, but not in the transverse direction. As a result, the rms fluctuation is significantly higher in the transverse direction than that in the wall-normal direction. Therefore, our 3D model shows that platelet diffusion in whole blood is not only inhomogeneous in the wall-normal direction, it is also anisotropic, particularly inside the CFL. The anisotropy increases with decreasing CFL thickness as the latter causes an increase in the platelet–RBC collision rate and at the same time an increased confinement. The anisotropy is likely to play an important role on the platelet motion near a thrombus where the thickness of the CFL is greatly reduced [38].

We find that the the strong anisotropy in platelet motion inside the CFL leads to platelet cluster formation, even in absence of any platelet–platelet aggregation. Although short-lived, such hydrodynamically-driven clusters may serve as the precursor

to the formation of a hemostatic plug and thrombus. The size and number of clusters are found to increase with decreasing CFL thickness in a qualitatively similar way that the transverse velocity fluctuation increases. The increasing platelet diffusion in the transverse direction with decreasing CFL thickness leads to higher probability of platelet cluster formation. Such a mechanism of cluster formation is absent in a 2D model.

Our model further shows that due to the 3D nature of the RBC–platelet collisions, the platelet axis of revolution continually moves out of the shear plane leading to a strong rotational diffusion that increases with increasing hematocrit. The rotational diffusivity is estimated to be one to two orders of magnitude higher than the Brownian rotational diffusivity. Our simulations show that the platelet dynamics in whole blood differs significantly from that of an isolated platelet. Inside the RBC-rich zone, the platelet tumbling frequency is well below that of an isolated platelet. The highest frequency is attained just outside the RBC-rich zone. The tumbling motion is highly irregular due to RBC–platelet collision. Inside the CFL, the platelet dynamics is determined by two competing effects, namely, the confinement by the wall and the RBCs at the edge of the CFL, and the collisions with the RBCs. While the former induces a sliding motion of the marginated platelets, the latter induces the tumbling. While most marginated platelets are observed to tumble just outside the RBC-rich zone, we find that the platelets further inside the CFL flow with an intermittent dynamics that alters between sliding and tumbling. The transition from sliding to tumbling and vice versa is a result of the off-shear plane rotational diffusion, and hence, less likely to happen in a 2D simulation. As a result of the transition, we find that platelet sliding occurs less frequently than tumbling. A platelet in tumbling

motion instantaneously comes closer to the wall than a sliding platelet, but the average wall-to-platelet surface distance is found to be higher in tumbling than in sliding.

In conclusion, 3D simulations of whole blood presented here demonstrate the importance of finite cell size, anisotropy, and three-dimensionality in platelet–RBC interaction, platelet margination, and platelet–wall adhesion. The overall picture that arises from this study is as follows: The local anisotropy in RBC distribution in whole blood results in a fast and discontinuous platelet margination, which we termed as waterfall phenomenon (this will be further discussed for platelet-sized particles of different shapes in Chapter 5). The anisotropic nature of the platelet translational diffusion inside the CFL leads to platelet cluster formation, and increases the likelihood of clot formation. The rotational diffusion of the platelets with respect to their off-shear plane orientation converts the motion of the marginated platelets from sliding to tumbling and bring them closer to the wall increasing the likelihood of platelet–wall contact. This study underscores the significance of platelet motion in the transverse direction, and warrant further experiments in which platelet motion in whole blood can be tracked over time and simultaneously in all three dimensions.

Chapter 5

Microparticle Shape Effects on Their Transport and Dynamics in Blood Flow

5.1 Introduction

As mentioned in Chapter 1, intravascular injection is one of the most widely used routes for drug administration and biomedical imaging. To lower the side effects of drug molecules and contrast agents, targeted delivery is desired. This is achieved by accompanying the agents with ligand molecules that specifically bind to overexpressed receptors on targeted cells. Since micro- and nanoparticles can be engineered to carry different molecules, they are ideal candidates for vascular carriers [32, 33]. While the carrier–cell binding is essential for the targeted delivery, such goal cannot be achieved unless the carrier particles flow in close proximity to the wall of the blood vessels and make frequent contacts with the wall. A well-designed drug carrier is the one that can quickly drift or 'marginate' from the center of a blood vessel towards the wall, make physical contact with the wall, and eventually form a stable adhesion with the targeted cell linings. As such, considering the latest advances in fabrication of micro/nano- particles, significant research efforts have been directed in recent years towards optimal design of the carrier particles. It has been recognized that the particles' geometrical features, namely, their size and shape, are key design parameters, among others, as they strongly influence the motion of such particles

in a flowing medium [43–47]. Typical particle shapes considered are spherical, disk-like (oblate) and rod-like (prolate). Efforts are currently directed to understand the margination and adhesion characteristics of such particles under flowing conditions. For instance, through experiments in laminar shear flow, Gentile et al. [48] showed that discoidal microparticles outperformed spherical ones in terms of margination. Doshi et al. [49] showed that the adhesion propensity of microparticles in bifurcating networks increased with particle size and nonsphericity, especially for rod-like particles. Adriani et al. [50] demonstrated a higher adhesion propensity of disk-like particles than rod-like particles in parallel-plate flow chambers. Shah et al. [51] considered a computational study and observed that nanorods had a significantly higher wall binding probability compared to nanospheres. Similar results were obtained by Toy et al. [52] through an experimental study in which it was shown that nanorods exhibited higher margination rates compared to nanospheres in parallel-plate flow chambers. Anselmo et al. [53] designed nanoparticles that mimick platelets in terms of geometrical, physical and biochemical properties, and demonstrated that such particles exhibited enhanced surface-binding compared to spherical particles. Similar results were obtained by Decuzzi and Ferrari [54] in a theoretical study in which it was shown that oblate particles adhered more effectively to the biological substrate than spherical particles of same volume.

The aforementioned studies were, however, conducted in cell-free environments. As mentioned in Chapter 1, at the scale of carrier particles, blood must be considered as a suspension of RBCs, rather than a single-phase fluid. It has been recognized that margination and adhesion of carrier particles are strongly dependent on their interaction with the RBCs. As such, several studies considered particle shape and

size effects on margination and adhesion in flowing blood, in vivo and in vitro. As mentioned in Chapters 1, 3 and 4, it was well known from earlier experimental studies that blood platelets marginate towards the vessel wall due to their interaction with the RBCs [12–15].

Lee et al. [55], Namdee et al. [56], and Charoenphol et al. [57] observed that microparticles outperform nanoparticles in terms of margination. van de Ven et al. [58] observed that disk-like microparticles exhibited a higher near-wall accumulation compared to other shapes in tumor, and that an optimal size existed for such particles. Thompson et al. [59] observed a higher margination rate for microrods than spherical particles. In an in-vivo study, Muro et al. [60] studied the effect of micro- and nanoparticles geometry and observed that disk-like particles exhibited higher targeting specificity compared to spherical ones. Muller et al. [61] considered a computational study of margination of micro- and nanoparticles in flowing RBC suspensions, and observed that the margination was enhanced with increasing particle size, and that spherical particles exhibited a slightly higher margination rate compared to ellipsoidal particles. Additionally, they proposed that ellipsoidal shape was a better candidate for drug delivery compared to spherical shape.

While the aforementioned studies generally tend to suggest that micro-scale particles of nonspherical shapes are better candidates than spherical particles for intravascular drug carriers, they do not seem to agree whether disk-like or rod-like particles would provide a superior performance. Furthermore, it is important to note that in many experimental studies the margination is measured based on the number of particles adhered to the walls, although margination and adhesion are different phenomena. As mentioned above, the delivery of carrier particles to specific targets

occurs in three sequential sub-processes: (i) margination from the center of the blood vessel towards the wall, (ii) contact with the wall, and (iii) firm adhesion to the wall. The biophysical mechanisms underlying these three sub-processes are different. This point can be further illustrated by considering blood as a suspension of RBCs. As mentioned in Chapter 1, normal healthy RBCs are extremely deformable. In a shear flow, the RBCs experience a wall-normal force which arises due to their deformation, and propels them away from the wall creating a cell-free layer (CFL) near the wall and a cell-rich region in the core of the vessel. The flow of the carrier particles in the vessel core is governed by their collisions with the RBCs which lead to shear-induced diffusion of such particles. As mentioned in Chapters 1, 3 and 4, classical experimental studies attribute such RBC-induced dispersion to volume exclusion due to RBC migration away from the wall [5, 17–21, 23, 24, 159]. However, such migration also causes nonuniformity in RBC concentration in the lateral direction and consequently a spatially varying RBC–platelet collision rate which further affects the margination [32-36]. In this regard, in a theoretical work, Mehrabadi et al. [63] explained the platelet margination by their RBC-induced dispersion in the RBC-rich core and their near-wall entrapment inside CFL. In a 2D computational study, Crowl and Fogelson [36, 37] show that only volume exclusion cannot entirely explain the microparticles near-wall excess. Therefore, they proposed a spatially varying RBC-induced drift that enhances the margination of microparticles. The first 3D simulation of microparticle transport in RBC suspension was performed by Zhao and colleagues [41,42] who also confirmed the notion of additional drift due to RBC-particle hydrodynamic interactions. They also considered the effect of particle size and shape and showed that

spherical and platelet-like microparticles exhibit higher shear-induced diffusivity compared to tracer particles. Once marginated, the carrier particles flow inside the CFL where they are 'sandwiched' between the wall and the layer of RBCs, but experience less frequent encounters with the RBCs. Finally, once they make an initial adhesion with the wall, the stability of the adhesion is dictated by the balance between the hydrodynamic force, occasional collisions with the RBCs, and adhesion strength. Evidently, margination and adhesion are separate events which were not unambiguously differentiated in many experimental studies. As such, a carrier particle exhibiting a higher margination rate may not be the one that would firmly adhere to the wall. For instance, in a computational study by Reasor et al. [62], higher values of margination rate was obtained for spherical microparticles compared to disk-like ones, although it is well known that discoidal particle outperform spherical ones in terms of adhesion to endothelium due to their larger contact area [48, 50, 53, 54].

We hypothesize that the carrier particles' shape influences their dynamics differently in different sub-processes of the margination-adhesion cascade, namely, margination, wall contact and adhesion, due to differences in the underlying biophysical mechanisms. A specific shape exhibiting a superior performance in one sub-process may not exhibit a superior performance in another. The superiority of a drug carrier of a specific shape can only be established by understanding its behavior separately in the three sub-processes. Quantification of the carrier particle dynamics and RBC-carrier particle interaction at the cellular scale through experimental observation in whole blood is a difficult task. High-fidelity computer simulations which model blood as a suspension of RBCs provide an alternative approach. To that end, in this chapter we consider a high-fidelity cellular-scale 3D computational modeling approach to

study the transport, margination and adhesion of micro-scale particles of different shapes (spherical, oblate and prolate) in whole blood represented as a suspension of deformable RBCs. We show that microparticles of different shapes interact differently with the RBCs leading to their different behaviors during margination, near-wall dynamics, and adhesion. Specifically, we show that microparticles' rotational orientation in three-dimensional space and the frequency of their collisions with the flowing RBCs in presence of a bounding wall are the key factors that dictate their differential behavior in the margination-adhesion cascade. Quantification of such micro-scale dynamics of individual particle and their influence on particle margination and adhesion in whole blood does not exist in the literature, and is the focus of this chapter.

5.2 Problem Setup

Margination of microparticles, their near-wall dynamics, and adhesion to wall are simulated in suspension of flowing RBCs. The flow is a linear shear flow described as $\mathbf{u} = \{\dot{\gamma}y, 0, 0\}$ and bounded between two plates mimicking a parallel-plate flow chamber (Figure 5.1). More details on the computational domain and boundary conditions are given in Chapter 2. The surface of each RBC is discretized using 20480 triangular elements (or, 10242 Lagrangian nodes), and particle using 1280 triangular elements (or, 642 nodes). The Eulerian resolution is ~ 9 mesh points/μm in y direction, and 6.8 mesh points/μm in x and z directions. There are at least 53 Eulerian points across one RBC diameter, which is sufficient to resolve the cell dynamics based on our prior studies. We use the radius of the equivalent sphere $a_o = (3V/4\pi)^{1/3}$ as the length scale, where V is the RBC volume, and the inverse shear rate $\dot{\gamma}^{-1}$ as the time scale. The dimensionless time is denoted by $t^* = t\dot{\gamma}$. The

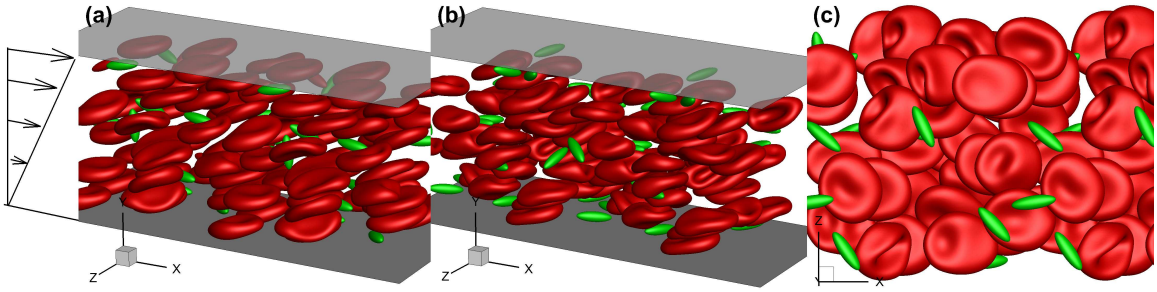

Figure 5.1: Representative snapshots showing instantaneous red blood cell (colored red) and microparticle (colored green) distribution in shear flow in a channel. (a) and (b) are views at dimensionless time $t^* = 20$ and 300, and (c) is the view from the bottom of the channel.

effect of inertia is small as the Reynolds number $\mathrm{Re} = \rho a_o^2 \dot{\gamma}/\mu_o \lesssim 10^{-2}$, where μ_o is the plasma viscosity.

We performed a total of 27 simulations of RBC suspensions along with microparticles of different shapes (oblate, prolate and spherical) flowing in channels of heights 27 and 54 μm and lengths 36, 54, and 71 μm at a constant shear rate $\sim 1000\ \mathrm{s}^{-1}$, and hematocrit $H_t = 24\%$. The volume of the microparticles is kept constant at 7.238 $\mu\mathrm{m}^3$ which is same as the volume of a normal, inactivated platelet. The particle shape is characterized by the aspect ratio (AR) which is defined as the ratio of the minor to major axis. Thus, AR $\longrightarrow 0$ for rod- and disk-like particles, and AR $= 1$ for spheres. We consider five different particle shapes: spheres, oblates of AR $= 0.3$ and 0.5, and prolates of AR $= 0.3$ and 0.5. The number of RBCs in the computational domain ranges from 42 to 90, and microparticles from 6 to 20. As such, the volume fraction of microparticles ranges from ~ 0.02 to 0.04%.

5.3 Results

5.3.1 Particle Shape Effect on Near-wall Accumulation

Figures 5.1(a) and (b) show snapshots from one simulation at $t^* \approx 20$ and 300. The RBCs are deformed significantly; the resting biconcave shape is no longer visible and the cells assume a more elongated disk-like shape. The motion of each cell is quite irregular due to interaction with the neighboring cells which results in further deformation. The initial arrangement is quickly disturbed, and cell and particle distribution reaches a pseudo-random nature. While the RBCs mostly align their major axis with the flow, microparticles have a wider orientation distribution as seen in the figure. Figure 5.1(c) shows a view from the bottom of the channel resembling a close-packed distribution of the RBCs along the vorticity direction.

Figure 5.2(a) compares the concentration profiles of oblate particles of AR = 0.3 and RBC across the channel at $t^* \approx 450$. Microparticles and cells are uniformly distributed at the beginning of simulations. As the simulations progress, a cell-free layer (CFL) develops near the walls. At the same time, microparticle concentration near the walls increases indicating particle margination and near-wall accumulation. Over time, more particles marginate towards the wall resulting in an increasing near-wall concentration of microparticles. Simulations are stopped between $t^* = 300$ and 450 when sufficient number of particles are marginated to the CFL. There are still particles inside the RBC-rich zone which are expected to marginate if simulations are to be continued. In most cases, particle margination is irreversible, i.e., marginated particles rarely come out of the CFL and re-enter in to the RBC-rich zone.

We now compare the concentration profiles of microparticles of different shapes.

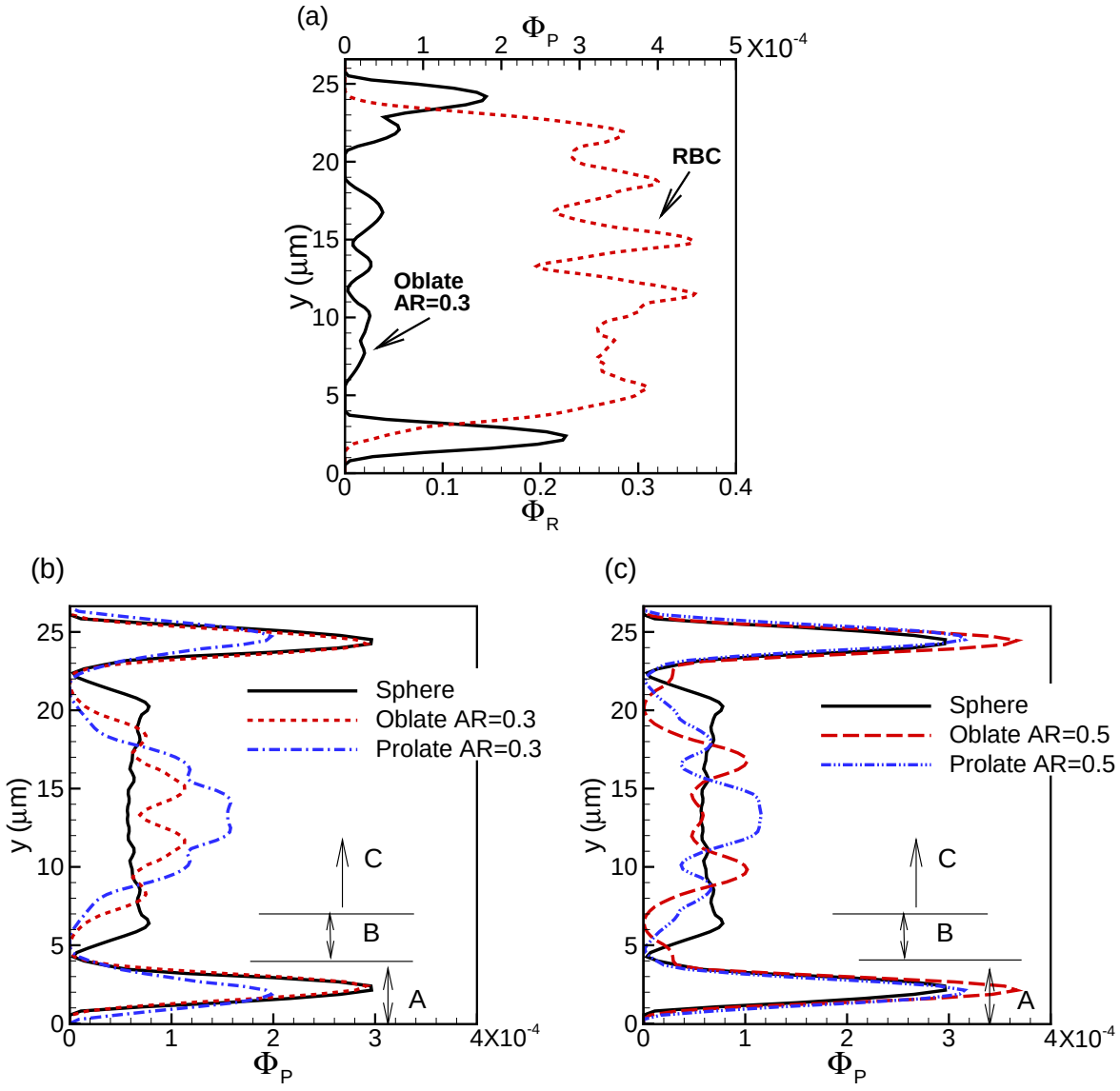

Figure 5.2: Microparticle concentration profiles across channel height. (a) Concentration of oblate particles of AR = 0.3 (Φ_p, black solid line, top axis) is compared with that of RBC (Φ_r, red dash line, bottom axis) at $t^* \approx 450$. (b) Comparison of concentration profiles for different microparticle: microspheres (black solid line), oblate of AR = 0.3 (red dash line), prolate of AR = 0.3 (blue dash-dot line). (c) Comparison of concentration profiles for different microparticle: microspheres (black solid line), oblate of AR = 0.5 (red dash line), prolate of AR = 0.5 (blue dash-dot line).

Figure 5.2(b) shows the concentration profiles of oblate (AR = 0.3), prolate (AR = 0.3) and spherical particles, and Figure 5.2(c) shows the results for AR = 0.5, all at $t^* \approx 300$. As seen in Figure 5.2(b), the near-wall concentration of the oblate AR = 0.3 and spherical particles are nearly same, but higher than that of the prolate particles. It may seem, therefore, that the prolate particles underperform compared to the oblate and spherical particles in terms of near-wall accumulation. This result is in contradiction to several experimental studies which observed a greater number of disk-shaped and rod-like particles adhered to the walls compared to spherical particles [48–50, 56, 57]. This apparent contradiction will be further elucidated in following sections. In Figure 5.2(c), which is for AR = 0.5, the oblate particles have the highest near-wall concentration, followed by the prolate and spherical particles. Hence, the oblate particles in our simulations outperform other shapes in terms of near-wall accumulation. By comparing Figure 5.2(b) and (c), we observe that both oblate and prolate particles with AR = 0.5 show a greater near-wall accumulation than their counterparts with AR = 0.3. Hence, the near-wall accumulation is observed to be less for particles of large asphericity compared to those of moderate asphericity.

The second important observation in Figure 5.2(b) is that there is a significant drop in particle concentration near the edge of the RBC-rich region (marked as zone B in the figure). A high particle concentration is present also in the interior of the RBC-rich zone (marked as zone C). Note that particles were distributed uniformly at the beginning of simulations. Therefore, the particles that are flowing relatively close to the edge of the RBC-rich zone, are able to quickly marginate to the CFL resulting a near-zero particle concentration in zone B, but those located further interior of the RBC-rich zone, are much slower to migrate laterally. These results suggest that a 'fast'

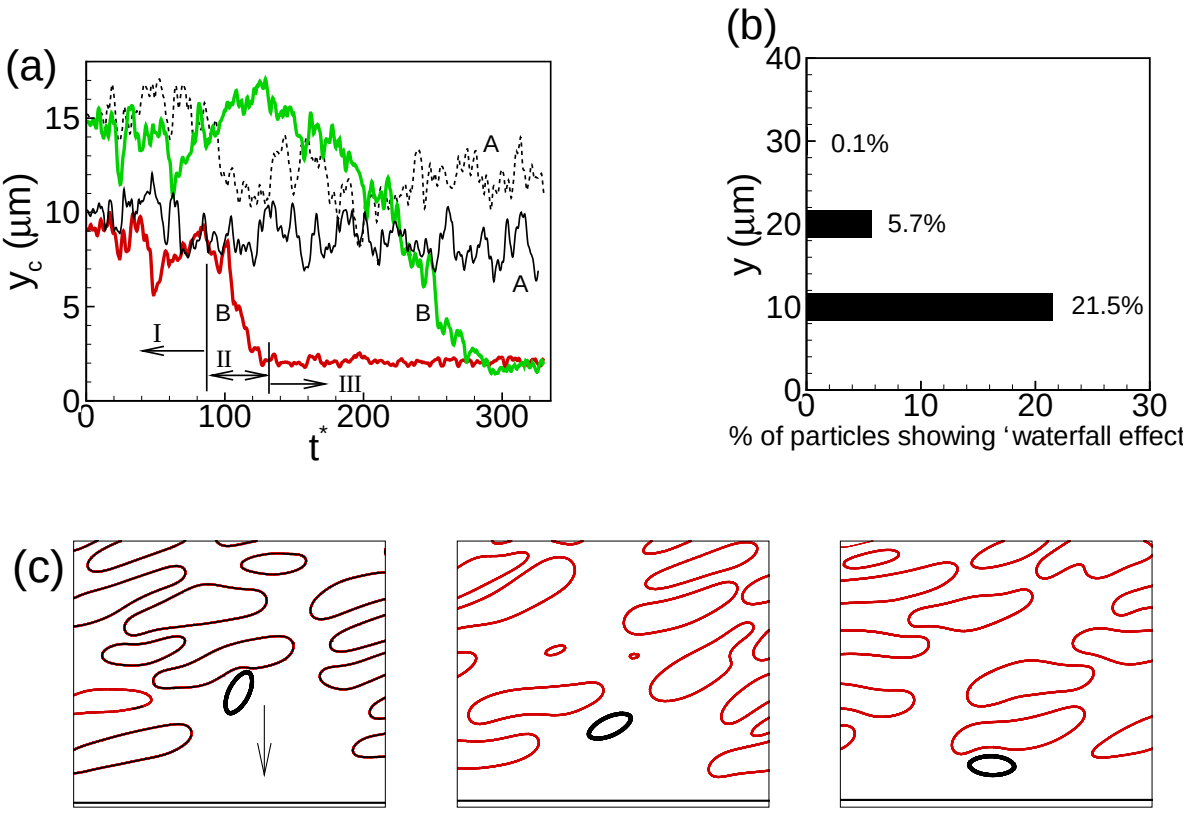

Figure 5.3: (a) Sample microparticle trajectories from our simulations. Trajectories showing a continuous and slow lateral diffusion are marked by 'A', and trajectories showing a large abrupt lateral displacement (the 'waterfall effect') are marked by 'B'. For type 'B', the margination consists of a slow diffusive motion (phase I), the abrupt large change in lateral position (phase II), and a nearly wall-parallel motion inside the CFL (phase III). (b) Fraction of microparticles exhibiting the waterfall effect in different sections of the channel. (c) Time resolved 2D snapshots to show that the waterfall effect is a result of the RBC (red) microstructures. A microparticle (black) finds its way to the CFL through an RBC-void region while being pushed by an RBC cluster on top.

margination occurs for particles that flow near the CFL-edge, and a much 'slower' margination occurs for particles residing further away from the wall. In what follows, we illustrate these two margination processes and their dependence on microparticle shape, and eventually explain the observed differences in near-wall accumulation for particles of different shapes.

5.3.2 Waterfall Phenomenon

We start by considering sample particle trajectories which are shown in Figure 5.3(a). The lateral position of the particle center over time is plotted here. Similar to the results presented in Chapter 4 for platelets, two different classes of trajectories, 'A' and 'B' as identified in the figure, are observed in our simulations. In type 'A', microparticles mostly flow along the longitudinal direction while slowly moving in the lateral direction due to repeated collisions with the flowing RBCs. This type of motion occurs mostly in the interior of the RBC-rich zone, and represents the so-called shear-induced diffusion. It is a rather slow process as particles flowing in the interior of the RBC-rich zone would take a long time to reach the CFL using this process. In type 'B' trajectories, particles undergoing the shear-induced 'slow' lateral drift suddenly exhibit a large lateral displacement that brings them inside the CFL. Hence, type 'B' provides a fast and discontinuous pathway for margination. As such, type 'B' consists of three phases as marked in the figure. Phase I is the slow diffusive motion as in type 'A'. Phase II is the large, abrupt lateral drift bringing the particles out of the RBC-rich layer and into the CFL. Once within the CFL (phase III), trajectories are nearly parallel to the wall with fluctuations caused by their collision with the RBCs. Similar to Chapter 4, the large, abrupt lateral drift associated with phase II of type 'B' trajectories is termed here as the 'waterfall phenomenon'. As will be shown later, the microparticles' shape affects the waterfall phenomenon which, in turn, causes the shape-dependency of the near-wall accumulation.

Figure 5.3(b) shows the fraction of particles that exhibit the waterfall effect within the simulation window of $t^* \approx 0$–300. Here we divide the channel height in to three sections: one around the edge of the CFL ($y \lesssim 15$ μm), an intermediate region 15

$\gtrsim y \lesssim 25$ μm, and one farther interior of the RBC-rich zone ($y \gtrsim 25$ μm). In the first section, more than 21% of all particles flowing in this region exhibit the waterfall effect, while 5.7% show this effect in the intermediate region. For the farthest region, only 0.1% particles exhibit such behavior. Thus the waterfall effect is dominant within certain distance from the edge of the CFL. Hence, particles that are flowing just above the CFL edge, may rapidly marginate and move into the CFL by this mechanism, which in turn creates a particle-depleted region above the CFL edge as observed in Figures 5.2(b) and (c). For particles located in the interior of the RBC-rich zone, the waterfall effect is nearly absent. Hence, these particles must first drift using the slow diffusion process (type 'A' trajectory) to reach closer to the CFL edge; once they reach closer to the CFL edge, the rapid margination by the waterfall mechanism may occur.

Before proceeding further on microparticle shape effects, we briefly present the physical origin of the waterfall phenomenon. The discontinuous margination was noted recently by Lee et al. [55] in their experimental study of submicron particle dispersion in mouse microvasculature. Platelet trajectories presented in [42] also suggested the occurrence of the fast margination as noted in Figure 5.3(a). Although these authors conjectured that such a process is most likely associated with RBC-particle interaction, the physical origin of it was not discussed. In Chapter 4 we proposed that the waterfall effect is due to the microstructures formed by the RBCs. In the simulations, we observe that the RBCs often flow by forming 'clusters' in which they are stacked vertically, while there are 'cavities' between adjacent clusters that are depleted in RBCs. These clusters and cavities form the microstructures in the suspension making the instantaneous and local RBC distribution highly anisotropic.

More cavities form near the CFL edge due to decreasing RBC concentration towards the wall. Often times, these cavities can extend from the wall into the RBC-rich region. A particle may find its way to the wall through such cavity while being pushed by one or multiple RBCs (cluster) on the top, as illustrated by a sequence of snapshots in Figure 5.3(c). An abrupt drop in the particle lateral position is a result of its fast lateral movement through the cavity causing the waterfall phenomenon. Similar notion on the enhancement of margination by RBC cluster formation can be found in the context of RBC aggregation (rouleaux) in flowing blood: Formation of rouleaux was shown to enhance WBC margination and adhesion in experimental [100, 101, 104, 176] and computational studies [126, 177].

Until now, we establish that the lateral motion of the microparticles located further interior of the RBC-rich zone is due to the 'slow' shear-induced diffusion process (type 'A' trajectory). To compare the particle shape effect on such lateral diffusion, we plot in Figure 5.4(a) the mean-squared displacements (MSD) in wall-normal (y) direction. While all different shapes show nearly linear behavior of the MSD, no strong conclusion can be drawn from this result about the role of particle shape on diffusion. Rather, it appears that the range of particle shapes considered here does not have a strong influence on shear-induced diffusion of microparticles. From this plot, diffusivity for all shapes is obtained as $D = \langle y'^2 \rangle / 2t \sim 4\text{–}5 \times 10^{-7}$ cm^2/s at shear rates ~ 1000 s^{-1}. The range of diffusivity is in agreement with previously reported values for platelet diffusion in RBC suspension [24, 41], and is 2 to 3 orders of magnitude higher than the Brownian diffusivity, suggesting that collisions of microparticles with the flowing RBCs 'augment' their diffusion. However, the RBC-augmented diffusion is nearly the same for microparticles of different shapes. Hence, based on this result,

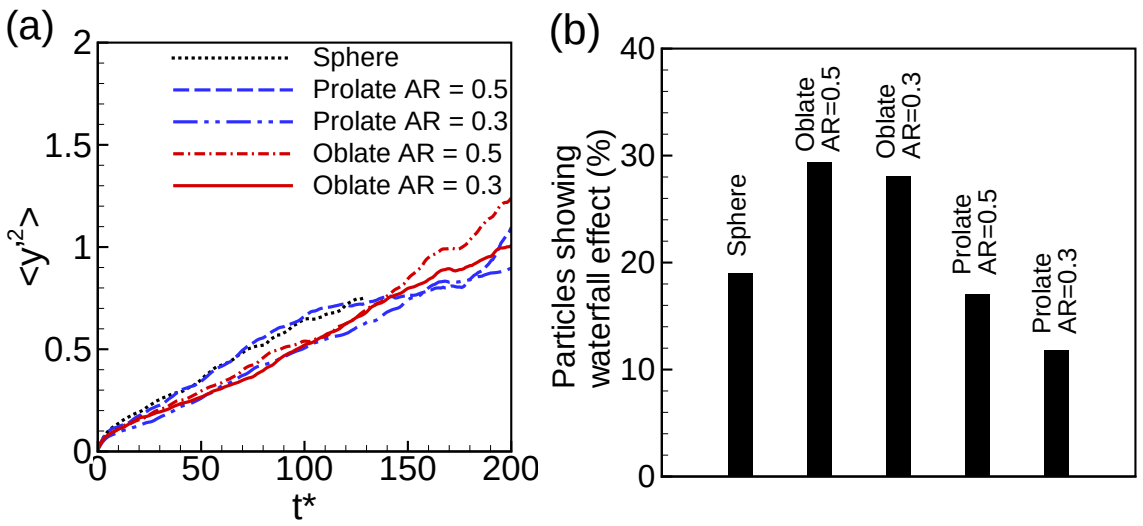

Figure 5.4: (a) Mean-squared-displacement $\langle y'^2 \rangle$ for lateral (wall-normal) motion of microparticles inside the RBC-rich zone. (b) Percentage of particles showing the waterfall phenomenon.

it can be stated that the shear-induced diffusion alone cannot be the sole reason for the observed shape-dependency of the near-wall accumulation.

In order to see whether the near-wall accumulation is related to the waterfall phenomenon, we plot in Figure 5.4(b) the fraction of particles of different shapes that exhibit this phenomenon. The figure shows that indeed the probability of the waterfall phenomenon depends on the particle shape. Oblate particles of AR = 0.5 yield the highest probability, followed by oblate of AR = 0.3, sphere, prolate of AR = 0.5, and prolate of AR = 0.3. This trend of the particle shape effect on the probability of the waterfall phenomenon is quite similar to the trend observed in the near-wall accumulation. Therefore, this result together with the MSD plots of Figure 5.4(a) lead to two important conclusions: (i) the RBC-augmented diffusion interior of the RBC-rich region does not strongly affect the shape-dependency of the microparticles' near-wall accumulation, and, (ii) the shape effect is important once a particle is relatively closer to the CFL edge as it strongly affects the probability of the waterfall phenomenon which provides a mechanism for rapid margination.

5.3.3 Effect of Individual Particle Dynamics and RBC-Microparticle Binary Interaction on Margination

In order to understand why microparticles' shape affects the probability of the waterfall phenomenon as reported in Figure 5.4(b), we analyze the dynamic behavior of individual particles flowing in the RBC suspension and their binary interaction with the RBC. First, we consider the three-dimensional orientation dynamics of the oblate and prolate particles in the suspension which is shown in Figure 5.5. In absence of the RBCs, and far from a bounding wall, an isolated rigid particle in a shear flow executes a 3D orbital rotation that can be described by the theoretical work of Jeffery [169] which predicts that the particle would assume any one of infinite numbers of time-invariant orbits depending on the initial orientation and precess about the vorticity axis of the background shear flow. Jeffery mentioned that the degeneracy of his solution was due to the linearity of the Stokes flow, and proposed that in case the degeneracy was broken, the axes of revolution of prolate ellipsoids would eventually align with the vorticity axis, and those of oblate ellipsoids would align in the plane of the shear flow. Several studies have demonstrated that if nonlinearity was introduced, e.g., due to particles' inertia or deformability, they indeed adopted a preferred orientation [179–182].

The three-dimensional orientation of an ellipsoidal microparticle in space can be quantified by an off-shear plane angle ϕ, which is the angle between the axis of revolution of the particle and the shear plane of the flow. When $\phi = \pi/2$, the axis of revolution is aligned with the vorticity axis (z), and when $\phi = 0$, it is aligned in the shear plane (x-y plane - see Figure 5.5). Figures 5.6(a) and (b) show the probability distribution of ϕ for particles of different shapes that are flowing in the

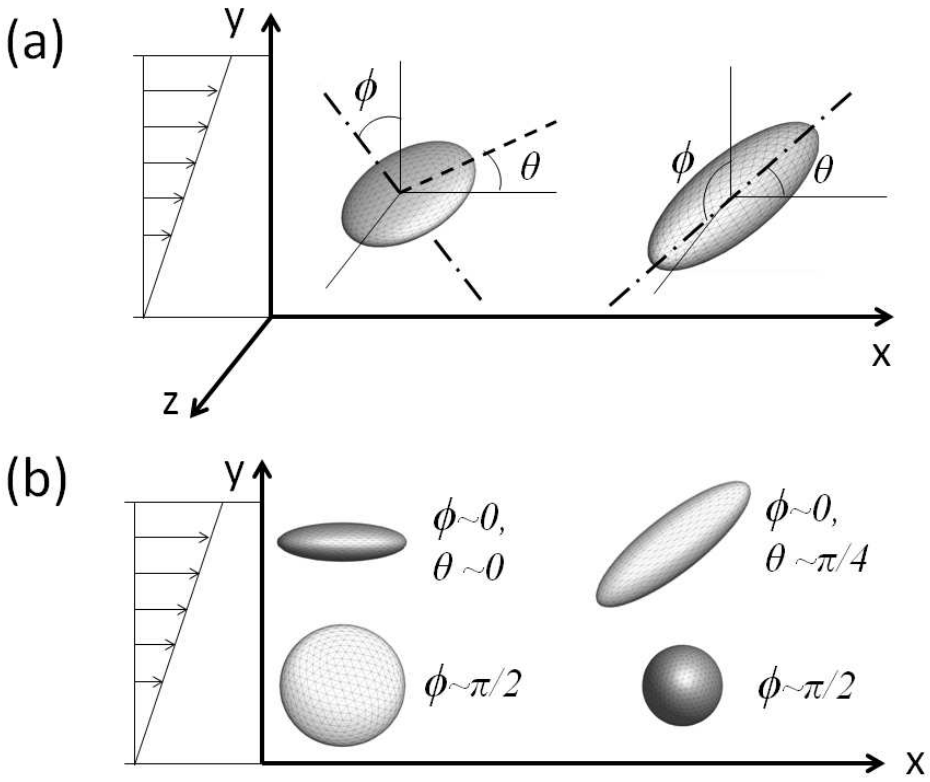

Figure 5.5: (a) Definition of the off-shear plane angle ϕ, and the shear plane inclination θ; ϕ is the angle between the axis of revolution of the particle and the shear plane of the flow (x-y plane), and θ is the angle between the flow direction and the projection of the particle's axis of revolution onto the shear plane. (b) Examples showing the oblate (left) and prolate (right) inside the shear plane (top row) and along the vorticity axis (bottom row).

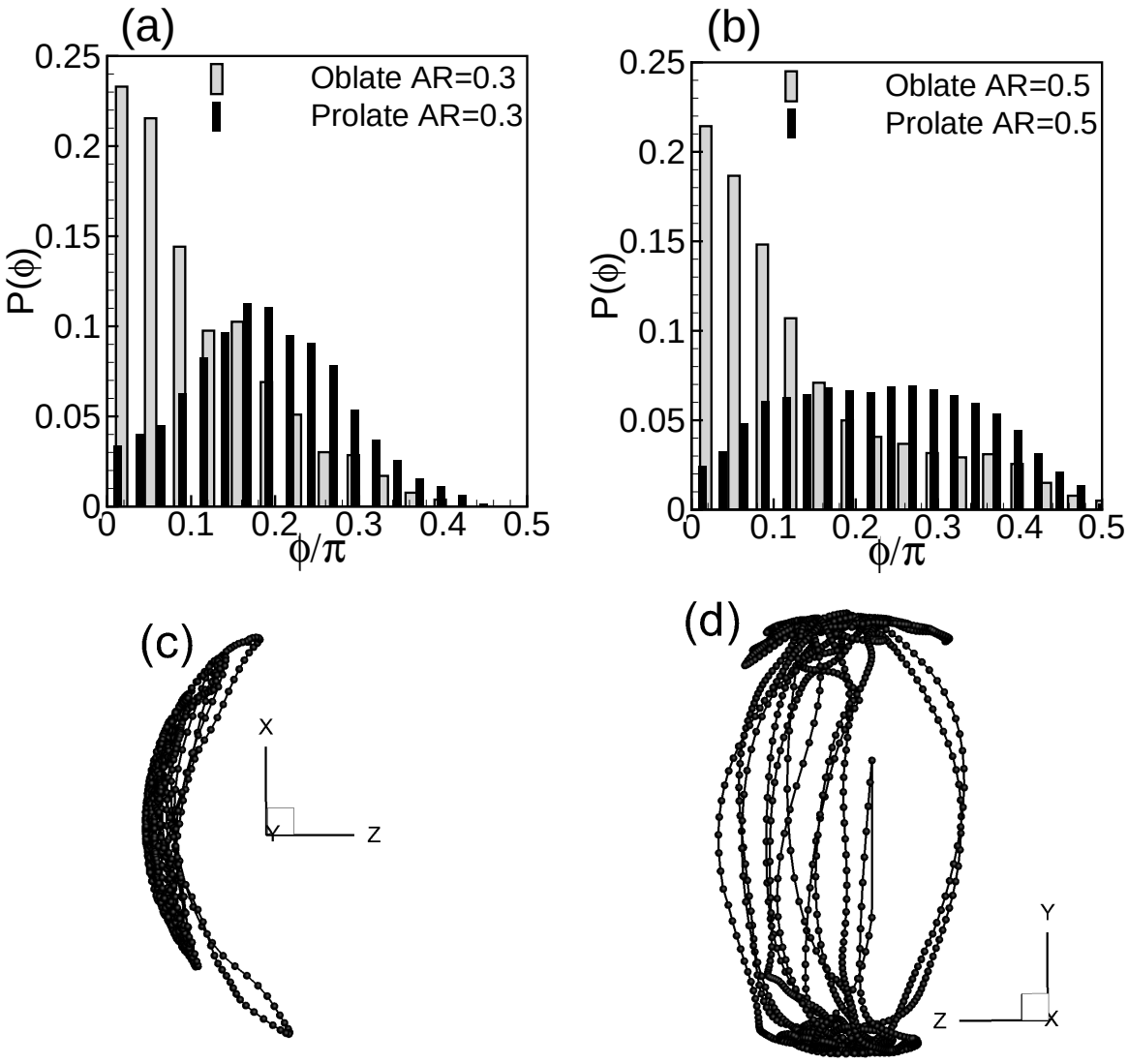

Figure 5.6: (a), (b) Probability distribution of the off-shear plane angle ϕ which is the angle between a particle's axis of revolution and the plane of shear (x-y plane). Here $\phi = 0$ represents the axis lying in the shear plane, and $\phi = \pi/2$ represents the axis aligned along the vorticity direction (z). (c), (d) Sample time trace of a particle's axis of revolution for prolate and oblate, respectively.

RBC suspension just above the CFL edge. The data suggest that oblates of AR = 0.3 and 0.5 mostly align their axes in the shear plane as the peaks occur at $\phi = 0$ for these particles. In contrast, for prolate particles, the distribution is wider and the peaks shift to higher values of ϕ. For prolates of AR = 0.3, the peak is at around 0.2π. For prolates of AR = 0.5, the distribution is significantly flatter.

Figure 5.6(c) and (d) show the time trace of a particle's axis of revolution. Here each dot represents the location of a point on the axis at a specific time. For the prolate, the dots are concentrated around the vorticity (z) axis, whereas for the oblate they are concentrated near the x-y plane. The dynamic behavior is a precessing motion of the axis of revolution about the vorticity axis in case of the prolate, and a back-and-forth oscillation about the shear plane in case of the oblate. Together, the data in Figure 5.6 suggest that the oblates preferentially orient their axis of revolution close to the shear plane while for the prolates the axis shifts towards the vorticity direction but with a wider angular distribution. As will be shown below, this difference in the 3D orientation of oblate and prolate microparticles has a strong effect on the way they interact with the flowing RBCs and consequently on their near-wall accumulation.

Evidently, the degeneracy of the Jeffery's orbit is broken for the microparticles. Since these particles are small, the effect of inertia is negligible. We hypothesize that the degeneracy is broken due to nonlinearity arising from repeated collisions of these particles with the RBCs, and due to the wall effect as our computational domain is relatively small and wall-bounded. In order to illustrate that the preferred orientations of the prolates and oblates are indeed due to repeated collisions with the RBCs and the wall effect, we consider a series of simulations where binary collisions

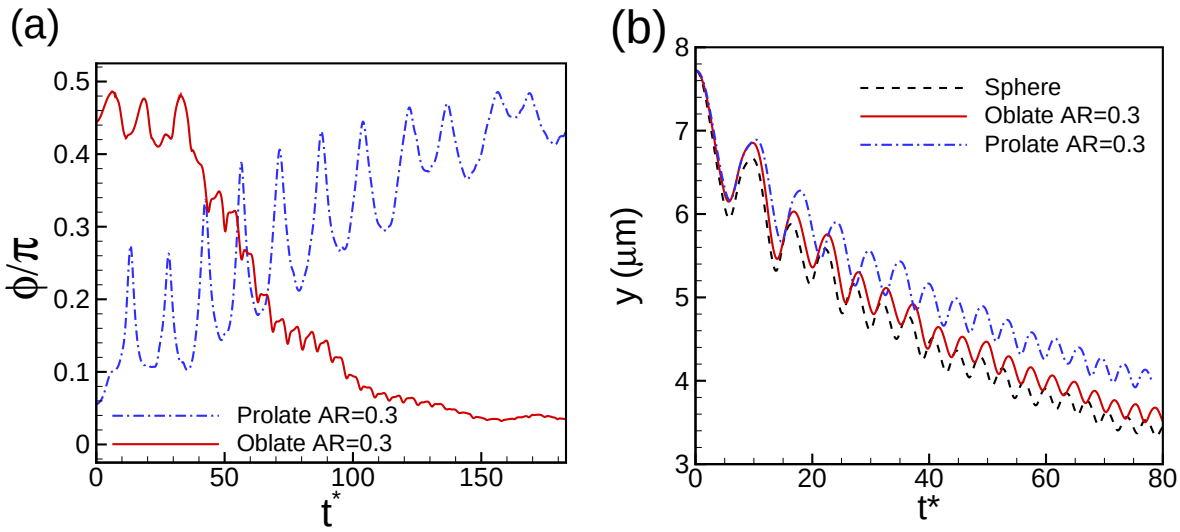

Figure 5.7: Simulation of repeated binary collisions between a microparticle and an RBC near a wall. (a) Time history of the off-shear plane angle ϕ is shown for a prolate (blue dash-dot line) and an oblate (red solid line). At the beginning of the simulations, the axis of revolution of the oblate was aligned close to the vorticity axis ($\phi \approx \pi/2$), while that of the prolate was aligned close to the shear plane ($\phi \approx 0$). Due to repeated collisions with the RBC, the axis of the oblate eventually aligns close to the shear plane, and that of prolate aligns close to the vorticity axis. (b) Lateral trajectories of oblate, prolate and spherical microparticles obtained from repeated binary collision simulations.

between a microparticle and an RBC is simulated in wall-bounded shear flow (see Figure 5.8(b) for a schematic). The microparticle is released with a slight offset in the lateral direction with respect to the RBC. Due to a non-zero relative velocity, the particle approaches the RBC. After the interaction, the particle moves away from the RBC and leaves the domain. Since the domain is periodic in the streamwise direction, the same particle re-enters the domain and approaches and interacts with the RBC again. Figure 5.7(a) shows the time history of the off-shear plane angle ϕ due to such repeated collisions for an oblate and a prolate. At the beginning of the simulations, the axis of revolution of the oblate was aligned close to the vorticity axis ($\phi \approx \pi/2$), while that of the prolate was aligned close to the shear plane ($\phi \approx 0$). Due to repeated collisions with the RBC, and the fact that the microparticle is 'sandwiched' between the RBC and the wall, the axis of the oblate eventually aligns close to the shear plane,

and that of prolate aligns close to the vorticity axis. This result further illustrates that oblates and prolates are preferentially oriented due to their interaction with the RBCs and the wall effect, and that their respective orientations are different. Figure 5.7(a) further shows that while the oblate reaches a steady orientation near the end of the simulation, the prolate exhibits more fluctuations in ϕ and would take a longer time to reach a steady orientation. Thus, the probability distribution of ϕ would show a narrower distribution and a strong peak near $\phi = 0$ for the oblates, but a much wider distribution and a weaker peak towards $\phi = \pi/2$ for the prolates. Therefore, the results of the binary collisions agree with the distribution of ϕ obtained from our suspension simulations as shown earlier in Figure 5.6(a)-(b).

Due to their different preferential orientations in cellular suspensions, microparticles of oblate and prolate shapes perform different dynamics as illustrated earlier in Figure 5.6(c)-(d): Prolates perform precessing motion about the vorticity axis of the flow, while oblates, with their axis of revolution in the shear plane, undergo flipping motion. As it will be shown later, these two different dynamics affect differently on how an individual microparticle interacts with an RBC, and consequently on its margination.

Figure 5.7(b) shows the lateral trajectories of microparticles of different shapes obtained in the simulations of repeated binary collisions between a particle and an RBC. Each collision results in an increase in lateral separation between the two. The figure shows that after several collisions the spherical and oblate particles are laterally displaced more than the prolate particles. If such repeated collisions occur near the CFL in a multi-cell suspension, the oblate and spherical particles would marginate at a higher rate than the prolate particles. Therefore, this result can partly explain the

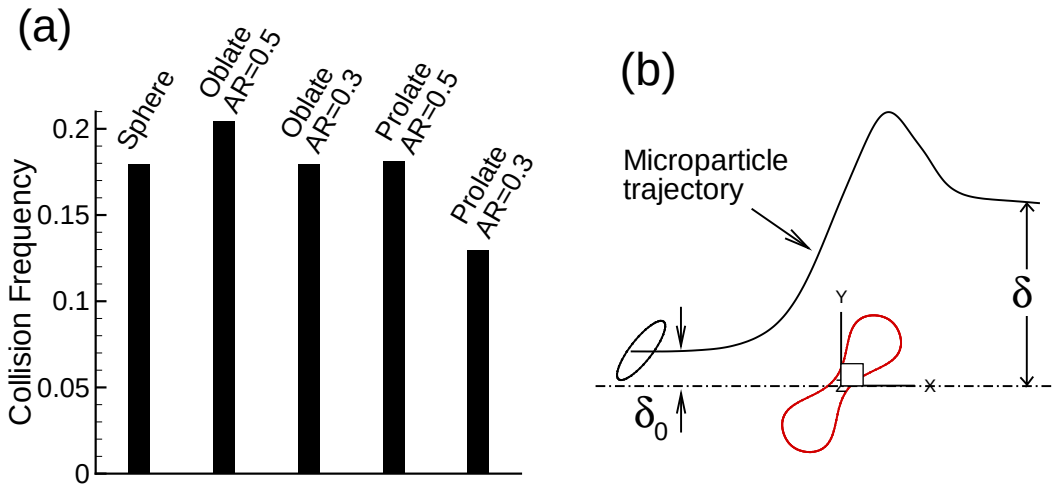

Figure 5.8: (a) Frequency of collisions between microparticles and RBCs obtained from our suspension simulations for particles flowing near the CFL edge. (b) Schematic of a binary cell-particle collision simulation. The initial lateral offset between the centers of the cell and particle is denoted by δ_0, and the final lateral displacement is δ.

higher near-wall accumulation of oblate particles and spherical particles compared to prolate particles as observed earlier in Figure 5.2(b)-(c) for our suspension simulations.

One limitation of the repeated binary collision simulations is that the lateral distance between the microparticle and the RBC gradually increases reducing the influence of the RBC on the particle after a few collisions. In contrast, in the suspension, the particles are always in close proximity to the RBCs. As a result, the binary interactions are close-range and have a much greater influence on particle's lateral displacement. The lateral displacement resulting from each individual close-range binary interaction collectively leads to particle margination. We hypothesize that particle margination is determined by two factors: (i) The frequency of collisions between a particle and an RBC, and (ii) the lateral displacement resulting from each individual collision. A microparticle can significantly move in the lateral direction either due to very frequent collisions with the RBCs, or due to a large lateral displacement resulting from individual collisions that are occurring less frequently. In

what follows, these two hypotheses are validated.

From our suspension simulations, we extracted the frequency of collision between microparticles and RBCs and present the data in Figure 5.8(a). The maximum collision frequency is obtained for oblates of AR = 0.5 and the minimum for prolates of AR = 0.3, while intermediate and nearly similar frequencies are obtained for spherical particles, oblates of AR = 0.3, and prolates of AR = 0.5. This trend in collision frequency for different particles is similar to the trend observed for near-wall accumulation shown earlier in Figure 5.2(b)-(c). Hence, this result confirms our first hypothesis that the frequency of particle–RBC collision is a factor in determining the margination rate of microparticles.

To verify the second hypothesis, we simulated binary collision between a microparticle and an RBC in a shear flow. Since a tank-treading RBC naturally aligns at an angle with the flow direction [178], such a collision would laterally deflect the particle further away from the RBC (see Figure 5.8(b) for a schematic). The amount of the lateral deflection δ, defined by the center-to-center lateral separation, is of interest here for various particle shapes. It is important to note that the final displacement δ depends on the initial lateral separation between the particle and the RBC, i.e., δ_o as illustrated in Figure 5.8(b). It also depends on the initial three-dimensional orientation of the microparticle since that would dictate the relative orientation of the particle and the RBC at the time of collision (See Chapter 3). The initial orientation of the microparticle is characterized by two angles: the initial off-shear plane orientation angle ϕ_o which is the angle between the particle's axis of revolution and the shear plane, and the initial shear-plane inclination angle θ_o which is the angle between the flow direction and the projection of the particle's axis of revolution onto the shear

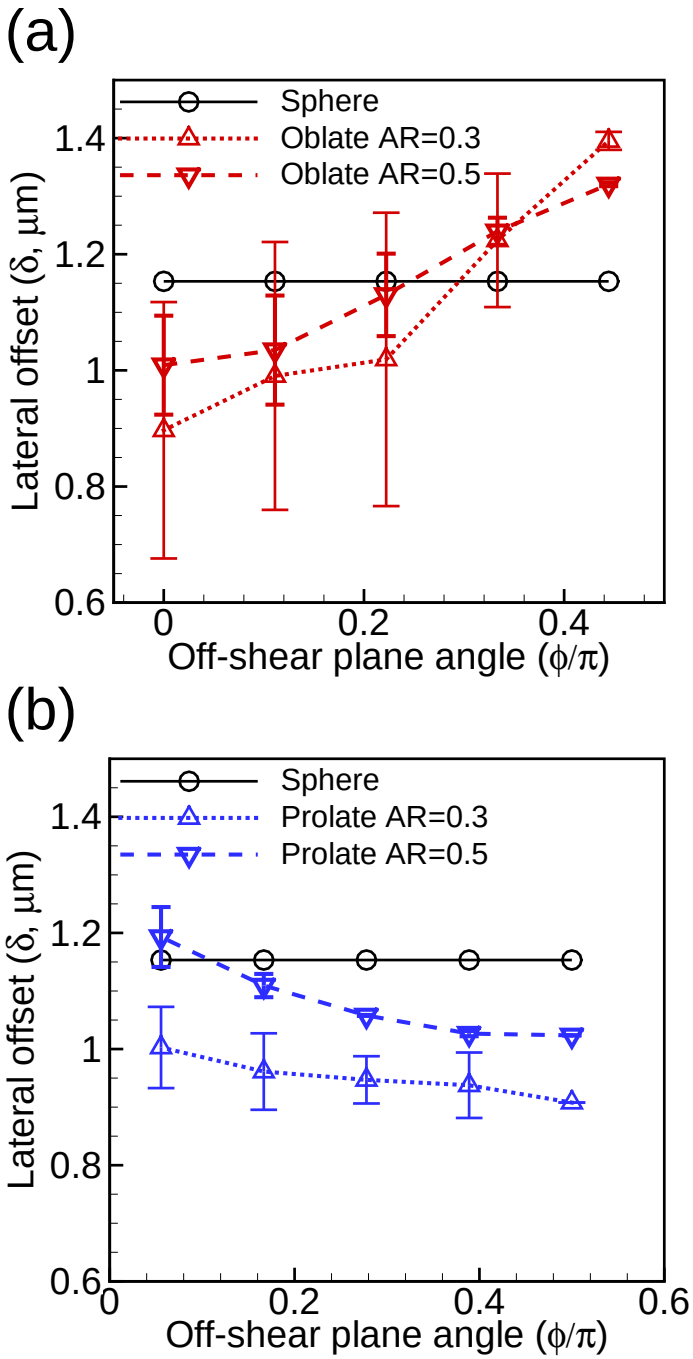

Figure 5.9: Results from binary collision simulations between an RBC and a microparticle. (a), (b) Lateral displacement δ of microparticles of different shapes as a function of off-shear plane angle ϕ_o. The error bars represent the range of δ obtained in the simulations for the range of initial shear-plane inclination angle θ_o (0 to 2π).

plane (see Figure 5.5). We simulated binary collisions for different values of ϕ_o and θ_o while keeping δ_o constant at 1.13 μm. Figure 5.9 shows the lateral separation δ as a function of ϕ_o and for various particle shapes. Here each data point represents an average of the values of δ obtained over a range of θ_o, from 0 to 2π. The error bars represent the range of δ. Figure 5.9(a) shows that for $\phi_o \gtrsim 0.2\pi$, the oblate particles have higher lateral displacement than the spherical particles. Moreover, for $\phi_o > 0.35\pi$ the oblates of AR = 0.5 yield higher values of δ than the oblates of AR = 0.3. We further note from the earlier results of Figure 5.6 that the oblates of AR = 0.5 have a higher probability of orientation at $\phi \gtrsim 0.3\pi$ than the oblates of AR = 0.3. Hence a higher number of oblates of AR = 0.5 would have a larger lateral displacement than AR = 0.3. A larger lateral separation for AR = 0.5 also means a larger relative velocity between the particle and an RBC upon collision, and hence, a higher collision frequency. Therefore, a higher lateral separation along with the highest collision frequency lead to the maximum near-wall accumulation for oblates of AR = 0.5 as shown earlier in Figure 5.2.

Figure 5.9(b) shows δ for the prolate particles obtained from binary collision simulations. For all ϕ_o and θ_o, the prolates of AR = 0.3 yield a significantly lower δ compared to other shapes considered. A lower value of δ also means a smaller relative velocity between the RBC and the microparticle upon collision, and, hence, a lower collision frequency. Therefore, this observation of the binary collision simulations agrees with the collision frequency data obtained in our suspension simulation, and explains why the prolates of AR = 0.3 yield the lowest near-wall accumulation as noted earlier in Figure 5.2.

5.3.4 Shape Effect on the Initial Particle–Wall Contact

In the previous section, our results on multicell suspension showed that the oblate particles of moderate aspect ratio (AR = 0.5) have the highest near-wall accumulation, while more elongated prolate particles (AR = 0.3) have the lowest accumulation. Ultimately, the efficacy of these particles will be determined by whether they can establish physical contacts and firm adhesion to the wall. In this section we present results on microparticle shape effects on particle–wall contact initiation. The initial contact with the wall can be established by the particles which are accumulated in the near-wall region, i.e., inside the cell-free layer. Dynamics of such particles are considered in this section.

Figure 5.10(a) shows the trajectory of a sample particle (prolate, AR = 0.3) that has marginated out of the RBC-rich zone, and is flowing inside the CFL. The lateral location of the particle center and the off-shear plane angle ϕ are shown, which fluctuate in time due to interactions of the particle with the RBCs flowing near the CFL edge. Of interest is the minimum separation distance ζ between the surface of a particle and the wall. A smaller value of ζ indicates a higher probability of particle–wall contact. From our simulations we extracted the distribution of ζ for the marginated particles and presented the data in Figure 5.10(b) for different particle shapes. The result implies that a greater number of prolate particles of AR = 0.3 come closer to the wall than particles of other shapes. The peak of the distribution for the prolates of AR = 0.3 occurs at $\zeta \approx 700$ nm, which is within the length scale of large adhesive molecules, e..g., ultralarge von-Willebrand factor. Thus, although the prolates of AR = 0.3 had the lowest near-wall accumulation compared to other microparticles considered, they are more likely to make the initial contact with the

wall.

As before, the dynamics of individual particles inside the CFL explains why prolates of AR = 0.3 are more likely to make the initial contact with the wall. Figures 5.10(c) and (d) show the distribution of the off-shear plane angle ϕ for the marginated particles. The data suggests that most oblates flow with their axes of revolution aligned in the shear plane. In this orientation, a freely suspended oblate would perform a continuous flipping motion. But such a flipping motion is hindered for oblate particles flowing close to the wall. Instead, the particles undergo a sliding motion in which they flow almost parallel to the wall while their axis of revolution remain normal to the wall [61, 173]. The flipping motion is further prevented as the oblates are sandwiched between the wall and the RBCs. Such a restricted motion prevents the oblate particles from coming closer to the wall. For the prolate particles, the peak distribution is towards larger values of ϕ, meaning that their axis of revolution is shifted towards the vorticity axis, and hence aligned parallel to the wall. However, the distribution is flatter for prolate particles, meaning that there are significant fluctuations in ϕ. Because of their rod-like shape, even a relatively small fluctuation can bring the surface of a prolate particle closer to the wall.

The above results suggest that the rod-like elongated particles are more likely to form the initial contact with the wall, although they have a much lower near-wall accumulation compared to the spherical and disk-shaped particles. This result is consistent with a previous experimental study which noted a higher wall-adhesion rate for rod-like particles [56].

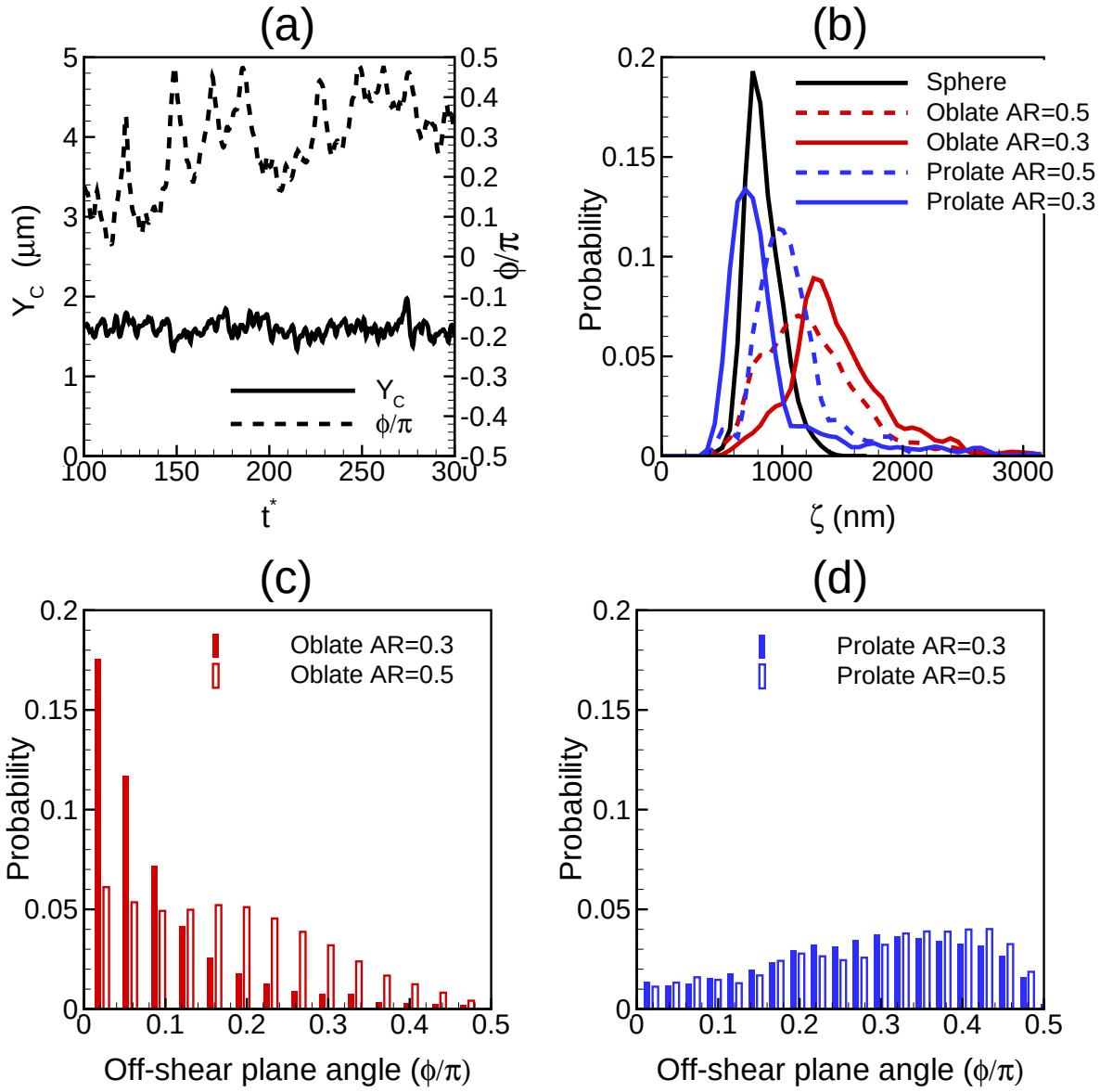

Figure 5.10: Microparticle dynamics inside the CFL. (a) A sample particle trajectory showing the lateral location of the particle center (Y_c, left axis, solid line) and off-shear plane angle ϕ (right axis, dash line). (b) Distribution of the minimum distance ζ between a particle's surface and the wall for different particle shapes. (c), (d) Distribution of off-shear plane angle ϕ.

5.3.5 Shape Effect on Particle Adhesion

Once microparticles establish the initial contact, they must then firmly adhere to the wall. In this section, we address the microparticle shape effects on particle–wall adhesion. We have simulated adhesion between the flowing microparticles and the wall in presence of multiple flowing red blood cells by combining our multi-RBC–multiparticle model with the stochastic adhesive dynamics model described in Chapter 2. Microparticles under the combined action of the fluid shearing force, collision with the RBCs, and the force from the bonds undergo adhesive rolling motion along the wall. Figure 5.11(a) shows a snapshot from our simulations for spherical particles undergoing adhesive rolling motion in the shear flow while the RBCs flow above them. For different particle shapes, we observe steady rolling motion, intermittent stop-and-go type of motion, and firm adhesion. We observe that microspheres, and prolates of AR = 0.5 undergo a steady rolling motion. Most prolates of AR = 0.3 also undergo a steady rolling motion albeit with a reduced velocity, while some are firmly adhered to the wall. Oblates of AR = 0.5 exhibit an intermittent motion in which they are mostly adhered but occasionally flip on the wall, resulting in a stop-and-go motion. Oblates of AR = 0.3 are mostly firmly adhered.

The average rolling velocity obtained from our time-sequence data and averaged over similar class of particles is shown in Figure 5.11(b). Also shown is the average number of adhesive bond-sites that are observed on particle surfaces. The rolling velocity is maximum for the spherical microparticles, and it decreases progressively for prolates of AR = 0.5, oblates of AR = 0.5, prolates of AR = 0.3, reaching the minimum for the oblates of AR = 0.3. The number of bond sites shows exactly opposite trend of the rolling velocity. This result suggests that the disk-shaped particles are more

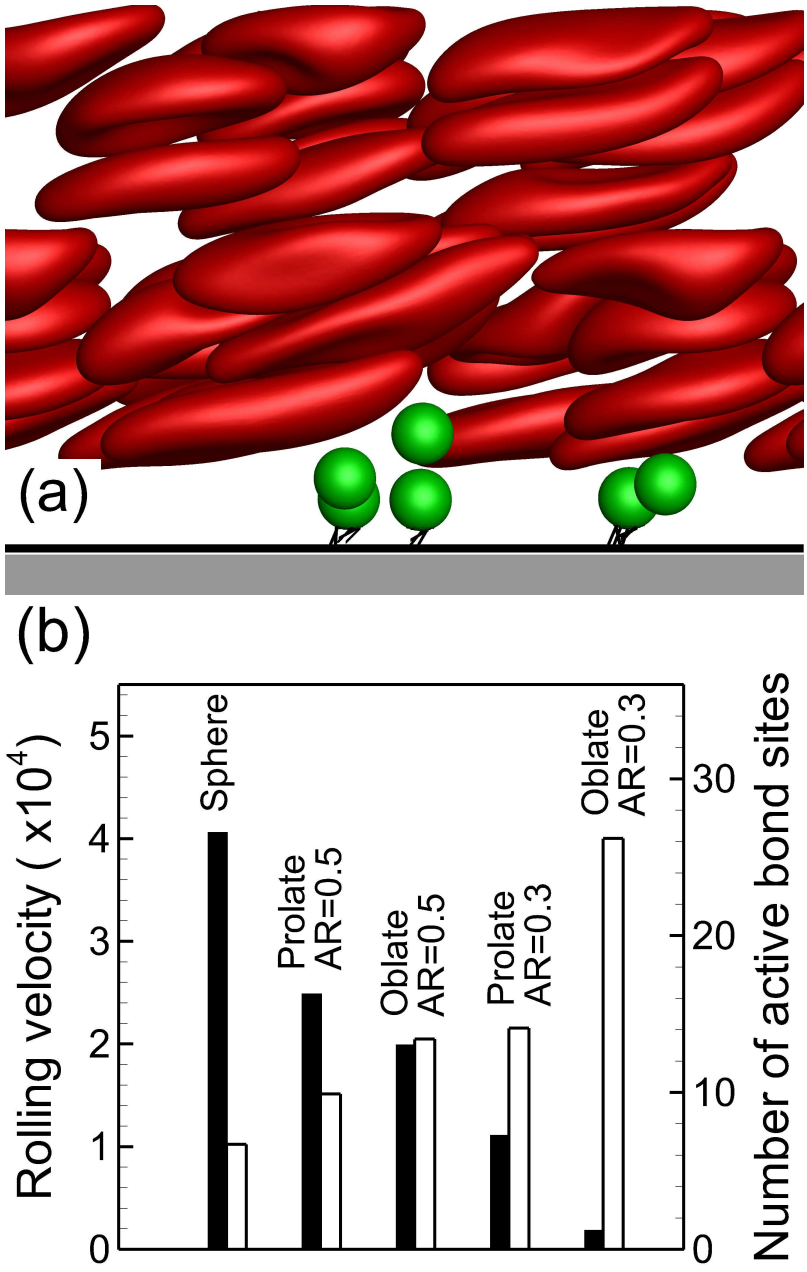

Figure 5.11: (a) A snapshot from our simulations on microparticles (colored in green) rolling along and adhering to a surface in the shear flow with flowing red blood cells (colored in red) above. Active (instantaneous) bonds formed between the particle surface and the wall are also indicated. Here the flow is from left to right. (b) Average rolling velocity (scaled by $\dot{\gamma} a_o$, left axis, filled bars) and average number of active bond sites (right axis, unfilled bars) for microparticles of different shapes.

likely to form a firm adhesion with the wall. Unsurprisingly, this result is related to the particle surface area-to-volume ratio and its near-wall dynamics. Due to its flipping motion, when an oblate particle makes a contact with the wall, its major axis is nearly perpendicular to the wall. In this configuration it experiences a significant drag from the flow which, in turn, makes it flip and lie parallel to and on the wall providing a significant surface area for adhesion. If enough bonds are formed, the particle firmly adheres. In contrast, a sphere rolls along the surface and makes a point contact with the surface, while a prolate flows parallel to the wall without any flipping and makes a line contact. Consequently, the number of bond sites is reduced for the prolates and is minimum for the spheres, leading to the observed trend of the rolling velocity.

It should be noted that while we presented the results for three different stages of margination-adhesion cascade, we used the same simulation for the first two stages, i.e. the accumulation and contact formation stages are obtained from the same simulations with homogeneously distributed particles. For the adhesion simulation, we considered separate simulations due to time-step restriction. Nevertheless, we can use these two sets of simulations to obtain an estimate of the overall probability of microparticle adhesion starting from the homogeneous distribution. The first set of simulations gives us the probability of accumulation and contact formation, while the second set gives the probability of adhesion of the particles that are already near the wall. The overall probability can be found as the product of the two which is plotted in Figure 5.12. Now we observe that particle adhesion plays a major role in determining the overall efficiency. Although spherical particles showed relatively high margination rates (Figure 5.2), their overall efficiency is observed to significantly

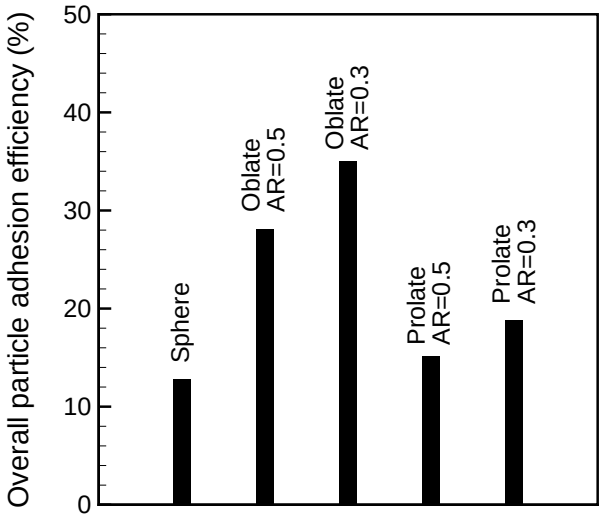

Figure 5.12: Overall probability of adhesion starting from the homogeneous distribution of microparticles.

decrease due to their higher rolling velocity along the surface. Oblates outperform prolates due to their higher margination rate (in case of moderate AR) and their superior adhesive dynamics (in case of low AR).

5.4 Conclusion

We presented a 3D modeling study of transport, margination, near-wall dynamics, and adhesion of micro-scale particles of different shapes (spherical, oblate and prolate) in whole blood represented as a suspension of deformable red blood cells. Quantification of the shape effects on the micro-scale dynamics of RBC–particle interaction and its influence on particle margination and adhesion in whole blood does not exist in the literature, and is accomplished here for the first time. As such, this study complements the earlier experimental [48–50, 52, 53, 55–60], and theoretical/computational studies [36–38, 41, 41, 51, 54, 61].

The major finding of this study is that the microparticles of different shapes interact differently with the RBCs leading to their differential behavior in different sub-processes in the margination-adhesion cascade, that is, the margination from the RBC-rich vessel core to the RBC-depleted CFL layer, the flow of the marginated particles inside the CFL and their physical contact with the wall, and the firm adhesion of such particles to the wall. Dynamics of individual particles of different shapes are quantified separately in these three sub-processes. Specifically, we show that microparticles' rotational orientation in three-dimensional space, and the frequency of their collisions with the flowing RBCs are the key factors that dictate their differential behavior in the margination-adhesion cascade.

We observe that the first stage of the margination process occurs in the core of the RBC-rich region by the shear-induced diffusion process augmented by the RBC–microparticle collisions. The augmented diffusion, although several times faster than the Brownian diffusion, is a generally slow process, and has been known for platelets in whole blood suspension [12–15]. Our results show that the RBC-augmented diffusion is nearly the same for microparticles of different shapes, and, hence, cannot explain the observed shape-dependency of the near-wall accumulation. Similar values of microparticles diffusivity was also observed by Zhao et al. [42] for platelets and platelet-size microspheres.

Once a drifting microparticle reaches within a certain distance of the CFL, a fast and discontinuous margination process occurs during which the particle abruptly and rapidly traverses a large lateral distance and move into the CFL. We termed this event as the 'waterfall effect' due to the similarity in the particle trajectory.

This phenomenon which has also been observed in a recent experiment [55], provides a mechanism of rapid particle margination from the RBC-rich region to the CFL, and gives microscopic details on the inhomogeneous diffusivity or the spatially varying additional drift proposed by previous studies to explain margination enhancement [23,24,28,29,36,37,41,42,159]. Our simulations indicate that the waterfall effect is a result of anisotropy in RBCs instantaneous configuration along the wall-normal direction which is a consequence of formation of microstructures such as cavities by RBCs stacks. Similar notion on the enhancement of margination by RBC cluster formation can be found in the context of RBC aggregation (rouleaux) in flowing blood: Formation of rouleaux was shown to enhance WBC margination and adhesion in experimental [100, 101, 104, 176], and computational studies [126, 177]. In the present study, we focus on such phenomenon to explain the differences we observe in margination rate of different shaped particles. In fact, we observe that the frequency of the waterfall incident strongly depends on the particle shape: oblate particles of moderate aspect ratio exhibited the highest frequency, while very elongated prolate particles exhibited the lowest frequency. Accordingly, the near-wall accumulation observed in our simulations was highest for the moderate aspect ratio oblate particles, followed by microspheres, and lowest for the very elongated prolate particles. Interestingly, a recent computational study by Reasor et al. [62] observed a slower margination rate for disk-like particles; they attributed this to the confinement of such flat particles between RBC layers. However, they did not consider particles of moderate aspect ratios. Their study combined with ours suggest that a higher margination rate is likely to occur for moderately aspherical particles, rather than highly aspherical ones.

To provide further insight on the particle shape effect on the observed near-wall

accumulation, we analyzed the dynamics of individual particles in the suspension. We observed that due to repeated collisions with the flowing RBCs and the effect of a bounding wall, an oblate particle aligned its axis of revolution close to the shear plane, while a prolate particle aligned its axis close to the vorticity axis of the flow. Because of such specific orientations, the frequency of RBC—microparticle collisions and the lateral displacement resulted from each collision are maximum for the oblate particles of moderate aspect ratio, followed by microspheres, and minimum for the very elongated prolates. This trend of collision frequency and lateral displacement follows the frequency of the waterfall phenomenon, and the near-wall accumulation, thereby explaining the observed shape-dependency.

The particle shape, however, has an entirely different effect on establishing the wall–particle contact. We observed that very elongated prolate particles flow with their axis of revolution aligned close to the vorticity axis but with large fluctuations in their orientation resulting in more frequent contacts with the wall. Thus, although these particles exhibited the lowest near-wall accumulation rate, they are most likely to form the initial contact with the wall. This phenomenon which is directly observed in our study has been proposed earlier in an experimental study on margination of rod-like microparticles [56]. Microspheres slightly underperform the elongated prolate particles, while the oblate particles exhibited the poorest performance in terms of wall contact due to the fact that their tumbling motion is considerably hindered by wall effects. The observed decrease in oblate particles' tumbling frequency near the wall is consistent with prior studies on platelets [38], and ellipsoidal particles [61].

We further simulated adhesion between flowing microparticles and wall in presence of multiple flowing red blood cells by combining our 3D deformable cell suspension

model with the stochastic adhesive dynamics model. We observed that the oblate particles are more likely to form a firm adhesion due to their large surface area. In contrast, the prolate particles mostly perform slow rolling motion as they make line contacts with the wall, although firm adhesion was observed for a few very elongated prolate particles. The microspheres did not make a firm adhesion, and they exhibited the highest rolling velocity among all particles. When overall probability of adhesion starting from initially homogeneous distribution is considered, we observed that adhesion plays a major role. As such, microspheres exhibited lower overall probability, while oblates exhibited the highest overall probability. As noted in Section 5.1, many experimental studies [48–50, 52, 53] considered micro- and nano-particle adhesion under cell-free environments. Such a simplification might be valid for nanoparticles, but not for microparticles considering the typical CFL thickness observed. Other studies [55–60] considered particle adhesion using whole blood; however, the effects of diffusion and margination are combined because of the macroscopic measurements provided. It should be noted that the objective of this study is not to identify the optimal shape for the drug carriers. Instead, we intended to shed light on the physics of microparticle dynamics as they interact with the RBCs. Although the general conclusion that asphericity increases microparticles' performance in the prior studies and the present work agrees, the latter provides more physical insights by considering individual particle dynamics at different stages of the margination-adhesion cascade.

It should be noted that in a real circulatory system, the flow is pressure driven, while we have considered flows with a constant shear rate. The present set-up is relevant if the interest is in a region relatively closer to the wall in larger arteries, e.g. near regions prone to atherosclerotic plaque formation which typically occur in

larger vessels. Given the size of microparticle and RBCs compared to vessel size, and the fact that particle diffusion is linearly dependent on shear rate, we expect that the curvature of the velocity profile can only have a secondary effect. Additionally, in circulatory systems there are vessel bifurcations, tapering, and uneven vascular wall. It is unclear whether these effects play less dominant role than the velocity profile curvature effect in the near-wall region.

In summary, this study shows that the shape of the carrier particles affects their dynamics differently at different stages in the margination-adhesion cascade. While oblate particles of moderate aspect ratio show the highest near-wall accumulation, very elongated particles are more likely to form initial wall contact. Once the contact is established, disk-like particles are more likely to firmly adhere. Consequently, the optimum shape of the intravascular drug carriers depends on the hemorheological conditions at the targeted site. For example, for a blood vessel with a small cell-free layer thickness and a large flow rate, the disk-like particles may be a better candidate due to their higher accumulation rate and large surface area. In contrast, for a large CFL thickness and a reduced flow rate, very elongated prolate particles may be a better candidate as they are more likely to form the initial contact with the wall. Therefore, one must consider the specific vascular conditions at the targeted site while designing and selecting the optimum shape of the drug carriers.

Chapter 6

Blood Flow in Stenosed Microvessels

6.1 Introduction

Vascular stenosis is a term that is commonly used to describe narrowing of blood vessels as a result of plaque formation. When the stenosis occurs in a large artery, for example, aorta, coronary and carotid arteries, the disease is referred to as atherosclerosis, or large vessel disease [64]. Research over the past several decades has established the important role of fluid flow in mediating atherogenic cascade [11, 65–67]. In recent years, however, there is an apparent paradigm shift in our understanding of vascular stenosis. It has been established now that stenosis can and often occur in smaller arteries (arterioles) with internal diameters ranging up to a few hundred microns [68, 69]. The condition, known as arteriosclerosis or microvascular disease, could have severe consequences such as blockage of microvessels supplying blood to heart muscles, in which case it is referred to as the coronary microvascular disease or CMVD [70, 71]. Additionally, microvascular stenosis is known to cause lacunar infarcts or blockage of smaller arteries supplying blood to the deep interior of the brain, as well as blockage of retinal and renal arteries [69, 72, 73]. Flow blockage in small vessels can occur also by adherent leukocytes, gas emboli, etc. [74–77]. Apart from physiological examples, in vitro microstenosis geometry are utilized in biomedical devices, e.g., for cell separation [78, 79].

Fluid mechanics of a microvascular stenosis is expected to be very different from that of a macrovascular stenosis since blood behaves as a Newtonian fluid in large arteries but as a non-Newtonian fluid in microvessels [80]. While shear-thinning fluid models of blood have been used by several studies [81, 82] to address hemodynamics in micro-vascular stenosis, these continuum models have several limitations. For example, such models require specifying the characteristics of the cell-depleted region (CFL) near the vascular wall. Although experimental data on CFL thickness exists for non-stenosed vessels [83], no such data exist for stenosed vessels, rendering the applicability of the continuum models quite limited. As mentioned in Chapter 1, the cell-free layer forms due to the migration of the RBCs away from the wall, which in turn is caused by a hydrodynamic lift acting on these highly deformable cells. The thickness of the CFL is expected to greatly vary over the length of a stenosis, unlike a constant CFL thickness observed in non-stenosed vessels and assumed in the continuum models. Studies using microfluidic conduits with severe constrictions showed greatly enhanced plasma and cell separation and increased downstream CFL thickness [78]. As such, the cellular nature of blood must be considered in any modeling study of microvascular stenosis. As mentioned in previous sections, illustrations of the cellular nature of blood flow in small vessels are the well known Fahraeus-Lindqvist and Fahraeus effects, which refer to a reduction of the apparent blood viscosity and RBC volume fraction or hematocrit, respectively, with decreasing vessel diameter [80, 86–88]. What is the apparent viscosity of blood in stenosed microvessels? How are the Fahraeus-Lindqvist and Fahraeus effects altered in presence of a stenosis? Could the apparent viscosity of blood obtained in vessels of uniform

cross-section be used to predict the Fahraeus-Lindqvist effect in stenosed microvessels? Answering these questions requires addressing cellular blood flow in stenosed vessels.

While the apparent viscosity is a useful average quantity that dictates the pumping power required for the heart, it is the local hemodynamic condition at the stenosis that dictates the growth and progression of the plaque [11, 64–67, 89]. Endothelial cells (ECs) lining the inner wall of blood vessels are known to respond to local hemodynamic conditions, such as the wall shear stress, and mediate atherogenesis via, e.g., suppression of nitric oxide (NO) release [90, 91]. EC response, along with complex flow conditions near a stenosis trigger thrombus formation via platelet aggregation and adhesion [92–94]. Not only the mean shear stress, the flow oscillations and shear gradients also affect the EC response [91, 93]. Unlike in large blood vessels where flow oscillations and shear gradients arise primarily from the interaction between flow pulsatility and stenosis geometry [11,64–67]. in small vessels the motion of individual blood cells causes temporal and spatial variations leaving 'footprints' on ECs [86]. While temporal and spatial flow oscillations in non-stenosed microvessels have been measured experimentally [83], and also predicted via full numerical simulations [86], they are nonexistent for stenosed microvessels. Are these quantities enhanced or suppressed in stenosed microvessels compared to non-stenosed vessels?

To address the questions raised above, we consider a computational study of the flow of deformable RBCs in stenosed microvessels. It is shown that the discrete nature of the cell motion significantly affects the flow physics in microvascular stenosis with apparently different physiological consequences than in macrovascular stenosis. Not only the Fahraeus and Fahraeus-Lindqvist effects are observed to be significantly

affected by the interaction of the cells and stenosis geometry, several nonintuitive phenomena, such as a transient upstream flow reversal and several folds increase in flow fluctuations, are also observed. These new findings also question the applicability of the continuum two-phase flow models of blood to the study of microvascular stenosis.

6.2 Problem Setup

We simulate the motion of multiple deformable RBCs through constricted tubes. The vessel geometry is shown in Figure 6.1. We consider both axisymmetric and asymmetric constrictions. The axisymmetric constriction is defined by a cosine function of wavelength L_s and amplitude $\mathcal{A}$ rotated about the centerline of the tube. For the asymmetric constriction, the amplitude of the cosine function is varied as the function is rotated. We consider a fixed $L_s = 2D/\pi$ where D is the tube diameter away from the constriction, but vary the amplitude $\mathcal{A}$. An area blockage $\mathcal{B}$, defined as the ratio of the blocked cross-sectional area at the throat of the constriction to the nominal cross-sectional area of the vessel far away from the constriction, is varied up to 84%.

As noted before, RBCs exhibit large and complex deformation while flowing through small blood vessels. The membrane shear modulus and bending stiffness used in the simulations are about 2.5×10^{-6} N/m, and $6{\times}10^{-19}$ J, respectively. The surface of each RBC is discretized using 20480 triangular elements (or, 10242 Lagrangian nodes).

The flow in the vessels is driven by a mean pressure gradient, and governed by the Stokes equation as inertial effects are neglected. Based on the results of our simulations, the Reynolds number at the stenosis throat remains in the order of $10^{-}2$, which justifies the above assumption. The length of the vascular segment simulated

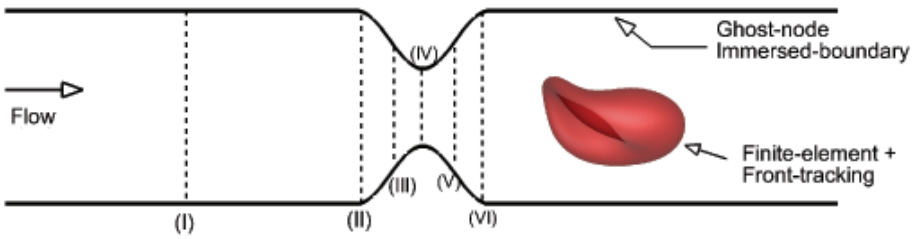

Figure 6.1: Geometry of a stenosed microvessel considered in the study. (I)–(VI) are streamwise locations where some flow quantities are measured for analysis.

is $L = 4D$. More details on the computational domain and boundary conditions are given in Chapter 2. The vessel diameters considered are 11, 17, and 25 μm, and the Eulerian resolution used are $320 \times 80 \times 80$, $480 \times 120 \times 120$, and $640 \times 160 \times 160$, respectively. The relevant parameters are the vessel diameter D, the area blockage $\mathcal{B}$ as defined above, the volume fraction or hematocrit H_t of the red blood cells, and the driving mean pressure gradient which is defined in dimensionless form as $\beta = -\left(d\overline{P}/dx\right) / \left(16\mu_o U_c/D^2\right)$, where U_c is an arbitrary velocity and μ_o is the plasma viscosity. The number of cells ranges from 5 to 132, depending on vessel size and hematocrit. Hematocrit ranges from 0 to 24%, the lowest limit corresponding to the flow of cell-free plasma fluid, and the upper limit corresponding to physiological conditions in small arterioles. The mean pressure gradient β ranges from 1 to 4. The mean flow rate increases with increasing β. For each D, H_t and β, cell motion in non-stenosed vessels (i.e., vessels of uniform circular cross-section) is also simulated for comparison with stenosed vessels.

6.3 Results

Figure 6.2 shows instantaneous visualization of the RBCs flowing through the stenosed vessels for a few representative cases. Some general observations can be made here.

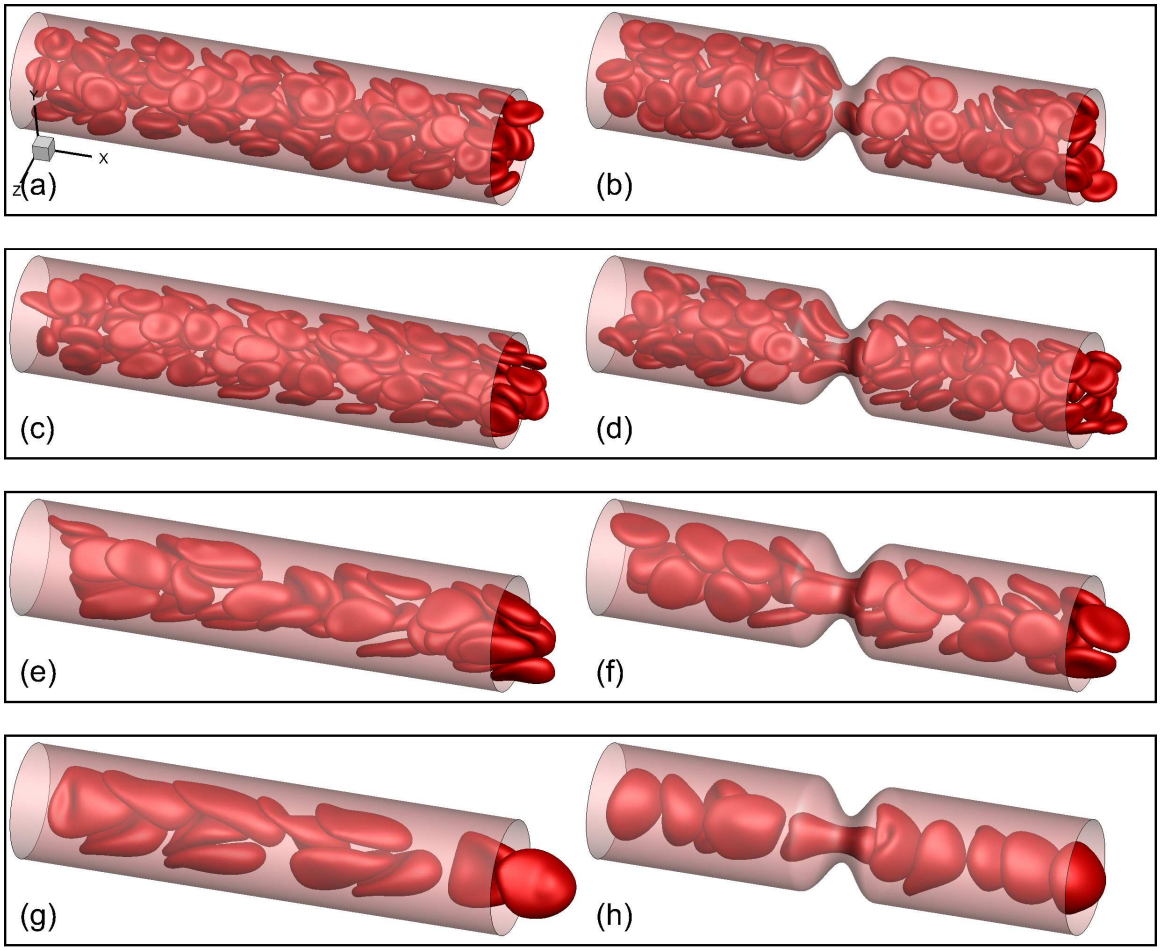

Figure 6.2: Snapshots showing instantaneous RBC distribution from a few representative simulations for non-stenosed (left column) and 84% stenosed (right column) vessels at $H_t \approx 22$–24%. (a), (b) $\beta = 1$, (c)-(h) $\beta = 4$. From the top row to the bottom one, $D = 25$ μm, $D = 17$ μm, and $D = 11$ μm, successively.

Cells deform significantly in smaller vessels where they assume the slipper and parachute shapes as observed in experiments [4]. In larger vessels, the resting biconcave shape is somewhat maintained at low flow rates, but not at high flow rates. For the range of vessel size considered here, the RBCs flow in multifiles. Formation of the CFL near the vessel wall is also clearly observed throughout the vessel segment in non-stenosed tubes and away from the stenosis in the stenosed tubes. The CFL thickness is observed to increase with increasing flow rate, in agreement with prior experimental and numerical studies of non-stenosed vessels [83, 184, 186].

The presence of a stenosis causes a geometric focusing of the cells. For the smallest tube considered ($D = 11$ μm), the multi-file motion that would occur without a stenosis is now converted to a single-file motion. Cells are significantly deformed as they squeeze before entering the stenosis, and bounce back upon exit. While most cells assume the slipper shape in the non-stenosed tube ($D = 11$ μm), nearly all assume the parachute shape in the stenosed tube. The discrete motion of cells results in large oscillations in flow rate over time. The flow rate drops immediately before a cell enters the stenosis, and regains as it bounces out. The squeezing and recovery of the cells result in a higher CFL thickness upstream the stenosis but a lower CFL thickness downstream. As the vessel diameter is increased, cells are able to follow the contour of the stenosis. Multiple cells can simultaneously flow through the stenosis. As many cells simultaneously enter the stenosis, a momentary reduction in the flow rate and a downstream region devoid of cells are observed. At a lower flow rate, crowding of the cells upstream the stenosis is also observed in larger vessels which causes a significant reduction of the CFL thickness there.

6.3.1 Enhancement of the Fahraeus-Lindqvist Effect

The most striking result from this study is that the Fahraeus-Lindqvist effect is significantly enhanced in stenosed vessels as shown in Figure 6.3 where the apparent viscosity is plotted with respect to vessel diameter. The apparent viscosity is defined as $\mu_{\text{rel}} = Q_P/\overline{Q}$ where Q_P is the flow rate of plasma (i.e., no RBC) in a non-stenosed vessel, and $\overline{Q}$ is the mean flow rate in presence of the cells. To illustrate the enhancement effect, four cases are considered in the figure: the non-stenosed tubes with the RBCs, the 84% stenosed tubes with the RBCs, the 84% stenosed tubes with plasma,

and with Newtonian fluids of the viscosity equal to the apparent viscosity of blood in a non-stenosed tube of the same diameter. For the non-stenosed tubes with cells, the computed values of μ_{rel} increase from 1.2 to 1.8 as the vessel diameter increases from 11 to 25 μm, in agreement with in-vitro measurements [187]. Therefore, the simulations faithfully reproduce the Fahraeus-Lindqvist effect in tubes of constant diameters. A significant increase in μ_{rel} is observed in the stenosed vessels in presence of RBCs. For the nominal diameter of 25 μm, μ_{rel} in the 84% stenosed tube is more than four times that in the non-stenosed tube. Not only the flow resistance has increased dramatically, the rate of increase of μ_{rel} with increasing D, as evident from the slope of the curves, is also much higher in the stenosed tubes compared to the non-stenosed tubes.

In order to see if the large increase in μ_{rel} in the stenosed tubes can be accounted for by geometric blockage only, we plot μ_{rel} in the 84% stenosed tube that would occur when only plasma fluid is driven without any cell (dash line in the figure). While μ_{rel} is observed to increase due to the blockage effect, it is significantly below the values obtained in presence of the RBCs. Then, we consider the flow of Newtonian fluids of viscosity equal to the apparent viscosity of the cellular blood obtained from the simulations of the non-stenosed tubes (dash-dot lines in the figure). Even with this higher apparent viscosity, which accounts for the macroscopic effects of the cells, the values are significantly less than those predicted in the simulations with cells. Evidently, the significantly elevated values of μ_{rel} in the stenosed tubes are due to the interaction between the vascular geometry and the blood cells, the latter being the cause of non-Newtonian nature of blood in microvessels.

The augmentation of the Fahraeus-Lindqvist effect due to the interaction of blood

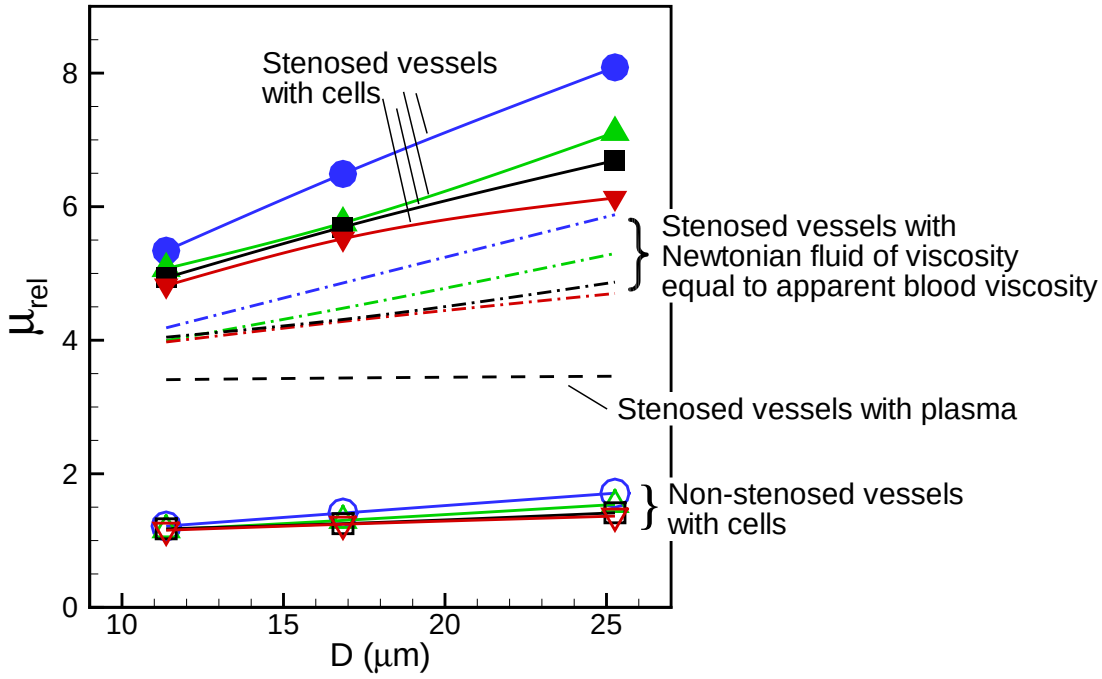

Figure 6.3: Apparent viscosity of blood showing a significant enhancement of the Fahraeus-Lindqvist effect in the stenosed vessels. Lines with unfilled symbols are for non-stenosed tubes with RBCs, and lines with filled symbols are for stenosed tubes ($\mathcal{B}$ = 84%, H_t ≈22-24%) with RBCs, for various values of β = 1 (◯, blue), 2 (Δ, green), 3 (□, black), 4 (∇, red). Dash line is for stenosed tubes with plasma only. Dash-dot lines are for stenosed tubes with Newtonian fluids having viscosities same as the apparent viscosity of blood in non-stenosed tubes of the same diameters (colors are for different values of β as before).

cells and vascular geometry can be further corroborated by simulating the motion of the RBCs through an asymmetric stenosis. The geometric feature of the asymmetric stenosis was mentioned previously. A snapshot from such a simulation is shown in Figure 6.4(a) for an area blockage of 84% and stenosis length $L_s = 2D/\pi$, same as those considered for the symmetric cases. The relative viscosity variation with increasing tube diameter for symmetric and asymmetric stenosis is compared in Figure 6.4(b). As much as 40% increase in the relative viscosity is observed in the asymmetric stenosis compared to the symmetric one. Also shown in the figure is relative viscosity obtained in the asymmetric stenosis for a Newtonian fluid having viscosity equal to the apparent blood viscosity in the non-stenosed tubes of the same diameter. As before, here also the Newtonian fluid significantly underpredicts the apparent viscosity obtained in the asymmetric stenosis in presence of the RBCs. Furthermore, the slope of the curve in the asymmetric stenosis in presence of the RBCs is higher than that obtained for the Newtonian fluid, and also for the symmetric stenosis, implying additional augmentation of the Fahraeus-Lindqvist arising from the complex interaction between the RBCs and vascular geometry.

Another important observation in Figure 6.3 is the dependence of μ_{rel} on the driving pressure gradient β. In general, μ_{rel} is observed to decrease with increasing pressure gradient, as a result of the shear-thinning nature of blood. Since increasing pressure gradient causes the mean flow rate, and hence the mean shear rate, to increase, the latter in turn causes a decrease in μ_{rel}. What is more striking, though, is that the sensitivity of μ_{rel} to changes in β increases with increasing diameter for both stenosed and non-stenosed vessels. Consider first the non-stenosed vessels for which μ_{rel} is observed to increase by 6% in $D = 11$ μm tube and 25% in $D = 25$ μm

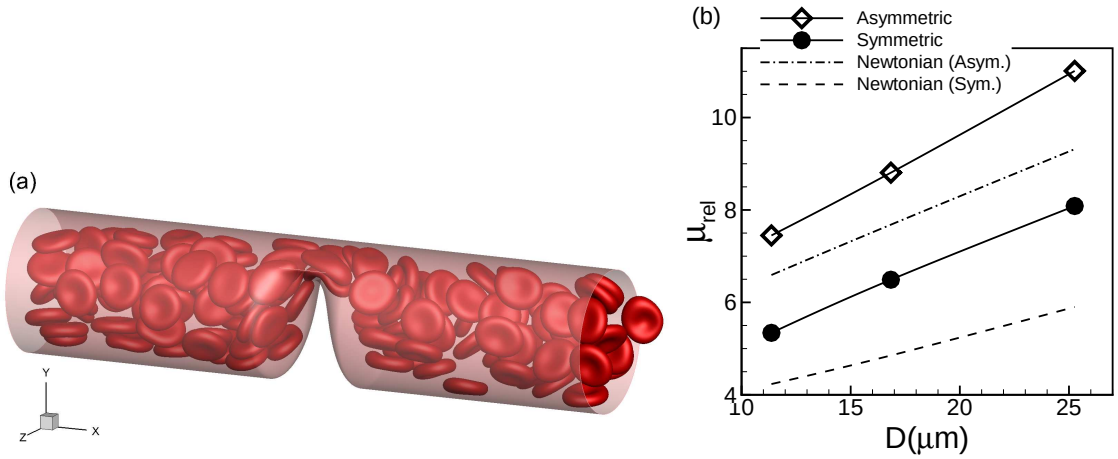

Figure 6.4: (a) RBCs flowing though an asymmetric stenosis ($\mathcal{B} = 84\%$, $D = 25$ μm, $\beta = 1$, and $H_t = 24\%$). (b) Comparison of the Fahraeus-Lindqvist effect in symmetric (continuous line, $\bullet$) and asymmetric (continuous line, $\diamond$) stenosis. The dash-dot line is the relative viscosity obtained in the asymmetric stenosis for a Newtonian fluid having viscosity equal to the apparent blood viscosity in non-stenosed tubes of same diameter; similarly, the dashed line corresponds to a Newtonian fluid in the symmetric stenosis.

as β is reduced from 4 to 1. On the other hand, if the vessel diameter is significantly increased, e.g., $\gtrsim 300$ μm, the blood is known to behave as a Newtonian fluid, and hence, $\mu_{\rm rel}$ in that limit would be independent of the applied pressure gradient. Thus, for small to medium size arterioles, for which D is in the range of 15–100 μm, the apparent viscosity is dependent on the pressure gradient. Hence, there is no unique $\mu_{\rm rel}$ vs. D curve (i.e., the Fahraeus-Lindqvist curve) in this range of vessel diameter. Furthermore, since $\mu_{\rm rel}$ increases with decreasing pressure gradient, it is expected that the Newtonian limit of $\mu_{\rm rel}$ as $D \to \infty$ would be approached at a faster rate at lower pressure gradients than at higher pressure gradients.

The effect of β on $\mu_{\rm rel}$ is more enhanced in the stenosed vessels. In 84% stenosis, the apparent viscosity increases by 11% for $D = 11$ μm and 31% for $D = 25$ μm tube as β is reduced from 4 to 1. The increased influence of pressure gradient in the stenosed tubes also comes from the shear-thinning nature of blood: A reduced

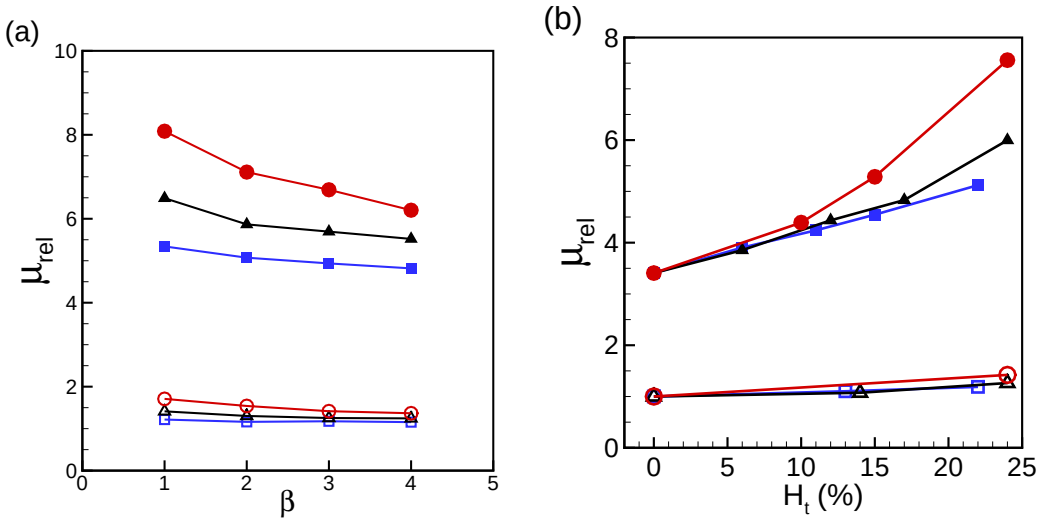

Figure 6.5: (a) Effect of mean pressure gradient β and (b) hematocrit H_t on the apparent viscosity for non-stenosed (continuous lines with unfilled symbols), and 84% stenosed tubes (continuous lines with filled symbols) for D = 11 (□), 17 (Δ), and 25 μm (◯). In (a) $H_t = 24\%$ is kept constant and β is varied; in (b) $\beta = 3$ is kept constant and H_t is varied.

flow rate in the stenosed tubes causes a reduction in the mean shear rate, and hence a decrease in μ_{rel}. In Figure 6.5(a), μ_{rel} is plotted against β for different vessels, which further illustrates the strong dependence of μ_{rel} on β for the stenosed tubes. The figure also shows that the influence of β on μ_{rel} increases with increasing D for both stenosed and non-stenosed vessels. Additionally, the figure shows that the slope of the curves decreases with increasing pressure gradient at a faster rate in larger vessels and with stenosis, as expected for a shear-thinning fluid and could be understood by considering the nature of RBC deformation. Since the volume and surface area of a cell remain constant, it can be deformed up to a certain limit. In the case of the smallest D, the cells are significantly deformed due to the geometric blockage even at the lower values of β. Increasing β for the smallest D does not significantly increase the amount of RBC deformation, and consequently, μ_{rel} reaches a saturation. For larger D, the intercellular space allows the suspension to compress

more with increasing β and, hence, allows a greater change in μ_{rel}. The saturation of μ_{rel} with increasing flow rate was also noted in [184] for RBCs flowing in capillary vessels.

Variation of μ_{rel} with hematocrit H_t is shown in Figure 6.5(b). In general, μ_{rel} increases with increasing H_t; however, the rate of increase is significantly higher for the stenosed vessels at larger diameter. As noted earlier in Figure 6.2, the RBCs flow in a single-file manner in the smallest stenosed tube. Here H_t can be increased only up to a certain limit, and increasing H_t does not alter the single-file motion. The thickness of the cell-free layer decreases by a lesser amount, and the fluid energy is spent to deform and move the increasing number of cells against the viscous force. For the larger vessels, increasing H_t causes a greater reduction in the CFL thickness. In addition, the RBCs crowd upstream the stenosis (Figure 6.2) further reducing the CFL, and, hence, rapidly increasing the flow resistance.

The Fahraeus effect is shown in Figure 6.6 where the ratio of the tube hematocrit to discharge hematocrit H_t/H_d is plotted against vessel diameter. The hematocrit ratio is computed as the ratio of the average blood velocity to the average RBC velocity. In general, H_t/H_d is reduced in presence of a stenosis compared to its values in non-stenosed vessels. The difference in H_t/H_d values in the stenosed and non-stenosed vessels is greater in smaller vessels due to the conversion of the multi-file motion to single-file motion as noted before in Figure 6.2. The difference decreases with increasing vessel diameter, as the multi-file motion of the RBCs is recovered in the stenosed vessels, and CFL is reduced due to cell crowding. Also interesting is to note the effect of the mean pressure gradient β on H_t/H_d. For the smallest vessel, the effect of β is less as the cells are maximally deformed by the geometric blockage

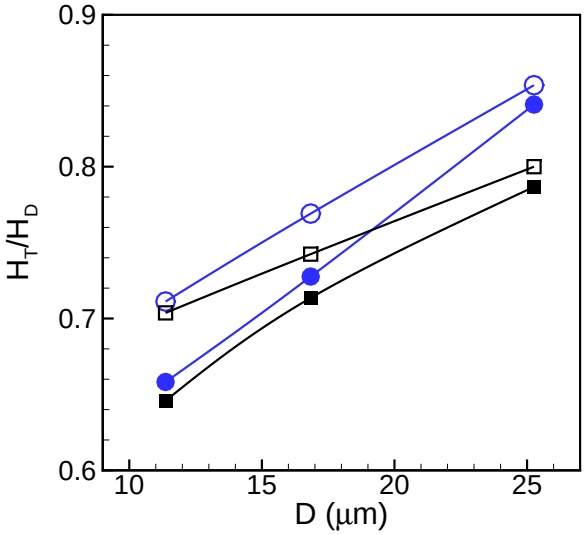

Figure 6.6: Comparison of the Fahraeus effect in 84% stenosed (filled symbols) and non-stenosed (unfilled symbols) vessels. Here hematocrit ratio H_t/H_D is shown as a function of tube diameter D for $\beta = 1$ (◯, blue), and 3 (□, black), for $H_t = 24\%$.

of the vascular wall. As the vessel diameter is increased, the multi-file motion is established and the intercellular space allows the suspension to be compressed more with increasing β leading to a reduction in the hematocrit ratio.

6.3.2 Asymmetry in the CFL and the Flow Characteristics

Quantitative results on the RBC spatial distribution and CFL thickness are shown in Figure 6.7 after averaging in time and azimuthal direction. The cell distribution is not symmetric up- and downstream the stenosis. For $D = 11$ μm, there exists a large cell-free layer upstream, the extent of which increases in radial direction with increasing pressure gradient. As noted previously in Figure 6.2, the RBCs flow in single file in $D = 11$ μm tube in presence of the stenosis. Immediately before entering the stenosis, a cell squeezes creating a wide CFL. Cell deformation increases with increasing pressure gradient, which in turn widens the CFL. As the cell squeezes out of the constriction, it bounces back to regain the parachute shape, thereby causing a

reduction in the CFL downstream, and an asymmetry in the cell distribution along the length of the stenosis. The nature of asymmetry is reversed in the $D = 25$ μm vessel where the upstream CFL is smaller than the downstream one due to cell crowding. The spatial variation of the CFL thickness in the stenosed and non-stenosed vessels is also presented in Figures 6.7(c), (f), and (i), which quantitatively show the asymmetry of the CFL thickness along the stenosis, and the reversal of the trend as the vessel diameter is increased. Here it can be noted that the CFL thickness increases ahead of the stenosis throat, but decreases significantly at the throat. Also shown in Figure 6.7(j) is the RBC distribution for an asymmetric stenosis. Here the CFL is observed to decrease near the vascular wall opposite to the stenosis, which also contributes to additional increase of μ_{rel} for asymmetrically stenosed vessels.

The variation of the CFL and cell distribution helps us to understand the enhancement of the Fahraeus-Lindqvist effect. The driving pressure gradient is spent on deforming and moving the cells against the fluid drag. For the stenosed vessels, a part of the external energy is spent on additional deformation that the cells experience as they squeeze through the stenosis. The reduced intercellular distance as multiple cells simultaneously squeeze through the stenosis also causes additional frictional loss. The CFL on the other hand provides a near-wall layer of a low viscosity fluid and alleviates the loss. For the smaller vessels, the large increase in CFL thickness observed upstream the constriction (Figures 6.7(c) and (f)) compensates for the decrease in the CFL at the throat. In contrast, such a compensating effect is not observed in the larger vessels, where, instead the upstream CFL is reduced due to cell crowding. As a result, the flow resistance increases at a greater rate as the vessel diameter increases, and a much higher slope is observed for the Fahraeus-Lindqvist curve for the stenosed

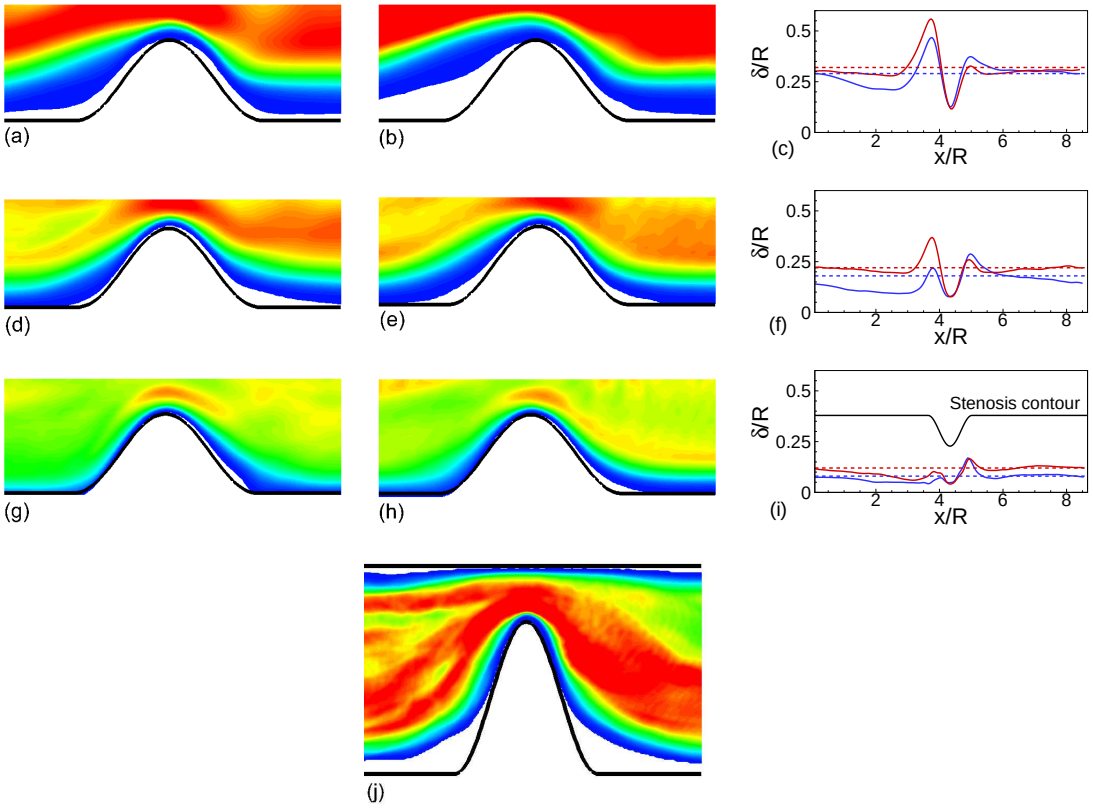

Figure 6.7: Time- and azimuthally-averaged RBC distribution at $\beta = 1$ (a,d,g) and 4 (b,e,h), and spatial variation of CFL thickness δ/R (c,f,i) for $D = 11$ μm (a,b,c), 17 μm (d,e,f), and 25 μm (g,h,i). (j) shows RBC distribution for an asymmetric stenosis. For the RBC distribution, contours are plotted from 0 (blue) to 0.5 (red) with 0.01 increment. For the CFL thickness, dotted lines are for non-stenosed vessels, continuous lines for stenosed vessels, $\beta = 1$ (blue) and 4 (red). Here $\mathcal{B} = 84\%$, and $H_t = 24\%$.

vessels than for the non-stenosed vessels as noted earlier in Figure 6.3.

The flow asymmetry up- and downstream the stenosis is also evident in average velocity profiles as shown in Figure 6.8. The well-known plug-flow profile is observed far up- and downstream the stenosed region (location I as marked in Figure 6.1). However, differences exist between up- and downstream velocity profiles (e.g., at locations II and VI in the figure) near the stenosed region. At similar distances from the throat, the downstream profile is flatter than the upstream profile due to the differences in the CFL thickness. It should be emphasized that the velocity asymmetry arises due to the presence of cells. If instead, the flow of a Newtonian fluid is considered, the velocity profiles up- and downstream would be symmetric as there is no inertia. The asymmetry in the velocity profiles also leads to an asymmetry in the average wall shear stress (WSS) up- and downstream in the vicinity of the stenosed region. At similar distances from the throat, downstream WSS is higher than upstream WSS. Higher velocity and reduced CFL result in a large WSS at the throat; conversely, a wider CFL around locations II and VI results in a region of low shear. The rapid variation of WSS over the stenosis length causes a large shear gradient. For the two larger diameters, the average WSS in the vicinity of the stenosis in presence of the RBCs is also less than that when pure plasma is considered. The reduction of WSS is more pronounced in case of an asymmetric stenosis. Such a low shear region and large shear gradients in the vicinity of the stenosis along with asymmetric WSS up- and downstream can have a significant physiological impact in terms of endothelial cell response and, hence, further growth of the plaque.

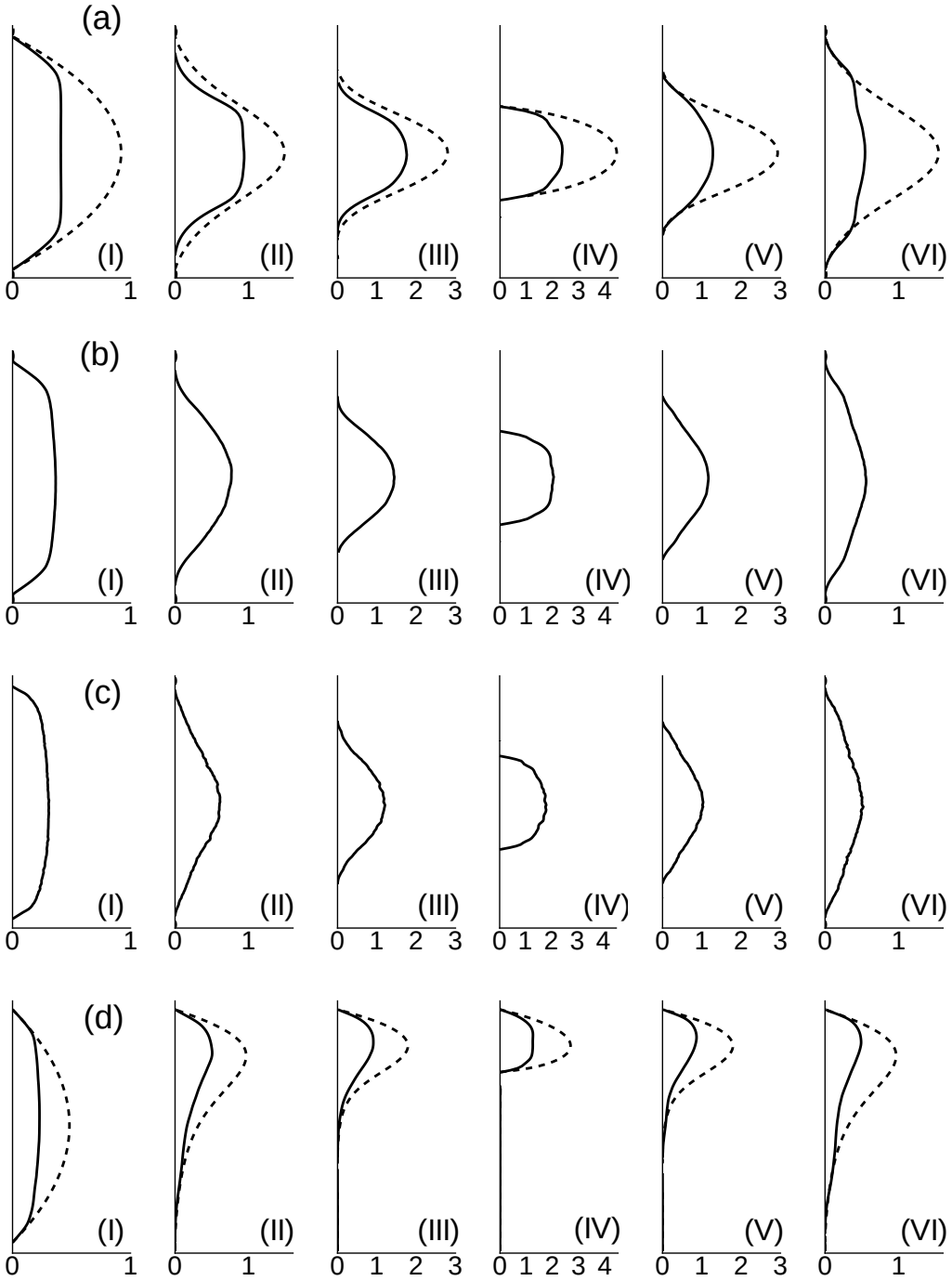

Figure 6.8: Average velocity profiles for symmetrically stenosed vessels (a,b,c) at different locations. $D = 11$ μm (a), 17 μm (b) and 25 μm (c). The dash line is the velocity profiles for pure plasma. (I) to (VI) correspond to different locations in the vessel as shown in Figure 6.1. Here $\mathcal{B} = 84\%$, $\beta = 1$, and $H_t = 24\%$. Results for the asymmetric vessel ($D = 17$ μm, $\beta = 3$) are shown in (d).

6.3.3 Temporal Variations in the Flow Characteristics

The asymmetry in velocity along the stenosis is even more pronounced if instantaneous velocity profiles are considered as shown in Figure 6.9. Surprisingly, a flow reversal upstream the stenosis is observed from time to time. In contrast, no flow reversal is observed downstream. Furthermore, no flow reversal occurs in absence of the RBCs. As shown in the figure, the reverse flow is highly transient and is observed at different azimuthal locations: At one instant a reverse flow is observed near the upper surface (Figure 6.9(a)), and at a later instant it is observed near the bottom surface (Figure 6.9(b)), while at other times it may not occur. Such transient flow reversals make the instantaneous WSS also highly fluctuating and, at times, negative, which in turn are known to play a significant physiological role in terms of endothelial cell response leading to further growth of the stenosis. Additionally, the flow reversal also causes an increase of the residence time of flowing platelets, WBCs, and macromolecules near the upstream section of the stenosis. It should be re-emphasized that the flow reversal is not observed in absence of the RBCs for the range of stenosis geometry considered here. The reverse flow occurs when cells squeeze through the stenosis displacing the near-wall fluid both up- and downstream. Additionally, cell jamming upstream the neck causes an instantaneous build-up of a high pressure and, hence, a local adverse pressure gradient leading to the observed flow reversal.

Time-dependent flow rates $Q(t)$ for representative simulations are shown in Figure 6.10(a) for stenosed and non-stenosed vessels. Flow rate oscillates in time for both cases; however, for the stenosed vessels oscillations have higher magnitude and they occur at higher frequencies. The rms (root-mean-square) of flow rate oscillations defined as $\left(\sqrt{\int_T (Q(t)-\overline{Q})^2 dt/T}\right)/\overline{Q}$, where $\overline{Q}$ is the mean flow rate, and T

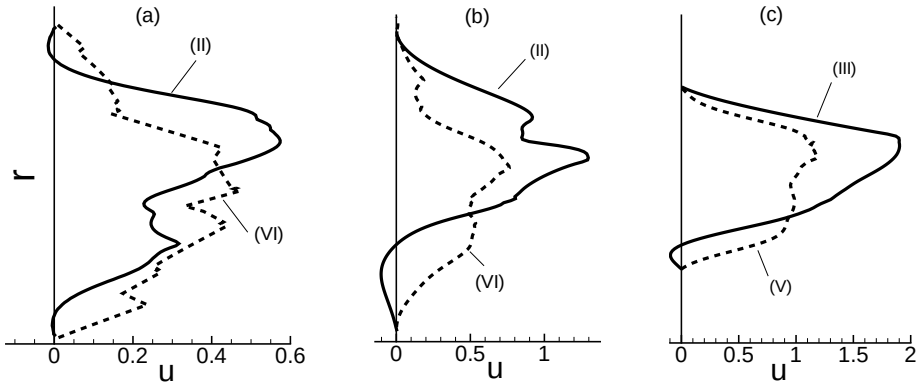

Figure 6.9: Upstream flow reversal in presence of RBCs: Shown here are instantaneous velocity profiles up- and downstream a symmetric stenosis ($D = 25$ μm, $\mathcal{B} = 84\%$, $\beta = 3$, $H_t = 24\%$). (a), (b) and (c) refer to three different time instants. Continuous lines represent upstream velocity profiles at locations (II) or (III) as indicated (see Figure 6.1 for locations), and dash lines represent downstream profiles at locations (V) or (VI).

is the averaging time window, is shown in Figure 6.10(b). The rms fluctuation could be one order of magnitude higher in the stenosed vessels than in the non-stenosed vessel. Also, it is interesting to note that the fluctuation intensity increases with decreasing pressure gradient as the cell motion transforms from a continuous to a more discrete flow. Fourier spectra of $Q(t)/\overline{Q}$ are plotted in Figure 6.10(c), which also shows that while for the non-stenosed vessels the fluctuation energy decays continually with increasing frequency, for the stenosed vessel the energy increases at intermediate frequencies before decaying at higher frequencies leading to nearly an order of magnitude higher amplitude of oscillations at moderate to high frequency range. It may be noted again that a steady flow is established in absence of the cells.

The oscillations in flow rate arises from the discrete nature of the cell motion though the stenosis. This is further illustrated in Figure 6.11 where a close-up of the cell motion is shown at two time instants corresponding to the local extrema

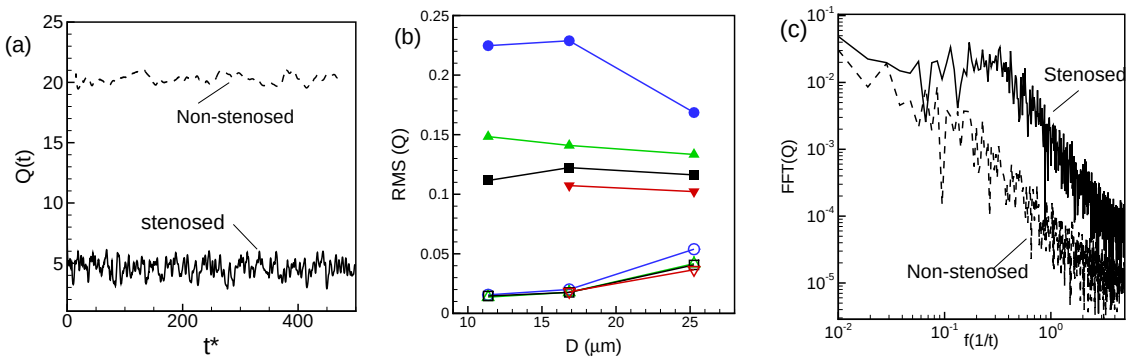

Figure 6.10: (a) Representative time-dependent flow rate $Q(t)$ in stenosed (——) and non-stenosed (- - - - -) vessels; (b) RMS of fluctuations of $Q(t)/\overline{Q}$ versus vessel diameter for $\beta = 1$ (◯), 2 (Δ), 3 (□), and 4 (∇); filled symbols are for stenosed vessels, and unfilled symbols for non-stenosed vessels. (c) Representative FFT of flow rate $Q(t)/\overline{Q}$ for stenosed (——) and non-stenosed (- - - - -) vessels.

of $Q(t)$. The flow rate reaches a local minimum when multiple cells simultaneously attempt to enter the throat thereby blocking the flow area. The instantaneous flow rate can be further reduced if there is a reverse flow as discussed before. A small region downstream the throat that is void of the RBCs is observed at this instant. As the cell cluster squeezes out of the throat, the flow rate increases. The flow oscillations become more regular (but still aperiodic) for the smallest diameter due to the single-file motion, but the overall picture remains the same, i.e., the flow rate drops momentarily just as a cell is about to squeeze through the neck, and increases as it bounces out.

As shown previously in Figure 6.10(a), flow oscillations also exist in non-stenosed vessels, albeit of much reduced magnitude, and for a different reason. The flow oscillations in the non-stenosed vessels is due to the formation of cell clusters as shown in Figures 6.11(d), (e), and (f). The fast moving cells near the center of the vessels push the slower moving cells further towards the wall reducing the thickness of the CFL and thereby reducing the flow rate momentarily.

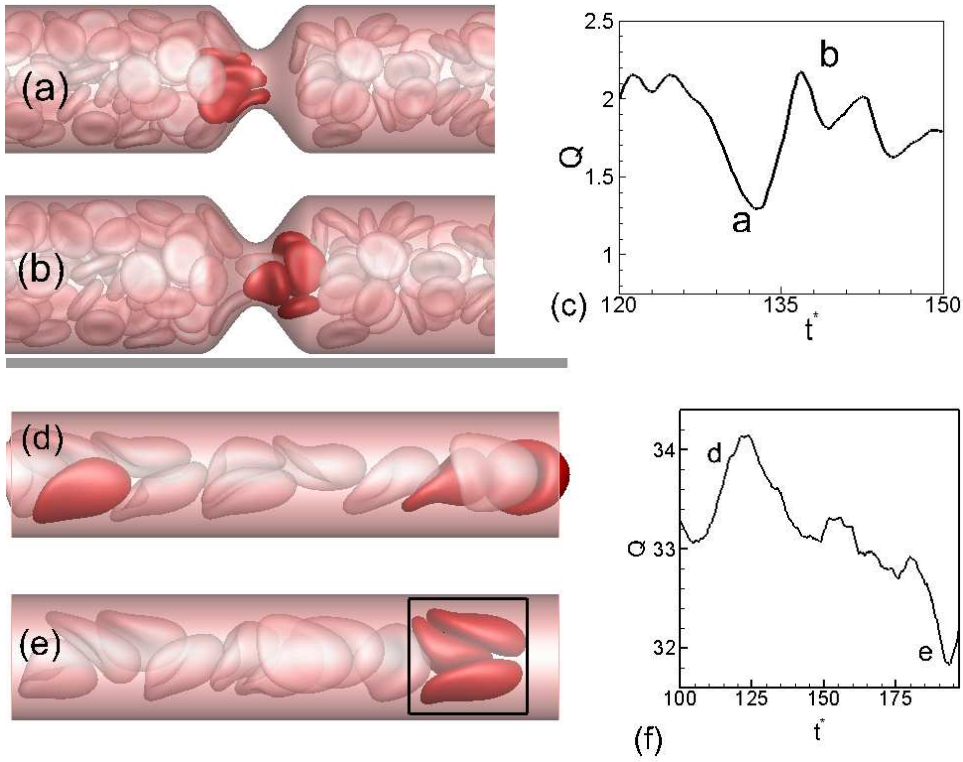

Figure 6.11: (a),(b) Cell distribution in the vicinity of the stenosis at two instances corresponding to local extrema in instantaneous flow rate $Q(t)$ shown in (c). (d), (e) and (f) are for a non-stenosed vessel where flow rates drop momentarily as the slower moving cells flowing near the wall are pushed further towards the wall by the faster moving cells flowing near the center, thereby reducing the CFL.

Further insights of the flow physics can be obtained by considering instantaneous Eulerian velocity at certain locations. Figure 6.12(a) shows the streamwise component of the Eulerian velocity at a fixed distance of 2.4 μm from the wall of the vessel, which is close to the edge of the CFL and at three different streamwise locations: one far upstream (location I as defined in Figure 6.1), at the beginning of the stenosis (location II), and end of stenosis (location VI). The velocity is scaled by the local time-averaged velocity $\overline{u_{\mathrm{E}}}$ as $u^*_{\mathrm{E}} = u_{\mathrm{E}}/\overline{u_{\mathrm{E}}}$. Of interest are the fluctuations in the Eulerian velocity. They are significantly high near the stenosis compared to those far upstream. Furthermore, close to the stenosis, the fluctuations at the upstream location II are higher than those at the downstream location VI, although both locations are at equal distance from the throat of the stenosis. Also note that the instantaneous velocity at location II becomes negative quite often, but that at location VI remains mostly positive, suggesting that frequent flow reversals occur immediate upstream while the flow remains unidirectional downstream. The RMS of fluctuations of u^*_{E} is shown in Figure 6.12(b) for the above three locations, and also for a far downstream location. The RMS at the far up- and downstream locations are nearly the same but significantly smaller than those in the vicinity of the stenosis. Additionally, the RMS obtained at location II is higher than that at location VI. The Fourier spectra of u^*_{E} for the three locations are shown in Figure 6.12(c). A continuous decay of u^*_{E} is observed far from the stenosis. In contrast, the spectra at locations II and VI show higher energy at intermediate to high frequency range. Between locations II and VI, the former shows higher energy than the latter at higher frequency range. These results further illustrate the role of the RBCs in creating the up- and downstream asymmetry along the length of the stenosis, which is not observed without

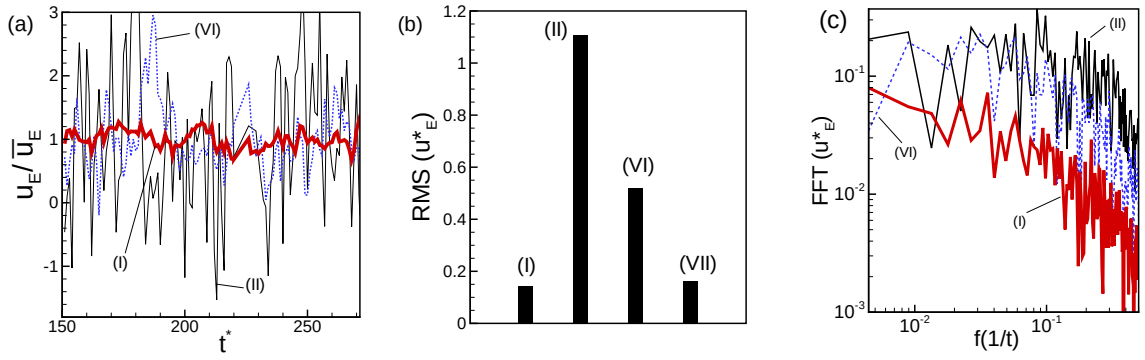

Figure 6.12: (a) Representative time-dependent Eulerian velocity u^*_E at a fixed distance of 2.4 μm (near the edge of the CFL) from the wall but at three different streamwise locations: At a location far upstream (red thick line, location (I) as defined in Figure 6.1), at the beginning of stenosis (black thin line, location II), and at the end of stenosis (blue dotted line, location VI). The Eulerian velocity has been scaled by the time-averaged velocity at the same location as $u^*_E = u_E/\overline{u_E}$. (b) RMS of fluctuations of u^*_E for the cases shown in (a). Also added is the RMS at a location far downstream marked as (VII). (c) Spectra of u^*_E for the three cases shown in (a). Here $D = 25$ μm, $\beta = 3$, and $H_t = 24\%$.

the cells. Additionally, these results further corroborate the previous observation that the presence of a stenosis increases the flow oscillations significantly over and above that in non-stenosed vessels.

6.4 Conclusion

A study of the flow of RBCs in stenosed microvessels representing small arterioles was presented in this chapter. The major finding of the study is that the Fahraeus-Lindqvist effect, which refers to an increase in apparent blood viscosity with increasing vessel diameter in the range ∼10–300 μm, is significantly enhanced due to the presence of a stenosis. Not only the apparent viscosity (μ_{rel}) of blood is observed to increase by several folds compared to that in non-stenosed vessels, the rate of increase of the apparent viscosity with increasing vessel diameter D is also higher than that in non-stenosed vessels. When an asymmetric stenosis is considered, the apparent viscosity

and the slope of the μ_{rel}-D curves increase even further. The apparent viscosity is observed to be more strongly dependent on the flow rate (or, the driving pressure gradient) in stenosed vessels, but weakly on non-stenosed vessels. The increase in μ_{rel} and the slope of the μ_{rel}-D curve is higher at low flow rates. Additionally, the Fahraeus effect, which refers to an increase in hematocrit with increasing vessel diameter, is also affected. The hematocrit is reduced in presence of a stenosis by a significant amount in smaller vessels and by a lesser amount in larger vessels.

The large increase in μ_{rel} in stenosed vessels cannot be predicted by using the apparent viscosity of blood in non-stenosed vessels of same nominal diameters. Furthermore, the shear-thinning models of blood, such as the Casson fluid model, are inapplicable as these models assume a uniform thickness of the cell-free layer along a vessel [81]. The present study shows that the CFL thickness greatly varies along the length of a stenosis, unlike in a non-stenosed vessel of uniform diameter where the thickness of the time-averaged CFL remains constant.

The distribution of the RBCs in stenosed vessels, in addition to their large deformation while moving through a stenosis, is observed to play a major role in the enhancement of the Fahraeus-Lindqvist and Fahraeus effects. The presence of a stenosis results in a geometric focusing [78], and, hence, an asymmetric distribution of the cells along the length of the stenosis. While the cell-free layer thickness is reduced significantly at the throat of a stenosis in all vessels, it is increased significantly but not equally immediate up- and downstream a stenosis. In smaller vessels, the presence of a stenosis converted the multi-file arrangement of the cells into a single-file arrangement. The cells squeeze before entering the stenosis, but bounce back upon

exit, leading to a higher CFL upstream than downstream. The increased CFL provides a wider low-shear region and partly compensates for the frictional loss at the throat. In contrast, in larger vessels, cells crowd upstream, and thereby significantly reduce the CFL thickness leading to a large increase in the apparent viscosity.

The up- and downstream asymmetry in the cell distribution also results in an asymmetry in average velocity and wall shear stress (WSS) along the length of a stenosis. The average velocity profiles downstream are flatter than those upstream. Consequently, the WSS upstream is less than that downstream. Furthermore, the WSS near the beginning and end of a stenosis is significantly below that observed far away from the stenosis, while it is several folds higher at the throat. As a result, a large WSS gradient is generated in the vicinity of the stenosis that is not identical up- and downstream. Note that the average velocity profiles and the WSS up- and downstream would be identical in absence of the cells since inertia is neglected.

The discrete motion of the cells through a stenosis causes large time-dependent fluctuations in flow properties. In particular, the rms of flow rate fluctuations in presence of a stenosis could be an order of magnitude higher than that in non-stenosed vessels. The flow rate drops when cells are about to enter the stenosis reducing the available flow area, and increases when they come out of the stenosis. In contrast, a steady flow is established in absence of the cells. Similarly, several folds increase in Eulerian velocity fluctuation is observed in the vicinity of the stenosis than that far away and also in non-stenosed vessels. Furthermore, the velocity fluctuation immediate upstream is much higher than that downstream. Surprisingly, a transient flow reversal is observed upstream a stenosis but not downstream. Such a flow reversal would not occur in absence of the cells.

The results presented here highlight the important role of cellular microstructure of blood in understanding fluid mechanics of microvascular stenosis, and the inapplicability of the two-phase flow models in predicting not only the time-dependent variations in flow quantities and their asymmetric distribution along the length of a stenosis, but also in average quantities, such as the apparent viscosity and hematocrit. The present findings are also physiologically important: A significantly elevated apparent viscosity and reduced hematocrit in stenosed vessels as predicted here imply a reduced tissue perfusion and oxygenation in downstream capillary vessels, a condition that is referred to as ischemia and that could lead to organ failure [68–74]. The elevated flow oscillations along with the transient flow reversal, and the reduced fluid velocity and WSS upstream the stenosis are likely to favor an increased residence time for platelets, WBCs, and macromolecules, and, hence, a greater likelihood of plaque growth upstream than downstream [89–94].

The present results can be further appreciated by putting them in perspective of macrovascular stenosis where blood behaves as a Newtonian fluid and the flow is inertia dominated. Under these conditions, a flow reversal which is often sustained for long time typically appears downstream the stenosis [11,64–67], as opposed to the upstream flow reversal observed here in microvascular stenosis. Thus, the growth and progression of the plaque are likely to occur in the downstream region in a macrovascular stenosis, but in the upstream region in a microvascular stenosis. Furthermore, the flow and WSS oscillations in the macrovascular stenosis arise mostly due to the pulsatile nature of blood flow and, to some extent, a weakly turbulent nature of the flow present at high inertia [11, 65–67]. In contrast, in case of microvascular stenosis, the oscillations arise entirely due to the discrete motion of the cells. While fluid

mechanics of the macrovascular stenosis has received attention for more than three decades, the paradigm is now shifting towards microvascular disease which is thought to progress in a 'silent' manner. The present study apparently is the first one to consider the cellular blood flow in microvascular stenosis.

Chapter 7

Adhesion of microparticles in microvessels – role of RBCs and microparticle deformability

7.1 Introduction

As mentioned in Chapter 1, one of the most common ways in drug administration for disease treatment is intravascular delivery. Targeted delivery of drug to the site of disease is desired in order to reduce the adverse effects on healthy tissues while imparting the maximum lethality to the diseased cells. Drug molecules are generally encapsulated in nano-/micron-sized drug carrier particles decorated with receptor molecules that can bind to the ligand molecules expressed on targeted cells. Significant research efforts have been directed in recent years towards optimization of the chemical and physical properties of vascular drug carriers. Similarly, particles carrying contrast agents for biomedical imaging have been subjected to research studies (see Chapters 1 and 5).

As discussed in details in Chapter 5, there is a significant effect of particle geometrical properties, namely size and shape, on their adhesion propensities, which has been recognized through numerous experimental studies [43–51, 55–60]. These studies have established the essential effects of RBCs as well as particle geometry on their adhesion efficiency. It is known that due to collisions with RBCs, microparticles marginate towards the wall and into the CFL [23, 24, 159]. Inside the CFL,

further interactions with RBCs bring the microparticles closer to the wall, where binding reaction between adhesion molecules results in the capture of particles on the endothelium [28, 29]. It has also been shown that asphericity enhances particle adhesion by increasing the surface area exposed to the vessel wall [54–57, 60]. Following adhesion, particles start adhesive rolling on the vessel wall.

The aforementioned studies are focused on rigid particles. Utilization of deformable carrier particles such as capsules and vesicles (liposomes) is also common, and has been suggested to improve targeting properties [95, 96]. However, most of the studies on adhesion of deformable particles are solely limited to white blood cells (WBCs) [97–106, 113–121]. These studies have shown a number of observations similar to that of adhesion of rigid particles. For instance, experiments by Abbit and Nash [104] showed that RBCs enhance WBC adhesion by causing margination, WBC wall-contact, and formation of initial adhesive bonds. The results of an in-vivo study by Melder et al. [120] confirmed that RBCs increase the number of adhering and rolling WBCs in the range of physiological shear rate. Munn et al. [120] demonstrated that the presence of RBCs increases the WBC–wall collision and binding frequencies. Bagge et al. [188] observed that in the absence RBCs, WBC adhesion to post-capillary venules does not occur.

Several important observations that are specific to WBCs because of their deformability have also been obtained through previous studies. For example, Subramaniam et al. [98] hypothesized that WBC recruitment is enhanced due to deformation and consequent increase in surface area of adhesion. Yago et al. [123] showed that deformability of WBCs causes the adhesive rolling velocity to decrease, and that it increases the resistance against detachment that occurs due to wall shear stress.

Firrell and Lipowsky [122] suggested that the rolling velocity of WBC is insensitive to shear because of the increased WBC deformation at elevated shear which results in an increased surface area of adhesion. Similarly, a theoretical model proposed by Lei et al. [124] predicted that WBC rolling velocity versus shear stress reaches a plateau as the shear increases.

The above studies indicate the importance of deformability in particle adhesive rolling motion. The effect of particle deformation on its wall-contact and initial formation of adhesive bonds is also of great importance. As mentioned in Chapter 1, a deformable microparticle in shear flow in close proximity of the wall experiences a driving force towards the vessel centerline [5]. Such deformation-induced lift, which is dependent on particle size and deformability as well as the shear rate, could potentially resist against RBC-induced microparticle adhesion. In close proximity of the vessel wall, larger particles experience a larger lift in shear flow [189]. Also, an increase in the shear rate or particle deformability results in an increase in particle deformation, and consequently the lift. Collision with RBCs is required to overcome the lift so that the microparticle wall-contact and then the adhesion takes place. Therefore, the RBC hematocrit is also of great importance. Each of the parameters mentioned, vary significantly in different physiological/pathological conditions and biomedical applications. The effect of each parameter on the RBC-induced microparticle adhesion is of great interest. However, as mentioned earlier, most of the relevant studies in this regard are limited to WBCs, in which the size effect is not considered. Furthermore, the aforementioned studies are mostly focused on adhesive rolling rather than the effect of RBCs on particle wall-contact and formation of initial adhesive bonds.

Besides, the majority of the in-vitro experimental studies on adhesion use parallel-plate channel flow setup to collect the data. Although extensive insight and information have been provided through these studies, several limitations motivate further investigation.

Firstly, in most of the experiments, the number of particles adhered to the flow chamber walls are used to measure adhesion efficiency, margination propensity and diffusivity at the same time. However, as was shown in Chapter 5, each of these processes can be differently affected by the properties of cellular/particulate components.

Secondly, a parallel-plate setup can model hemodynamics in larger microvessels where the cell/particle size is negligible against the vessel wall curvature. The applicability to smaller vessels such as capillaries and small arterioles, though, is limited since the effect of tubular geometry and significant wall confinement is partly neglected. The importance of such a limitation is understood by considering the targeting of tumor cells. Tumor microvasculature consists of numerous branching microvessels with an average diameter of 10 μm [125]. This is despite the fact that the channel height in experiments generally ranges between few hundreds of micrometers [55–57, 59, 104, 120]. The confined geometry of small arterioles and capillaries is expected to affect the microparticle deformation and consequently the RBC-induced adhesion and the following adhesive rolling. In this regard, the results of a computational study by Khismatullin and Truskey showed that a decrease in channel height results in an increase in the contact area of adhesion, and suggested that chamber studies underestimate WBC adhesion in microcirculation [103].

Thirdly, experimental observation of individual cell-cell/cell-particles interaction is a very difficult task. Such observation is, however, necessary in many cases to

confirm the hypotheses that are based on experimental results on the collective behavior of cells/particles. For instance, a study on adhesion of rigid microparticles by Namdee et al. [56] demonstrated an interesting biphasic behavior in dependence of particle adhesion propensity on RBC hematocrit. The authors hypothesized that as the CFL thickness is decreased (with an increase in hematocrit) to values less than the particle size, particle adhesion is reduced due to their negative collisions with RBCs. The nature of such negative collisions is, however, unclear as the experimental observation of RBC-particle interactions during wall-contact and the following adhesive rolling encounters technical complications.

The above discussion suggests that high-fidelity computer simulations could be used as a potential alternative approach. Few computational studies on WBCs in which hydrodynamic cellular interactions are simulated in micro-tubular geometry can be found in the literature. For instance, Fedosov and Gompper [126, 127] showed that efficient WBC margination is found in an intermediate range of hematocrit and relatively low flow rates. Isfahani and Freund [77] demonstrated a significant augmentation of streamwise forces imparted by RBCs on a wall-bound WBC model. They also showed a considerable dependence of those forces on hematocrit and WBC shape. In the above two studies, however, the deformability of WBC was neglected. In a more recent study by Takeishi et al. [121], WBC deformability has been taken into consideration and shown to be of great importance at higher shear rates corresponding to arterioles. In this work, it is demonstrated that at high shear rates, the WBC–wall separation becomes significant due to WBC deformation. Therefore, WBCs would not adhere to the vessel wall at such high shear; despite they move in close proximity of the wall due to interactions with RBCs. It should be noted that

the adhesive interactions between receptor/ligand molecules was not considered in any of the mentioned computational works.

Evidently, in order to improve our understanding of microparticles adhesion in microcirculation, a computational study that integrates the confined tubular geometry of microvessels, the microscale hydrodynamic interactions between cellular/particulate components, and the nanoscale reactions between the adhesion molecules into one model is needed.

To that end, in this chapter, we use our three-dimensional multiscale multiphysics model to study the adhesion of microparticles in microvessels. We focus on the hydrodynamic interactions between RBCs and microparticles during the formation of initial adhesive bonds, and thereafter during adhesive motion of the microparticle on the vessel wall. The effects of microparticle size and deformability, as well microvessel diameter, hematocrit, and pseudo-shear rate on such interactions are studied in a quantitative manner. The results of this study show that the interaction between RBCs and microparticles is highly dependent on particle size and deformability, as well as microvessel pseudo-shear and diameter. Therefore, it is suggested that in order to efficiently benefit from the superior properties of deformable particles in adhesive rolling, the particle size and deformability should be chosen based on the local hemorheological conditions of targeted site.

7.2 Problem Setup

The adhesion of deformable and rigid spherical microparticles is simulated in the flow of RBC suspension inside microvessels. The particle diameter considered here ranges from 2 to 14 μm. The RBC hematocrit varies between $H_t \approx 0$ – 23%. The particle

deformability spans from perfectly rigid particles to deformable capsules with shear moduli ranging from 2.5×10^{-8} to 8.3×10^{-7} N/m. The deformable particles under consideration do not have bending rigidity. The RBC membrane shear modulus and bending stiffness used in the simulations are 2.5×10^{-6} N/m, and $6{\times}10^{-19}$ J, respectively. Similar to RBCs, our deformable microparticles resist against area dilatation in such a way that the change in their total surface area remains less than 1%. The surface of microparticles and RBCs are discretized using 5120, and 20480 triangular elements, respectively (or, 2562, and 10242 Lagrangian nodes).

The flow is pressure driven, and governed by the Stokes equation. The vascular segment length is $L = 4D_T$, where D_T is the vessel diameter. More details on the computational domain and boundary conditions are given in Chapter 2. The microvessel diameters considered here are 8, 11, 14 and 17 μm, and the Eulerian resolution used are $240 \times 60 \times 60$, $320 \times 80 \times 80$, $400 \times 100 \times 100$, and $480 \times 120 \times 120$, respectively. The relevant parameters are the vessel diameter D_T, the particle diameter D_P, the volume fraction or hematocrit of the RBCs H_t, the capillary number of deformable microparticles defined as $Ca_P = \mu_o U_c / G_{s,P}$, and that of RBCs defined as $Ca_R = \mu_o U_c / G_{s,R}$, where $G_{s,R}$ and $G_{s,P}$ are the shear elastic moduli of RBCs and microparticles, respectively; μ_o is the plasma viscosity, and U_c is an arbitrary characteristic velocity. The driving mean pressure gradient is defined in dimensionless form as $\beta = -\left(d\overline{P}/dx\right) / \left(16\mu_o U_c / D_T^2\right)$. Such pressure gradient is applied along the microvessel length in x-direction (see Chapter 2). The number of microparticles and RBCs ranges from 1 to 3, and 4 to 40, respectively, depending on the microvessel size and hematocrit. The mean pressure gradient β ranges from 3 to 5. The pseudo-shear rate can be defined as the average flow velocity (flow rate divided by microvessel cross

Table 7.1: Adhesion parameter values used in the simulations [148–150].

Parameter	**Value**	**Units**
Bond free length (λ)	600	nm
Spring constant (k_0)	5	pN/nm
Reactive compliance (r_0)	0.73	nm
Reverse reaction constant (k_r^0)	0.12	s^{-1}
Receptor density (on particle)	1.207	num. of molec./μm^2
Ligand density (on vessel wall)	10.866	num. of molec./μm^2

section area) divided by D_T. The flow rate is determined by RBC capillary number, Ca_R, and the mean pressure gradient, β. Most of the simulations were performed at $Ca_R = 0.3$, $\beta = 4$, $H_t = 23\%$, and in case of deformable microparticles, at shear modulus of 2.5×10^{-8} N/m; therefore, unless indicated explicitly, these values hold for the results presented in this chapter. The adhesion parameters used in the simulations are listed in Table 7.1 (see Chapter 2 for definition of each parameter). The values for adhesion parameters can vary significantly for different adhesion molecules. Representative values determined from experiments as well as range of values for different cells and receptor-ligand pairs are found in [148–150]. The typical values in those ranges were used for the adhesion parameters presented in Table 7.1.

The problem setup for two representative simulations can be seen in Figure 7.1. The focus of this chapter is mainly the adhesion of microparticles rather than their margination.

7.3 Results

The results are presented in the following two sections. In the first section, the role of RBCs on microparticles wall-contact and formation of initial adhesive bonds is studied. Effects of RBCs on adhesive rolling of microparticles on the vessel wall,

which is followed by wall-contact, is the subject of the second section.

7.3.1 RBC-Induced Microparticle Adhesion

Figure 7.1 shows snapshots of the instantaneous flow configuration for two representative simulations. Several observations, general to our simulations, are noticed. Similar to what observed in Chapters 3 and 4, it is seen that the RBCs often flow in clusters, in which they are laterally stacked. Since there is no adhesion potential for RBCs in our model, the clusters are short-lived, and form and break solely due to hydrodynamic interactions. Figure 7.1(a-c) shows the motion of deformable $D_P = 6$ μm particles in a $D_T = 17$ μm microvessel. It is observed that due to interactions with an RBC cluster, the microparticle is pushed towards the wall into the adhesion region (600 nm from the vessel wall), where it initiates bond formation and tethers to the vessel wall. Motion of a similar microparticle in absence of RBCs is demonstrated in Figure 7.1(d). It is observed that without interactions with RBCs, the microparticle moves away from the wall and towards the vessel centerline. As mentioned in Chapter 1, such motion is a result of particle asymmetric deformation and the consequent lift imparted on it [5]. The trajectories of sample particles (deformable and rigid) in presence and absence of RBCs are compared in Figure 7.1(h). In this figure, the radial location of the particle centroid is denoted by r. As shown by the black lines, in a cell-free flow, due to absence of any radial force imparted on the microparticle towards the wall, the adhesion does not occur. However, as demonstrated by the red lines, due to interactions with RBCs, the microparticle is adhered to the wall in presence of RBCs.

The above observation indicates that RBCs induce microparticle adhesion to vessel

walls: through hydrodynamic interaction between RBC clusters and microparticle, it is displaced towards the wall into the adhesion region where it forms initial adhesive bonds.

Our results also demonstrate that the RBC-induced adhesion does not necessarily occur for all of the microparticles under consideration. The motion of a deformable $D_P = 10$ μm particle in a $D_T = 14$ μm microvessel is demonstrated in Figure 7.1(e-g). The result of this simulation demonstrated that despite interactions with RBCs, the microparticle does not adhere to the wall. Our results show that RBC-induced microparticle adhesion is dependent on the microparticle size.

Comparing the snapshots shown in Figure 7.1(e-g) with the ones in Figure 7.1(a-c), shows a major difference in terms of RBC–microparticle hydrodynamic interactions between the two adhering and non-adhering cases. In the adhering case, the approaching RBCs pass over the microparticle and displace it towards the wall. This kind of interaction has been reported in the literature for WBC adhesion [121,190]. However, in the non-adhering case, as shown for a sample simulation in Figure 7.1(e-g), the approaching RBCs deform and move away from the microparticle. Such interaction, along with the near-wall deformation that is observed in the microparticle membrane, explain the size dependency of RBC-induced adhesion: deformation of the particle in close proximity of the wall forms a wedge-like gap that keeps the particle surface outside the adhesion region (see Figure 7.1(e)). Passing motion of the RBCs creates a radial force that pushes the particle towards the wall and reduces that gap. Once the gap thickness becomes less than adhesive bond free length, the microparticle surface forms bonds with the wall and adheres. Geometrical blockage of large particles, as shown in Figure 7.1(e-g), prevents the passing motion of RBCs, and consequently

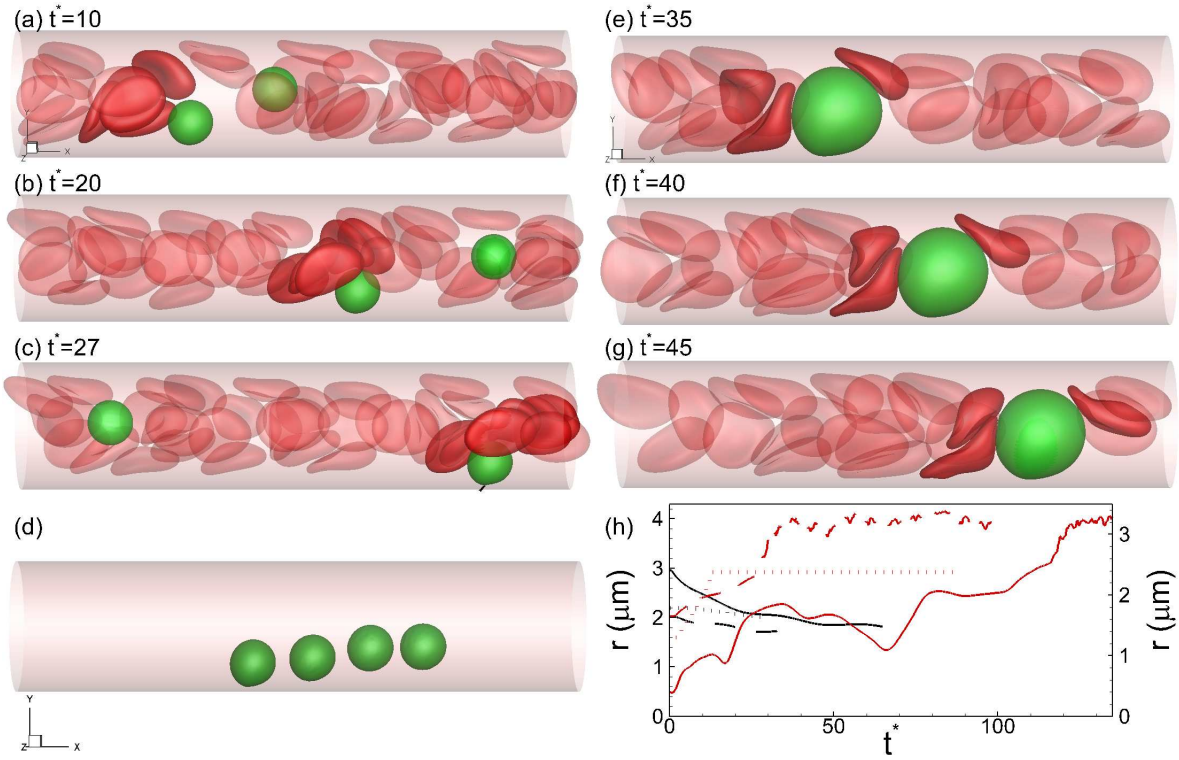

Figure 7.1: (a-c) Representative snapshots showing instantaneous configuration of RBCs (colored red) and $D_P = 6$ μm deformable particles (colored green) in a $D_T = 17$ μm microvessel; (d) lateral migration of the same particle in absence of RBCs (particle is shown at $t^* = 2$, 8, 14, and 19); (e-g) snapshots showing flow configuration in a simulation with $D_P = 10$ μm and $D_T = 14$ μm; (h) Representative trajectories of particle centroid in presence (red lines) and absence (black lines) of RBCs: solid lines show the case in which $D_P = 7$ μm (deformable) and $D_T = 14$ μm (left y-axis), dashed lines show $D_P = 6$ μm (deformable) and $D_T = 11$ μm (right y-axis), and dotted lines show $D_P = 6$ μm (rigid) and $D_T = 11$ μm (right y-axis).

microparticle adhesion to the wall.

The passing motion of RBCs is facilitated by the separation space provided between the microparticle surface and the vessel wall. That separation is determined by the particle size and the vessel diameter. Therefore, the RBC-induced adhesion depends on size effects, in the sense that it occurs only when the diameter difference between the microvessel and the particle provides large enough space for the passing motion of RBCs. Figure 7.2 shows the effects of particle and microvessel size on RBC-induced adhesion of deformable microparticles. Each data point is corresponding to

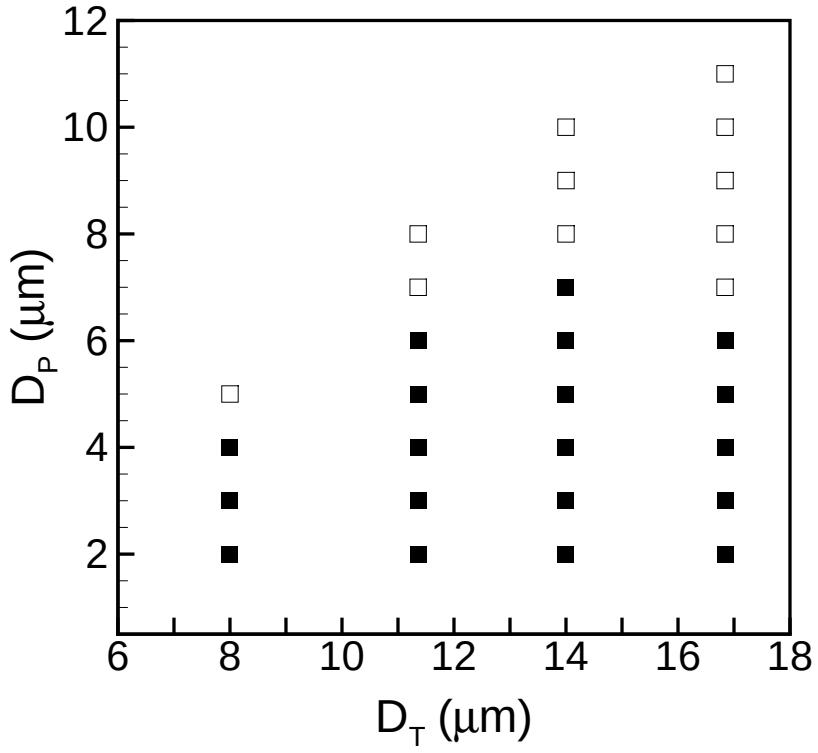

Figure 7.2: Deformable microparticle adhesion map as a function of particle size and vessel diameter. Filled squares indicate the cases in which the particle adheres to the wall and empty ones indicate the non-adhering cases. The results remains the same at $H_t = 11$ and 17% for $D_T = 11$ and 14 μm.

a simulation. Filled and empty symbols indicate the occurrence of adhering and non-adhering cases, respectively. It is observed that at each vessel diameter, there exists a maximum size for deformable particles above which the RBC-induced adhesion does not take place. The maximum size is defined as the 'critical particle diameter', and denoted by $D_{P,crit}$.

Interestingly, our results show that the critical particle size is non-existent for perfectly rigid particles. All of the diameters considered for rigid particles resulted in RBC-induced adhesion, and no non-adhering cases were observed. To explain this behavior, interactions of a non-adhering deformable particle and an adhering rigid particle of the same size with RBCs are compared in Figure 7.3. This figure shows

such comparison between a $D_P = 7$ μm deformable (Figure 7.3(a-b)) and rigid (Figure 7.3(d-e)) microparticle in a $D_T = 11$ μm microvessel.

Figure 7.3(a-b) shows that despite the interactions with RBCs, which keep the microparticle close to the vessel wall, the deformable particle is not adhered. As explained earlier, this is because of the formation of a near-wall gap as a result of microparticle membrane deformation, together with the inhibition of RBC passing motion due to geometrical blockage. However, as demonstrated in Figure 7.3(d-e), the absence of such a near-wall gap in case of a perfectly rigid particle leads to its adhesion to the wall even without the passing motion of the RBC. Figure 7.3(f) compares the membrane configuration of the rigid and deformable microparticle. It is observed that the increased separation distance between the particle surface and the vessel wall prevents the adhesion of the deformable microparticle. Figure 7.3(h) shows sample trajectories of deformable and rigid microparticles of the same size. Variations in the radial position of the particle centroid is shown in this plot. It is seen that while rigid microparticles eventually adhere to the wall, deformable ones exhibit an irregular oscillatory motion towards and away from the wall. Those fluctuations are due to the balance between lift and hydrodynamic interactions with RBCs. The former drives the particle away from the wall, and the latter brings it towards the wall.

Another important observation in Figure 7.2 is the biphasic dependence of $D_{P,crit}$ on D_T. As the vessel diameter is increased from 8 to 14 μm, $D_{P,crit}$ is increased. Then, with an increase in D_T from 14 to 17 μm, the value of $D_{P,crit}$ is reduced. The initial increasing trend is explained by the geometrical blockage created by the large

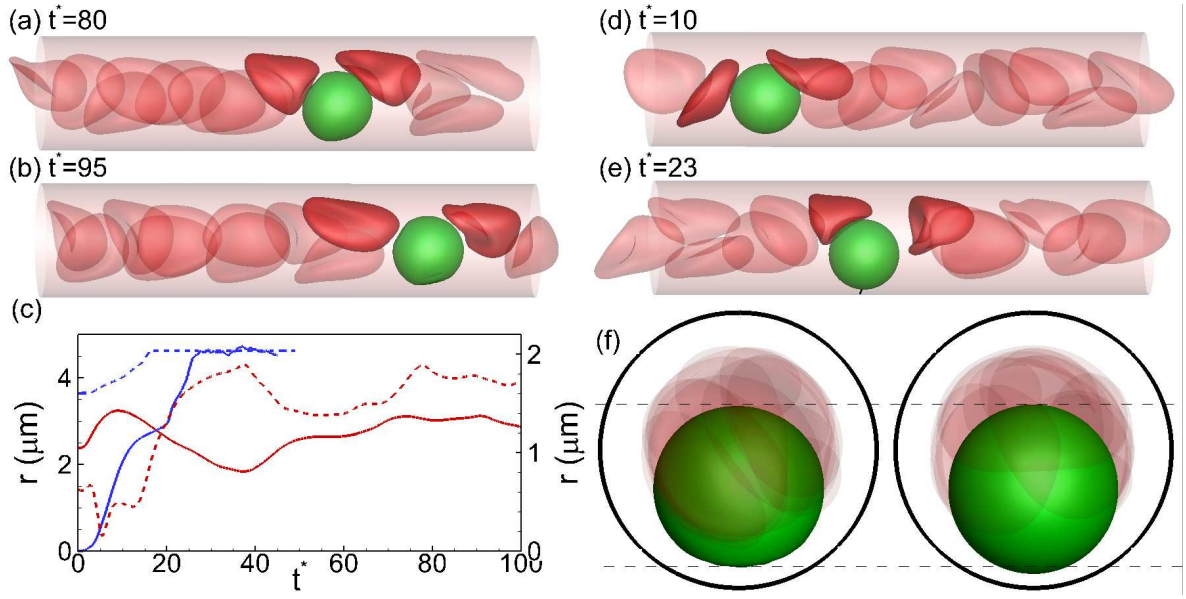

Figure 7.3: Representative snapshots showing instantaneous flow configuration for a deformable $D_P = 7$ μm microparticle (a-b) and a rigid particle of the same size (d-e) in a $D_T = 11$ μm microvessel; (c) deformable (red line) and rigid (blue line) microparticle centroid trajectory for $D_P = 7$ μm and $D_T = 11$ μm (solid lines - right y-axis), and $D_P = 7$ μm and $D_T = 17$ μm (dashed line - left y-axis); (h) particle membrane near the wall in case of a rigid and a deformable $D_P = 7$ μm microparticle in a $D_T = 11$ μm microvessel

microparticles. In a larger vessel, a larger particle is required to inhibit the passing motion of RBCs. Therefore, $D_{P,crit}$ increases with D_T. However, the reduction observed in $D_{P,crit}$ from $D_T = 14$ to 17 μm, seems surprising. Besides, the results presented in Figure 7.2 indicate that the value of $D_{P,crit}$ is generally smaller than what is predicted by the size of the separation space provided between the particle surface and the wall for RBC passage (which is approximately equal to the thickness of an RBC subtracted from D_T) For instance, Figure 7.2 shows that a 7 μm microparticle does not adhere to the vessel walls in a 17 μm microvessel, although enough space exists for the RBCs passing motion. Comparing the hydrodynamic interactions between the RBC clusters and adhering and non-adhering microparticles of the same size in two different microvessels explains the reason. Figure 7.4 shows such interactions for $D_P = 7$ μm and $D_T = 14$ and 17 μm.

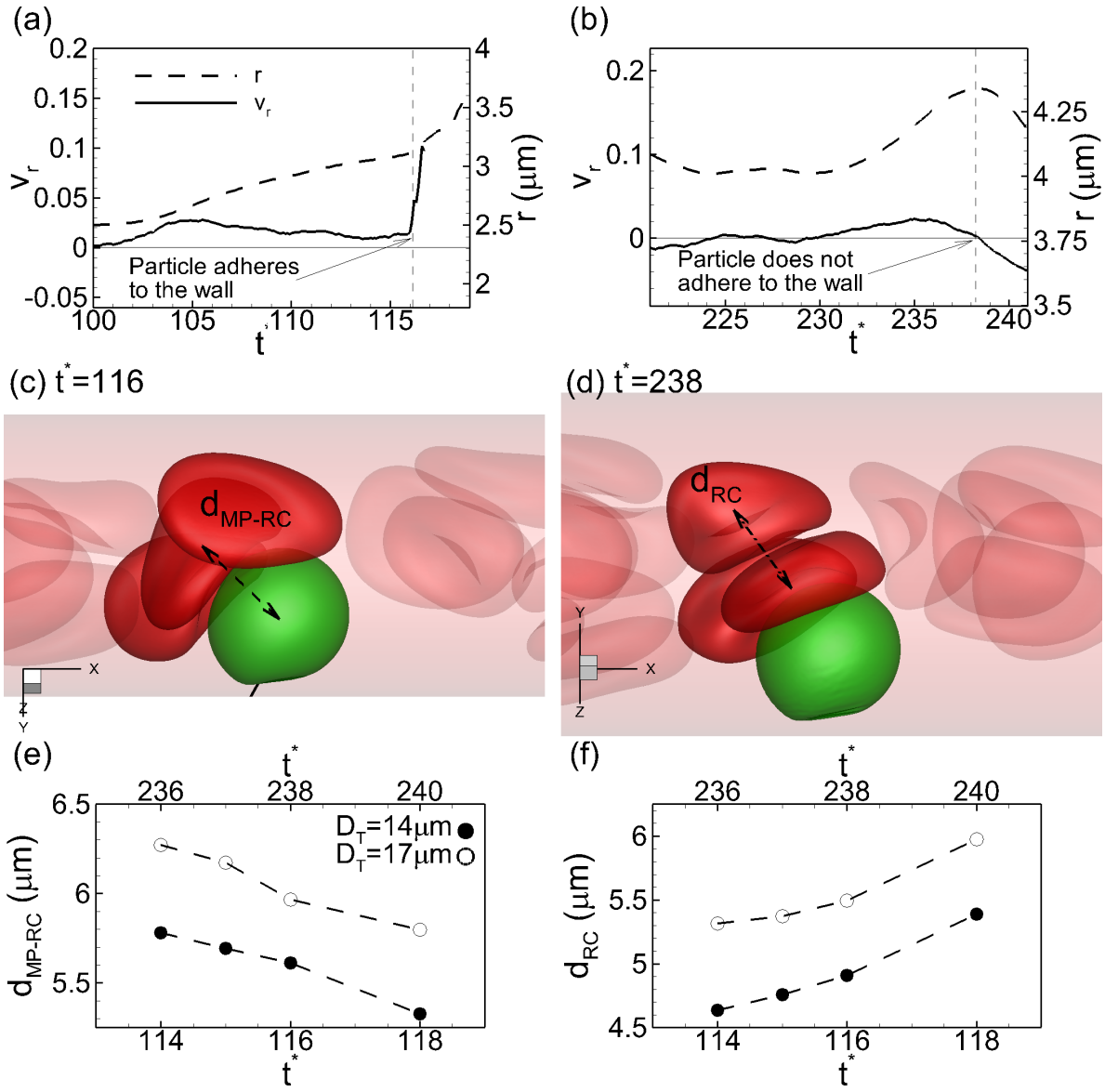

Figure 7.4: Deformable particle dynamics in close proximity of adhesion region in case of $D_P = 7$ μm, and $D_T = 14$ μm (a), and $D_T = 17$ μm (b). v_r denotes the radial velocity of particle centroid towards the wall, and r denotes the centroid radial position. The vertical dashed line shows the instant prior to adhesion in case (a), and the instant in which the particle is closet to wall in case (b); flow configuration in case (a) at $t^* \sim 116$ and in case (b) at $t^* \sim 238$ are shown in (c) and (d), respectively; temporal variations in average microparticle-RBC cluster distance (e) and average RBC-RBC distance in the cluster (f) for the cases presented in (a) and (b).

The trajectory of particle centroid is shown by dashed lines for the two cases in Figure 7.4(a-b). It is observed that in case of $D_T = 14$ μm, once the particle comes in close proximity of the wall (vertical line at $t^* \sim 116$ in Figure 7.4(a)), it adheres. This is seen by the solid line in Figure 7.4(a), which shows the radial velocity of the particle centroid towards the wall, v_r. The value of v_r rises significantly following $t^* \sim 116$, as the initial adhesive bonds are formed and the particle is pulled further towards the wall. However, Figure 7.4(b) shows that in case of $D_T = 17$ μm, once the particle radial position reaches its maximum (vertical line at $t^* \sim 238$), i.e. the separation distance between the particle and the wall becomes minimum, it does not adhere; instead, it starts moving away from the wall. This is seen as a significant decrease in the values of r and v_r in Figure 7.4(b) following $t^* \sim 238$. Note that the hematocrit in both cases is same ($H_t = 23\%$).

The flow configuration in the above two cases is shown in Figure 7.4(c-d). Figure 7.4(c) corresponds to $t^* \sim 116$ in Figure 7.4(a), and Figure 7.4(d) corresponds to $t^* \sim 238$ in Figure 7.4(b). The RBC clusters interacting with the microparticle are shown in these figures. The clusters are identified based on the surface-to-surface distance between the RBCs that are in contact with the microparticle. Due to formation of a lubrication layer between the particulate components in our model, such distance does not become less than 4 Eulerian grid points, which corresponds to about 600 nanometers. This value is used as a criterion to identify the RBC clusters. Figure 7.4(c-d) also schematically demonstrates two lengthscales that we defined to study the differences between the two clusters in the adhering and non-adhering cases under consideration. The average of center-to-center distances between each RBC in the cluster and the microparticle is denoted by d_{MP-RC}; and the average center-to-center

distance between the RBCs themselves is denoted by d_{RC}. Figure 7.4(e-f) compares the variations of these parameters in the vicinity of time instants shown in Figure 7.4(c-d). It is observed that over the time interval under consideration, both parameters exhibit lower values in the adhering case ($D_T = 14$ μm) in comparison with the non-adhering case ($D_T = 17$ μm). This shows that the RBC cluster that is interacting with the microparticle when it is closest to the wall, is denser in the $D_T = 14$ μm microvessel than the one in the $D_T = 17$ μm microvessel (see Figure 7.4(f)). It also shows that the RBCs are generally closer to the microparticle in the case in which RBC-induced adhesion occurs (see Figure 7.4(e)).

The above observations indicate that the RBC-induced adhesion of microparticle to vessel wall depends on the formation of dense RBC clusters that impart large radial forces on the microparticle towards the wall. Similar values in variations of d_{MP-RC} and d_{RC} are obtained in other instants when the particle comes closest to the wall but does not adhere. Hence, it is hypothesized that not only the passing motion of RBCs is required for the RBC-induced adhesion of microparticles, but the formation of dense enough RBC cluster is also needed to impart large enough radial force towards the wall during the passing motion. In smaller vessels, transverse movement of RBCs past one another during the intrection between the RBC cluster and the microparticle is more difficult due to microvessel confinement effects. Therefore, the RBC cluster is dense and exerts a large force on the microparticle towards the wall. On the other hand, in larger vessels such transverse motion is easier, which in turn makes the RBC-induced microparticle adhesion less likely.

The above observation also indicates the potential enhancing role of RBC aggregation (formation of rouleaux) on adhesion of deformable microparticles. Several studies have shown the enhancing effect of RBC aggregation on WBC adhesion [99–101, 104, 126, 127, 176, 177, 190, 191].

So far it has been established that the RBCs induce microparticles adhesion to the vessel wall; and that such RBC-induced adhesion is strongly affected by particle deformability: while perfectly rigid particles of any size are adhered to the wall due to interactions with RBCs, the adhesion of deformable particles depends on the passing motion of RBCs as well as the formation of dense RBC clusters. Both of the mechanisms mentioned were shown to be dependent on size effects, i.e. the diameter of microparticle against the one of microvessel. The importance of the passing motion of RBCs has been mentioned in a recent computational study by Takeishi et al. [121] on WBC margination in arteriolar shear rates. In what follows, the effect of RBC hematocrit, particle deformability, and microvessel pseudo-shear rate is discussed.

As it is shown in Figure 7.2, our results on RBC-induced adhesion of deformable particles remains the same for $H_t = 11$, 17, and 23% in microvessels of $D_T = 11$ and 14 μm. This is rather surprising as the decrease in hematocrit implies a decrease in RBC–microparticle interaction. Considering the lateral migration of microparticles away from the wall, together with the previously mentioned importance of RBC cluster formation, it is expected that a change in hematocrit would affect $D_{P,crit}$. Figure 7.5 shows an observation in our simulations that explains the insensitivity of $D_{P,crit}$ to H_t in our simulations. The flow configuration right prior to adhesion of microparticles with diameters close or equal to $D_{P,crit}$ is shown in different cases with different hematocrits. It is seen that prior to bond formation, the microparticle significantly

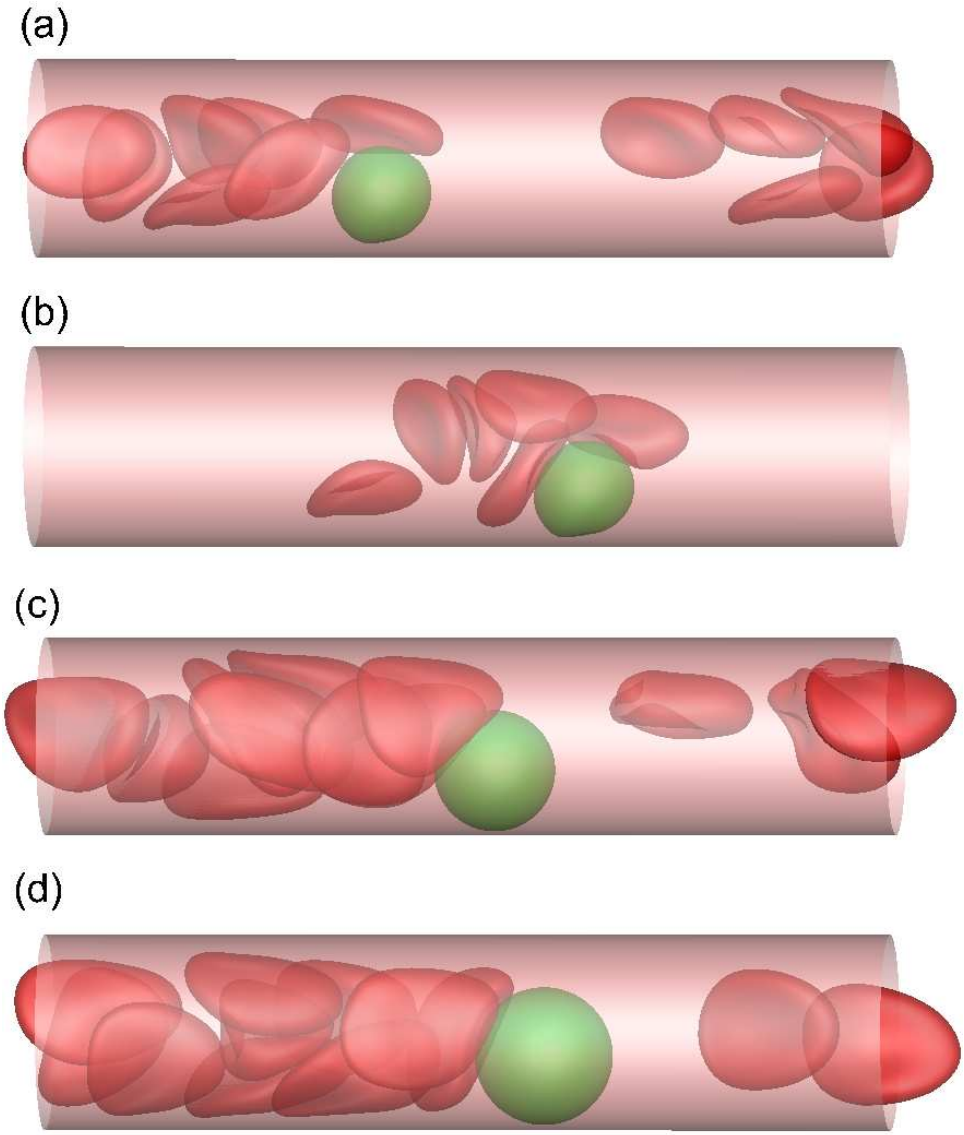

Figure 7.5: Flow configuration prior to particle adhesion for a $D_P = 7$ μm deformable particle in a $D_T = 14$ μm microvessel at $H_t = 11\%$ (a) and $H_t = 6\%$ (b), for a $D_P = 7$ μm rigid particle in a $D_T = 11$ μm microvessel at $H_t = 23\%$ (c), and for a $D_P = 8$ μm rigid particle in a $D_T = 11$ μm microvessel at $H_t = 23\%$ a while following adhesion initiation (d).

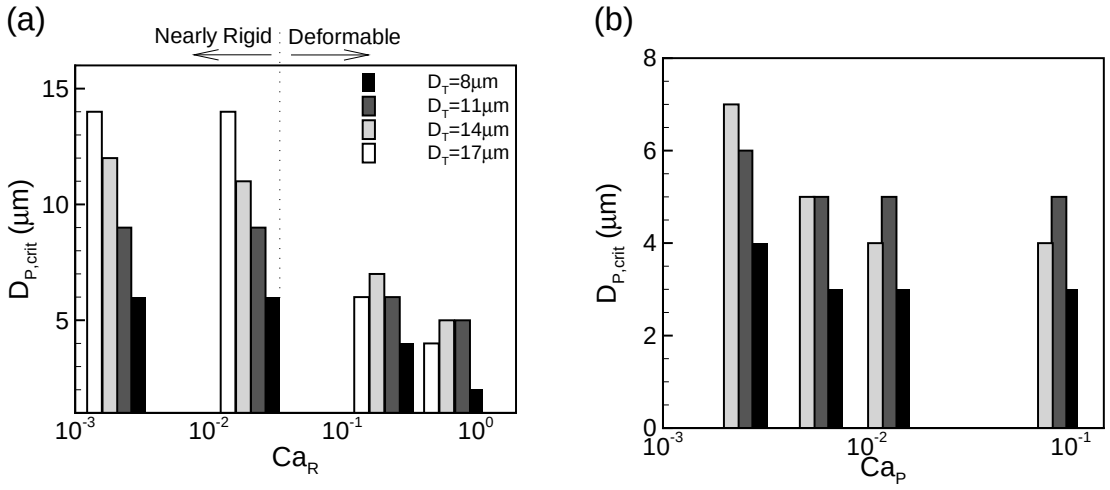

Figure 7.6: Effect of pseudo-shear rate (a) and microparticle deformability (b) on microparticle critical size in different sized microvessels. In (b) $Ca_R = 0.3$.

affects the RBC suspension microstructure by creating an RBC aggregate upstream the microparticle and a cell-free region downstream. This phenomenon, which has been mentioned in a number of previous studies on WBCs [190, 191], explains the insensitivity of microparticle critical size to hematocrit. As the particle size is increased against the vessel diameter, due to the increased geometrical blockage accompanied by reduced velocity of the near-wall particle, the RBC suspension upstream the microparticle is slowed down and an aggregate is formed. Such aggregate locally increases the hematocrit and creates similar RBC–microparticle interaction conditions as if the hematocrit was higher.

The effects of pseudo-shear rate and particle deformability on $D_{P,crit}$ are presented in Figures 7.6(a) and (b), respectively. As mentioned in Section 7.2 (problem setup section), the pseudo-shear rate is controlled by Ca_R, and β in our simulations. Higher values of Ca_R and β result in higher flow rates and consequently higher pseudo-shear rates and vice versa. Figure 7.6 shows that $D_{P,crit}$ is increased by a decrease in pseudo-shear rate and it is decreased by an increase in particle deformability. At lower

shear rate, the RBC deformation is reduced and therefore the streamline deflection is increased (see Chapter 3). This results in a higher level of RBC-induced microparticles dispersal. Besides, due to decreased shear gradient, the near-wall deformation of microparticles as well as the lift imparted on them are reduced. Therefore, larger particles encounter less difficulty coming into the adhesion region. Figure 7.6(a) shows that decreasing Ca_R to values lower than 0.03, where RBCs behave more like rigid disk-like particles rather than elongated deformable capsules, causes particles of all sizes under consideration to adhere to the wall. In this case, similar to the case of perfectly rigid microparticles, RBC passing motion is no longer required for RBC-induced adhesion, due to significant decrease in microparticle near-wall deformation. This result is in qualitative agreement with the physiological fact that WBC adhesion in venules, where the shear rate is low, is significantly higher compared to that in arterioles, where the shear rate is high [192].

As demonstrated by Figure 7.6(b), $D_{P,crit}$ is initially decreased by an increase in particle deformability, and then reaches a plateau. The initial decreasing trend is because of the increase in the deformation-induced near-wall gap between the microparticle membrane and the wall. However, since the particle elongation and consequently its near-wall deformation is limited due to significant resistance against area dilatation, such near-wall gap eventually saturates and so does the $D_{P,crit}$ plot. Such behavior is of great importance in terms of biomedical applications as it indicates that smaller particles are adhered in a wider range of deformability than larger ones. For instance, Figure 7.6(b) shows that a 5 μm particle flowing in a 14 μm microvessel adheres only if $Ca_P \leq 0.007$; however, a 3 μm particle adheres in all of the capillary numbers under consideration.

The results of this section were focused on the phenomena that are associated with the initial bond formation between microparticles and the vessel wall. The RBC-induced particle adhesion is followed by microparticle adhesive rolling on the vessel wall. Such adhesive dynamics in presence of RBCs is the subject of next section.

7.3.2 Microparticle Adhesive Dynamics in Presence of RBCs

Figure 7.7(a-c) shows sample snapshots for the initial stages of adhesive motion of a deformable microparticle after it reaches the adhesion region by hydrodynamic interactions with RBC clusters. The snapshots presented in Figure 7.7 correspond to the case in which $D_P = 7$ μm and $D_T = 14$ μm It is observed that following the formation of the first bond between the particle surface and the vessel wall, the tethered point becomes an anchor about which the microparticle rotates. (Figure 7.7(a-b)). The rotation is due to the torque created by the hydrodynamic shear forces as well as interactions with RBCs. Subsequently, the strong adhesive forces further pull the microparticle membrane towards the wall. This results in a teardrop-like shape as the particle lies on the vessel wall and follows its contour at the bottom surface (Figure 7.7(c)). The teardrop-like shape during adhesive rolling has been observed in previous experimental studies on WBCs [102, 106–108]. Another important observation in Figure 7.7 is the formation and breakage of adhesive bonds at the trailing end of the deformed microparticle, which has also been observed for WBCs in previous experiments [97, 103].

The deformation in microparticle membrane increases the surface area exposed to adhesion region, and consequently the number of bonds. It should be emphasized that

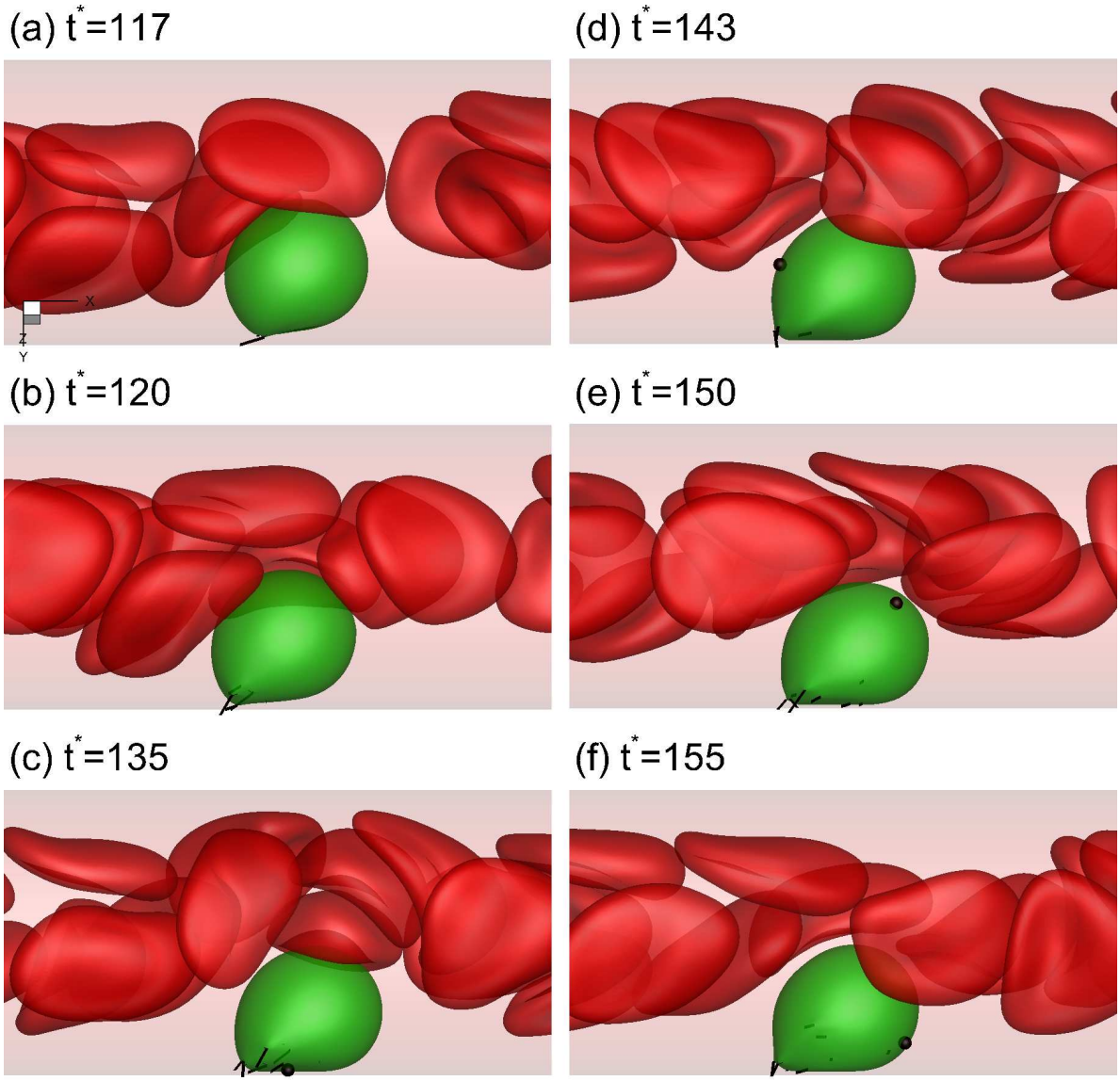

Figure 7.7: Representative snapshots showing instantaneous configuration of RBC suspension and a $D_P = 7$ μm deformable particle in a $D_T = 14$ μm microvessel immediately following the formation of the first bond.

without the presence of adhesive bonds in our simulations, the deformable microparticle does not come in such close proximity of the vessel wall solely due to interaction with RBCs. The deformation-induced wedge-like gap between the particle surface and the wall is only eliminated completely by adhesive forces, not the RBCs alone.

Once the deformable microparticle is adhered to the wall, it starts rolling on the substrate. This is shown by the marker point on the microparticle surface in Figure 7.7(c-f). As is it observed, while the adhered particle moves longitudinally with the flow on the vessel wall, its membrane exhibits a rotary motion.

The rolling velocity of the microparticle, and in a more general sense, the adhesive dynamics of the particle is determined by the balance between two competing effects: hydrodynamic and adhesive forces. While adhesive forces slow the microparticle down, the hydrodynamic drag and lift tend to disrupt the bonds and increase the particle rolling velocity. Hydrodynamic forces imparted on the microparticle are dependent on the particle size. Moreover, particle size affects the number of bonds through the surface area exposed to adhesion region. Our results show a variety of adhesive rolling behaviors for the adhered microparticles of different sizes. The regimes of motion that are observed in our simulations are demonstrated by sample particle trajectories in Figure 7.8.

This figure shows the variations in longitudinal displacement of different particles following the formation of initial bonds (marked by the arrow on the plots) in a 14 μm (a-d) and a 17 μm (e) microvessel. Figure 7.8(a) shows 'firm adhesion' in which the microparticle displacement following initial bond formation is negligible. Such behavior is only observed for relatively small microparticles ($D_P \leq 3$ μm) in our simulations. The intermittent 'stop-and-go' type motion, which is observed small

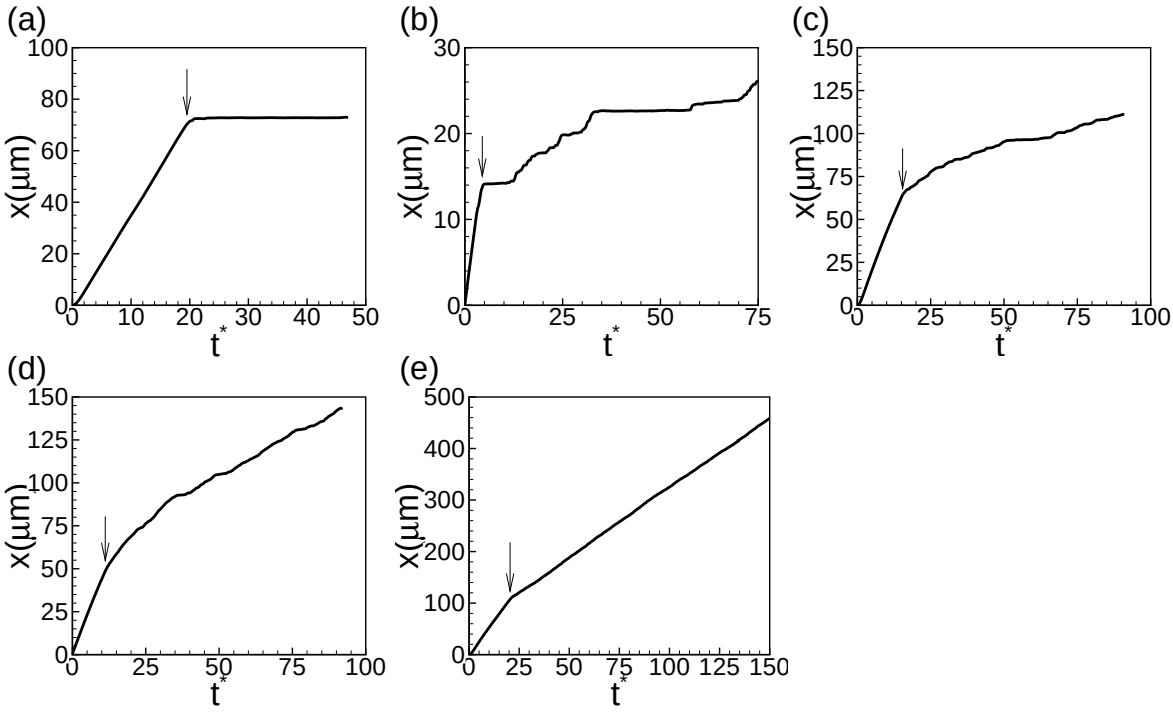

Figure 7.8: (a-d) Variations in longitudinal displacement of a deformable microparticle, x, following formation of initial bonds (marked by the arrow) in a $D_T = 14$ μm microvessel; each sample plot shows a different regime of motion: (a) firm adhesion ($D_P = 3$ μm), (b) stop-and-go motion ($D_P = 4$ μm), (c) unsteady rolling ($D_P = 5$ μm), (d) and semi-steady rolling ($D_P = 6$ μm); (e) steady rolling-sliding motion of $D_P = 4$ μm rigid microparticle adhered to the vessel walls in a $D_T = 17$ μm microvessel.

and moderate particles (3 μm $\leq D_P \leq$ 5 μm), is demonstrated in Figure 7.8(b). During this motion, due to random-based formation and breakage of adhesive bonds (see Chapter 2), the particle stands still for some time (stop), then starts rolling for a while (go), and then again stops, and the process continues during the simulation. Figures 7.8(c) and (d) show unsteady and semi-steady adhesive rolling behaviors, respectively. A relatively slow rolling motion with irregular fluctuations in the microparticle displacement is observed in the unsteady rolling behavior. On the other hand, a faster rolling behavior with a more uniform displacement variations is seen in the semi-steady rolling motion. These two behaviors are observed for relatively larger particles in our simulations ($D_P \geq 5$ μm). The above regimes of adhesive motion has been also recognized in modeling studies of WBCs rolling [150]. Another regime of motion that is observed to be specific to moderate and large rigid particles is the steady rolling-sliding motion, during which the particle adhesive rolling is accompanied by non-adhesive sliding motion (Figure 7.8(e)). Figure 7.9 demonstrates such behavior by showing the snapshots of the adhesive motion of a 4 μm microparticle in an 11μm microvessel. As it is observed, the particle is sliding at about $t^* \approx 46$ (Figure 7.9(a)), and rolling at about $t^* \approx 62$ (Figure 7.9(b)). In what follows, the effect of RBCs on the adhesive motion of microparticles on the vessel wall is discussed.

Figure 7.10 shows the effect of presence of RBCs on adhesive rolling motion of a deformable 6 μm particle in an 11 μm microvessel. In this figure, the microparticle adhesive dynamics in presence and absence of RBCs are compared under the same pseudo-shear rate conditions (i.e. time-averaged flow rate is equal in the two cases). As previously mentioned, without the presence of RBCs the microparticle does not

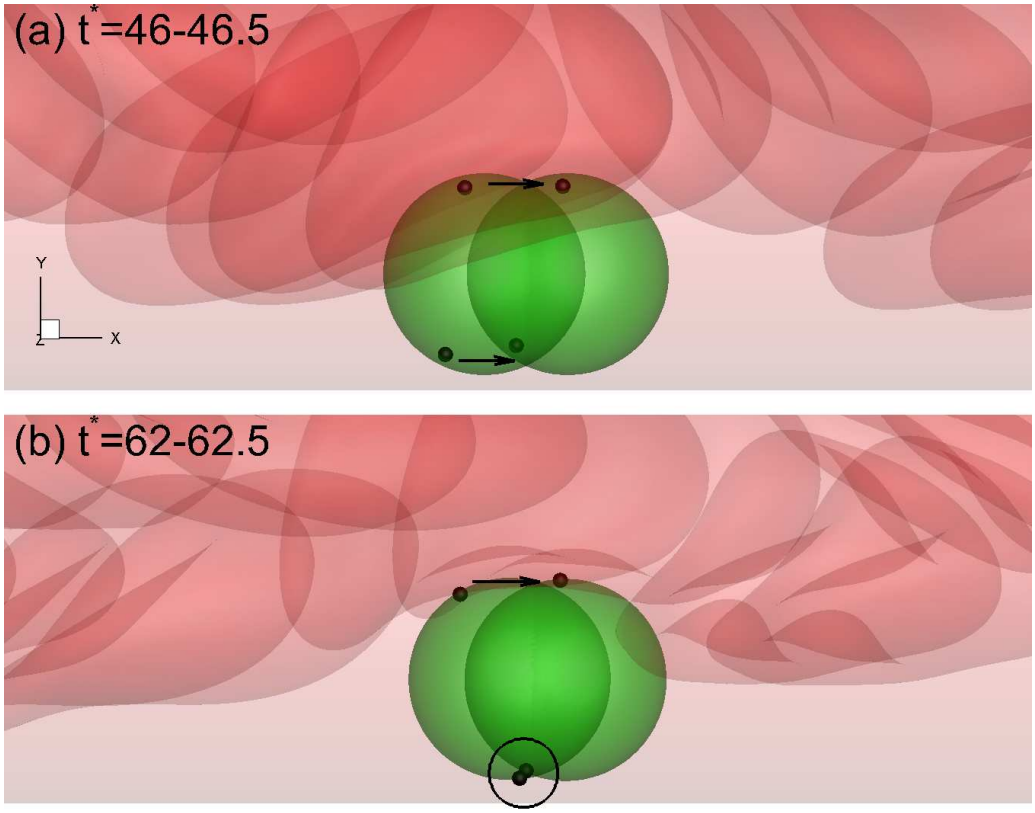

Figure 7.9: Sliding (a) and rolling (b) motion of a $D_P = 4$ μm microparticle in a $D_T = 11$ μ microvessel.

adhere to the wall. Hence, to obtain the results for the adhesive rolling of a microparticle in the absence of RBCs, we initially placed the particle in such a way that its surface is partly inside the adhesion region.

Figure 7.10(a) demonstrates the variations in microparticle rolling velocity, u^* (the velocity if the microparticle centroid along the flow direction x), in presence and absence of RBCs. Note that the velocities presented in this section are normalized by the microvessel average flow velocity. Figure 7.10(a) shows that RBCs increase the microparticle average rolling velocity. Figure 7.10(b) demonstrates the temporal variations in transverse velocity of the microparticle, v_θ, which is the velocity of the particle centroid along the wall in the plane that is perpendicular to the flow direction (y-z plane – see Chapter 2). The fluctuations of v_θ are observed to be larger in presence of RBCs. The increase in the average value of u^* and in the fluctuations of v_θ, results in a significant increase in microparticle displacement in presence of RBCs. This is seen in Figures 7.10(c) and (d), where the microparticle diplacement in flow direction, x, and in transverse direction, θ, is compared in presence and absence of RBCs. Note that θ represents the angular location of the microparticle centroid in y-z plane.

Interestingly, Figure 7.10(c) further shows that the regime of adhesive motion of the particle is altered from unsteady rolling to semi-steady rolling in the presence of RBCs. Such an alteration is facilitated through a decrease in the number of adhesive bonds in presence of RBCs which is observed from Figures 7.10(e) and (f). Similar results are observed for different values of D_P and D_T, showing that not only the RBCs enhance the rolling velocity of microparticles, they may also change the regime of adhesive motion.

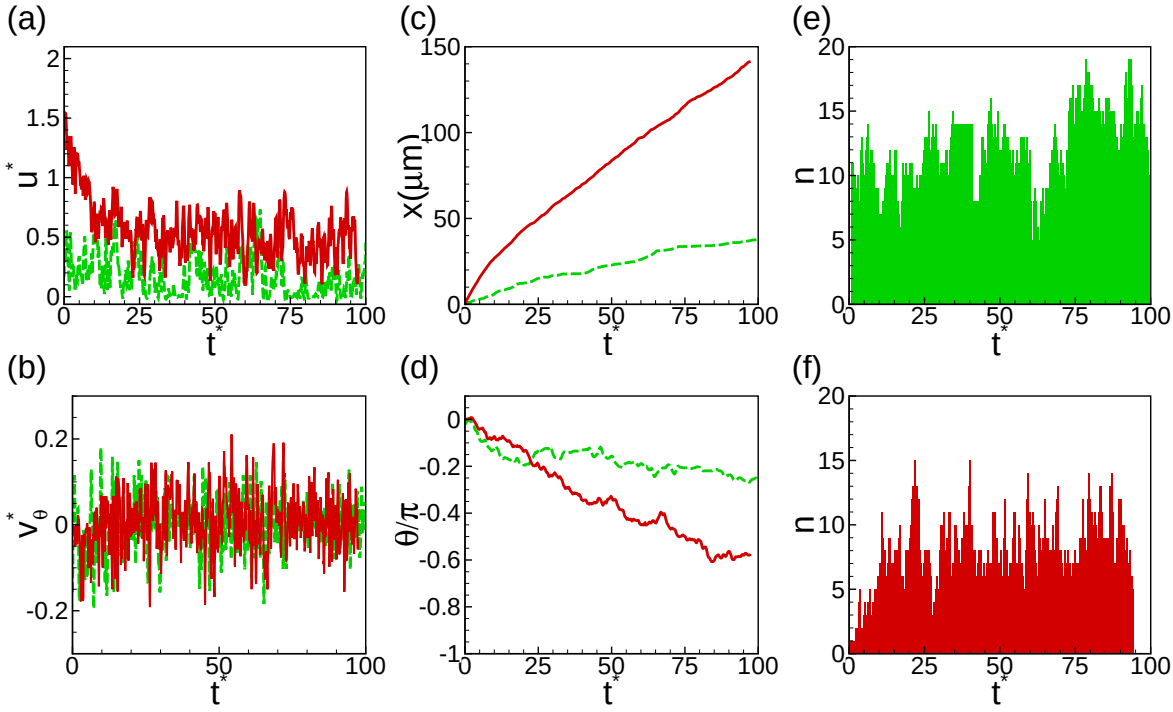

Figure 7.10: Adhesive dynamics of a $D_P = 6$ μm deformable microparticle in a $D_T = 11$ μm microvessel in presence (solid red lines) and absence (dashed green lines) of RBCs; temporal variations in microparticle centroid velocity along flow direction, u^* (a), and in transverse direction, v^*_θ (b); microparticle centroid trajectory along flow direction, x (c), and in transverse direction, θ (d); the number of bonds in absence (e) and presence (f) of RBCs.

Figure 7.11 shows the RBC-induced alteration in adhesive dynamics of microparticles of different diameters in an 11 μm microvessel. The adhesive motion of the particles in absence and presence of RBCs are shown by empty and filled bars, respectively. Figure 7.11 shows a significant increase in the average rolling velocity of microparticles, U^*, due to a decrease in the average number of bonds, N, in presence of RBCs for both deformable (Figure 7.11(a-b)) and rigid (Figure 7.11(c-d)) microparticles. The regimes of adhesive motion corresponding to the average velocities are also demonstrated in the Figures 7.11(a) and (c). Figure 7.11 also shows that the amount of RBC-induced increase in microparticle rolling velocity depends on microparticle size and deformability (this will be discussed in further details).

Note that the magnitude of the average rolling velocities obtained for deformable particles are generally lower than the rigid ones of the same size, due to larger surface area of adhesion provided by near-wall deformation. The deformation-induced decrease in rolling velocity has also been mentioned in previous studies on WBC adhesive rolling [113, 117]. The surface area of adhesion increases with an increase in particle size. In case of deformable particles, such increase is more significant due to near-wall deformation and results in an increase in the number of bonds with the particle size (see Figure 7.11(b)). However, for rigid particles, the increase in the surface area that is exposed to the adhesion molecules on the wall is relatively small and cannot compensate the increase in hydrodynamic drag. Therefore, the number of bonds decreases with an increase in particle size (see Figure 7.11(d)). Figure 7.11(d) also shows that average number of bonds for moderate to large rigid particles is less than unity, which is an indication of frequent instants when there are no bonds. During such instances the microparticles exhibits sliding instead of rolling as demonstrated

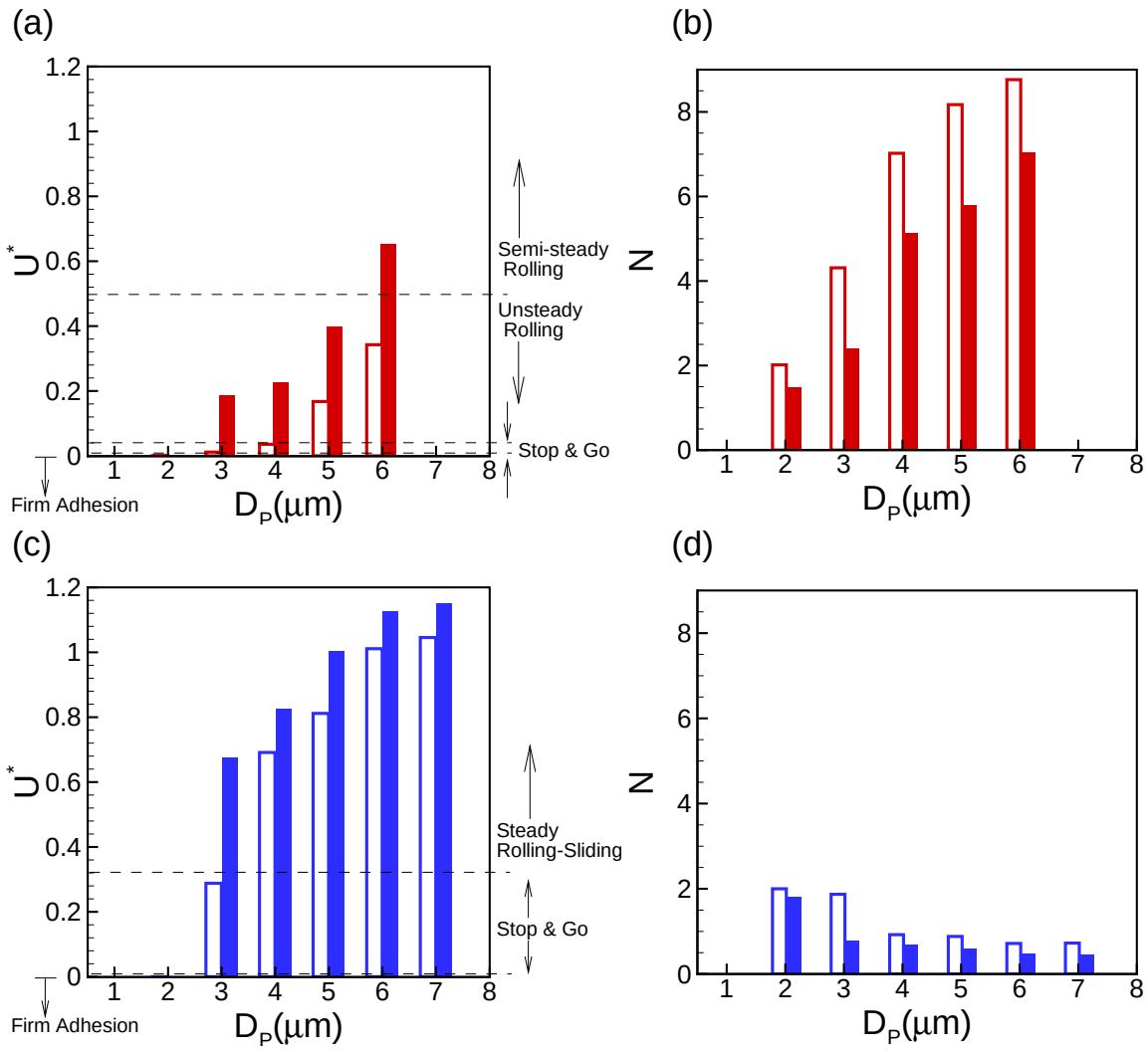

Figure 7.11: Normalized average rolling velocity (left column - (a) & (c)) and average number of bonds (right column - (b) & (d)) for different sized deformable (top row - (a) & (b)), and rigid (bottom row - (c) & (d)) particles in presence (filled bars) and in absence (empty bars) of RBCs in an 11 μm microvessel.

in Figure 7.9.

The presence of RBCs affects the adhesive rolling velocity through different mechanisms. RBCs alter the velocity profile across the microvessel from a parabolic curve to a blunt one [109–112]. This modification to the velocity profile increases the shear gradient near the vessel wall and decreases it near the centerline. The increase in near-wall shear gradient is expected to result in an increase in the disruptive forces on the bonds, an increase in the bond dissociation rate, and consequently an increase

in the rolling velocity. The RBCs also affect the adhesive dynamics through continuous interactions with the adhered microparticle, which impart longitudinal (along the flow) and radial (normal and towards to the vessel wall) forces on the particle. While the former increases the rolling velocity by pushing the particle forward, the latter decreases it by increasing the surface area of adhesion [120].

The effect of RBCs on adhesive rolling through changing the spatial distribution of the shear rate is experienced by particles of any size. However, the forces imparted by the RBCs on the microparticle are dependent on size effects. Simulations of this chapter and the results of the Chapter 6 indicate that the typical CFL thickness in the range of D_T and H_t under consideration varies between 3 and 4 μm. This indicates that the forces imparted by RBCs are mainly experienced by particles larger than 3-4 μm. Such notion has also been mentioned in a recent experimental study on adhesion of rigid particles in presence of RBCs [56]. Figures 7.11(a) and (c) demonstrate that the RBC-induced increase in rolling velocity occurs for all of values of D_P under consideration (ranging from 2 to 7 μm). Note that considering the CFL thickness in our simulations, microparticle of $D_P = 2$ and 3 μm are located inside the CFL and encounter minimal interactions with RBCs, specially along the flow direction.

Therefore, it is hypothesized that the effect of RBCs through varying spatial distribution of shear rate dominates their effects through hydrodynamic interactions with microparticles. Figure 7.12 shows the effect of RBCs on the flow velocity profile at multiple locations in the vicinity of a 4 μm particle adhered in an 11 μm microvessel. Here, the lateral distribution of longitudinal flow velocity, u_f^*, is demonstrated at different x-locations. The plane at which the velocities are obtained passes through both the microparticle centroid and the vessel centerline. The top row shows the

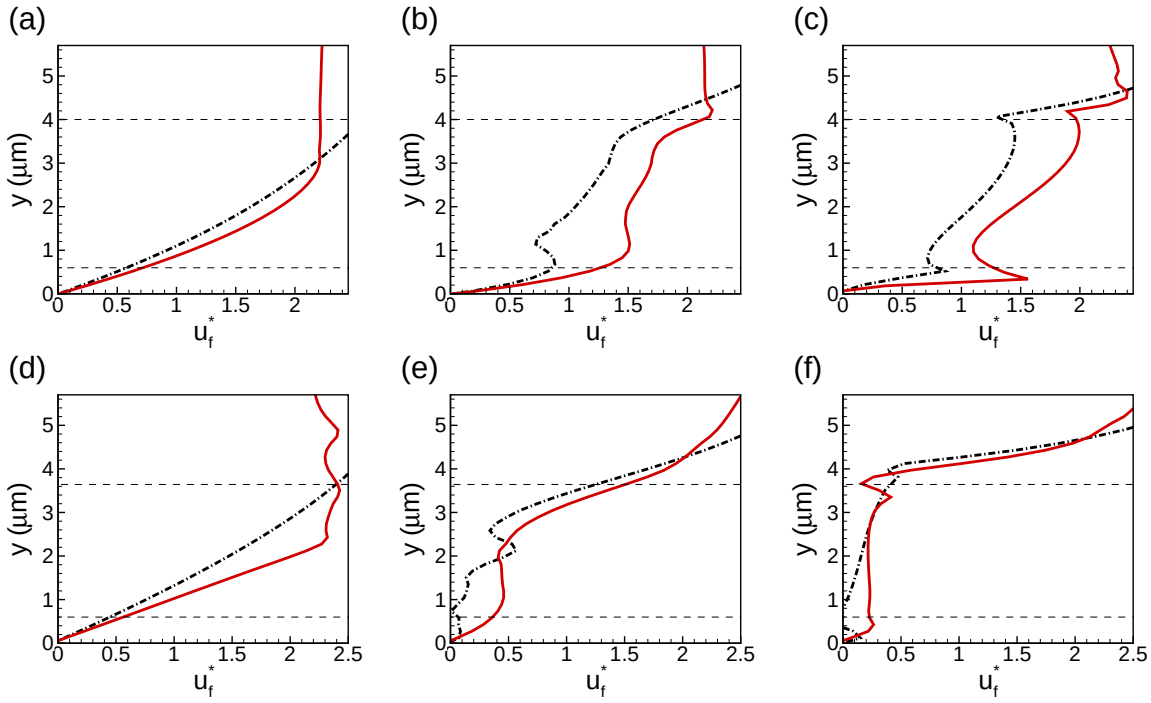

Figure 7.12: Instantaneous distribution of longitudinal flow velocity, u_f^*, in presence (red solid line) and absence (black dash-dot line) of RBCs for $D_P = 4$ μm, and $D_T = 11$ μm, far upstream the particle ((a) & (d)), immediate upstream the particle ((b) & (e)), and at microparticle centroid x-location ((c) & (f)). The profiles for deformable and rigid microparticle are shown in (a-c), and (d-f) respectively. The bottom horizontal dashed line shows the adhesion region and the top one shows the lateral extent of adhered microparticle.

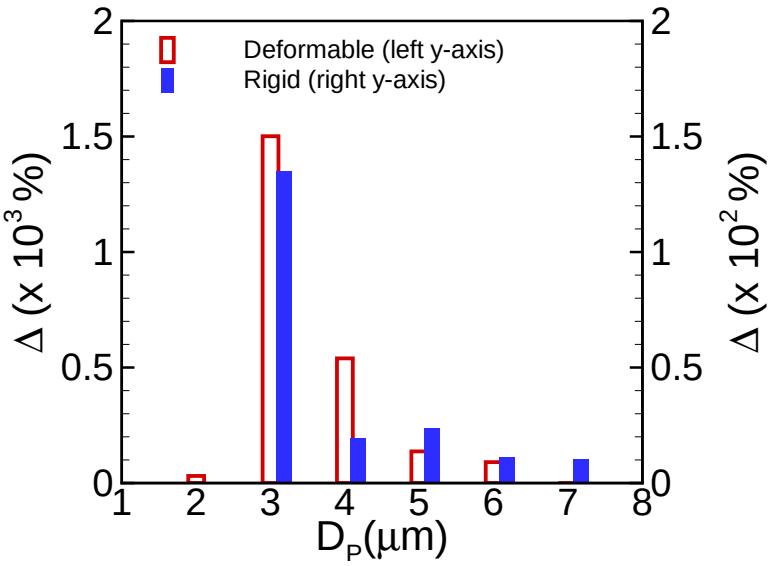

Figure 7.13: The percentage of RBC-induced increase in microparticle rolling velocity, Δ, as a function of particle size in $D_T = 11$ μm. The values are shown for deformable and rigid microparticles by empty red bars (left y-axes) and filled blue bars (right y-axes), respectively.

profiles for rigid particle and the bottom one for deformable particle. The velocity profile upstream and away from the microparticle, just upstream the particle, and at the x-location of particle centroid are shown in columns from left to right successively. It is observed that the flow velocity magnitude in presence of RBCs is considerably larger in the lateral locations at which the particle moves. This results in an increased hydrodynamic drag that is experienced by the particle. More specifically, it is seen that the near-wall velocity gradient in the adhesion region is significantly higher in the presence of RBCs, which is an indication of considerably larger disruptive shear forces on the bonds. The increase in the near-wall shear gradient and the hydrodynamic drag results in an increase in the bond breakage rate and consequently an increase in the rolling velocity.

The percentage of increase in the microparticle rolling velocity due to the presence

of RBCs (denoted by Δ) is demonstrated in Figure 7.13 for $D_T = 11$ μm. Extremely large values are observed in a number of cases due to the change of regime of adhesive motion. Specifically, alteration from stop-and-go motion to unsteady rolling in case of deformable particles, e.g. $D_P = 3$ & 4 μm, and from stop-and-go motion to steady rolling-sliding in case of rigid ones, e.g. $D_P = 3$ μm, results in highest values. Since the change of the regime of motion does not generally occur for larger particles, a decreasing trend in the value of Δ with the an increase in the particle diameter is observed. $D_P = 2$ μm case is an exception to this trend since the regime of motion (firm adhesion) remains unchanged in the presence of RBCs. Figure 7.13 also shows that the RBC-induced increase in particle rolling velocity is larger for deformable microparticles than the rigid ones of the same size. This is because the regime of motion for rigid particles of $D_P > 3$ μm, which is steady rolling-sliding with relatively high average rolling velocity, remains unchanged in presence of RBCs. However, for deformable particles of similar sizes, a change from stop-and-go motion to unsteady rolling ($D_P = 3$ & 4 μm), and from unsteady to steady rolling ($D_P = 6$ μm) is observed. Considering the very small average rolling velocity in stop-and-go motion and relatively small one in unsteady rolling, the values of Δ are significantly larger for deformable particles. Also, since the average rolling velocity in stop-and-go motion is observed to be higher for rigid particles compared to deformable ones (compare $D_P = 3$ μm rigid with $D_P = 3$ and 4 μm deformable particles in absence of RBCs in Figures 7.11 (a) and (c)), even for $D_P \leq 3$ μm larger values of Δ are seen in case of deformable particles.

The presence of RBCs not only affects the time-averaged adhesive behavior, but

also the temporal variations and fluctuations in adhesive motion (see Figure 7.10(a-b)). Since the bonds are constantly being formed and broken during the simulations, and considering the random-like basis of the probabilities for formation and breakage of bonds as explained in Chapter 2, the number of bonds shows random fluctuations in time (see Figure 7.10(e-f)). The fluctuations in number of bonds result in oscillations in instantaneous velocity of particle centroid along the flow and in the transverse direction. To measure such fluctuations, the RMS (root mean square) of normalized velocity oscillations defined as $\left(\sqrt{\int_T (u^*(t) - U^*)^2 dt/T}\right)/U^*$ (where U^* is the average rolling velocity, T is the averaging time window, and $u^*(t)$ is replaced by instantaneous velocities along the flow, u^*, and in the transverse directions, v_θ^*) was computed for the different cases.

The results are presented in Figure 7.14. Figure 7.14(a) shows that the presence of RBCs decreases the oscillations in longitudinal velocity of deformable particles. RBCs shift the regime of adhesive motion from unsteady irregular behaviors such as stop-and-go and unsteady rolling towards steady uniform motions such as semi-steady rolling. This results in decreased oscillations in particle motion in presence of RBCs. It is also seen that since a similar shift occurs with an increase in particle size, the RMS values decrease as the particle diameter increases. An opposite behavior is observed in Figure 7.14(b) for the fluctuations in the transverse velocity of deformable particles. An increase in the particle size increases the RMS of transverse velocity oscillations. The aforementioned shift in the regime of motion, gives more freedom to the particle to move in the transverse direction. Moreover, a significant increase in the surface area of adhesion with the particle size enables larger particles to reach for further away adhesion molecules on the vessel wall in the transverse direction. Therefore, larger

variations occur in transverse displacements of larger microparticles, which lead to larger RMS values of v_θ^*. Figure 7.14(b) shows that the presence of RBCs has a similar increasing effect on oscillations in particle adhesive motion in transverse direction. In presence of RBCs, the regime of motion is shifted and the rate of bond breakage is increased. Additionally, hydrodynamic interactions between the microparticle and the RBCs in the transvese direction also contribute to the increase in the RMS values.

Figure 7.14(c) shows the effect of RBCs on velocity fluctuation along the flow direction for rigid particles. A decreasing effect similar to the case of deformable particles is observed here for $D_P = 3$ μm rigid particle due to change of regime of motion. However, for $D_P = 4$ μm the effect is negligible and for larger particles (5-7 μm) a slight increasing effect of RBCs is observed. Figures 7.14(d) demonstrates the effect of RBCs on fluctuations in the transverse velocity of rigid microparticles. Again, a similar trend is observed. The increasing effect as in the case of deformable particles is observed for $D_P < 5$ μm. However, the effect becomes reversed for $D_P \geq 5\mu$m. Note that unlike the case of deformable particles, here an increase in particle size results in a decrease in fluctuations in v_θ^*, since the increase in surface area of adhesion with the particle size is relatively small and the average number of bonds decrease below unity with an increase in particle diameter (see Figure 7.11(d)).

The changing behavior that is observed in the effect of RBCs on the velocity fluctuations of rigid particles as a function of particle size, is due to the effects of rigid microparticles on RBCs micro-structure. When the rigid particle is large enough to obstruct the RBC suspension flow like a stenosis, a low frequency large scale oscillation in the flow rate is introduced due to transient formation and dissociation of RBC aggregate upstream the microparticle. Formation of such aggregates causes a

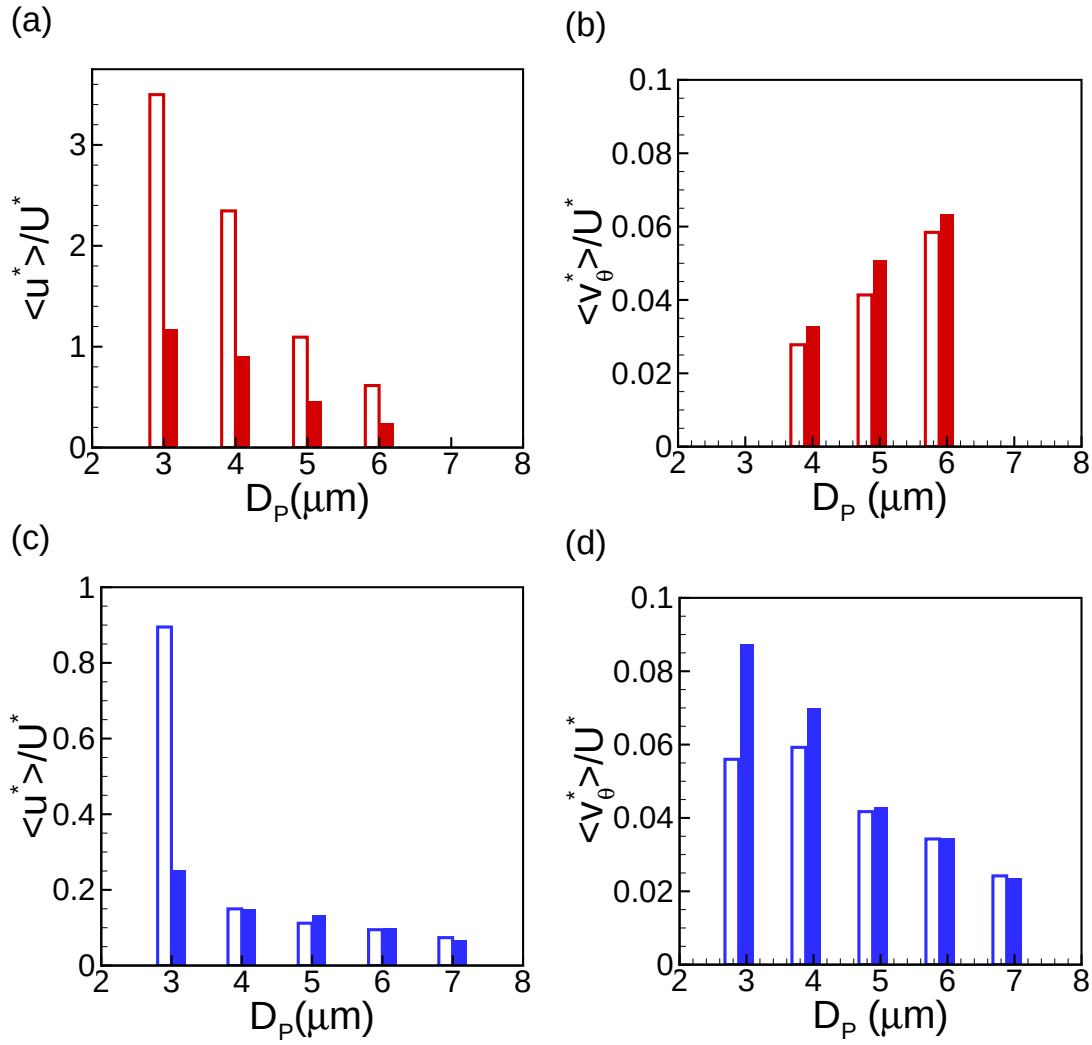

Figure 7.14: Oscillations in particle rolling velocity, u^* (first column - (a) & (c)), and transverse velocity, v^*_θ (second column - (b) & (d)), as a function of particle diameter for deformable (left column - red color) and rigid (right column - blue color) particles in absence (empty bars) and presence (filled bars) of RBCs. The oscillations is evaluated as the RMS of particle centroid velocity divided by its average value.

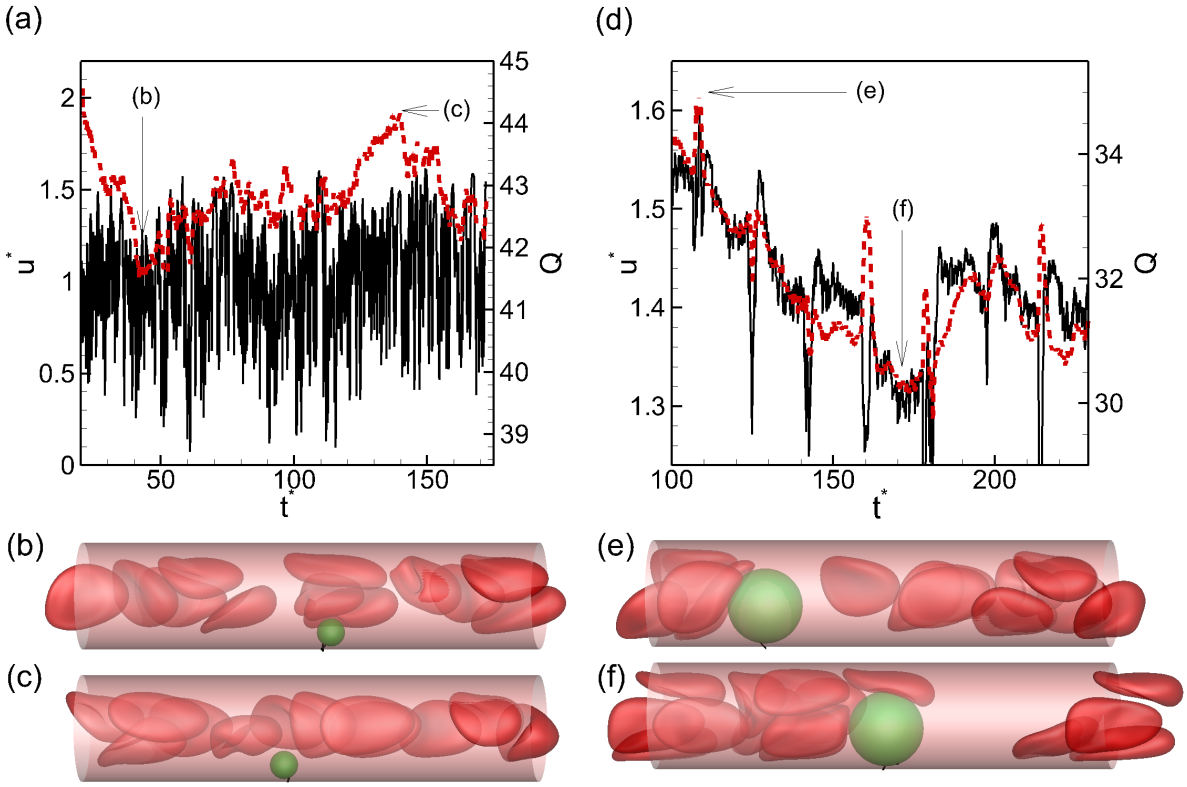

Figure 7.15: Time-dependent variations in microvessel flow rate, Q (red dashed line) and microparticle rolling velocity, u^* (black solid line), for a $D_P = 3$ μm (a) and a $D_P = 8$ μm (d) rigid microparticle adhered in a $D_T = 11$ μm microvessel; representative snapshots showing RBC distribution corresponding to highest and lowest microvessel flow rates are shown in (b-c), and (e-f) for cases (a) and (b), respectively.

drop in flow rate and therefore in the pseudo-shear rate, which results in a decrease in bond breakage and consequently a reduction in microparticle rolling velocity. Dissociation of RBC aggregates, thereafter increases the flow rate and consequently the pseudo-shear rate and the particle rolling velocity. Such large amplitude low frequency oscillations in rolling velocity significantly increase the RMS values for large rigid particles as it is seen in Figure 7.14(c). Moreover, the increased geometrical blockage results in hindered transverse motion, which explains the similar changning behavior observed in Figure 7.14(d). The effects of particles on RBC suspension microstructure are considerably less severe in case of deformable particles due to near-wall deformation and consequently less geometrical blockage.

Figure 7.15 shows sample rolling velocity fluctuations over time for rigid particles of 3 (Figure 7.15(a-c)) and 8 μm (Figure 7.15(d-f)) in a $D_T = 11$ μm microvessel. The corresponding snapshots of the flow configuration is also demonstrated. As it is seen in this figure, the amplitude of velocity fluctuations is significantly higher for the $D_P = 3$ μm compared to $D_P = 8$ μm. However, the low frequency variations in rolling velocity that is observed for $D_P = 8$ μm, is negligible for the $D_P = 3$ μm. The snapshots also demonstrate that while the RBC distribution is more or less uniform in different time instants for the $D_P = 3$ μm, it is considerably non-uniform in the case of $D_P = 8$ μm. The accumulation of RBCs upstream the rolling microparticle and the formation of a cell-free region downstream it is seen in Figure 7.15(e-f). The figure also shows that as the RBC squeezes through the gap between the particle and the wall (Figure 7.15(f)), the overall velocity of the particle drops significantly (although the high-frequency oscillations due to bond formation/breakage still exists); and as the RBC suspension micro-structure becomes more dispersed (Figure 7.15(e)), the particle velocity is increased. Figure 7.15(d) shows that the particle rolling velocity closely follows the variations in microvessel flow rate. This is while the rolling velocity correlation with flow rate fluctuations is much weaker in case of $D_P = 3$ μm particle (Figure 7.15(a)). Although similar correlation between flow configuration and flow rate variations, similar to what was presented in Chapter 6 for non-stenosed microvessel, is observed in this case (Look at the three RBCs just above the microparticle in Figure 7.15(b) blocking the flow passage and compare with the RBC distribution in Figure 7.15(c)).

The results of this section are similar to the previous section in the sense that they showed the significance of the presence of RBCs as well as microparticle deformation

in particle adhesion to vessel walls. In the previous section, the effects of those parameters on RBC-induced formation of initial adhesive bonds were discussed, and in this section those effects on microparticle adhseive rolling were focused. Our results show a dual role for both the presence of RBCs and the particle deformability during the two different stages of microparticle adhesion. In the first stage, i.e. microparticle initial adhesive bond formation, the presence of RBCs has an enhancing effect but the particle deformation has an adverse effect. On the other hand, in the second stage, i.e. microparticle adhesive rolling on the vessel wall, particle deformation is favorable but the effect of the presence of RBCs is adverse.

7.4 Conclusion

We performed a 3D multiscale multiphysics modeling study of microparticle adhesion in microvessels. We showed that the RBCs induce the formation of initial adhesive bonds between the microparticle and the vessel wall by pushing the particle into the adhesion region. It was observed that the deformability of microparticle is of crucial importance in the RBC-induced adhesion. The near-wall deformation of the particle creates a wedge-like gap that keeps the particle away from the adhesion region. Adhesion of a deformable microparticle to the vessel wall is only facilitated by the passing motion of RBC clusters that reduce the wedge-like gap by pushing the microparticle towards the wall.

Due to such near-wall deformation, a maximum particle size, termed as 'critical particle size', was found for deformable microparticles above which the RBC-induced adhesion does not occur. The existence of a critical particle size was not observed for perfectly rigid microparticles due to absence of near-wall deformation. The value of

the critical size for deformable microparticles was shown to be dependent on the microvessel size and pseudo-shear rate, and the particle deformability, but not sensitive to the RBC hematocrit in the physiological range (11 to 23%).

Our results showed that as the microvessel diameter, D_T, increases from 8 to 14 μm, the critical size increases; but then it decreases as D_T is increased to 17 μm. The initial increase was attributed to the geometrical blockage created by the particle against the RBCs passing motion. It was hypothesized that the adhesion of microparticles in larger microvessels (D_T = 14 & 17 μm where the RBCs motion is multifile) is not only dependent on RBCs passing motion, but also on the formation of dense enough RBC clusters that are able to create strong radial forces towards the wall. The formation of such dense clusters is more likely in smaller microvessels due to significant confinement of RBC suspension. Therefore, the critical size is reduced from D_T = 14 to 17 μm.

Our simulations showed that RBCs form aggregates just upstream the microparticles of critical size immediately prior to initial bond formation. Such phenomenon was proposed to explain the insensitivity of the critical particle size to RBC hematocrit. Transient formation of RBC aggregate locally increases the hematocrit just upstream the microparticle and creates the same effect as in high hematocrit case. We also showed that the critical particle size is reduced with an increase in pseudo-shear rate and an increase in particle deformability, due to the increased near-wall deformation.

We further showed that not only the initiation of particle adhesion to vessel wall is strongly dependent on the presence of RBCs as well as microparticle deformation, but the adhesive rolling that is followed is also considerably affected by those parameters. It was observed that the average rolling velocity of microparticles is increased in

presence of RBCs. This was attributed to the effect of RBCs on the flow velocity profile inside the microvessel. The blunted profile in presence of RBCs results in a higher near-wall shear gradient, and consequently larger disruptive forces on the adhesive bonds. This causes a reduction in the number of bonds and in turn an increase in the microparticle rolling velocity. The RBC-induced increase in the rolling velocity was observed to be significant enough to alter the regime of adhesive motion in a number of cases.

The change of regime of motion was observed to be more likely for deformable particles against rigid ones and for smaller particles against larger ones. Moreover, the values of average rolling velocity were observed to be generally larger for rigid particles compared to deformable ones (due to lack of deformation). Therefore, the increase in the average adhesive rolling velocity due to presence of RBCs was shown to be more pronounced for deformable and for relatively smaller particles.

Besides the time-averaged features of microparticle adhesive rolling, the time-dependent oscillations of the adhesive behavior were also observed to be affected by the presence of RBCs and the deformation of microparticles. The RMS of instantaneous oscillations in longitudinal velocity of deformable particle was shown to decrease in the presence of RBCs, since the adhesive regime of motion is shifted from irregular behaviors towards more uniform ones. On the other hand, the RMS of fluctuations in transverse velocity of the deformable microparticle was observed to increase in the presence of RBCs. Increased rate of bond breakage due to change of regime of motion and the consequent increase in freedom of particle motion in transverse direction, together with transverse interactions with RBCs contribute to such increase. Similar trends were seen for smaller rigid particles due to change of

regime of motion. However, the effect of RBCs was observed to be flipped for larger rigid particles because of the effects of microparticles geometrical blockage on the RBCs microstructure. The blockage was shown to create low-frequency large amplitude fluctuations in the flow rate and consequently the pseudo-shear rate. Since the pseudo-shear rate directly affects the microparticle adhesive dynamics, the RMS of rolling velocity oscillations is also increased. The blockage also leads to hindered microparticle transverse motion and decreases the RMS of transverse velocity. The effect of geometrical blockage is significantly less in case of deformable particles due to considerable near-wall deformation.

In conclusion, the mechanisms through which the microparticles and the RBCs suspension interact during microparticle adhesion to vessel walls have been studied in a quantitative manner through multi-scale numerical simulations. The results of this chapter demonstrated a dual role for both the presence of RBCs and the particle deformability in microparticle adhesion. In the first stage of adhesion, which is microparticle initial adhesive bond formation, the presence of RBCs has an enhancing effect but the particle deformation has an adverse effect. On the other hand, in the second stage, which is microparticle adhesive rolling on the vessel wall, particle deformation is favorable but the effect of the presence of RBCs is adverse. The results of this chapter are of importance for biomedical applications as they demonstrate a number of new phenomena related to adhesion of microparticles as commonly used drug/contrast agent carriers in drug delivery/biomedical imaging systems. Our results indicate that to benefit from the outperformance of deformable microparticles against rigid ones in terms of adhesive rolling, the particle size and deformability should be taken into consideration. This is because the formation of initial adhesive

bonds prior to adhesive rolling is dependent on microparticle geometrical/physical properties as well as the hemorheological conditions of targeted site. Our results further indicate that incorporating smaller deformable particles offer wider range of particle deformability and microvessel pseudo-shear rate for facilitated RBC-induced formation of initial adhesive bonds. Moreover, our results show that the geometrical and physical properties of drug carriers and contrast agents are also important during the adhesive rolling due to potential adverse effects on RBC flow suspension. Larger and less deformable particles might obstruct the passage of RBCs following the adhesion, which can lead to disruption of the oxygen transport to downstream.

Chapter 8

Conclusion and Directions for Future Work

8.1 Conclusion

In this thesis, multiscale/multiphysics three-dimensional numerical simulations of concurrent multiple cellular/particulate processes in microcirculatory blood flow were presented. Particularly, the transport, dynamics, and adhesion of cells/ microparticles in microcirculation were focused. The objective was to shed light on complex underlying biophysics that are involved in different phenomena related to the particulate transport in blood flow. Specifically, the effects of microparticles physical/geometric properties on their interactions with red blood cells during diffusion, margination, and adhesion in blood flow were studied. The transport and dynamics of blood cells in microstenosis, and their effects on the average macroscopic as well as time-dependent microscopic flow characteristics were also studied. The unique feature of this work was the implementation of complex geometries, many-cell multi-component suspension flow dynamics, complex cellular/particulate motion and deformation, and molecular adhesive bond dynamics into a single unified model. The findings of this thesis underscore the ability of computational modeling in integrating different scales (from nano- to macroscale), and various physics (from chemical reactions to cell mechanics and hydrodynamics), in order to improve our understanding of cellular/particulate

processes associated with microcirculation. Such understanding is of great importance for biomedical applications, such as the design of new targeting systems for drug delivery or biomedical imaging.

Our numerical technique is an immersed boundary/front-tracking method that simulates the complex dynamics of different particulate components in the flow of blood, namely, RBCs, platelets, WBCs, rigid microparticles, and deformable capsules and vesicles. The method is also embedded with a sharp-interface immersed boundary method to handle the complex geometries such as an asymmetric stenosis in microvessels. A stochastic Monte-Carlo method is also included in the model in order to coarse-grain the nanoscale molecular binding reactions that mediate adhesive interactions between the particulate components and the blood vessel walls. The main results of this thesis can be summarized as follows:

1. **Hydrodynamic interaction between a platelet and an RBC in a dilute suspension:** The influence of RBC dynamics in shear flow, namely tank-treading and tumbling, as well as the effects of the presence of a bounding wall, on the deflection of platelet trajectories was studied in a quantitative manner. Two types of interaction between the RBC-platelet pair were observed: a crossing event in which the platelet comes in close proximity to the RBC, rolls over it, and continues to move in the same direction; and a turning event in which the platelet turns away before coming close to the RBC. The crossing event was observed to occur when the initial lateral separation between the cells is above a critical separation, and the turning event when it is below the critical separation. The critical lateral separation was found to be higher during the tumbling motion than that during the tank-treading. In close proximity of a bounding wall, it was observed that when the RBC is flowing closer to

the wall than the platelet, the critical separation was observed to increase by several folds, implying the turning events have higher probability to occur than the crossing events. On the contrary, if the platelet is flowing closer to the wall than the RBC, the critical separation was observed to decrease by several folds, implying the crossing events are likely to occur. Based on this result, a mechanism of continual platelet drift from the RBC-rich region of the vessel towards the wall by a succession of turning and crossing events was proposed.

2. **Platelet transport and dynamics in blood flow:** Platelet dynamics in whole blood under shear flow was studied with a focus on the 3D effects of the platelet-RBC interaction on platelet margination and near-wall dynamics. It was found out that the RBC distribution in whole blood becomes naturally anisotropic and creates local 'clusters' and 'cavities'. A platelet can enter a 'cavity' and use it as an express lane for a fast margination towards the wall. Such a process was termed as 'waterfall phenomenon'. Once near the wall, the 3D nature of the platelet-RBC interaction was found to result in a significant platelet movement in the transverse (vorticity) direction, leading to an anisotropic platelet diffusion within the CFL. It was found that the anisotropy in platelet motion further leads to the formation of transient platelet clusters, even in absence of any platelet-platelet adhesion, which may act as a hydrodynamic precursor to the thrombus formation. The transverse motion, and the size and number of the platelet clusters were observed to increase with decreasing CFL thickness. It was also observed that the 3D nature of the platelet-RBC collision induces fluctuations in off-shear plane orientation and, hence, a rotational diffusion of the platelets. While most marginated platelets were observed to tumble just outside the RBC-rich zone, platelets further inside the CFL were observed to

flow with an intermittent dynamics that alters between sliding and tumbling. Such behavior is shown to be a result of the off-shear plane rotational diffusion. The findings underscored the importance of the cellular-scale 3D models of whole blood in understanding platelet margination and near-wall platelet dynamics.

3. **Microparticle shape effects on transport and dynamics in blood flow:** Transport of microscale drug carriers modeled as platelet-sized microparticles of different shapes (spherical, oblate, and prolate) in whole blood was studied to quantify the microparticles' shape effect on their margination, near-wall dynamics and adhesion. It was observed that the near-wall accumulation is highest for oblate particles of moderate aspect ratio, followed by spherical particles, and lowest for very elongated prolate particles. The result was explained using microscale dynamics of individual particles, and their interaction with the RBCs. It was observed that the microparticles' orientation in 3D space and the frequency of their collisions with the RBCs are the key factors affecting their margination. It was shown that due to repeated collisions with RBCs in presence of a bounding wall, the axes of revolution of the oblate particles align near the plane of the shear flow, but those of the prolate particles shift towards the vorticity axis with a wider distribution. Such specific orientations was shown to lead to more frequent collisions and a greater lateral drift for the oblate particles than microspheres, but less frequent collisions and a reduced lateral drift for the elongated prolate particles, resulting in the observed differences in their near-wall accumulation. Once marginated, it was observed that the particle shape has an entirely different effect on the likelihood of particle–wall contacts. It was found out that marginated prolate particles, due to their alignment along the vorticity axis and large angular fluctuations, are more likely to make contacts with the wall than

spherical and oblate particles. The adhesion between flowing microparticles and wall in presence of RBCs was also simulated. It was observed that once wall contacts are established, the likelihood of firm adhesion is greater for disk-like particles, followed by elongated prolates, and microspheres. The results showed that different stages of margination-adhesion cascade can be differently affected by the particle geometric properties. Therefore, it was suggested that the local hemorheological conditions near the targeted sites must be taken into consideration while selecting the optimum shape of the microscale vascular drug carriers.

4. **Blood flow in stenosed microvessels:** Flow of RBCs in stenosed microvessels typical of small arterioles was studied. It was observed that the Fahraeus-Lindqvist effect is significantly enhanced due to the presence of a stenosis. Not only the apparent viscosity of blood was observed to increase by several folds, the rate of increase with increasing vessel diameter was also observed to be higher than that in non-stenosed vessels, and could not be predicted by using the in-vitro blood viscosity. An asymmetric distribution of the RBCs, caused by the geometric focusing in stenosed vessels, was observed to play a major role in the enhancement of the Fahraeus-Lindqvist effect. In smaller vessels, the presence of a stenosis converted the multi-file flow of the cells to a single-file flow. In contrast, in larger vessels, cells were observed to crowd upstream region of the stenosis. The asymmetry in the cell distribution was also observed to result in an asymmetry in average velocity and wall shear stress along the length of the stenosis. The discrete motion of the cells through the stenosis was observed to cause large time-dependent fluctuations in flow properties. The rms of flow rate fluctuations in presence of a stenosis could be an order of magnitude higher than that in non-stenosed vessels. Similarly, several folds increase

in Eulerian velocity fluctuation was observed in the vicinity of the stenosis than that in non-stenosed vessels. Furthermore, the velocity fluctuation immediate upstream was observed to be much higher than that downstream. Surprisingly, a transient flow reversal was observed upstream a stenosis but not downstream. The observed asymmetry and fluctuations in flow quantities and the flow reversal would not occur in absence of the cells. It was concluded that the flow physics and its physiological consequences are significantly different in micro- versus macrovascular stenosis.

5. **Adhesion of microparticles in microvessels – role of RBCs and microparticle deformability:** Adhesion of deformable as well as perfectly rigid microparticles in microvessels was studied. The results demonstrated significant effects of RBCs as well as particle deformability on formation of the initial adhesive bonds and on the following adhesive motion of microparticle on the vessel wall. It was observed that hydrodynamic interactions with RBC clusters induce microparticle adhesion. The near-wall deformation of deformable microparticles was observed to result in a critical particle size above which RBC-induced microparticle adhesion does not occur. Such critical size was shown to be non-existent in case of perfectly rigid particles due to absence of the near-wall deformation. The dependence of the critical particle size on pseudo-shear rate, particle deformability, RBC hematocrit, and microvessel size was studied and discussed. An increase in the critical size with a decrease in pseudo-shear rate and particle deformability was observed due to the decrease in near-wall deformation. The critical size was observed to be insensitive to RBC volume fraction in the hematocrit range under consideration (11 to 23 %). Such behavior was attributed to the formation of transient RBC aggregate upstream the microparticle that is observed prior to the formation of initial adhesive bonds. A

nonlinear dependence of critical size on microvessel diameter, with an initial increase followed by a decrease with increasing vessel size, is observed. The nonlinear trend is explained by effects of microparticle geometrical blockage on RBC suspension as well as the interactions between RBC clusters and microparticles in confined tubular geometry of microvessels. Significant effects of RBCs and particle deformability was also shown on adhesive rolling of microparticles following the formation of initial adhesive bonds. The rolling velocity of microparticle was observed to be increased in presence of RBCs due to modification of velocity profile across the microvessel, which results in an increase in the shear gradient near the wall. The RBCs were also observed to alter the regime of adhesive motion in a number of cases. The RBC-induced increase in rolling velocity was shown to be more significant for smaller particles against larger ones and for deformable particles against rigid ones. Overall, our results suggested that both the presence of RBCs and the microparticle deformability have a dual role in particle adhesion to vessel wall. During the initiation of adhesion, the RBCs have favorable effects and the particle deformation has adverse effects. In contrast, during adhesive rolling, the effect of RBCs is adverse and the effect of particle deformation is favorable. It was concluded that to benefit from the superiority of deformable microparticles over rigid ones in terms of adhesive rolling for targeting applications, the hemorheological conditions of targeted site must be taken into account, as they determine the choice of microparticle deformability and size that result in effective formation of initial adhesive bond prior to adhesive rolling.

8.2 Future Work

The eventual objective of the studies presented in this thesis is to create a model that can fully resolve the multiscale/multiphysics nature of the simultaneous multicellular/particulate processes associated with microcirculation in realistic physical/geometric conditions. Subsequently, it is desired to use that model as a prediction tool for biomedical applications such as drug delivery and targeting. Towards that end, many of the essential phenomena that are involved in microcirculatory blood flow were successfully simulated. Examples include: large and complex deformation and dynamics of RBCs in a dense cellular suspension, complex three-dimensional rotational dynamics of platelets and vascular drug carriers of different nonspherical shapes in blood flow and their hydrodynamic interactions with RBCs, near-wall dynamics of platelets and different sized/shaped rigid/deformable microparticles, molecular adhesive bond interactions between the surface of particles and the cell lining on the vessel wall, and the interactions between the flow of a dense RBC suspension and a complex three-dimensional geometry such as stenosis. A number of implementations can further improve our model and bring it closer to the aforementioned final goal. Here we have summarized those as future directions with respect to this work.

Including vessel wall roughness: The endothelial cell lining on the inner surface of the blood microvessels is not perfectly smooth. The effects of the sub-micron irregularities in the geometry of ECs on the near-wall dynamics and adhesion of platelets and microparticles in small microvessels have not been addressed in the literature. The sharp-interface immersed method in our model can be used to create a more realistic geometry to simulate the cell lining on the microvessel walls. For instance, a wavy surface can be generated by the existing numerical method to model

ECs.

Including further complex geometries, e.g. bifurcation, branching network, microemboli, etc: Incorporating the sharp-interface immersed boundary method to simulate the solid boundaries such as microvessel wall and micro-stenosis, can be further extended to more complex geometries that exist in human body such as branching network, bifurcation, and microemboli. A considerable challenge in such improvement is the extensive number of solid nodes in the method that do not contribute to the flow/cell physics but increase the simulation work load and contribute to the computational cost. Therefore, significant modifications to the existing numerical method are required in this regard.

Including pulsatility of blood flow and deformability of vessel walls: The driving force in the circulation is the pumping work of heart muscles. As a result, blood flow is periodic and pulsatile. Also, blood vessels are not completely rigid and exhibit deformability to some extent. The combination of these two effects complicates the boundary condition required to be applied on the vessel walls in a realistic model. Such effects, however, significantly decay as the blood flows from larger vessels such as arteries into further downstream smaller vessels like arterioles and capillaries. Hence, we used no-slip boundary conditions on perfectly rigid geometries to model microvascular walls. Nevertheless, the effects of flow pulsatility and vessel wall deformability could be of interest in microcirculation in tumor tissue, in which the blood flow is known to be intensified due to the leaky microvasculature. The existing immersed boundary/front tracking can be modified to simulate deformable vessel walls to include such effects.

Modeling glycocalyx layer: Glycocalyx is a glycoprotein that protects the vascular walls from direct exposure to blood flow, serving as a vascular permeability barrier. The glycocalyx layer can be modeled as a porous layer on the vascular wall [168]. This, in fact, would lead to deviation of the boundary condition from no-slip condition, and consequently may influence the wall-normal migration of deformable RBCs. This in turn may affect platelets/microparticles margination and near-wall dynamics. Including such effects in our model in order to get even more realistic conditions requires modifications to the sharp-interface immersed-boundary method.

Simulation of blood cell aggregation: The effect of RBC aggregation (rouleaux) on WBC adhesion has been studied extensively in the literature [99–101, 104, 127, 176, 190, 191]. Considering the discussions presented in Chapters 4, 5, and 7 on the significance of the RBC suspension microstructure, RBC aggregation is expected to also affect the transport of platelets and vascular micron-sized drug carriers. Our model could be embedded with an adhesion model similar to what has been used for particle–vessel wall adhesive interactions, to include the effects of RBC aggregation. The adhesion model could be further used to simulate the platelet aggregation as the next step in hemostasis after the platelets capture on the vessel walls.

Modeling cell membrane electrical charge: It is known that the membrane of RBCs is negatively charged and can respond to electric fields [193]. Modifications to our model can include such effects to simulate the biomedical applications such as cell/particle separation via dielectrophoresis (DEP) [194–198].

References

[1] Q. Zhu, C. Vera, R. J. Asaro, P. Sche, and L. A. Sung. A hybrid model for erythrocyte membrane: A single unit of protein network coupled with lipid bilayer. *Biophysical Journal*, **93**(2):386, 2007.

[2] N. Mohandas and E. Evans. Mechanical properties of the red cell membrane in relation to molecular structure and genetic defects. *Annual Review of Biophysics & Biomolecular Structure*, **23**:787, 1994.

[3] D. H. Boal. *Mechanics of the cell.* Cambridge University Press, 2002.

[4] C. Pozrikidis. *Modeling and simulation of capsules and biological cells.* Chapman & Hall/CRC, 2003.

[5] H. L. Goldsmith. Red cell motions and wall interactions in tube flow. *Federation Proceedings*, **30**:1578-1590, 1971.

[6] J. Happel, and H. Brenner. *Low Reynolds Number Hydrodynamics.* Kluwer, 1983.

[7] A. R. Pries, D. Neuhaus, and P. Gaehtgens. Blood viscosity in tubeflow: dependence on diameter. *Am. J. Physiol.*, **263**:H1770H1778, 1992.

[8] Y. C. Fung. *Biomechanics: Mechanical properties of living tissues.* Springer-Verlag, 1993.

[9] M. H. Flamm, and S.L. Diamond. Multiscale systems biology and physics of thrombosis under flow. *Annal. Biomed. Eng.*, DOI: 10.1007/s10439-012-0557-9, 2012.

[10] Z. M. Ruggeri, and G.L. Mendolicchio. Adhesion mechanisms in platelet function. *Circ. Res.*, **100**:1673-1685 2007.

[11] D. M. Wootton, and D.N. Ku. Fluid mechanics of vascular systems, diseases, and thrombosis. *Ann. Rev. Biomed. Eng.*, **1**:299-329, 1999.

[12] C. Xu, and D. M. Wootton. Platelet near-wall excess in porcine whole blood in artery-sized tubes under steady and pulsatile flow conditions. *Biorheology.*, **41**:113-125, 2004.

[13] C. Yeh, and E. C. Eckstein. Transient lateral transport of platelet-sized particles in flowing blood suspensions. *Biophys. J.*, **66**:1706-1716, 1994.

[14] E. C. Eckstein, D. L. Blisker, C. M. Waters, J. S. Kippenhan, and A. Tilles. Transport of platelets in flowing blood. *Ann. N.Y. Acad. Sci.*, **516**:442-452, 1987.

[15] G. J. Tangelder, H. C. Teirlinck, D. W. Slaaf, and R. S. Reneman. Distribution of blood platelets flowing in arterioles. *Am. J. Physiol.*, **248(3 Pt 2)**:H318-H323, 1985.

[16] P. A. Aarts, S. A. van den Broek, G. W. Prins, G. D. Kuiken, J. J. Sixma, and R. M. Heethaar. Blood platelets are concentrated near the wall and red blood cells, in the center in flowing blood. *Arteriosclerosis*, **8**: 819-824, 1988.

[17] V. T. Turitto, and C. L. Hall. Mechanical factors affecting hemostasis and thrombosis. *Thromb. Res.*, **92 (6, Suppl 2)**:S25-S31, 1998.

[18] H. L. Goldsmith, D. N. Bell, S. Braovac, A. Steinberg, and F. McIntosh. Physical and chemical effects of red cells in the shear-induced aggregation of human platelets. *Biophys. J.*, **69**:1584-1595, 1995.

[19] W. S. Uijttewaal, E. J. Nijhof, P. J. Bronkhorst, E. Den Hartog, and R, M. Heethaar. Near-wall excess of platelets induced by lateral migration of erythrocytes in flowing blood. *Am. J. Physiol. Heart*, **264**: H1239-H1244, 1993.

[20] A. W. Tilles, and E. C. Eckstein. The near-wall excess of platelet-sized particles in blood flow: its dependence on hematocrit and wall shear rate. *Microvasc. Res.*, **33**:211-223, 1987.

[21] P. A. M. M. Aarts, R. M. Heethaar, and J. J. Sixma. Red blood cell deformability influences platelets– vessel wall interaction in flowing blood. *Blood*, **64**:1228-1233, 1984.

[22] J. F. Koleski, and E. C. Eckstein, Near wall concentration profiles of 1.0 and 2.5 μm beads during flow of blood suspensions. *Trans. Am. Soc. Artif. Intern. Organs*, **37**:9-12, 1991.

[23] G. Antonini, G. Guiffant, and A. M. Dosne. Estimation of platelet diffusivity in flowing blood. *Biorheology*, **15**:111-117, 1978.

[24] T. E. Diller Comparison of red cell augmented diffusion and platelet transport. *J. Biomech. Eng.*, **110**:161-163, 1988.

[25] W. Wang, and M. R. King Multiscale modeling of platelet adhesion and thrombus growth *Annals of Biomed. Eng.*, **40**:2345-2354, 2012.

[26] M. B. Lawrence, and T. A. Springer. Leukocytes roll on a selectin at physiologic flow rates: distinction from and prerequisite for adhesion through integrins. *Cell*, **65**:859-873, 1991.

[27] L. J. Rinko, M. B. Lawrence, and W.H. Guilford. The molecular mechanics of P- and L-selectin lectin domains binding to PSGL-1. *Biophys. J.*, **86**:544-554, 2004.

[28] A. A. Tokarev, A. A. Butylin, and F. I. Ataullakhanov. Finite platelet size could be responsible for platelet margination effect. *Biophys. J.*, **101**:1835-1843, 2011.

[29] A. A. Tokarev, A. A. Butylin, and F. I. Ataullakhanov. Platelet adhesion from shear blood flow is controlled by near-wall rebounding collisions with erythrocytes. *Biophys. J.*, **100**:799-808, 2011.

[30] A. Kumar and M. D. Graham. Margination and segregation in confined flows of blood and other multicomponent suspensions *Soft Matter*, **8**:10536, 2012.

[31] A. Kumar and M. D. Graham. Segregation by membrane rigidity in flowing binary suspensions of elastic capsules. *Phys Rev E Stat Nonlin Soft Matter Phys*, **84**:066316, 2011.

[32] T. M. Allen, and P. R. Cullis. Drug delivery systems: entering the mainstream *Science*, **303**:1818-1822, 2004.

[33] J. E. Schnitzer. Vascular targeting as a strategy for cancer therapy. *N. Engl. J. Med.*, **339**:472-474, 1998.

[34] T. AlMomani, H. S. Udaykumar, J. S. Marshall, and K. B. Chandran. Microscale dynamic simulation of erythrocyte-platelet interaction in blood flow. *Ann. Biomed. Eng.*, **36**:905-920, 2008.

[35] V. Govindarajan, H. S. Udaykumar, and K. B. Chandran. Two dimensional simulation of flow and platelet dynamics in the hinge region of a mechanical heart valve. *J. Biomech. Eng.*, **131**:031002, 2009.

[36] L. M. Crowl, and A. L. Fogelson. Computational model of whole blood exhibiting lateral platelet motion induced by red blood cells. *Int. j. numer. method. biomed. eng.*, **26**:471-487, 2010.

[37] L. M. Crowl, and A. L. Fogelson. Analysis of mechanisms for platelet near-wall excess under arterial blood flow conditions. *J. Fluid Mech.*, **676**:348-375, 2011.

[38] T. Skorczewski, L. C. Erickson, and A. L. Fogelson. Platelet motion near a vessel wall or thrombus surface in two-dimensional whole blood simulations. *Biophys. J.*, **104**:1764-1772, 2013.

[39] L. Shi, T. W. Pan, and R. Glowinski. Numerical simulation of lateral migration of red blood cells in Poiseuille flows. *Int. J. Numer. Methods Fluids.*, **68**:1393-1408, 2010.

[40] E. Lac, and D. Barthes-Biesel. Pairwise interaction of capsules in simple shear flow: three-dimensional effects. *Phys. Fluids.*, **20**:040801, 2008.

[41] H. Zhao, and E. S. G. Shaqfeh. Shear-induced platelet margination in a microchannel. *Phys. Rev. E Stat. Nonlin. Soft Matter Phys.*, **83**:061924, 2011.

[42] H. Zhao, E. S. G. Shaqfeh, and V. Narsimhan. Shear-induced particle migration and margination in a cellular suspension. Phys. Fluids., **24**:011902-012000, 2012.

[43] R. B. Huang, S. Mocherla, M. J. Heslinga, P. Charoenphol. and O. Eniola-Adefeso, Dynamic and cellular interactions of nanoparticles in vascular-targeted drug delivery (review) *Mol. Membr. Biol.*, **27**:190-205, 2010.

[44] M. Caldorera-Moore, N. Guimard, L. Shi, and K. Roy. Designer nanoparticles: incorporating size, shape and triggered release into nanoscale drug carriers. *Expert Opin. Drug Delivery*, **7**:479-495, 2010.

[45] J. D. Pillai, S. S. Dunn, M. E. Napier, and J. M. DeSimone. Novel platforms for vascular carriers with controlled geometry. *IUBMB Life*, **63**:596-606, 2011.

[46] Y. Liu, A. Thomas, D. Ou-Yang, and V. R. Muzykantov. The shape of things to come: importance of design in nanotechnology for drug delivery. *Ther. Delivery*, **3**:181-194, 2012.

[47] J. Chen, N. E. Clay, N. Park, H. Kong. Non-spherical particles for targeted drug delivery *Chem. Eng. Sci.*, **125**:20-24, 2015.

[48] F. Gentile, C. Chiappini, D. Fine, R. C. Bhavane, M. S. Peluccio, M. M. Cheng, X. Liu, M. Ferrari, and P. Decuzzi. The effect of shape on the margination dynamics of non-neutrally buoyant particles in two-dimensional shear flows. *J. Biomech.*,**41**:2312-2318, 2008.

[49] N. Doshi, B. Prabhakarpandian, A. Rea-Ramsey, K. Pant, S. Sundaram, and S. Mitragotri. Flow and adhesion of drug carriers in blood vessels depend on their shape: a study using model synthetic microvascular networks. *J. Controlled Release*,**146**:196-200, 2010.

[50] G. Adriani, M. D. de Tullio, M. Ferrari, F. Hussain, G. Pascazio, X. Liu, and P. Decuzzi. The preferential targeting of the diseased microvasculature by disk-like particles. *Biomaterials*, **33**: 5504-5513, 2012.

[51] S. Shah, Y. Liu, W. Hu, and J. Gao. Modeling particle shape-dependent dynamics in nanomedicine. *J. Nanosci. Nanotechnol.*, **11**:919-928, 2011.

[52] R. Toy, E. Hayden, C. Shoup, H. Baskaran, and E. Karathanasis. The effects of particle size, density and shape on margination of nanoparticles in microcirculation. *Nanotechnology*, **22**:115101, 2011.

[53] A. C. Anselmo, C. L. Modery-Pawlowski, S. Menegatti, S. Kumar, D. R. Vogus, L. L. Tian, M. Chen, T. M. Squires, A. S. Gupta, and S. Mitragotri. Platelet-like nanoparticles: mimicking shape, flexibility, and surface biology of platelets to target vascular injuries. *ACS Nano*, **8**:11243- 11253, 2014.

[54] P. Decuzzi, and M. Ferrari The adhesive strength of non-spherical particles mediated by specific interactions. *Biomaterials*, **27**:5307-5314, 2006.

[55] T. R. Lee, M. Choi, A. M. Kopacz, S. H. Yun, W. K. Liu, and P. Decuzzi. On the near-wall accumulation of injectable particles in the microcirculation: smaller is not better. *Sci. Rep.*, **3**:2079, 2013.

[56] K. Namdee, A. J. Thompson, P. Charoenphol, and O. Eniola- Adefeso. Margination propensity of vascular-targeted spheres from blood flow in a microfluidic model of human microvessels. *Langmuir*, **29**:2530-2535, 2013.

[57] P. Charoenphol, R. B. Huang, and O. Eniola-Adefeso. Potential role of size and hemodynamics in the efficacy of vascular-targeted spherical drug carriers. *Biomaterials*, **31**:1392-1402, 2010.

[58] A. L. van de Ven, P. Kim, O. Haley, J. R. Fakhoury, G. Adriani, J. Schmulen, P. Moloney, F. Hussain, M. Ferrari, X. Liu, S. H. Yun, and P. Decuzzi. Rapid tumoritropic accumulation of systemically injected plateloid particles and their biodistribution. *J. Controlled Release*, **158**: 148-155, 2012.

[59] A. J. Thompson, E. M. Mastria, and O. Eniola-Adefeso. The margination propensity of ellipsoidal micro/nanoparticles to the endothelium in human blood flow. *Biomaterials*, **34**:5863-5871, 2013.

[60] S. Muro, C. Garnacho, J. Champion, J. Leferovich, C. Gajewski, E. H. Schuchman, S. Mitragotri, and V. R. Muzykantov. Control of endothelial targeting and intracellular delivery of therapeutic enzymes by modulating the size and shape of ICAM-1-targeted carriers. *Mol. Ther.*, **16**:1450-1458, 2008.

[61] K. Muller, D. A. Fedosov, and G. Gompper. Margination of micro- and nanoparticles in blood flow and its effect on drug delivery. *Sci. Rep.*, **4**: 4871, 2014.

[62] D. A. Reasor Jr, M. Mehrabadi, D. N. Ku, and C. K. Aidun. Determination of critical parameters in platelet margination. *Ann. Biomed. Eng.*, **41**:238-249, 2012.

[63] M. Mehrabadi, D. N. Ku, and C. K. Aidun A continuum model for platelet transport in flowing blood based on direct numerical simulations of cellular blood flow. *Ann. Biomed. Eng.*, **43(6)**:1410-1421, 2015.

[64] A.J. Lusis. Atherosclerosis. *Nature*, **407**:233, 2000.

[65] J.M. Tarbell, Z.-D. Shi, J. Dunn, and H. Jo. Fluid mechanics, arterial disease, and gene expression. *Annu. Rev. Fluid Mech.*, **46**:591, 2014.

[66] D.N. Ku. Blood flow in arteries. *Ann. Rev. Fluid Mech.*, **29**:399, 1997.

[67] D.P. Giddens, C.K. Zarins, and S. Glagov. The role of fluid mechanics in the localization and detection of atherosclerosis. *J. Biomech. Eng.*, **115**:588, 1993.

[68] G.A. Lanza, and F. Crea. Primary coronary microvascular dysfunction: clinical presenta- tion, pathophysiology, and management. *Circulation*, textbf121:2317, 2010.

[69] M. Kanbay, L.-G. Sanchez-Lozada, M. Franco, M. Madero, Y. Solak, B. Rodriguez-Iturbe, A. Covic, and R.J. Johnson. Microvascular disease and its role in the brain and cardiovascular system: a potential role for uric acid as a cardiorenal toxin. *Nephrol Dial Transplant*, **26**:430, 2011.

[70] B. Ahmed. New insights into the pathophysiology, classification, and diagnosis of coronary microvascular dysfunction. *Coronary Artery Disease*, **25**:439, 2014.

[71] M.R. Vesely, and V. Dilsizian. Microvascular angina: Assessment of coronary blood flow, flow reserve, and metabolism. *Curr. Cardiol. Rep.*, **13**:151, 2011.

[72] E.H. Wong, P.M. Pullicino, and R. Benedict. Deep cerebral infarcts extending to the subinsular region. *Stroke*, **32**:2272, 2007.

[73] D. H. Kang, J. Kanellis, C. Hugo, L. Truong, S. Anderson, D. Kerjaschki, G.F. Schreiner, and R.J. Johnson. Role of microvascular endothelium in progressive renal disease. *J. American Soc. Nephrology*, **13**:806, 2002.

[74] J.J. Wang, S. Cugati, M.D. Knudtson, E. Rochtchina, R. Klein, B.E.K. Klein, T.Y. Wong, and P. Mitchell. Retinal arteriolar emboli and long-term mortality: pooled data analysis from two older populations. *Stroke*,**37**:1833, 2006.

[75] G.B Chapman, and G. R. Cokelet. Flow resistance and drag forces due to multiple adherent leukocytes in postcapillary vessels. *Biophys. J.*, **74**:3292, 1998.

[76] J.L. Bull. Cardiovascular bubble dynamics. *Critical Rev. Biomed. Eng.*, **33**:299, 2005.

[77] A.H.G. Isfahani, and J.B. Freund. Forces on a wall-bounded leukocyte in a small vessel due to red cells in the blood stream. *Biophys. J.*, **103**:1604, 2012.

[78] M. Faivre, M. Abkarian, K. Bickraj, and H.A. Stone. Geometrical focusing of cells in a microfluidic device: An approach to separate blood plasma. *Biorheol.*, **43**:147, 2006.

[79] H. Fujiwara, T. Ishikawa, R. Lima, N. Matsuki, Y. Imai, H. Kaji, M. Nishizawa, and T. Yam- aguchi. Red blood cell motions in high-hematocrit blood flowing through a stenosed microchannel. *J. Biomech.*, **42**:838, 2009.

[80] Y. C. Fung. *Biomechanics: Circulation.* Springer-Verlag, 1993.

[81] B. Das, P.C. Johnson, and A.S. Popel. Computational fluid dynamic studies of leukocyte adhesion effects on non-Newtonian blood flow through microvessels. *Biorheol.*, **37**:239, 2000.

[82] V.P. Srivastava, and M. Saxena. Two-layered model of Casson fluid flow through stenotic blood vessels: applications to the cardiovascular systems. *J. Biomech.*, **27**:921, 1994.

[83] S. Kim, R.L. Kong, A.S. Popel, M. Intaglietta, and P.C. Johnson. Temporal and spatial variations of cell-free layer width in arterioles. *Am. J. Physiol. Heart Circ. Physiol.*, **293**:H1526, 2007.

[84] G. Drazer, J. Koplik, B. Khusid, and A. Acrivos. Deterministic and stochastic behaviour of non-Brownian spheres in sheared suspensions. *J. Fluid Mech.*, **460**:307-335, 2002.

[85] M. Marchioro, and A. Acrivos. Shear-induced particle diffusivities from numerical simulations. *J. Fluid Mech.*, **443**:101-128, 2001.

[86] J.B. Freund. Numerical simulation of flowing blood cells. *Annu. Rev. Fluid Mech.*, **46**: 67, 2014.

[87] A.S. Popel, and P.C. Johnson. Microcirculation and hemorheology. *Annu. Rev. Fluid Mech.*, **37**:43, 2005.

[88] A.R. Pries, T.W. Secomb, and P. Gaehtgens. Biophysical aspects of blood flow in the microvasculature. *Cardivasc. Res.*, **32**:654, 1996.

[89] M.T. Hinds, Y.J. park, S.A. Jones, D.P. Giddens, and B.R. Alevriadou. Local hemodynamics affect monocytic cell adhesion to a three-dimensional flow model coated with E-selectin. *J. Biomech.*, **34**:95, 2001.

[90] C. Hahn, and M. Schwartz. Mechanotransduction in vascular physiology and atherogenesis. *Nat. Rev.*, **10**:53, 2009.

[91] J.S. Uzarski, E.W. Scott, and P.S.McFetridge. Adaptation of endothelial cells to physiologically- modeled variable shear stress. *PLOS One*, textbf8:e57004, 2013.

[92] F.J. Tovar-Lopez, G. Rosengarten, M. Nasabi, V. Sivan, K. Khoshmanesh, S.P. Jackson, A. Mitchell, and W.S. Nesbitt. An investigation on platelet transport during thrombus formation at microscale stenosis. *PLOS One*, **8**:e74123, 2013.

[93] L. Rouleau, I.B. Copland, J. C. Tardif, R. Mongrain, and R.L. Leask. Neutrophil adhesion on endothelial cells in a novel asymmetric stenosis model: effect of wall shear stress gradients. *Annals Biomed. Eng.*, **38**:2791, 2010.

[94] A.L. Fogelson, and K.B Neeves. Fluid mechanics of blood clot formation. *Annu. Rev. Fluid Mech.*, **47**:377, 2015.

[95] R. van der Meel, M. Fens, P. Vader , W. W. van Solinge, O. Eniola-Adefeso, and R. M. Schiffelers. Extracellular vesicles as drug delivery systems: Lessons from the liposome field. *J. Controlled Release*, **195**:72-85, 2014.

[96] J. J. Rychak, J. R. Lindner, K. Ley, and A. L. Klibanov. Deformable gas-filled microbubbles targeted to P-selectin. *J. Controlled Release*, **114**:288-299, 2006.

[97] M. R. King, and D. A. Hammer. Multiparticle adhesive dynamics: hydrodynamic recruitment of rolling leukocytes. *Proc. Natl. Acad. Sci. USA.*, **98**:14919-14924, 2001.

[98] D. R. Subramaniam, D. J. Gee, and M. R. King. Deformable cell-cell and cell-substrate interactions in semi-infinite domain. *J Biomech.*, **46(6)**:1067-1074, 2013.

[99] T. Watts, M. Barigou, and G. B. Nash. Comparative rheology of the adhesion of platelets and leukocytes from flowing blood: why are platelets so small? *Am J Physiol Heart Circ Physiol*, **304**:H1483-H1494, 2013.

[100] G. B. Nash, T. Watts, C. Thornton, and M. Barigou Red cell aggregation as a factor influencing margination and adhesion of leukocytes and platelets. *Clin. Hemorheol. Microcirc.*, **39**:303-310, 2008.

[101] A. Jain, L. L. Munn. Determinants of Leukocyte Margination in Rectangular Microchannels. *PLoS One*, **4(9)**:e7104, 2009.

[102] E.R. Damiano, J. Westheider, A. Tozeren, and K. Ley. Variation in the velocity, deformation, and adhesion energy density of leukocytes rolling within venules. *Circulation Research*, **79**:1122-1130, 1996.

[103] D. B. Khismatullin, and G. A. Truskey. A 3D numerical study of the effect of channel height on leukocyte deformation and adhesion in parallel-plate flow chambers. *Microvascular Research*, **68**:188-202, 2004.

[104] K. B. Abbitt, and G. B. Nash. Rheological properties of the blood influencing selectin-mediated adhesion of flowing leukocytes. *Am. J. Physiol. Heart. Circ. Physiol.*, **285**:H229-H240, 2003.

[105] M. B. Kim, and I. H. Sarelius. Role of shear forces and adhesion molecule distribution on P-selectin-mediated leukocyte rolling in postcapillary venules. *Am. J. Physiol. Heart Circ. Physiol.*, **287**:H2705-H2711, 2004.

[106] C. Dong, J. Cao, E. J. Stuble, and H. H. Lipowsky. Mechanics of Leukocyte Deformation and Adhesion to Endothelium in Shear Flow *Annals Biomed. Eng.*, **27**, 298-312, 1999.

[107] G. W. Schmid-Schoenbein, Y. Fung, and B. W. Zweifach. Vascular endothelium-leukocyte interaction: sticking shear force in venules. *Circ. Research*, **36**:173-184, 1975.

[108] A. Tozeren, K. Ley. How do selectins mediate leukocyte rolling in venules? *Biophys. J.*, **63(3)**:700-709, 1992.

[109] J. J. Bishop, P. Nance, A. S. Popel, M. Intaglietta, and P. C. Johnson. Effect of erythrocyte aggregation on velocity profiles in venules. *Am. J. Physiol.*, **280**:H222-H236, 2001.

[110] J. J. Bishop, A. S. Popel, M. Intaglietta, and P. C. Johnson. Effect of aggregation and shear rate on the dispersion of red blood cells flowing in venules. *Am. J. Physiol.*, **283**:H1985-H1996, 2002.

[111] M. Sharan, and A. S. Popel. A two-phase model for flow of blood in narrow tubes with increased effective viscosity near the wall. *Biorheology.*, **38**:415-428, 2001.

[112] P. Bagchi Mesoscale simulation of blood flow in small vessels. *Biophys. J.*, **92**:1858-1877, 2007.

[113] V. Pappu, P. Bagchi. 3D computational modeling and simulation of leukocyte rolling adhesion and deformation. *Computers in Biology and Medicine*, **38(6)**:738-753, 2008.

[114] V. Pappu, S. K. Doddi, P. Bagchi. A computational study of leukocyte adhesion and its effect on flow pattern in microvessels. *J. Theor. Biol.*, **254(2)**:483-498, 2008.

[115] M .R. King, D. Bansal, M. B. Kim, and I. H. Sarelius, The effect of hematocrit and leukocyte adherence on flow direction in the microcirculation. *Ann. Biomed. Eng.*, **32**:803-814, 2004.

[116] T. N. Thompson, P. L. L. Celle, and G. R. Cokelet Perturbation of red blood cell flow in small tubes by white blood cells *Pflugers Arch.*, **413**:372-377, 1989.

[117] D. B. Khismatullin, and G. A. Trueskey. Leukocyte rolling on P-selectin: a three-dimensional numerical study of the effect of cytoplasmic viscosity *Biophys. J.*, **102**:1757-1766, 2012.

[118] M. J. Mitchell, M. R. King. Leukocytes as carriers for targeted cancer drug delivery. *Expert Opin. Drug Deliv.*, **12(3)**:375-392, 2015.

[119] B. P. Helmke, S. N. Bremner, B. W. Zweifach, R. Skalak,G. W. Schmid-Schonbein. Mechanisms for increased blood flow resistance due to leukocytes *Americ. J. Physiol. Heart Circ. Physiol.*, **42**:H2884-H2890, 1997.

[120] L. L. Munn, R. J. Melder, and R. K. Jain. Role of erythrocytes in leukocyte-endothelial interactions: mathematical model and experimental validation *Biophys. J.*, **71**:466-478, 1996.

[121] N. Takeishi, Y. Imai, K. Nakaaki, T. Yamaguchi, and T. Ishikawa. Leukocyte margination at arteriole shear rate *Physiol Rep.*, **2(6)**:e12037, 2014.

[122] J. C. Firrell , and H. H. Lipowsky Leukocyte margination and deformation in mesenteric venules of rat. *Americ. J. Physiol. Heart Circ. Physiol.*, **256(6)**:H1667-1674, 1989.

[123] T. Yago, A. Leppanen, H Qiu, W. D. Marcus, M. U. Nollert, C. Zhu, R. D. Cummings, R. P. McEver. Distinct molecular and cellular contributions to stabilizing selectin mediated rolling under flow. *J. Cell Biol.*, **158**: 787-799, 2002.

[124] X. Lei, M. B. Lawrence, and C. Dong. Influence of cell deformation on leukocyte rolling adhesion in shear Flow. *J. Biomech. Eng.*, **121(6)**:636-643, 1999.

[125] J. R. Less, T. C. Skalak, E. M. Sevick, and R. K. Jain. Microvascular architecture in a mammary carcinoma: branching patterns and vessel dimensions. *Cancer Res.*, **51(1)**:265-273, 1991.

[126] D. A. Fedosov, J. Fornleitner, and G. Gompper. Margination of white blood cells in microcapillary flow. *PRL*, textbf108:028104 2012.

[127] D. A. Fedosov, and G. Gompper. White blood cell margination in microcirculation. *Soft Matter*, **10**:2961, 2014.

[128] N. A. Mody, and M. R. King. Platelet adhesive dynamics. Part I: Characterization of platelet hydrodynamic collisions and wall Effects. *Biophys. J.*, **95**:2539-2555, 2008.

[129] N. A. Mody, and M. R. King. Platelet adhesive dynamics. Part II: High shear-induced transient aggregation via GPIba-vWF-GPIba bridging. *Biophys. J.*, **95**:2556-2574, 2008.

[130] A. Guazzelli, and J. F. Morris. *A Physical Introduction to Suspension Dynamics.* Cambridge University Press, 2012.

[131] C. S. Peskin. Numerical analysis of blood flow in the heart. *Journal of Computational Physics*, **25**:220, 1977.

[132] S. O. Unverdi and G. Tryggvason. A front-tracking method for viscous, incompressible, multi-fluid flows. *Journal of Computational Physics*, **100**:25, 1992.

[133] G. Tryggvason, B. Bunner, A. Esmaeeli, N. Al-Rawahi, W. Tauber, J. Han, S. Nas, and Y. Jan. A front-tracking method for the computations of multiphase flow. *Journal of Computational Physics*, **169**:708, 2001.

[134] S. K. Doddi and P. Bagchi. Effect of inertia on the hydrodynamic interaction between two liquid capsules in simple shear flow. *International Journal of Multiphase Flow*, **34**:375, 2008.

[135] S. K. Doddi and P. Bagchi. Lateral migration of a capsule in a plane poiseuille flow in a channel. *International Journal of Multiphase Flow*, **34**:966, 2008.

[136] S. K. Doddi. Three-dimensional computational modeling and simulation of biological cells and capsules. *PhD thesis*, 2008. Rutgers University.

[137] J. M. Charrier, S. Shrivastava, and R. Wu. Free and constrained inflation of elastic membranes in relation to thermoforming-non-axisymmetric problems. *The Journal of Strain Analysis*, **24** (2):55, 1989.

[138] S. Shrivastava and J. Tang. Large deformation finite element analysis of non-linear viscoelastic membranes with reference to thermoforming. *The Journal of Strain Analysis*, **28**:31, 1993.

[139] C. D. Eggleton and A. S. Popel. Large deformation of red blood cell ghosts in a simple shear flow. *Physics of Fluids*, **10**(8):1834, 1998.

[140] R. Skalak, A. Tozeren, P. R. Zarda, and S. Chien. Strain energy function of red blood cell membranes. *Biophysical Journal*, **13**:245, 1973.

[141] E. Lac, D. Barthès-Biesel, N. A. Pelekasis, and J. Tsamopoulos. Spherical capsules in three-dimensional unbounded stokes flows: effect of the membrane constitutive law and onset of buckling. *Journal of Fluid Mechanics*, **516**:303, 2004.

[142] W. Helfrich. Elastic properties of lipid bilayers: Theory and possible experiments. *Z. Naturforsch C*, **28**:693, 1973.

[143] O. -Y. Zhong-can and W. Helfrich. Bending energy of vesicle membranes: General expressions for the first, second, and third variation of the shape energy and applications to spheres and cylinders. *Physical Review A*, **39**:5280, 1989.

[144] M. M. Dupin, I. Halliday, C. M. Care, L. Alboul, and L. L. Munn. Modeling the flow of dense suspensions of deformable particles in three dimensions. *Physical Review E*, **75**: 066707, 2007.

[145] M. Dembo, D. C. Torney, K. Saxman, and D. Hammer. The reaction-limited kinetics of membrane-to-surface adhesion and detachment *Proc. R. Soc. Lond. B*, **234**:55-83, 1988.

[146] G. I. Bell. Models for the specific adhesion of cells to cells: a theoretical framework for adhesion mediated by reversible bonds between cell surface molecules. *Science*, **200**:618-627, 1978.

[147] G. I. Bell, M. Dembo, and P. Bongrand. Competition between nonspecific repulsion and specific bonding *Biophys. J.*, **45**:1051-1064, 1984.

[148] M. R. King, D. A. Hammer. Multiparticle adhesive dynamics. interactions between stably rolling cells. *Biophys. J.*, **81**: 799-813, 2001.

[149] D. A. Hammer, S. M. Apte. Simulation of cell rolling and adhesion on surfaces in shear flow: general results and analysis of selectin-mediated neutrophil adhesion. *Biophys. J.*, **63**:35-57, 1992.

[150] K. Chang, D. F. J. Tees, and D. A. Hammer. The state diagram for cell adhesion under flow: leukocyte rolling and firm adhesion. PNAS, **97**: 11262-11267, 2000.

[151] M. Dembo. On peeling an adherent cell from a surface *Lect. Math. Life Sci.*, **24**: 51–77, 1994.

[152] P. Bagchi and R. Murthy Kalluri. Rheology of a dilute suspension of liquid-filled elastic capsules. *Physical Review E*, **81**:056320, 2010.

[153] A. Yazdani, and P. Bagchi. Three-dimensional numerical simulation of vesicle dynamics using a front-tracking method *Phys. Rev. E*, **85**:056308, 2012.

[154] V. T. Turitto, and H. J. Weiss. Platelet and red cell involvement in mural thrombogenesis. *Ann. N.Y. Acad. Sci.*, **416**:363-376, 1983.

[155] V. T. Turitto, and H. J. Weiss, Red blood cells: their dual role in thrombus formation. *Science*, textbf207:541-543 1980.

[156] V. T. Turitto, and H. R. Baumgartner. Platelet interaction with subendothelium in a perfusion system: physical role of red blood cells. *Microvasc. Res.*, **9**:335-344, 1975.

[157] E. C. Eckstein, J. F. Koleski, and C. M. Waters. Concentration profiles of 1.0 and 2.5 μm beads during blood flow. Hematocrit effects. *Trans. Am. Soc. Artif. Intern. Organs*, **35(3)**:188-190, 1989.

[158] V. T. Turitto, A. M. Benis, and E. F. Leonard, Platelet diffusion in flowing blood. *Ind. Eng. Chem. Fundam.*, **11**:216-223, 1972.

[159] E. C. Eckstein, and F. Belgacem. Model of platelet transport in flowing blood with drift and diffusion terms. *Biophys. J.*, **60**:53-69, 1991.

[160] S. P. Kim, K. Ong, O. Yalcin, M. Intaglietta, and P. C. Johnson. The cell-free layer in microvascular blood flow. *Biorheology*, **46**:181-189, 2009.

[161] T. M. Fischer, M. Stohr-Liesen, and H. Schmid-Schonbein. The red cell as a fluid droplet: tank-tread like motion of the human erythrocyte membrane in shear flow. *Science*, **202**:894, 1978.

[162] S. R. Keller, and R. Skalak. Motion of a tank-treading ellipsoidal particle in a shear flow. *J. Fluid Mech.*, **120**:27-47, 1982.

[163] M. Abkarian, M. Faivre, and A. Viallat. Swinging of red blood cells under shear flow. Phys. Rev. Lett., **98**:188302, 2007.

[164] J. M. Skotheim, and T. W. Secomb. Oscillatory dynamics and the tank-treading-to-tumbling transition. *Phys. Rev. Lett.*, **98**:078301, 2007.

[165] Y. Sui, Y. T. Chew, P. Roy, Y. P. Cheng, and H. T. Low, Dynamic motion of red blood cells in simple shear flow. *Phys. Fluids*, **20**:112106, 2008.

[166] D. V. Le, and K. H. Chiam, Hydrodynamic interaction between two nonspherical capsules in shear flow. *Phys. Rev. E*, **84**:056322, 2011.

[167] G. Leone, S. Sica, P. Chiusolo, L. Teofili, and V. De Stefano, Blood cell diseases and thrombosis. *Haematologic*, **86**:1236-1244, 2001.

[168] T. W. Secomb, R. Hsu, and A. R. Pries, A model for red blood cell motion in glycocalyx-lined capillaries. *Am. J. Physiol.*, **274**: H1016-H1022, 1998.

[169] G. B. Jeffery, The motion of ellipsoidal particles immersed in a viscous fluid. *Proc. R. Soc. London Ser. A*, **102**:161-170, 1922.

[170] M. Loewenberg, and E. J. Hinch, Collision of two deformable drops in shear Flow. *J. Fluid Mech.*, **338**:299-315, 1997.

[171] A. M. Forsyth, J. Wan, P. D. Owrutsky, M. Abkarian, and H. A. Stone. Multiscale approach to link red blood cell dynamics, shear viscosity, and ATP release. *Proc Natl. Acad. Sci. U.S.A.*, **108**: 10986-10991, 2011.

[172] H. L. Goldsmith, and V. T. Turitto, , Rheological aspects of thrombosis and hemostasis: basic principles and applications. ICTH-Report 781 Subcommittee on Rheology of the International Committee on Thrombosis and 782 Hemostasis. *Thromb. Haemost.*, **55(3)**:415-435, 1986.

[173] N. A. Mody, and M. R. King. Three-dimensional simulations of a platelet-shaped spheroid near a wall in shear flow. *Phys. Fluids.*, **17**:113302, 2005.

[174] C. Pozrikidis. Flipping of an adherent blood platelet over a substrate. *J. Fluid Mech.*, **568**:161-172, 2006.

[175] Y. Han, A. M. Alsayed, M. Nobili, J. Zhang, T. C. Lubensky, A. G. Yodh. Brownian motion of an ellipsoid. *Science*, **314**:626-630, 2006.

[176] M. J. Pearson, and H. H. Lipowsky. Effect of fibrinogen on leukocyte margination and adhesion in postcapillary venules. *Microcirculation*, **11**: 295-306, 2004.

[177] C. Sun, and L. L. Munn. Influence of erythrocyte aggregation on leukocyte margination in postcapillary expansions: a lattice Boltzmann analysis. *Phys. A*, **362**:191-196, 2006.

[178] A. Z. K. Yazdani, and P. Bagchi. Phase diagram and breathing dynamics of a single red blood cell and a biconcave capsule in dilute shear flow. *Phys. Rev. E: Stat., Nonlinear, Soft Matter Phys.*, **84**:026314-026310, 2011.

[179] C. Dupont, A. V. Salsac, and D. Barthes-Biesel. Off-plane motion of a prolate capsule in shear flow. *J. Fluid Mech.*, **721**:180-198, 2013.

[180] C. Dupont, F. Delahaye, A. V. Salsac, and D. Barthes-Biesel. Off-plane motion of an oblate capsule in a simple shear flow. *Comput. Methods Biomech. Biomed. Eng.*, **16(sup1)**, 4-5, 2013.

[181] Z. Wang, Y. Sui, P. D. M. Spelt, and W. Wang. Three-dimensional dynamics of oblate and prolate capsules in shear flow. *Phys. Rev. E: Stat., Nonlinear, Soft Matter Phys.*, **88**:053021, 2013.

[182] D. Cordasco, and P. Bagchi. Orbital drift of capsules and red blood cells in shear flow. *Phys. Fluids*, **25**:091902, 2013.

[183] J. B. Freund, and J. Vermot. The wall-stress footprint of blood cells flowing in microvessels. *Biophys. J.*, **106**:752, 2014.

[184] J. B. Freund, and M. M. Orescanin. Cellular flow in a small blood vessel. *J. Fluid Mech.* , **671**:466, 2011.

[185] W. Wang, T. G. Diacovo, J. Chen, J. B. Freund, and Michael R. King Simulation of Platelet, Thrombus and Erythrocyte Hydrodynamic Interactions in a 3D Arteriole with In Vivo Comparison *PLOS ONE*, **8(10)**:e76949, 2013.

[186] D.A. Fedosov, B. Caswell, A.S. Popel, and G.E. Karniadakis. Blood flow and cell-free layer in microvessels. *Microcirculation*, **17(8)**:615, 2010.

[187] A.R. Pries, A. Fritzsche, K. Ley, and P. Gaehtgens. Redistribution of red blood cell flow in microcirculatory networks by hemodilution. *Circ. res.*, **70**:1113, 1992.

[188] U. Bagge, A. Blixt, and K. G. Strid. The initiation of post-capillary margination of leukocytes: studies in vitro on the influence of erythrocyte concentration and flow velocity. *Int. J. Microcirc. Clin. Exp.*, **2(3)**:215-27, 1983.

[189] T. Hibiki, M. Ishii. Lift force in bubbly flow systems *Chem. Eng. Sci.*, **62**:6457-6474, 2007.

[190] G. W. Schmid-Schonbein, S. Usami, R. Skalak, and S. Chien. The interaction of leukocytes and erythrocytes in capillary and postcapillary vessels *Microvascular Research*, **19(1)**:45-70, 1980.

[191] G. Tomaiuolo, L. Lanotte, G. Ghigliotti, C. Misbah, and S. Guido. Red blood cell clustering in Poiseuille microcapillary flow *Phys. Fluids*, **24**:051903, 2012.

[192] T. Omori, Y. Imai, K. Kikuchi, T. Ishikawa, and T. Yamaguchi. Hemodynamics in the Microcirculation and in Microfluidics *Annal. Biomed. Eng.*, **43(1)**:238-257, 2014.

[193] K. Jan, and S. Chien. Role of surface electric charge in red blood cell interactions *J. General Physiol.*, **61**:638-654, 1973.

[194] J. Yang, Y. Huang, X. B. Wang, F. F. Becker, and P. R. Gascoyne. Cell separation on microfabricated electrodes using dielectrophoretic/gravitational field-flow fractionation. *Anal Chem.*, **71(5)**:911-8, 1999.

[195] P. R. Gascoyne, X. B. Wang, Y. Huang, and F. F. Becker. Dielectrophoretic separation of cancer cells from blood *IEEE Trans. Ind. Appl.*, **33(3)**:670-678, 1997.

[196] J. Yang, Y. Huang, X. B. Wang, F. F. Becker, and P. R. Gascoyne. Differential analysis of human leukocytes by dielectrophoretic field-flow-fractionation. *Biophys J.*, **78(5)**:2680-2689, 2000.

[197] P. R. Gascoyne, and J. Vykoukal. Particle separation by dielectrophoresis. *Electrophoresis.*, **23(13)**:1973-1983, 2002.

[198] X. B. Wang, J. Yang, Y. Huang, J. Vykoukal, F. F. Becker, and P. R. Gascoyne. Cell separation by dielectrophoretic field-flow-fractionation *Anal. Chem.*, **72**:832-839, 2000.